Properties of the interstellar medium of the star-forming galaxy, IC10, at various spatial scales

Fiorella Lucia Polles

NNT : 2017SACLS276

Thèse de doctorat de l'Université Paris-Saclay préparée au Université Paris-Sud

Ecole doctorale n°127
Astronomie et astrophysique d'Île-de-France
Spécialité de doctorat : Astronomie et astrophysique

par

Mme Polles Fiorella Lucia

Properties of the interstellar medium of the star-forming galaxy, IC 10, at various spatial scales

Thèse présentée et soutenue à Gif-sur-Yvette, le 29 september 2017.

Composition du Jury :

M.	Verstraete Laurent	Professeur Université Paris-Sud XI/IAS	(Président du jury)
Mme	Satyapal Shobita	Professeur George Mason University	(Rapporteur)
M.	Schilke Peter	Professeur University of Koeln	(Rapporteur)
Mme	Meixner Margaret	Professeur Space Telescope Science Institute	(Examinatrice)
Mme	Habart Emilie	Maître de Conférence Université Paris-Sud XI/IAS	(Examinatrice)
Mme	Hughes Annie	Astronome adjoint IRAP, CNAP	(Examinatrice)
Mme	Madden Suzanne	Ingenieur CEA, AIM	(Directrice de thèse)

Abstract

The InterStellar Medium (ISM) provides the details of the environment and processes that lead to star formation, which in turn, drives the evolution of a galaxy. Moreover, it is the site of stellar birth and the repository of stellar ejecta, hosting the signatures of metal enrichment. How stars have been formed in galaxies in the early universe, when heavy elements are deficient, is a fundamental issue in astrophysics. While it is hard to analyze the ISM chemistry at high redshifts, the Local Group of galaxies offers the opportunity to study several 'chemically-young' dwarf galaxies in detail. These dwarfs are perfect laboratories to investigate how the metal-poor ISM affects the interplay between gas, dust and stars.

This thesis project investigates the properties of the multi-phase ISM of the nearby dwarf galaxy IC10, which has a metallicity of 1/3 solar. In particular, it focuses on the analysis of the physical properties of the compact HII regions and the diffuse ionized gas, traced by the mid- and far-infrared cooling lines. The proximity of this galaxy (d=700 kpc) enables the analysis of the ISM on different spatial scales: from the compact, bright clumps ($\sim$25 pc) to the whole star-forming body of the galaxy ($\sim$650pc). It has been observed with the space telescopes *Spitzer* and *Herschel*, providing a set of $\sim$16 infrared emission lines. I complemented this dataset with new observations made with the SOFIA airborne telescope.

I have studied the spatial distribution of the far-infrared (FIR) lines (linear resolution $\sim$40 pc). I found that [OIII] 88μm is the brightest infrared cooling line everywhere along the body of the galaxy, suggesting a high filling factor of diffuse ionized gas. The ISM is very porous, allowing UV photons to leak from the HII regions and traverse large distances, unique to low metallicity galaxies with low dust abundance. [CII] 157.7 μm, which can arise from both ionized and neutral gas, is the second brightest FIR cooling line. Despite the prominent ionized gas phase, the ratio [CII] 157.7 μm/[NII] 121.9 μm shows that most of the [CII] 157.7 μm emission (at least 98%) comes from the neutral Photo-Dissociation Regions (PDRs), not from the ionized gas.

To assess the physical properties (e.g., density, extinction) of the ISM and the nature of the ionizing sources, the observed mid-infrared (MIR) and FIR lines were compared to photoionization and photodissociation models. Using CLOUDY (Ferland et al. 2013), I have built grids of models adapted to the specific case of IC 10 and I have tested two different strategies to compare the observations with the model predictions: line ratios and absolute flux values. Since the sensitivity and the spatial coverage of the observations were not homogeneous, it was not possible to select the same combinations of tracers at the different scales. Hence, exploring those methods was necessary to extract the best possible constraints on the physical properties. The investigation suggested that, based on the dataset, the best choice was to compare all of the available tracers at each scale using the line absolute values.

The modeling enabled me to determine the properties of the brightest clumps within the galaxy and demonstrate that the emission at large scales ($\sim$300 pc) is dominated by that of the compact, bright clumps that lie in the region. Moreover, at those large scales we found that a simple description of a single component model was not sufficient to reproduce all of the tracers. A second ionized gas component, with lower density, filling the ISM between the compact HII regions, is required.

In order to draw a complete resolved picture of the ISM composition in metal-poor galaxies, it is important to extend the analysis to the PDR/molecular phase. The next step following the PhD work is the application of the modelling method refined in this project to the PDR phase including the tracers [OI] 63.2 μm, [OI] 145.5 μm, [CII] 157.7 μm, CO lines as well as the total infrared luminosity (L_{TIR}).

Résumé

Le milieu interstellaire (MIS), composé de gaz et de poussière, renferme les informations essentielles sur l'environnement et les processus menant à la formation d'étoiles qui, à son tour, influe sur l'évolution d'une galaxie. C'est le lieu où les étoiles naissent et déposent de la matière, dont les métaux ou éléments lourds. La structure du MIS n'est pas homogène; au contraire, le MIS contient plusieurs composantes avec des compositions chimiques, densités, températures, etc. différentes. L'élément en phase gazeuse le plus abondant étant l'hydrogène, une façon simplifiée de décrire les composantes du MIS est basée sur l'état d'ionisation de l'hydrogène : la phase atomique ionisée, où l'hydrogène est sous la forme ionisée notée H^+, la phase atomique neutre, où l'hydrogène est sous la forme neutre notée H^0/HI, et la phase moléculaire, où l'hydrogène est sous la forme de molécule de dihydrogène notée H_2.

Une des questions fondamentales en astrophysique actuellement est de comprendre comment les étoiles se sont formées dans les galaxies et notamment dans l'univers jeune où les métaux, importants pour le refroidissement, sont absents. S'il est difficile d'accéder à la chimie du MIS à grand redshift, le Groupe Local offre la possibilité d'étudier en détails plusieurs galaxies peu évoluées chimiquement. Ces galaxies naines sont de parfaits laboratoires pour voir comment le contenu en métaux (ou métallicité) du MIS affecte l'interaction entre le gaz, la poussière et les étoiles. Dans ce sens, le programme Herschel le Dwarf Galaxy Survey (DGS ; Madden et al. 2013) a ouvert une nouvelle porte pour l'étude des propriétés physiques du MIS dans ces galaxies. L'analyse du MIS des galaxies du DGS, à échelle intégrée donc sans résoudre spatialement les différentes phases du MIS, a mis en avance l'importance de la phase diffuse ionisée et la faiblesse de l'émission de CO (Cormier et al. 2015). Comme la molécule H_2 ne peut pas être observée directement car elle est symétrique et monucléaire, ce sont les raies de rotation du monoxyde de carbone, CO, qui sont généralement utilisées pour tracer le réservoir de gaz moléculaire. Et c'est à partir de ce réservoir que se forment les nouvelles étoiles. La faible émission de CO dans les galaxies à faible métallicité (Leroy et al. 2009; Schruba et al. 2012; Cormier et al. 2014)

semble donc contraster avec la forte activité de formation d'étoiles et le grand réservoir de HI dans les galaxies du DGS. Ce décalage peut se comprendre par le fait que le MIS à faible métallicité contient des photons ionisants très énergétiques qui peuvent pénétrer plus profondément à l'intérieur des nuages atomiques et moléculaires quand la poussière est moins abondante. Ainsi ces photons peuvent dissocier les molécules comme CO plus facilement alors que la molécule de H_2, qui est beaucoup plus abondante, est moins affectée car elle peut s'auto-écrantè plus efficacement. La phase de gaz correspondant aux régions où CO est photo-dissocié et H_2 est auto-écranté s'appelle le gaz 'sombre en CO'. L'existence de cette composante de gaz sombre en CO a été suggérée d'abord à travers des observations de la raie de [CII] 157.7 μm dans le LMC par Poglitsch et al. (1995) et dans IC 10 par Madden et al. (1997). Son existence a aussi été confirmée dans la Voie Lactée (ex: Grenier et al. 2005; Planck Collaboration et al. 2011). Voir Chapitre 1.

Mon projet de thèse porte sur les propriétés du MIS multi-phases de la galaxie naine IC 10, dont la métallicité est 1/3 solaire (Chapitre 1). La proximité de cette galaxie (d=700 kpc) offre la possibilité d'analyser le MIS à plusieurs échelles spatiales: des nuages brillants compacts (25 pc) au corps entier de la galaxie formant des étoiles (650 pc). En particulier, je me suis intéressée à l'analyse des propriétés physiques des régions HII compactes et du gaz ionisé diffus, que l'on trace avec les raies de refroidissement en infrarouge moyen (MIR) et lointain (FIR). Les raies de structure fine en MIR et FIR sont des traceurs puissants des propriétés du MIS ainsi que de l'activité de formation stellaire, et elles sont moins affectées par l'extinction par la poussière que les raies en optiques. Cela est important dans le cas de IC 10 car cette galaxie se situe très près du plan Galactique (b=-3.3°). IC 10 a été observée avec les télescopes spatiaux *Spitzer* et *Herschel*, fournissant un jeu d'environ 16 raies d'émission en infrarouge. J'ai complété ce jeu avec des observations que j'ai effectuées grâce au télescope aéroporté SOFIA (Chapitre 2).

Au Chapitre 3, je présente l'étude de la distribution spatiale des raies FIR, dont la résolution est d'environ 40 parsecs. J'ai trouvé que [OIII] 88.4 μm est la raie de refroidissement FIR la plus brillante, et ce, tout du long du corps de la galaxie, suggérant un facteur de remplissage du gaz diffus ionisé élevé. Le MIS de IC 10 semble être très poreux, ce qui permet aux photons UV de s'échapper des régions HII denses et de parcourir des distances importantes, une caractéristique unique aux galaxies avec un contenu faible en métaux et en poussière. La raie de [CII] 157.7 μm dont l'émission peut provenir à la fois des phases ionisées et neutres, est la seconde raie FIR la plus brillante. Malgré une phase diffuse ionisée importante, le rapport de [CII] 157.7 μm/[NII] 121.9 μm indique que la plupart de l'émission de [CII] 157.7 μm (au moins 98%)

provient du gaz neutre, des régions de photodissociation (PDR) et non du gaz ionisé. Enfin, le rapport des raies de souffre, [SIII] 33.5 μm/[SIII] 18.7 μm, révèle que la densité du gaz ionisé est d'environ 500 cm^{-3}.

L'émission des raies de refroidissement est fonction des conditions physiques des phases du MIS. Afin d'estimer les propriétés physiques des phases principales (densités, extinction, etc.) et la nature des sources de rayonnement ionisant, j'ai confronté les observations des raies MIR et FIR à des modèles de photoionisation et photodissociation. Pour cela, j'ai utilisé le code de synthèse spectrale CLOUDY (Ferland et al. 2013) et construit des grilles de modèles adaptées au cas de IC 10 (Chapitre 4). Afin de produire un spectre observé, le code considère un nuage de gaz et de poussière à géométrie plan-parallèle et divise ce nuage en plusieurs zones en fonction de la profondeur du nuage. Ensuite, le champ de radiation à l'entrée du nuage est propagé à travers ces zones et, à chaque étape, les processus physiques tels que le transfert radiatif, les réactions chimiques, les niveaux de population, etc. sont traités. Contrairement à d'autres codes, CLOUDY permet un calcul cohérent de la structure thermique et chimique du gaz à travers la région HII et la PDR. CLOUDY est donc un outil idéal pour extraire les informations physiques des nombreux traceurs infrarouge observés qui proviennent de plusieurs phases du MIS. Dans l'étude de IC 10, l'histoire de formation d'étoiles des amas stellaires responsables de l'ionisation du gaz est représentée par une flambée d'étoiles unique. Cette hypothèse est peut-être valable pour une région HII individuelle mais le gaz distribué à plus grande échelle spatiale est probablement chauffé et ionisé par des populations stellaires d'âges variés. Un scenario avec un taux de formation stellaire continu pourrait être envisagé, mais la pente du continu spectral UV en-deçà de 10^3 Å (énergies plus de 13.6 eV) est quasiment indépendante de l'âge de la population stellaire, ce qui rend ce scenario difficile à tester avec seulement des traceurs du gaz ionisé en main. Une étude de suivi, modélisant à la fois les raies du gaz ionisé et les raies du gaz neutre et sondant ainsi une gamme d'énergies plus large, permettra peut-être de tester ce scenario de formation d'étoiles continue.

Un des objectifs majeurs de mon projet est de comparer les conditions physiques du gaz ionisé obtenues à partir des traceurs observés aux différentes échelles spatiales étudiées. Pour cela, j'ai choisi trois échelles spatiales:

1. les "clumps", la plus petite échelle spatiale réalisable avec la résolution des instruments. La meilleure résolution possible avec les observations de *Spitzer*/IRS SL est de 4", ce qui correspond à 14 pc à la distance de IC 10. Avec cette résolution, je peux séparer les nuages brillants compacts d'une composante d'émission plus diffuse. Bien que plusieurs *clumps* pourraient être étudiés, je me suis restreinte à ceux qui sont les

plus brillants en MIR et FIR dans les cartes de raies d'émission *Spitzer* et *Herschel*. J'ai ainsi identifié cinq de ces *clumps* : trois dans la région centrale et deux dans le premier arc.

2. les "zones", de grandes régions dans la galaxie (aire de quelques kpc^2) dans lesquels on s'attend à ce que les conditions physiques locales soient différentes d'une région à l'autre. Certaines *zones* incluent des *clumps* et des structures visibles en Hα alors que d'autres *zones* sont choisies pour examiner le milieu diffus ionisé.

3. le "body", la plus grande échelle correspondant à la majeure partie du corps de la galaxie avec une activité de formation d'étoiles notable. D'une taille de 608 pc $\times$ 855 pc, cette échelle inclus la plupart des *zones* étudiées individuellement.

J'ai développé et testé deux méthodes différentes de comparaison des observations aux prédictions des modèles : l'une basée sur des rapport de raies, l'autre sur les valeurs absolues des flux des raies (Chapitre 5). Comme la sensibilité et la couverture spatiale des observations de IC 10 ne sont pas homogènes, il est impossible de sélectionner et modéliser la même combinaison de raies pour toutes les échelles spatiales. Ainsi, l'exploration de ces méthodes a été nécessaire pour établir les meilleures contraintes possibles sur les conditions physiques des régions de IC 10. Les deux méthodes diffèrent principalement dans la façon d'explorer l'espace de paramètres des modèles. La méthode de rapport des raies permet de combiner des raies provenant d'un même instrument ou d'un même élément, minimisant ainsi certaines incertitudes. Cependant, le choix des raies à combiner pour créer les rapports a un impact sur les résultats et sur les meilleurs modèles trouvés. En effet, j'ai montré qu'en choisissant un ensemble de rapports différent, les valeurs des paramètres reproduisant au mieux ces rapports et donc les meilleurs modèles peuvent changer. A l'inverse, la méthode des flux des raies considère les raies telles qu'elles et ne nécessite aucune combinaison de raies. Les résultats de cette étude suggèrent que, avec le jeu de données en main, la méthode la plus performante pour comparer tous les traceurs disponibles à chaque échelle spatiale est celle utilisant les valeurs absolues des flux. Cette méthode suggère toutefois le besoin d'une seconde composante dans les modèles, une phase diffuse ionisée, pour mieux reproduire certaines raies observées telles que [OIII] 88.4 μm.

Mon travail de modélisation a permis de déterminer les propriétés des nuages les plus brillants dans cette galaxie ainsi que les propriétés de régions plus grandes (300 parsecs), et j'ai démontré que l'émission à grande échelle spatiale est dominée par celle des *clumps* (Chapitre 6). Les propriétés

physiques des *clumps* sont plutôt uniformes, suggérant une origine commune de leur activité de formation d'étoiles. L'origine des sources ionisantes dans les régions HII analysées ici pourrait être reliée à la rétroaction des vents stellaires et supernovae dus à la génération d'étoiles précédente. Pour chaque *clump*, l'extinction peut être calculée, d'une part, en comparant le flux Hα observé avec celui prédit par les meilleurs modèles, et d'autre part, de façon théorique avec le rapport de Huα(7-6)/Hα(3-2). Je trouve que ces deux méthodes donnent des valeurs d'extinction similaires. Un résultat important concernant les *clumps* est qu'ils semblent être délimités par la matière, c.-à-d. qu'il n'y a pas assez de matière pour absorber tous les photons ionisants et la taille de la région HII est définie par la taille du nuage de matière. Ainsi, les *clumps* sont quasiment transparents au champ de radiation, ce qui permet à une fraction importante des photons ionisants de s'échapper de la région HII. A plus grandes échelles, le gaz devient de plus en plus délimité par la radiation et non par la matière, c.-à-d. les régions sont optiquement épaisses au champ de radiation, ce à quoi on s'attend car les photons ionisants s'échappant des régions HII ont plus de chance d'être absorbés au fur et à mesure que le volume de gaz augmente. Ce scenario de photons ionisant qui s'échappent et l'échelle spatiale typique qu'ils traversent avant d'être absorbés est très intéressant dans le contexte d'un MIS poreux à faible métallicité. De plus, à grande échelle, je trouve qu'aucun modèle n'arrive, seul, à reproduire l'émission de tous les traceurs de manière satisfaisante. En effet, une deuxième composante de gaz ionisé est nécessaire, avec une plus faible densité et remplissant le MIS entre les régions HII compactes. Cependant, le nombre de contraintes observationnelles n'est pas suffisant pour construire un modèle fiable du MIS avec plusieurs composantes. Enfin, je me suis intéressée à l'origine de l'émission des raies de [CII] 157.7 μm, [FeII] 25.9 μm et [SiII] 34.8 μm pour déterminer quelle fraction de leur émission provient du gaz ionisé (et non du gaz neutre). En comparant l'émission prédite par les meilleurs modèles aux observations, j'ai trouvé que la plupart de l'émission de ces raies de [CII], [FeII] et [SiII] provient de la PDR.

Pour finir, le Chapitre 7 présente les perspectives offertes par mon travail de thèse. Cette étude de modélisation de IC 10 suggère que, pour toutes les échelles spatiales étudiées, le gaz ionisé contient probablement plusieurs composantes aux caractéristiques différentes (ex : densités). L'ajout d'une autre composante dans les modèles est possible mais requiert davantage d'observables. Une possibilité serait d'inclure les raies optiques comme contraintes additionnelles. Par exemple, le rapport des raies optiques [SII] 6716Å / [SII] 6731Å est généralement un bon traceur de la densité du gaz au front d'ionisation des régions HII. Des spectres optiques ont été obtenus pour un des *clumps* analysé ici avec le spectro-imageur Postdam Multi-Aperture Spec-

trograph disponible sur le télescope de 3.5m à l'observatoire de Calar Alto, avec une resolution de 3.9pc × 3.9pc (López-Sánchez et al. 2011). Malgré les problèmes d'extinction, la spectroscopie optique fournit une résolution spatiale supérieure à celle de la spectroscopie infrarouge, et permettra peut-être une modélisation plus détaillée de la structure du MIS. Une autre perspective intéressante est le James Webb Space Telescope, une mission de la NASA dont le lancement est prévu pour fin 2018. En particulier, l'instrument en infrarouge moyen MIRI couvre les longueurs d'ondes de 4.9 μm à 28.8μm. MIRI va permettre d'observer les mêmes raies spectrales que l'IRS ainsi que des raies dont l'émission est plus faible grâce à sa sensibilité accrue, à une meilleure résolution spatiale et spectrale, ce qui sera suffisant pour séparer les diverses composantes du gaz ionisé. Cependant, avec le champ de vue restreint de MIRI (3.9" × 7.7"), on ne pourra pas faire de grande carte de IC 10 et seules des petites régions HII bien ciblées pourront être observées dans IC 10 et dans les galaxies proches.

Etendre l'analyse du gaz ionisé à la phase neutre atomique et au gaz moléculaire est important pour établir une vue complète du MIS résolu dans les galaxies à faible métallicité. La prochaine étape suivant ce travail de thèse sera donc d'appliquer la méthode de modélisation que j'ai développée à la phase PDR en incluant les traceurs: [OI] 63.2 μm, [OI] 145.5 μm, [CII] 157.7 μm, CO lines ainsi que L_{TIR}. Un de mes objectifs est d'utiliser les modèles PDR pour estimer spatialement la masse de gaz moléculaire sombre en CO dans cet environnement à faible métallicité. Parmi les paramètres les plus importants à prendre en compte pour cela sont le rapport de gaz-sur-poussière et l'extinction des nuages.

Certains de mes résultats, comme la délimitation des régions par la matière ou par la radiation ou encore l'importance de la phase ionisée, reflètent des changements notables dans la balance des phases et dans le transport de radiation à faible métallicité; et cela peut avoir de fortes implications pour le refroidissement et l'évolution des galaxies dans l'univers jeune. De plus, une des perspectives principales les plus captivantes pour l'évolution des galaxies est de mieux comprendre comment les processus qui agissent aux échelles locales, comme la formation stellaire, dépendent des processus qui agissent à plus grandes échelles voire à l'échelle d'une galaxie entière, comme le MIS ou la dynamique globale d'une galaxie. Dans ce cadre, étendre mon analyse multi-échelles des propriétés du MIS (densités, champs de radiation, masses, facteurs de remplissage, etc.) à des galaxies recouvrant une gamme étendue de conditions va permettre de mieux relier les petites et les grandes échelles et de fournir des diagnostics directs sur les propriétés physiques en fonction de l'environnement galactique.

Contents

List of Figures

List of Tables

Chapter 1

The Interstellar Medium of Dwarf Galaxies

Contents

1.1 Galaxy

The word galaxy is derived from the Greek galaxias ($\gamma\alpha\lambda\alpha\xi\acute{\iota}\alpha\varsigma$), literally "milky", a reference to the Milky Way. Until well into the twentieth century, it was by no means clear that any object existed beyond the confines of the Milky Way. In the mid-eighteenth century Immanuel Kant published his treatise, General Natural History and Theory of the Heavens, in which he suggested that the Milky Way might not be the only stellar system, and that some of the nebulae (faint, fuzzy, approximately elliptical patches of light seen in the sky) might be complete island universes, similar in structure to the Milky Way but viewed from large distances and at a variety of angles to the line of sight. Towards the end of the eighteenth century, increasingly powerful telescopes led to more systematic studies of nebulae. In 1922, Edwin Hubble observed Cepheid variable stars in the Andromeda Nebula and estimated their luminosities. Measuring their apparent brightness then yielded a direct estimate of their distances. Using this method, Hubble obtained a value for the distance to Andromeda of some 300 kpc. So it firmly demonstrated that the Andromeda Nebula was not an element within the Milky Way, but it was a comparable stellar system in its own right.

A galaxy is a gravitationally-bound collection of stars, stellar remnants, an interstellar medium (ISM) of gas and dust, surrounded by a dark matter halo with each component emitting at a different wavelength. In the band between the ultraviolet (UV) and near-infrared (NIR), the radiation is mainly due to an ensemble of stars, with spectra resembling black bodies having emission peaks at different wavelengths, depending on the temperature. Young stars (few Myr) peak in the UV at $\sim$ 0.1 μm, while older stars (0.1 - 1 Gyr) peak in the visible at $\sim$0.5 μm. At longer wavelengths, thermal emission from warmer dust is observed (hundreds of K) in the mid-infrared (MIR), to colder dust (tens of K) in the far-infrared (FIR). At radio wavelengths, synchrotron emission from relativistic particles, accelerated by supernovae explosions and thermal free-free emission from ionized plasma, can be observed. The distribution of the total energy emitted by a galaxy at various wavelengths is the spectral energy distribution (SED). The emission from gas, unlike that of stars and dust, is not contributing to the continuum emission of the SED, but through spectral line emission and absorption over the whole electromagnetic spectrum.

The repartition of these different components can vary from galaxy to galaxy, influencing the evolution and the properties we observe. In the Milky Way, for example, the total baryonic mass is dominated by the stellar mass, while the ISM (dust and gas) represents only 2.5% (Tielens 2005). The luminosity of the ISM, however, contributes to 30% of the total luminosity

of the Milky Way.

All of the galaxy components are interrelated and participate in the evolution of the galaxy, which is due to the cyclic process between stars and the ISM. The low mass stars, through their stellar winds, eject dust and metals produced by the stellar nucleosynthesis, to the surrounding medium. The more massive stars explode in supernovae at the end of their lives, enriching the ISM with metals. The gas and dust of the ISM, now more metal rich, is then recycled, forming clouds that collapse gravitationally to form stars. A schematic view of this continuous interplay between the star, gas and dust components, is shown in Figure 1.1.

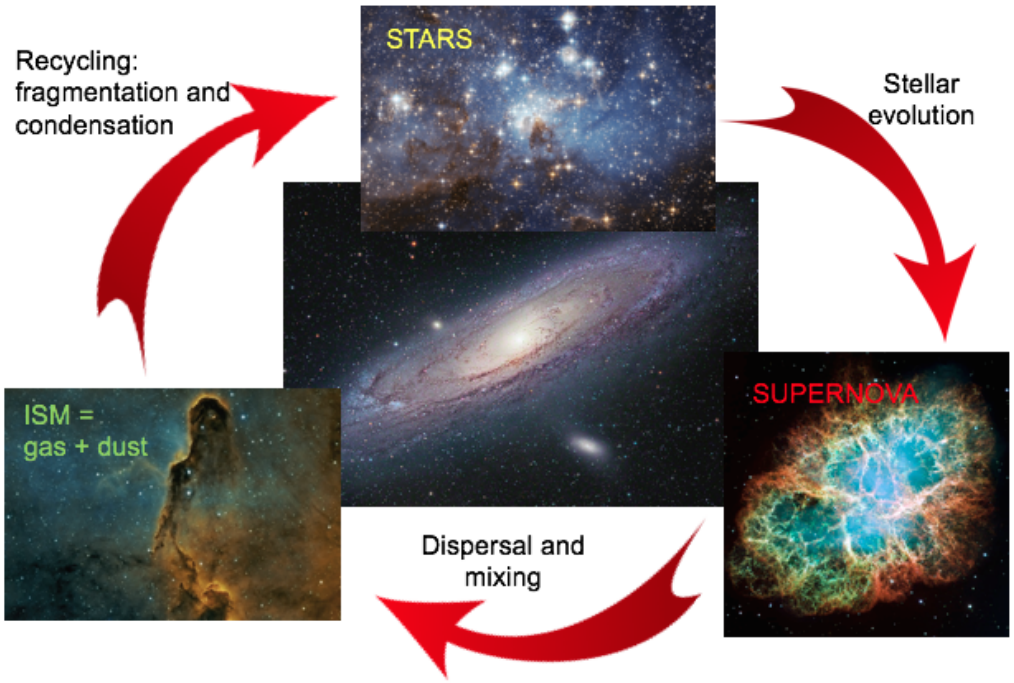

Figure 1.1: Schematic view of the interplay between the components of a galaxy. The visible components of a galaxy are the stars, the gas and the dust. All of those components are related: at the end of their lives, massive stars explode in supernovae, releasing metal elements into the surrounded medium. The gas and dust, thus enriched, then collapse to form a new generation of stars.

Hence, the ISM is a fundamental component of a galaxy. It is the birthplace of stars, and on the other hand its properties, structure, composition and chemical evolution are driven by feedback processes, such as stellar winds, supernovae, emission of ionizing photons, etc. In order to trace a galaxy's evolution, it is thus fundamental to understand the processes that link the ISM to the stars and how the properties of the dust and gas affect

the star formation activity of galaxies.

1.2 Phases of the Interstellar Medium

This work is focused on the investigation of the gas components of the ISM, which represent around 99% of the ISM. Most of the gas is hydrogen (∼71.8%), followed by helium (∼27%), the rest consists of gaseous metals. The ISM gas structure is not homogeneous; on the contrary it shows a multi-component structure of different compositions, densities, temperatures, abundances, etc. A rather simplified way to view the ISM, since the dominant element of the gas is hydrogen, is to consider the ISM based on the ionization state of hydrogen: ionized atomic phase, where the hydrogen is in the H^+, neutral atomic phase, where the hydrogen is in the neutral atomic form, H, and molecular phase, where hydrogen is in the molecular form, H_2. Typical physical properties of the different gas phases are summarized in Table 1.1 and shown in schematic form in Figure 1.2. More details on the chemistry and physics of the ISM can be found in Tielens (2005) and Osterbrock & Ferland (2005).

1.2.1 Ionized phase

Photons with energies greater than 13.6 eV, produced by hot stars, ionize the surrounding gas creating HII regions. These are normally young stars (≤15 Myr), typically O and B stars, which link the HII regions to the recent star formation. Therefore, HII regions are often studied to determine the present day chemical abundances (Yin et al. 2010; López-Sánchez et al. 2011; Garnett 1990). The compact HII regions around the ionizing sources are typically characterized by densities of $\sim 10^5$ cm^{-3} while the more diffuse ionized regions are on the order of ~ 1 cm^{-3}. Temperatures of HII regions can be $\sim 10^2$ to 10^4 K. Their linear scales can be a few parsecs, such as the Orion nebula (D∼8 pc) to hundreds of parsecs, such as NGC5471 (D∼1 kpc; García-Benito et al. 2011).

Ionizing photons escaping from HII regions, ionize the diffuse ISM, creating the Warm Ionized Medium (WIM). This component is characterized by very low densities (10^{-1} cm^3) and can have one of the largest filling factors in galaxies.

The primary heating source of the ionized phases is photoionization. Ionized species collide with electrons in the gas and fine structure lines are emitted via radiative decay from UV to IR wavelengths. Highly ionized species, such as S^{3+} and Ne^{2+}, probe the dense HII regions in close proximity to the

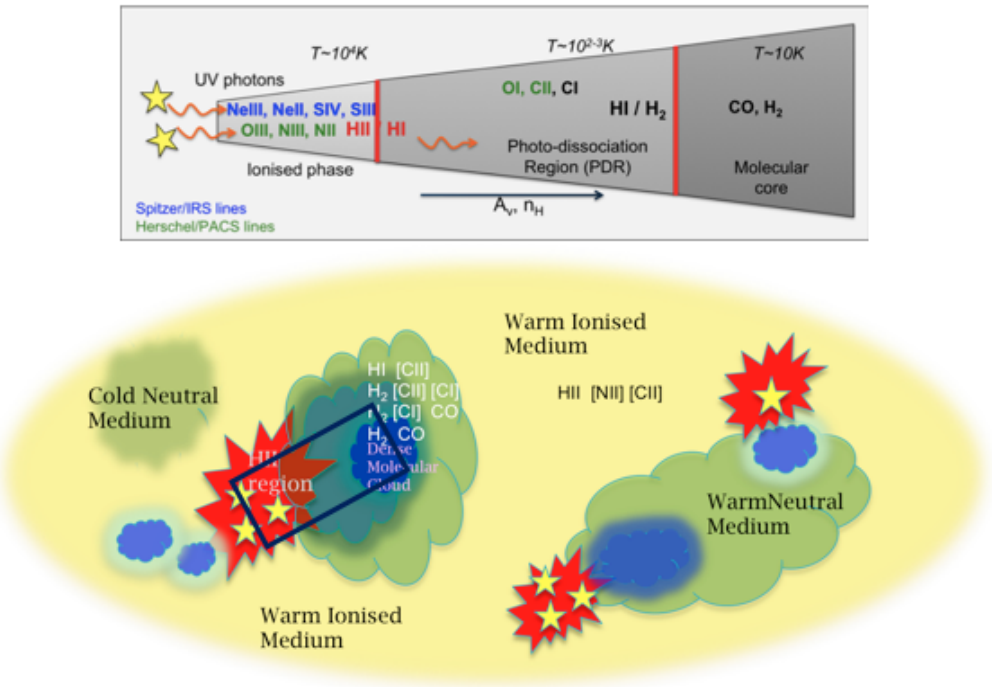

Figure 1.2: Schematic of the phases of the ISM of galaxies. *Bottom*: A global picture of the complex ISM phases of a galaxy showing ionized regions and neutral atomic and molecular cloud complexes embedded within a more diffuse phase, which can be neutral in part and mostly ionized. *Top*: A zoom into the layered interfaces of the ionized, neutral and molecular phases (Figure from Cormier 2012). UV photons produced by the stars ionize the surrounding gas creating a HII region. Photons with energy less than 13.6 eV (ionization potential of H^0) escape from the HII region and penetrate deeper into the cloud, creating the photodissociation region, where the hydrogen is neutral, CO is photodissociated and carbon is ionized (ionization potential of C^0 is 11.3 eV). Finally, deeper into the cloud, the gas is in molecular form. Each of these phases can be traced by various emission lines (Section 1.2.4).

exciting stars since they require the most energetic photons, while species with lower ionization states, such as N^+ and Ne^{2+} originate in the more extended, diffuse ionized gas.

The Hot Ionized Medium (HIM) is characterized by extreme temperatures ($\sim 10^5$ - 10^6 K) and very diffuse gas ($\sim 3\times10^{-3}$ cm^{-3}), carrying a small mass fraction of the ISM. This phase is ionized normally by shocks generated by supernovae explosions and stellar winds and emits thermal X-ray continuum and highly-excited emission lines, such as N^{4+}, O^{6+} and O^{7+}.

1.2.2 Neutral atomic phase

Much of the ISM of galaxies is composed of neutral atomic hydrogen, particularly in disk galaxies. The atomic phase is identified by the dominance of atomic H in the interface phase where the UV photons have energy less than 13.6 eV, but where H_2 molecules do not exist. This phase, consisting of neutral atomic species such as H^0, C^0 and O^0, is most easily traced by the 21 cm HI line.

The neutral phase can be divided in two very different components: the Cold Neutral Medium (CNM) and the Warm Neutral Medium (WNM). The CNM is a cool, diffuse HI cloud with typical temperatures of ∼100 K and densities of ∼50 cm^{-3}. The WNM is an intercloud gas at temperatures typically of ∼8000 K and densities of ∼0.5 cm^{-3}.

The neutral interface between the HII region and the molecular core is the PhotoDissociation Region (PDR; Figure 1.2). The physics and chemistry of this transition phase is controlled by FUV photons which have escaped the HII region with $6 < h\nu <$13.6 eV. These photons ionize species with ionization potentials less than 13.6 eV, such as C, Si and S and dissociate molecular hydrogen. Deeper into the cloud the ionizing photons are sufficiently attenuated allowing H_2 to exist, forming the dense, molecular core. In dense PDRs this transition between the PDR and the molecular phase occurs near visual extinction, A_V (see section 1.2.5), ∼2 magnitudes.

The heating of this phase is primarily via two processes: the photoelectric effect and FUV pumping of H_2. The photoelectric effect occurs when a FUV photon is absorbed by a dust grain and an energetic electron is ejected into the gas, transferring energy to heating the gas. This process is illustrated in Figure 1.3. The efficiency of the photoelectric heating depends on the size and the charge of the grains. The efficiency increases inversely with grain size. Hence the most efficient dust components are the smallest grains, the polycyclic aromatic hydrocarbons (PAHs) and other small grains. The charge of the grains is given by the balance between the photoionization and the electron recombination, which is controlled by $\gamma = G_0 T^{1/2}/n_e$, where G_0 is the radiation field (Tielens & Hollenbach 1985) and n_e is the electron density. The second source of heating in the PDRs is the FUV pumping of H_2. The molecule H_2 absorbs photons via the Lyman-Werner electronic transitions ($\Delta E >$ 11.2 and 12.3 eV). Most of the time the H_2 cascades to an excited vibrational level in the ground electronic state via fluorescence while 10 to 15% of the FUV pumping events, the molecule will dissociate via fluorescence to the ground electronic state.

The cooling of the PDR gas is due mainly to IR fine-structure line emission from species such as [CII] 157.7 μm, [OI] 63.2 μm and [OI] 145.5 μm.

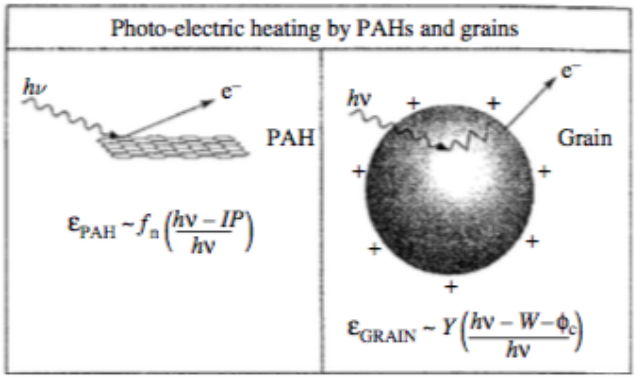

Figure 1.3: Schematic of the photoelectric heating via the dust grains and PAHs (Figure from Tielens 2005). The efficiency, ϵ, is a function of f_n for PAH and of Y for the grains. f_n is the probability of the PAH to be ionized by the FUV photons, while Y is the probability that the electron escapes from the grain.

1.2.3 Molecular phase

The molecular phase is the densest component of the ISM and exists where H_2 dominates the gas phase. While H_2 is the most abundant molecule, other molecules are forming within this phase, shielded from dissociating photons, such as CO, HCN, O_2. The molecular phase is characterized by densities $> 10^2$ cm^{-3} and temperatures on the order of $\sim$10 K.

Molecules can form on the surface of dust grains and can be destroyed by UV photons if their self-shielding efficiency or the shielding from the dust is insufficient. For example, for H_2 the Lyman-Werner bands become optically thick at high density; hence the molecule can be shielded from starlight. On the other hand, CO, which is the second most abundant molecule, is not as efficiently self-shielded, but relies on the dust to shield it from the dissociating photons.

FUV photons and cosmic rays are the main heating sources of molecular clouds. Molecules, excited by collisions and shocks, cool the gas via vibrational and rotational transitions emitted in the FIR to submillimeter (submm) wavelength range. A prominent coolant in the molecular gas phase is CO in its various rotational transitions.

1.2.4 Observational tracers

The state of the ionized, PDR, and molecular phases can be derived by studying the emission lines, which emit at various wavelengths. Baldwin et al. (1981), for example, proposed the [OIII]λ5007/Hβ and [NII]λ6584/Hα diagnostic diagram (the BPT diagram) to separate the line-emission objects based on the excitation mechanism: HII regions, planetary nebulae, and shock heated media, such as active galactic nuclei (AGN). Moreover, even

Table 1.1: Typical characteristics of the ISM phases in the Galaxy and principal ways to observe the phases. Table adapted from Tielens (2005)

Phase	T [K]	n [cm^{-}3]	M$^{(a)}$ [10^9 M$_\odot$]	Observation
Hot Ionized Medium	10^5 - 10^6	0.003	-	Thermal X-ray emission Ionized metal absorption/emission lines Thermal radio emission
HII regions	10^4	1 - 10^5	0.05	Thermal radio emission Hα recombination line FIR fine-structure lines Bright MIR continuum
Warm Ionized Medium	8000	0.1	1.0	Hα recombination line Thermal radio emission
Warm Neutral Medium	8000	0.5	2.8	HI 21 cm absorption/emission line
Cold Neutral Medium	80	50	2.2	HI 21 cm emission line
Molecular cloud	10	> 200	1.3	CO rotational lines

(a) Representative mass of the phases in the Milky Way.

simple line ratios can sometimes characterize the physical properties of the emitted gas. For example, the ratio of lines of the same element but different ionization stage, such as [NeIII] 15.5 μm /[NeII] 12.8 μm , traces the temperature of the ionizing source, while the ratio of lines of the same ion but different transition, can estimate the electron density (Osterbrock & Ferland 2005; Abel et al. 2005). Consider two levels with the same excitation energy but with different Einstein A coefficients (rate of spontaneous emission and absorption) or collisional de-excitation rates, the excitation of these levels will be related only by different densities. Examples of ratios that can be used to measure the gas electron density are [SII]6716/[SII]6731 Å in the optical and [OIII]88/[OIII]52 μm in the IR. Figure 1.4 shows examples of infrared line ratios that trace different density regimes. Each line ratio, in fact, can trace the density of the gas when the value of the density lies between the critical densities of the two lines. The critical density is the density for which the collisional rate coefficient is equal to the radiative de-excitation coefficient. For densities higher that this threshold density, collisions dominate the de-excitation process.

Unlike the optical lines, infrared observations are slightly effected by extinction (see Section 1.2.5) and they cover a wide range of excitation potentials and critical densities (Figure 1.5; Kennicutt et al. 2011). The wavelengths, excitation potentials and critical densities of the MIR and FIR lines observed with *Spitzer* and *Herschel* space telescopes (see Chapter 2), are presented in Table 1.2.

Table 1.2: Properties of the infrared fine-structure cooling lines observed with *Spitzer* and *Herschel* space telescopes.

Species	λ $[\mu m]$	Transition	*Excitation Potential*$^{(a)}$ $[eV]$	$n_{crit}^{(b)}$ $[cm^{-3}]$
Spitzer/IRS				
$[ArII]$	6.99	$^2P_{1/2} - {}^2P_{3/2}$	15.75	$4 \times 10^5[e]$
$[ArIII]$	8.88	$^3P_1 - {}^3P_2$	27.63	$3 \times 10^5[e]$
$H2$	9.66	$(0-0)S(3)$	4.48	$9 \times 10^5[H]$
$[SIV]$	10.51	$^2P_{3/2} - {}^2P_{1/2}$	34.78	$5 \times 10^4[e]$
$Hu\alpha$	12.37	$^7S_1 - {}^6S_1$	–	–
$[NeII]$	12.81	$^2P_{1/2} - {}^2P_{3/2}$	21.56	$7 \times 10^5[e]$
$[NeV]$	14.32	$^3P_2 - {}^3P_1$	97.12	$3 \times 10^4[e]$
$[NeIII]$	15.55	$^3P_1 - {}^3P_2$	40.96	$3 \times 10^5[e]$
$H2$	17.03	$(0-0)S(1)$	4.48	$2 \times 10^4[H]$
$[SIII]$	18.71	$^3P_2 - {}^3P_1$	23.34	$2 \times 10^4[e]$
$[ArIII]$	21.83	$^3P_1 - {}^3P_0$	27.63	$5 \times 10^4[e]$
$[FeIII]$	22.93	$^5D_3 - {}^5D_4$	16.19	$1 \times 10^5[e]$
$[NeV]$	24.32	$^3P_1 - {}^3P_0$	97.12	$3 \times 10^4[e]$
$[FeII]$	25.99	$a^6D_{7/2} - a^6D_{9/2}$	7.90	$3 \times 10^4[e]$
				$2 \times 10^6[H]$
$[OIV]$	25.89	$^2P_{3/2} - {}^2P_{1/2}$	54.93	$1 \times 10^4[e]$
$H2$	28.22	$(0-0)S(2)$	4.48	$2 \times 10^2[H]$
$[SIII]$	33.48	$^3P_1 - {}^3P_0$	23.34	$7 \times 10^3[e]$
$[SiII]$	34.81	$^2P_{3/2} - {}^2P_{1/2}$	8.15	$2 \times 10^3[e]$
				$4 \times 10^5[H]$
$[NeIII]$	36.01	$^3P_0 - {}^3P_1$	40.96	$5 \times 10^4[e]$
Herschel/PACS				
$[OI]^{(c)}$	63.18	$^3P_1 - {}^3P_2$	–	$5 \times 10^5[H]$
$[OIII]$	88.36	$^3P_1 - {}^3P_0$	35.12	$5 \times 10^2[e]$
$[NII]$	121.90	$^3P_2 - {}^3P_1$	14.53	$3 \times 10^2[e]$
$[OI]$	145.52	$^3P_0 - {}^3P_1$	–	$1 \times 10^5[H]$
$[CII]$	157.74	$^2P_{3/2} - {}^2P_{1/2}$	11.26	$50[e]$
				$3 \times 10^3[H]$

(a) Energy required to create the ion. (b) Critical density for collisions with electrons [e] or with hydrogen atoms [H].

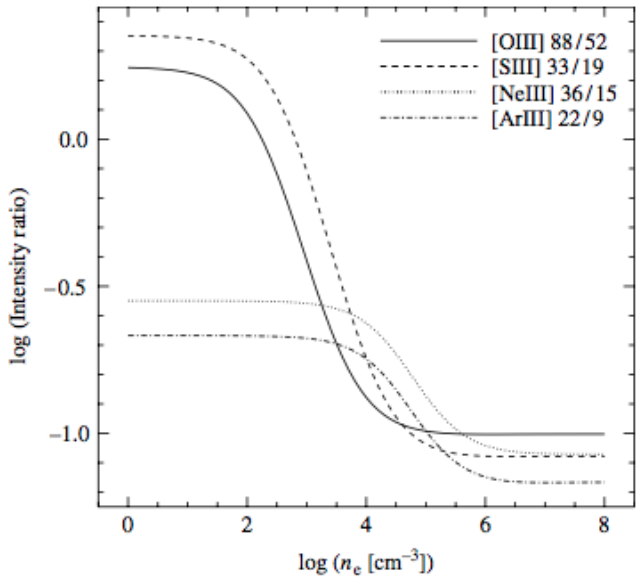

Figure 1.4: Intensity ratios of the infrared lines of [OIII], [SIII], [NeIII] and [ArIII] as a function of the electron density. (Figure from Tielens 2005).

MIR fine-structure lines

The MIR fine-structure lines, observed by *Spitzer*, are diagnostics mostly of the compact ionized gas (Spinoglio et al. 2015; Abel et al. 2005), due to their high critical density and excitation potential. In the following I present the MIR tracers that I have used in my PhD study.

- [ArII] 6.9 μm and [ArIII] 8.9 μm

  Ar^0 and Ar^+ have ionization potentials of 15.7 and 27.6 eV, respectively, and critical densities for collisions with electrons of 4×10^5 cm^{-3} for [ArII] 6.9 μm and 3×10^5 cm^{-3} for [ArIII] 8.9 μm. Since these two lines are emitted by two different ionization stages of the same element, the ratio [ArIII] 8.9 μm /[ArII] 6.9 μm traces the hardness of the radiation field. [ArIII] 8.9 μm, requiring the higher energy to ionize, would originate closer to the radiation source in the dense HII regions than [ArII] 6.9 μm, which would be emitted more from the outer shell of the HII regions. Therefore, the ratio [ArIII] 8.9 μm /[ArII] 6.9 μm can trace the leakage of ionizing photons from the HII regions (Section 4.3.2).

- [NeII] 12.8 μm and [NeIII] 15.5 μm

  Of the two MIR neon lines, the [NeIII] 15.5 μm has a much higher excitation potential, requiring 41 eV photons to ionize the Ne^+ while

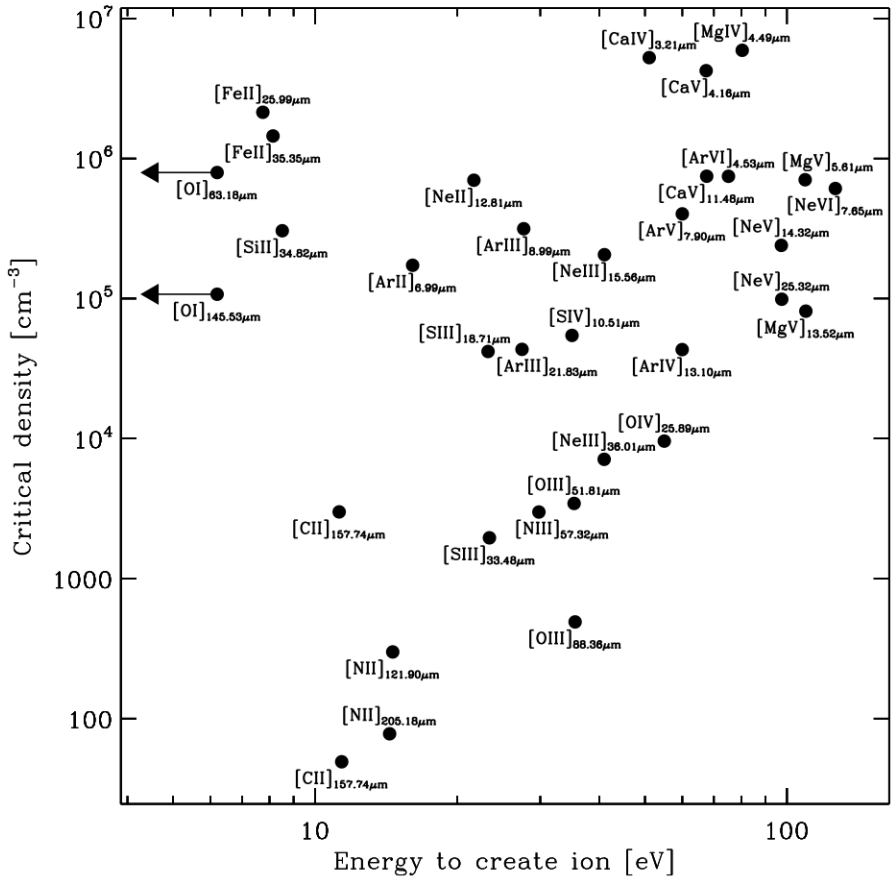

Figure 1.5: Excitation potential versus critical density for the fine-structure cooling lines observed with *Spitzer* and *Herschel* space telescopes. (Adapted from Kennicutt et al. 2011).

Ne^0, requires 21.6 eV to create Ne^+ (Table 1.2). The [NeII] 12.8 μm and [NeIII] 15.5 μm are exclusively found in HII regions. The critical density of [NeII] 12.8 μm for collisions with electrons is 7×10^5 cm^{-3}, while for [NeIII] 15.5 μm the critical density with electrons is lower, 3×10^5 cm^{-3}. However, while [NeIII] 15.5 μm is associated only with dense, hot HII regions, [NeII] 12.8 μm can arise from HII regions as well as relatively diffuse low-ionization gas (Cormier et al. 2012; Dimaratos et al. 2015). Since these two lines are emitted by different ionization stages of the same element, the ratio [NeIII] 15.5 μm/[NeII] 12.8 μm traces the hardness of the radiation field.

- [SIII] 18.7 μm, [SIII] 33.5 μm and [SIV] 10.5 μm

  S^+ has an ionization potential of 23.3 eV and traces the ionized gas. The two [SIII] transitions at 18.7 μm and 33.5 μm have critical densities with electrons of 2×10^4 cm^{-3} and 7×10^3 cm^{-3}, respectively. Hence the ratio [SIII] 33.5 μm/[SIII] 18.7 μm is a useful density tracer.

  S^{2+}, has an ionization potential of 34.7 eV and [SIV] has a critical density for collisions with electrons of 5×10^4 cm^{-3}, tracing the dense hot HII regions. The combination of [SIV] 10.5 μm with [SIII] 18.7 μm, as well as [SIII] 33.5 μm, provides useful ratios to measure the hardness of the radiation field.

- [FeII] 25.9 μm and [SiII] 34.8 μm

  Fe^+ and Si^+ ions require ionizing photons lower than that of hydrogen (7.9 eV to ionize Fe^0 and 8.2 eV to ionize Si^0; see Figure 1.5). Therefore, Fe^+ and Si^+ may exist in the neutral gas, excited mostly by H^0, H_2 and free electrons, as well as in the ionized gas, excited by electrons. In order to understand which phase these lines trace, modeling of the full suite of lines is required.

FIR fine-structure lines

The FIR fine-structure lines are important diagnostics of the properties of the ionized phase as well as of the PDR phase (Wolfire et al. 1990; Kaufman et al. 2006). They have been observed in the past with ISO and the KAO, in more recent past with *Herschel* and now with SOFIA.

- [OIII] 88.4 μm

  [OIII] 88.4 μm has an excitation potential of 35.1 eV and a critical density 500 cm^{-3}, thus arises only from ionized gas. The combination of [OIII] 88.4 μm with [OIII] 52 μm, is a useful constraint of electron density the HII region (Lebouteiller et al. 2012). [OIII] 52 μm was not accessible with *Herschel*, but can now be observed with SOFIA (Section 2.4.3).

- [CII] 157.7 μm

  [CII] 157.7 μm is one of the most important cooling lines of the ISM. It has been studied in many different environments, including Galactic

PDRs (Bennett et al. 1994), dwarf galaxies (e.g. Madden et al. 1997; Cormier et al. 2015; Fahrion et al. 2016), spiral galaxies (e.g. Kapala et al. 2017), high-redshift galaxies (Neeleman et al. 2017). Usually it is the brightest FIR emission line in galaxies, which can sometimes be used to determine the redshift of galaxies (e.g. Bradač et al. 2017) and its luminosity can be used as a measure of the star formation rate in galaxies (e.g. De Looze et al. 2011).

The ionization potential of C^0 is 11.3 eV, less than that of hydrogen (13.6 eV). Thus C^+, in principle, may exist in the ionized phase, excited by collisions with electrons with a critical density of 50 cm^{-3}, as well as in the neutral phase, excited by H or H_2 with a critical density of $2.8{\times}10^3 cm^{-3}$. The potential for [CII] 157.7 μm to exist in different phases complicates the interpretation of this popular diagnostic. In our Galaxy, [CII] 157.7 μm has been found to trace the surface layers of PDRs. For example, Bernard-Salas et al. (2012) have found that in the Orion Bar $>$ 82% of the [CII] emission is coming from the PDR region. Similar conclusions have been determined for [CII] 157.7 μm observed around the 30Doradus region in the Large Magellanic Cloud (Chevance et al. 2016). However [CII] 157.7 μm has also been observed to originate in the ionized gas phase (Madden et al. 1993; Abel et al. 2005; Cormier et al. 2012).

There are several methods to disentangle the origin of [CII] 157.7 μm. It can be done through detailed modeling (e.g. Bernard-Salas et al. 2012; Cormier et al. 2012) or by inspecting key diagnostic line ratios, such as [CII] 157.7 μm/[NII] 121.9 μm as explained below (e.g. Oberst et al. 2011).

- [NII] 121.9 μm and [NII] 205.2 μm

  N^+ with an excitation potential of 14.5 eV originates only in the ionized phase. The two FIR transitions, [NII] 121.9 μm and [NII] 205.2 μm, with relatively low critical densities of 300 cm^{-3} and 45 cm^{-3}, respectively, when used as a ratio, become a useful electron density tracer of the diffuse ionized gas, as is shown in Figure 1.6. Since these lines can only arise from the ionized phase while the origin of [CII] 157.7 μm is ambiguous, the ratios [NII] 121.9 μm/[CII] 157.7 μm and [NII] 205.2 μm/[CII] 157.7 μm can be used to disentangle the origin of [CII] 157.7 μm. In particular, since [CII] 157.7 μm and [NII] 205.2 μm have very similar critical densities and excitation temperatures, the ratio of

[CII]/[NII] depends mostly on the abundances of N^+ and C^+ (Oberst et al. 2006; Oberst et al. 2011; Bernard-Salas et al. 2012).

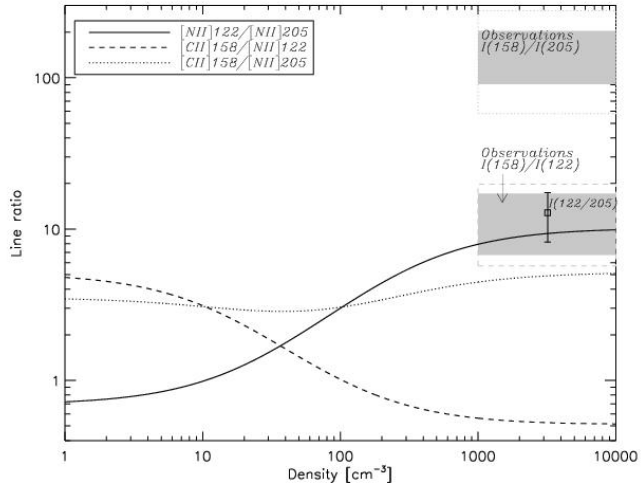

Figure 1.6: Theoretical ratios of [NII]122/205μm, [CII]/[NII]205μm and [CII]/[NII]122μm as a function of the density for a temperature of 9000 K. (Figure from Bernard-Salas et al. 2012).

- [OI] 63.2 μm and [OI] 145.5 μm

  The two [OI] lines at 63.2 and 145.5 μm, together with [CII] 157.7 μm , are the dominant coolants in PDRs. These two lines have critical densities of 5×10^5 and 10^5 cm^{-3}, respectively and excitation energies of 228 and 325 K. The ratio [OI] 145.5 μm /[OI] 63.2 μm is a popular diagnostic used to determine the physical conditions in PDRs (Kaufman et al. 1999). In particular, this ratio can be used to estimate the density and temperature of the neutral gas: the ratio increases with increasing temperature and decreases with decreasing density (Tielens & Hollenbach 1985). The [OI] 63.2 μm is one of the brightest cooling lines (Oberst et al. 2011; Bernard-Salas et al. 2012; Cormier et al. 2015) but is known to be affected by optical depth effects (Tielens & Hollenbach 1985; Abel et al. 2007; Chevance et al. 2016). The [OI] 145.5 μm line, however, is fainter than the 63.2 μm line, often by at least an order of magnitude, making it a challenge, even for *Herschel*, to map large regions in galaxies.

Molecular lines

- H_2

  H_2 is the most abundance molecule in galaxies. However, it is a symmetric molecule and does not have a permanent dipole moment, making this molecule difficult to observe. Nevertheless, its rotational quadrupole transitions ($\Delta J = \pm 2$; defining J as the rotational quantum number) have been observed in the MIR with *Spitzer*. These lines (3.4 to 28μm) are pure rotational transitions ($\Delta\nu = 0$), while the NIR lines (1 to 4μm) are vibrational transitions ($\Delta\nu = \pm 1$). However, these transitions need excitation temperatures > 500 K, hence they trace a warm neutral phase instead of the bulk of the cold molecular gas found in the star-forming disks of galaxies, for example.

  H_2 can also be observed in absorption in the UV in the Lyman-Werner band, from warm as well as cold diffuse gas heated by UV sources. It can also be a prominent emission line diagnostic in shocked regions tracing the turbulent cascade throughout the ISM (e.g. Guillard et al. 2009; Guillard et al. 2010)

  This molecule has been observed in a variety of objects, including star-forming regions and PDRs in our galaxy (e.g. Tielens & Hollenbach 1993; Lebouteiller et al. 2006), and in other galaxies (Roussel et al. 2007; Naslim et al. 2015).

- CO

  The H_2 reservoir is important to quantify since it is the fuel for star formation. Since the cold H_2 is difficult to observe, the usual tracers of the molecular phase are the CO emission lines. The CO rotational transitions emit in the FIR to submm wavelengths, excited by collisions with H_2. The CO rotational transitions can sometimes, arbitrarily, be divided into low-J transitions, namely J = 1-0, 2-1 and J=3-2; and high-J transitions where J = 3-2, 4-3, 5-4 and higher. Since the critical densities and the excitation temperatures increase with increasing transition level, the low-J transitions normally trace the bulk of the cold molecular gas, while the high-J transitions trace warmer molecular gas. The most commonly detected lines are ^{12}CO (1-0) and the isotopic version, ^{13}CO (1-0) (e.g. Wilson et al. 2009; Chevance et al. 2016). However, since CO forms deep inside the cloud, its lower rotational transitions can be affected by optical depth effects, in particular ^{12}CO(J =1 -0) transition is often optically thick.

1.2.5 Dust phase

Dust grains are formed in the envelopes of evolved stars as well as in novae and supernovae and are then ejected into the ISM by stellar winds and supernovae, which can also destroy them in the associated shock waves. Even though the dust represents only ∼1% of the total ISM mass, it is a fundamental component of the ISM. Dust grains provide the surfaces for the accretion and reaction of species that lead to the formation of molecules. They are also responsible for the stellar light extinction at wavelengths longer than 912Å, through the absorption and scattering of radiation, and its re-emission in the infrared. The monochromatic extinction is expressed in magnitudes as $A(\lambda)$ and is linked to the optical depth ($\tau(\lambda)$) of the cloud traversed by the emission through the relation: $A(\lambda) = 1.086 \times \tau(\lambda)$. Hence, for the monochromatic intensity emitted by the source $I(\lambda_0)$, the observed intensity $I(\lambda)$ is:

$$I(\lambda) = I(\lambda)_0 10^{-1.086 A(\lambda)} = I(\lambda)_0 e^{-\tau(\lambda)} \tag{1.1}$$

An example of a Galactic extinction curve, as a function of wavelength, is presented in Figure 1.7. Commonly, the extinction curve is given as $A_\lambda/E(B-V)$ as a function of $1/\lambda$. $E(B-V)$ is the colour excess defined as:

$$E(B-V) = A_B - A_V \tag{1.2}$$

where A_B and A_V are the extinctions calculated at the Johnson blue band B (centered close to 4400Å) and at the Johnson visible band V (centered near 5500Å), respectively. The total-to-selected extinction ratio, R_V, is:

$$R_V = A_V/E(B-V) \tag{1.3}$$

Since extinction decreases with increasing wavelength it is often called red-

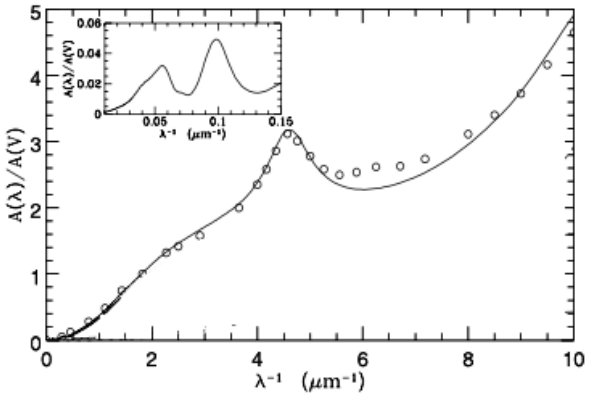

Figure 1.7: Example of a standard Galactic extinction curve normalized to the visible extinction, V band ($A(V) = A_V$). The circles correspond to observations by Savage & Mathis (1979). (Adapted from Lequeux 2005).

dening. The reddening measured for extragalactic objects, for example, IC 10, is a combination of the internal reddening, due to the absorption of dust grains within the galaxy, and foreground reddening, which is that due to the Galaxy along the line of sight to IC 10.

The processes of absorption and scattering of radiation, at the origin of extinction, are strongly related to the intrinsic properties of the grains: namely, their size and chemical composition. The different compositions and sizes of the dust grains manifest in the shape of the extinction curve within given wavelength ranges.

The most important components of the dust are: silicate grains, carbon grains (including graphite and amorphous carbon grains) and polycyclic aromatic hydrocarbons (PAHs). The silicate grains are responsible for the two absorption features at 9.7 and 18 μm in the infrared extinction curve. They are made from SiO_4 units and associated metals and can have a wide variety of compositions, such as Mg_2SiO_4 and $(Mg, Fe)_2SiO_4$. The feature observed at 2175Å is thought to be due to small graphitic or small amorphous carbon grains. The exact position and width of this peak depend on the grain shape and optical properties. PAHs are responsible for the emission features in the MIR spectrum around 3.3, 6.2, 7.7, 8.6 and 11.3 μm, as shown in Figure 1.8. The central wavelengths of these features depend on the structure of the molecules.

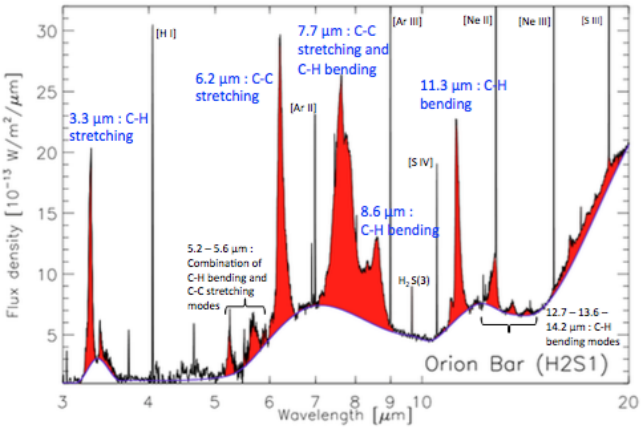

Figure 1.8: Infrared spectrum of the Orion nebula (image adapted from Peeters et al. 2004) illustrating the main PAH bands in red, their labels, in blue, indicating the vibrational modes that produce these features.

A model for the size distribution of grains found to exist in the Galaxy was proposed by Mathis et al. (1977) (MNR model), which consists of a power law distribution for grain sizes between 5 and 250 nm which can reproduce the interstellar extinction curve of the Milky Way between 0.1 and 1 μm:

$$n(a) \propto a^{-3.5} \tag{1.4}$$

where a is the grain radius. This model does not take into account the PAHs. A grain size distribution that also considers the PAHs, in addition to carbon and silicate grains, is presented in Zubko et al. (2004) dust models.

Variations in the dust properties, which depend on the local environment, leave their mark on the shape of the extinction curve. As examples, the extinction curves of the Milky Way, LMC and SMC are shown in Figure 1.9.

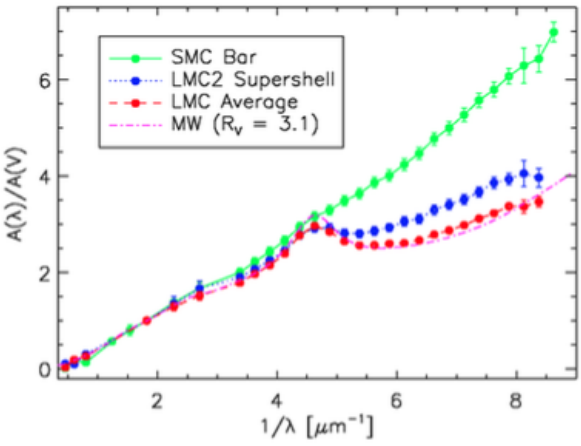

Figure 1.9: A comparison of the extinction curves for the Milky Way in pink (R_V=3.1), LMC in red (R_V=3.4), LMC-2 in blue (R_V=2.8) and SMC in green (R_V=2.7); from Gordon et al. 2003. The different trends in the curves are due to differences in the abundances of intermediate size grains (∼100Å) and big grains (2000Å).

The energy of the absorbed starlight is re-emitted in the IR emission bands and also in the MIR to submm continuum emission. Small grains can reach high temperatures (130-250 K) and emit predominantly in the MIR, which dominates the emission of grains in HII regions or in the warm phase of the ISM. The large grains, in both the diffuse ionized gas and neutral gas, have temperatures in the range of 15-60 K and thus dominate the FIR part of the dust thermal emission spectrum. Neglecting the NIR region, which is dominated by emission from stellar photospheres, the infrared spectrum thus arises primarily from the re-radiation of starlight by interstellar dust. The dust continuum has been photometrically-sampled by several space- and ground-based telescopes:

- 12, 25, 60, and 100 μm with IRAS
- 7 and 15 μm with ISO/ISOCAM
- 3.6, 4.5, 5.8 and 8 μm with *Spitzer*/IRAC, and 24, 70 and 100 μm with *Spitzer*/MIPS
- 3.4, 4.6, 12, and 22 μm with WISE

- 70, 100 and 160 μm with *Herschel*/PACS, and 250, 350 and 500 μm with *Herschel*/SPIRE
- 870 μm with APEX/LABOCA
- 450 and 850 μm with JCMT/SCUBA

Hence, with all of these bands covered, it is possible to observe the entire interstellar dust emission spectrum. Figure 1.10 shows examples of the SEDs for three different regions within the galaxy, IC 10.

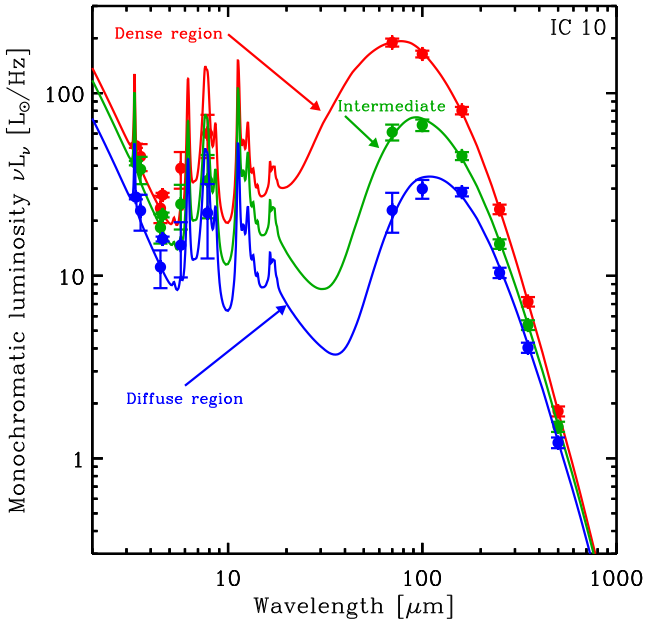

Figure 1.10: SED fitting of three regions of IC 10: dense region in red, diffuse region in blue and intermediate region in green. The points are WISE, *Spitzer* and *Herschel* observations (Lianou et al, in prep).

1.3 Metallicity

Local and/or global processes, such as turbulence or magnetic fields, as well as the different compositions of gas and/or dust, can modify the structure of the ISM and the characteristics of its phases. This work is focused on the effects of low-metallicity, which seem to most strongly influence the ISM structure (Cormier et al. 2015; Lebouteiller et al. 2017).

Metallicity (Z) is defined as the mass fraction of metals which are elements heavier than hydrogen or helium in the ISM.

$$Z = 1 - (X + Y) \tag{1.5}$$

where 'X' and 'Y' indicate the mass fraction of hydrogen and helium, respectively. The metals up to ^{7}Be have been created during the primordial nucleosynthesis, while the heavier metals are formed by stellar activity. The elements up to iron are produced with stellar nucleosynthesis and released in the ISM with stellar winds at the end of the life of a star. Solar-type stars can synthesize only helium, carbon, nitrogen and oxygen, while stars with mass $> 8M_\odot$ can produce elements up to iron. Heavier elements, instead, are synthesized in the supernovae explosions. Hence, the ISM is enriched by new and heavier elements during the evolution of the galaxy.

The metallicity is usually expressed as the ratio of oxygen and hydrogen abundances (O/H): 12 + log(O/H). Moreover, it is common to indicate the metallicity of an object relative to that of the solar neighborhood, namely $Z_\odot = 0.0142$ or $12 + \log(O/H)_\odot = 8.69$ (Asplund et al. 2009).

Abundance determination
In order to characterized the ISM it is important to know the abundances of all of the elements. Elemental abundances are important parameters used in the modeling of the ISM (Chapter 4). There are several methods to define the elemental abundances in a galaxy, as is presented in the review by Kunth & Östlin (2000). The fraction of heavy elements can be estimated by spectroscopic observations of HII regions or planetary nebulae. The former method gives access to the present time chemical abundances (Izotov et al. 2006; Garnett 1990), while the latter gives information on the previous chemical abundances (Pagel 1997; Peimbert et al. 2017). Another possibility is based on photometry of resolved stellar populations, since red giant branch populations can give observed values of [Fe/H].

1.4 Dwarf galaxies

There is not a precise criteria to define a dwarf galaxy. However, since they are in general low mass, low luminosity objects, a possible criteria to distinguish the dwarf galaxies from their more massive counterparts is the value of the absolute V-band magnitude, M_V: $M_V \geq$-18 mag is often used to identify a dwarf galaxy (Grebel et al. 2003; Thuan & Martin 1981). Due to their low luminosity, the study of dwarf galaxies is more or less restricted to the nearby universe, even though they are the largest population of galaxies, in numbers, of the universe.

Dwarf galaxies of the local universe exhibit a variety of properties that do not allow a unique classification. They cover a variety of luminosity ranges (down to 10^5 $L_\odot$), metallicity values (as low as $\sim 1/50 Z_\odot$ for I Zw 18, for

example) as well as a broad range of star formation activity and chemical enrichment.

In the hierarchical scenario of galaxy evolution (Dekel & Silk 1986), massive galaxies are formed by the merging of smaller building blocks. In this scenario, dwarf galaxies are small, metal-poor blocks necessary to build up the more evolved massive galaxies of the present-day universe. However, this theory is in question as evidence of downsizing is now evident (Cowie et al. 1996). In the downsizing scenario, star formation activity begins in massive galaxies and moves to smaller objects with the expansion of the universe. Nevertheless, while the dwarf galaxies are not necessarily considered to be the progenitors of the more massive galaxies, they are still key objects useful to understand galaxy enrichment and evolution, due to their chemically young nature.

How stars have been formed in galaxies in the early universe when heavy elements are deficient, is a fundamental issue in astrophysics which is a challenge to investigate with high redshift galaxies. On the other hand, the proximity of the dwarf galaxies of the Local Group, allows us to analyze in details their properties offering the opportunity to study several 'chemically -young' objects in order to try to extrapolate to primordial conditions.

1.4.1 Stellar population

Stellar population studies carried out in many dwarf galaxies (e.g. I Zw 18: Tosi et al. 2007; Haro 11: Cormier et al. 2012; IC 10: Lim & Lee 2015) show the existence of an old stellar population as well as a young stellar population. Some dwarf galaxies harbor super star clusters (e.g. 30 Doradus in LMC) and/or massive OB associations embedded in a more extended, older stellar population (e.g. Hodge et al. 1991). Others, for example IC 10 (Massey & Armandroff 1995), host Walf-Rayet (WR) stars, signaling intense star formation activity occurring within the last 10 Myr. These massive stars have a vigorous impact on the ISM, enriching it through strong stellar winds (Wilcots & Miller 1998; López-Sánchez et al. 2011). Hence, some dwarf galaxies are actively forming stars and their emission lines and infrared continuum are striking examples of starburst galaxies.

The combination of a young massive stellar population which produces hard UV photons, and a metal-poor ISM can result in a hard radiation field extending over galaxy-wide scales, with UV photons propagating relatively unhindered. As a consequence, ionized species are observed throughout the galaxy, even at relatively large distances from radiation sources, without much dust to absorb the photons (e.g. Cormier et al. 2015; see Section 1.5.1 for more details). As the stars age, they evolve off the main sequence, and

their spectral shape softens (Figure 4.4). On the other hand, in the more metal-rich star-forming regions, metals in the atmospheres of massive stars already absorb the UV photons, reducing the fraction of hard photons that are able to traverse large scales in the galaxy. Hence, the hardness of the radiation field decreases with the increase of the stellar age, and with the increase of metallicity.

1.4.2 Star formation

Star formation occurs in molecular clouds containing H_2, the densest and coldest components of the ISM (e.g. Kennicutt & Evans 2012) initially formed by gravitational collapse. The gravitational instability has to be above the gas density threshold Σ_{crit} (e.g. Kennicutt 1989) to allow star formation to occur. The star formation activity is then related to the gas reservoir following the Schmidt-Kennicutt law:

$$\Sigma_{SFR} \propto (\Sigma_{gas})^n \,, \; n \simeq 1.4 \tag{1.6}$$

where Σ_{SFR} is the star formation rate surface density and Σ_{gas} is the gas surface density. The exponent of the power law is not necessarily the same for all objects. For example, Boissier et al. (2003) obtained an exponent of $\sim$2 in nearby disk galaxies, while Bolatto et al. (2011) found an exponent of 2.2 in a spatial analysis of the Small Magellanic Clouds. In the case of dwarf galaxies Leroy et al. (2005) derived an exponent of 1.3 using only molecular gas (Σ_{H_2}) instead of the total gas, while Cormier et al. (2014) showed that dwarf galaxies can have higher Σ_{SFR} than that found in the Schmidt-Kennicutt relationship, if determining Σ_{H_2} from CO observations. However, taking into account the HI, which appears to be the dominant gas reservoir in star-forming dwarf galaxies, they also showed that the total gas more or less follows the Schmidt-Kennicutt relationship. The different slopes could be related to the different mechanism responsible for the star formation (collision, gravitational instability, etc.; Bigiel et al. 2008).

1.4.3 Cloud structure

Cold H_2 is not directly observable due to its symmetric, homonuclear nature. Instead, the CO rotational lines are used to trace the molecular reservoir. However, CO is difficult to observed in low metallicity galaxies (e.g. Leroy et al. 2009; Schruba et al. 2012; Cormier et al. 2015), despite their intense star formation and large reservoir of HI. This is explicable considering that in low-metallicity ISM, the hard, ionizing photons can penetrate deeper into a

surrounding molecular cloud, due to the combination of low dust abundances and the hardness of the radiation. Thus, the photons can more easily dissociate the CO and the other molecules that are not efficient in self-shielding (Wolfire et al. 2010; Shetty et al. 2011), while H_2, which can be more efficient at self-shielding, can survive. Hence, in low metallicity galaxies an important fraction of H_2 is not traced by CO, as is shown in Figure 1.11 but can be traceable by other fine-structure lines in the PDR, such as [CII] or [CI] (Madden et al in prep.). The molecular fraction that is not traced by

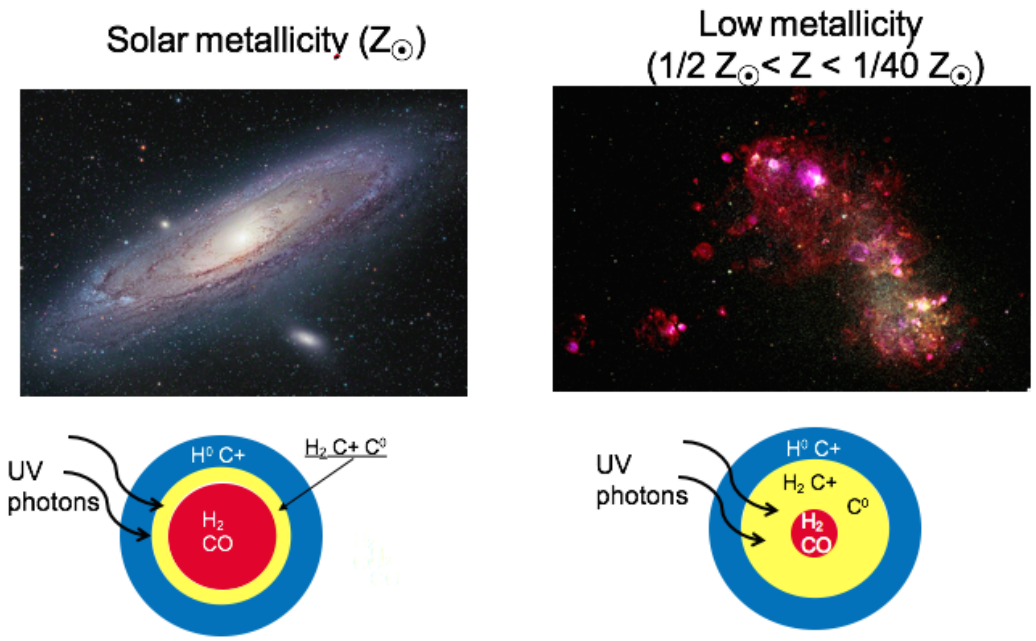

Figure 1.11: Illustration of the impact of the low metallicity environment on the structure of the molecular cloud. *Left*: figure of Andromeda and a schematic of a molecular cloud of solar metallicity; *Right*: figure of the low metallicity SMC and a schematic of a molecular cloud in low-metallicity environment. In this case the FUV photons penetrate deeper into the cloud, increasing the reservoir of H_2 that is not traced by CO (yellow zone). The red zone corresponds to the fraction of H_2 that is traced by CO, while the blue zone is the atomic phase.

CO is called 'CO-dark' gas. The existence of this 'CO-dark' gas component has been suggested via observation of [CII] 157.7 μm in dwarf galaxies (e.g. in LMC by Poglitsch et al. 1995 and in IC 10 by Madden et al. 1997) and it has been confirmed in the Galaxy by several studies (e.g. Grenier et al. 2005; Planck Collaboration et al. 2011). However, how to quantify this gas component as a function of metallicity is a current issue (e.g. Accurso et al. 2017 and Madden et al in prep.)

1.4.4 Dust properties

Dwarf galaxies have less dust mass compared to solar metallicity galaxies, since less metals are available to form dust grains.

Star-forming dwarf galaxies often have warmer dust temperatures, compared to more metal-rich galaxies. This effect can be observed in the dust SEDs which are often shifted to wavelengths lower than ∼80 μm compared to dustier galaxies with SEDs peaking at 100 - 200 μm (e.g. Helou 1986; Sauvage et al. 1990; Cannon et al. 2006; Rémy-Ruyer et al. 2013; Rémy-Ruyer et al. 2015). The dust SEDs of dwarf galaxies are also characterized by a steep rise of the MIR continuum emission (e.g. Sauvage et al. 1990; Galliano et al. 2003; Madden et al. 2006; Rémy-Ruyer et al. 2015), suggesting a larger reservoir of hot, small grains which may be produced by the sputtering and fragmentation of PAHs and larger grains due to the hard radiation field and supernovae.

Finally, the SEDs of some of these objects, show an excess at 500 μm (e.g. Galliano et al. 2003; Galametz et al. 2011; Dale et al. 2012; Rémy-Ruyer et al. 2014; Rémy-Ruyer et al. 2015; Dale et al. 2017). The origin of this excess is not yet clear. However it has been suggested to be related to several possibilities: a very cold gas component (T<10K; e.g. Galametz et al. 2011); temperature dependent grain opacity (e.g. Galliano et al. 2011); rapidly spinning dust grains (e.g. Ysard et al. 2011) or magnetic nanoparticles (Draine & Hensley 2012). Each of these interpretations implies different consequences on the dust properties. This observed submm excess still remains an open question.

1.5 Dwarf Galaxy Survey

The *Herschel* Dwarf Galaxy Survey (DGS, PI: S. Madden) is one of the three *Herschel* Guaranteed Time Key Programs of the SPIRE Local Galaxies consortium (SAG2) (Chapter 2). The two other programs are Very Nearby Galaxy Survey (VNGS, PI: C. Wilson) and *Herschel* Reference Survey (HRS, PI: S. Eales).

Since the first IRAS observations (Chapter 2) it was already clear that the ISM in dwarf galaxies shows different properties than those observed in metal rich galaxies, e.g. warmer dust on average. However before the advent of *Herschel*, it was not possible to investigate in the details the ISM structure provided by FIR/submm emission. With 230 hr of FIR and submm photometric and spectroscopic observations, the goals of the DGS are to study the dust and gas characteristics in low-metallicity environments, cov-

ering the broadest range of properties in morphology, metallicity and star formation rate of dwarf galaxies in our local universe. The sample consists of 50 local dwarf galaxies, with distances ranging from the nearest neighbor Magellanic Clouds (50 kpc) to the distance of HS0052 + 2536 (191 Mpc). The selection of the sources was made in order to obtain a statistical sample of nine galaxies in seven bins over a broad metallicity range, which covers two orders of magnitude, from half of solar metallicity 12+log(O/H) = 8.43 (He2-10) to extremely low metallicity values of 12+log(O/H) = 7.14 (IZw18, Z∼1/40 Z⊙). However, it was not possible to build a uniform metallicity sample due to observational limits in the extreme low metallicity regime (Figure 1.12). In terms of star formation, the DGS galaxies span four orders of magnitude, from 0.0007 of UGC4483 $M_{\odot}yr^{-1}$ up to 28 $M_{\odot}yr^{-1}$, reached by Haro 11. More details on the selection of the objects and their properties are presented in the Dwarf Galaxy Sample Overview (Madden et al. 2013). The targets of the DGS have been observed with the PACS and SPIRE photometers on *Herschel* (see Chapter 2), probing the dust emission in the FIR and submm. These data are crucial to model the shape of the SEDs and thus investigate the dust properties. The *Herschel* spectroscopic data obtained with PACS and SPIRE, together with *Spitzer* mid-infrared spectroscopic data, provide ∼ 20 mid-infrared and far-infrared fine-structure cooling lines to study the multi-phase gas in dwarf galaxies (Cormier et al. 2015). As shown in Figure 1.13, the DGS sources have been observed with numerous telescopes at different wavelengths, which allows an unprecedented detailed investigation of the multiphase components of dust and gas in low-metallicity environments.

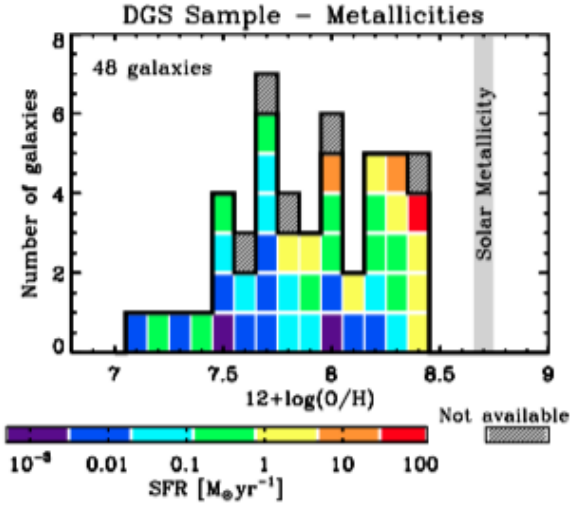

Figure 1.12: Metallicity distribution for the DGS sample, from 12+log(O/H) = 7.14 to 8.43 (Figure from Madden et al. 2013). The color code indicates the star formation rate of the galaxies in the sample. As a comparison, solar metallicity is indicated with the gray vertical line.

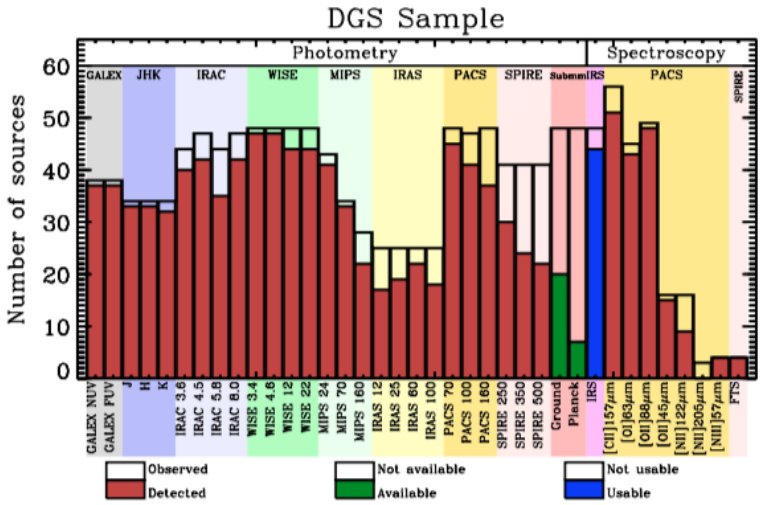

Figure 1.13: Histogram of the *Herschel* and *Spitzer* data and other ancillary data available for the DGS sources.

1.5.1 DGS analysis

The global analyses of the spectroscopic data of the full DGS have been conducted by D. Cormier, while that of the photometry by A. Reḿy-Ruyer A. during their PhDs.

1.5.2 Dust properties

The investigation of the dust properties of the DGS, through FIR photometric data, has revealed the following results (Rémy-Ruyer et al. 2013; Rémy-Ruyer et al. 2014; Rémy-Ruyer et al. 2015):

- The dust in the DGS is generally warmer than that of metal-rich galaxies: the median dust temperature of the DGS is ∼32 K, while that of the metal-rich galaxies is ∼23 K.
- Dust SED modeling of the DGS has confirmed a submm excess at the longest *Herschel* wavelength of 500μm. The excess emission is above that explicable by a standard dust SED model, such as Galliano et al. 2011. This may be related to a different composition of dust grains compared to Galactic dust or other phenomena which were also noted before *Herschel* (Section 1.2.5).
- The chemical evolution of low-metallicity galaxies, traced by their gas-to-dust ratio (G/D), is strongly affected by their local internal condi-

tions and individual histories. This is shown by the large scatter in the observed G/D at a given metallicity, reflecting the impact of various processes occurring during the evolution of a galaxy. Also at lower metallicities, the G/D becomes non-linear with respect to the metallicity. Little dust mass, relative to the gas mass, is measured in the lowest metallicity galaxies.

1.5.3 Gas properties

Analyses of FIR line emission revealed global properties of the state of the gas in dwarf galaxies (Cormier et al. 2012; Cormier et al. 2014; Cormier et al. 2015):

- [OIII] 88.4 μm is the brightest FIR cooling line in low metallicity galaxies, both at the peak of star formation sites and on global galaxy scales. This supports the hypothesis of the presence of a diffuse hard radiation field, previously suggested by high [NeIII] 15.5 μm/[NeII] 12.8 μm and [SIV] 10.5 μm/[SiII] 34.8 μm on galaxy-wide scales (Cormier et al. 2015).

- [CII] 157.7 μm is the second brightest and the most spatially extended line emission in these galaxies. Modeling the ISM phases of Haro11, Cormier et al. (2012) have found that most of [CII] 157.7 μm originates in the diffuse neutral/ionized gas rather than in PDRs. These results suggest that a large extended reservoir of diffuse gas is filling most of the volume of the ISM of the DGS.

- CO observations have been carried out for a subsample of the DGS. CO is weak, if detectable at all. The ratio [CII]/CO(1-0) $\geq 10^4$ confirm the small amount of CO in low metallicity dwarf galaxies associated with PDRs. However, the possibility of molecular gas that is not traced by CO, CO-dark gas, is suggested by the modeling of Haro11.

1.6 The dwarf irregular galaxy IC 10

IC 10 was identified as an external object by Mayall (1935) and as a member of the local universe by Hubble (1936). It has a metallicity of 12+log(O/H) = 8.26 (Garnett 1990, Lequeux et al. 1979, Richer et al. 2001, Magrini & Gonçalves 2009), between that of the Large and Small Magellanic Clouds.

Hodge & Lee (1990) discovered a large number (144) of HII regions, observing a correlation between HI and Hα, similar to that in the Galaxy,

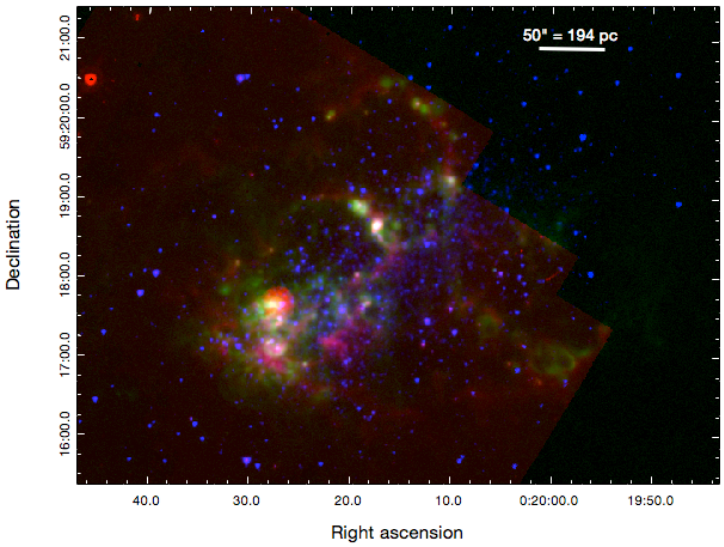

Figure 1.14: Three-color image of IC 10 with PAH emission (*Spitzer*/IRAC4; 8.0μm) in red, Hα (Hunter & Elmegreen 2004) in green, and stars (*Spitzer*/IRAC1; 3.6μm) in blue.

namely that large HI clouds tend to have, star formation, HII regions and molecular cloud around their edges. The starburst nature of the galaxy was confirmed by Massey & Armandroff (1995) who found 15 Wolf-Rayet (WR) stars (updated to 100 in Massey & Holmes (2002)), suggesting that the galaxy is undergoing current star formation activity. Other studies investigating this unexpected high number of WR stars followed. Crowther et al. (2003) identified in total 25 WR stars, 14 WC (WR star which spectrum is dominated by lines of carbon) and 11 WN (WR star which spectrum is dominated by lines of nitrogen), finding a surprisingly high WC/WN for a metal poor galaxy. Indeed, very massive stars first become WN and then evolve into WC, while less massive stars stop at the WN stage (Massey 2003).

Borissova et al. (2000) used JHK photometry to study the young massive red supergiants in IC 10, determining ages of 10-50 Myr. *HST* observations in U,V,I and Hα by Hunter (2001) identified several stellar clusters, but no super star cluster. Two of them are red clusters with ages $\geq$350 Myr, the others are younger with ages between 4-30 Myr. A very young cluster 3-4 Myr, located in the brightest part of the nebula [HG90]111 (see Hodge & Lee 1990), which is in our *Central main zone* (see Chapter 5, Figure 5.2), has been identified. Moreover, all of these analysis suggest that the star formation activity of IC 10 has created mostly OB stars in these star clusters. Vacca et al. (2007) focused the analysis on the *Central main zone*, concluding that the stellar population is well represented by at least two bursts of star formation: one $\sim$10 Myr and another 150-500 Myr. In particular, young blue stars are concentrated in [HG90]111, which consists of OB stars and 6 WR stars. Their analysis highlighted a clear spatial segregation between

young blue stars, ∼10 Myr, (WR and OB) and older stars, 150-500 Myr (red stellar population). Estimating the age of the stellar content, Sanna et al. (2009) identified a clear change in age distribution, from 12 to 300 Myr, moving from the *Central main zone* to the outer regions. They identified massive MS stars, old (HB) and intermediate age (RC) helium burning stars, indicating several star-forming episodes during the lifetime of the galaxy. Recently, Lim & Lee (2015) have found 66 stellar clusters including five in the halo of the galaxy. The star clusters in the halo are all older than 1 Gyr, while in the main body, they have a range of ages: from several Myr to older ages, more than 1 Gyr. The young clusters (<10Myr) are located in the Hα emission region, while the old clusters are distributed over a wide area of the disk. Investigations of the stellar component of IC 10 highlight a young stellar population (Sanna et al. 2009; Yin et al. 2010; Vacca et al. 2007), which is another confirmation of the hypothesis that IC 10 is currently undergoing a starburst phase, probably triggered by neutral gas falling from the HI envelope (Wilcots & Miller 1998).

IC 10 consists of a main body from which emanate several impressive star-forming arcs of gas and dust (Figure 1.14), sitting in an extended and complex HI envelope which is seven times larger then that of the optical diameter (Huchtmeier 1979; Ashley et al. 2014). Kinematic studies of the HI emission were performed by Wilcots & Miller (1998). They discovered that the HI halo of IC10 is characterized by a rotating disk embedded within a complex and extended distribution of gas. The center of the disk is dominated by an HI cloud where many WR stars, as well as supernovae, are located. HI emission exists in halos, shells and arcs that are formed by the stellar winds from the large population of WR and O stars. The second generation of star formation may have been triggered by the stellar winds (e.g. Yin et al. 2010; Vacca et al. 2007). On the other hand, the external structure of HI suggests that the galaxy is still forming via the accretion of the surrounded intergalactic gas. Nidever et al. (2013) explored the structure of atomic gas as traced by HI 21cm emission, identifying a feature in the northwest with a large radial velocity, higher than that of IC 10. They suggested that this structure could be related to a recent interaction with another dwarf galaxy, which could have triggered the recent starburst observed. IC 10 has a peculiar bubble in the south east which corresponds to a non-thermal cavity associated with a supernovae remnant (X-1; Shostak & Skillman 1989), which is the brightest X-ray source in the galaxy (Wang et al. 2005). Their analysis of this object suggests that the source is a black hole of $4M_{\odot}$, probably accreted by a WR companion. They also detected a diffuse X-ray component, mainly associated with the starburst region. They argued that it could be an optically thin thermal plasma, which is driving outflows from the starburst region.

However, reconciling the SF activity and the gas necessary to fuel the activity is still an open issue. IC 10 shows high SF activity compared to the molecular gas surface density, determined from CO observations (Leroy et al. 2006), while a large quantity of H_2 has been inferred from the CO-dark gas tracer, [CII] 158 μm Madden et al. (1997). Additionally on the global scale, the gas-to-dust mass ratio is observed to be 240 to 476, lower then that expected based on its metallicity ($\sim 10^3$) (Rémy-Ruyer et al. 2014).

The ionized gas looks to be linked to the HI velocity field (Thurow & Wilcots 2005), with supernovae remnants and winds from WR stars as sources of the kinematics of the ionized gas (Thurow & Wilcots 2005). The ionized gas is very extended beyond the main star-forming body of the galaxy, motivating Hidalgo-Gámez (2005) to investigate the origin of the Diffuse Ionized Gas (DIG) observed in this galaxy. They discard the possibility of shocks as the source of this extended ionization and suggest that a combination of photons leaking from the HII regions and of the ionization provided by the WR stars, is required.

In spite of all of these detailed studies of IC 10, the estimation of the distance to IC 10 has been a very complex issue, due to the location of this galaxy close to the Galactic plane (b= -3.3). The distance has been determined to be a few kpc to 3 Mpc. Several studies have been perform to define the real reddening and distance of this galaxy. Massey & Armandroff (1995) identified a blue plume of the main-sequence luminous stars in the BV color-magnitude diagram, obtaining the reddening of E(B-V)=0.75 - 0.80 and the distance of $\sim$1 Mpc. Borissova et al. (2000), comparing the supergiants of IC10 with those of IC1613, which has similar luminosity and metallicity of IC 10, have found reddening of E(B-V)=1.05$\pm$0.1 and distance of $(m - M)_0$=23.86. Moreover, in their analysis they identify two main star-forming regions that coincide with the *Central main zone* and *ArcA* of this work (see Chapter 5). For these regions they calculated the extinction with the ratio Brγ/Hα, where Brγ is a recombination line of hydrogen tracing hot young stars, finding 1.8$\pm$0.2 and a star formation rate (SFR) of 0.6 $M_\odot yr^{-1}$. Richer et al. (2001) studied optical spectroscopy of the HII region as well as UBVR photometry, finding a foreground reddening due to the Galaxy of E(B-V)=0.77$\pm$0.07 mag. Demers et al. (2004) have calculated the reddening and distance using 676 carbon stars, which can be used as standard candle (Demers et al. 2003). They find that the reddening varies across the galaxy and the distance to the galaxy is 741 kpc. More recently, Kim et al. (2009), using deeper near-infrared JHKs and UBV photometry, estimated the total reddening of E(B-V)= 0.98$\pm$0.06 and a distance to IC 10 of 715$\pm$10 kpc. In this work I will use the distance of 700 kpc (such as e.g. Lim & Lee 2015, Leroy et al. 2006), while the extinction will be discussed in Chapter 6. The

proximity of this galaxy allows observation at high spatial resolution. In particular, this galaxy is an ideal laboratory to investigate the effects of massive star formation on the different phases in metal-poor environments.

This thesis project investigates the properties of the multi-phase ISM of the nearby dwarf galaxy IC 10, focusing on the analysis of the physical properties of the compact HII regions and the diffuse ionized gas, traced by the mid- and far-infrared cooling lines. The proximity of this galaxy enables the analysis of the ISM on different spatial scales: from the compact, bright clumps (∼25 pc) to the whole star-forming body of the galaxy (∼650pc).

Chapter 2

Infrared telescopes: *Spitzer*, *Herschel* & SOFIA

Contents

In this chapter I present the telescopes and instruments that provided the observational data for our analysis. In particular I provide details on the spectrometers and the steps we followed to reduce the spectroscopic data on which my thesis is based.

2.1 Infrared observations

The incoming IR and submm radiation is mainly absorbed by water vapor in the Earth's atmosphere. Observing from high altitude or from space is necessary to probe this wavelength regime. Our exploration of the IR and mm universe started with IRAS, launched in 1983, followed by ISO, AKARI, *Spitzer*, WISE and *Herschel* in 2009. With each mission, higher spatial and spectral resolutions were reached and longer wavelengths could be investigated, as shown in Figure 2.1. In particular, *Herschel* allowed observations at wavelengths never observed before in order to investigate the cold universe. Moreover, its improved spatial resolution helped us separate various structures of nearby galaxies in the FIR and submm (arm/inter-arm, star-forming regions/diffuse emission, etc.).

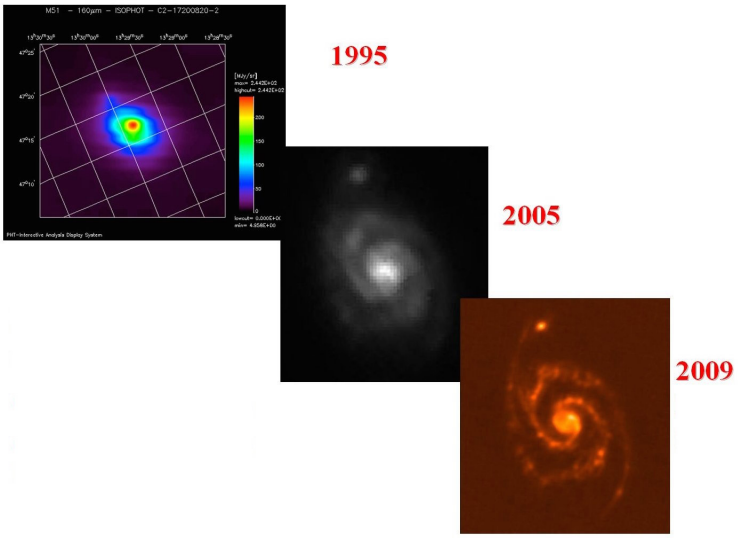

Figure 2.1: Images of M51 at 160 μm obtained by ISO, *Spitzer* and *Herschel*, showing a continuous improvement in resolution and sensitivity. (Image from *Herschel* Observer's manual).

Flying observatories such as the Stratospheric Observatory for Infrared Astronomy (SOFIA) and its predecessor, the Kuiper Airborne Observatory

(KAO) can observe at altitudes above 37,000 feet, thus eliminating about 99% of the atmosphere water vapor from the line of sight.

Table 2.1 summarizes the history of infrared observations, from the first space mission to the present day.

Table 2.1: List of infrared and submillimetre telescopes.

Telescope	*Launch year*	*Wavelength* [μm]	*Spatial*[(a)] *resolution* [*arcsec*]	*Spectral resolution* $\Delta R/R$	*Lifetime* [*years*]
IRAS	1983	$12 - 100$	150	–	1
ISO	1995	$2 - 240$	60	$10^2 - 10^4$	3
Spitzer	2003	$3 - 160$	40	$10^2 - 10^3$	*operating*
AKARI	2006	$1.7 - 180$	39	–	5
WISE	2006	$2.5 - 25$	–	–	6
Herschel	2009	$55 - 670$	10	$10^2 - 10^7$	3.5
KAO	1974	$1 - 500$	30	$\sim 10^4$	21
SOFIA	2011	$0.3 - 1600$	10	$10^3 - 10^8$	*operating*

(a) Spatial resolution estimated at 100 μm, except for AKARI (estimated at 90 μm) and *Spitzer* (estimated 160 μm).

2.2 The *Spitzer* Space Telescope

2.2.1 *Spitzer* Mission

The IR *Spitzer* Space Telescope was launched on the 23rd of August, 2003 with a primary mirror of 85 cm diameter and three scientific instruments covering wavelengths from 3.6 to 160 μm. It is the fourth of the NASA's Great Observatories program, which includes the Hubble Space Telescope, the Chandra X-Ray Observatory and the Compton Gamma ray Observatory. The life of this telescope was expected to be five years, which was the time needed for the onboard liquid helium, used to cool the telescope, to evaporate completely. The cryogenic lifetime ended in May 2009 but the telescope is still operating as part of the so-called *Spitzer* Warm Mission, observing with the two shortest-wavelength modules of the IRAC camera (Sec. 2.2.2). Their sensitivities were not affected after the exhaustion of the helium.

A schematic configuration of the *Spitzer* Space Telescope is shown in Figure 2.2. The spacecraft operates at ambient temperature. The cryogenic

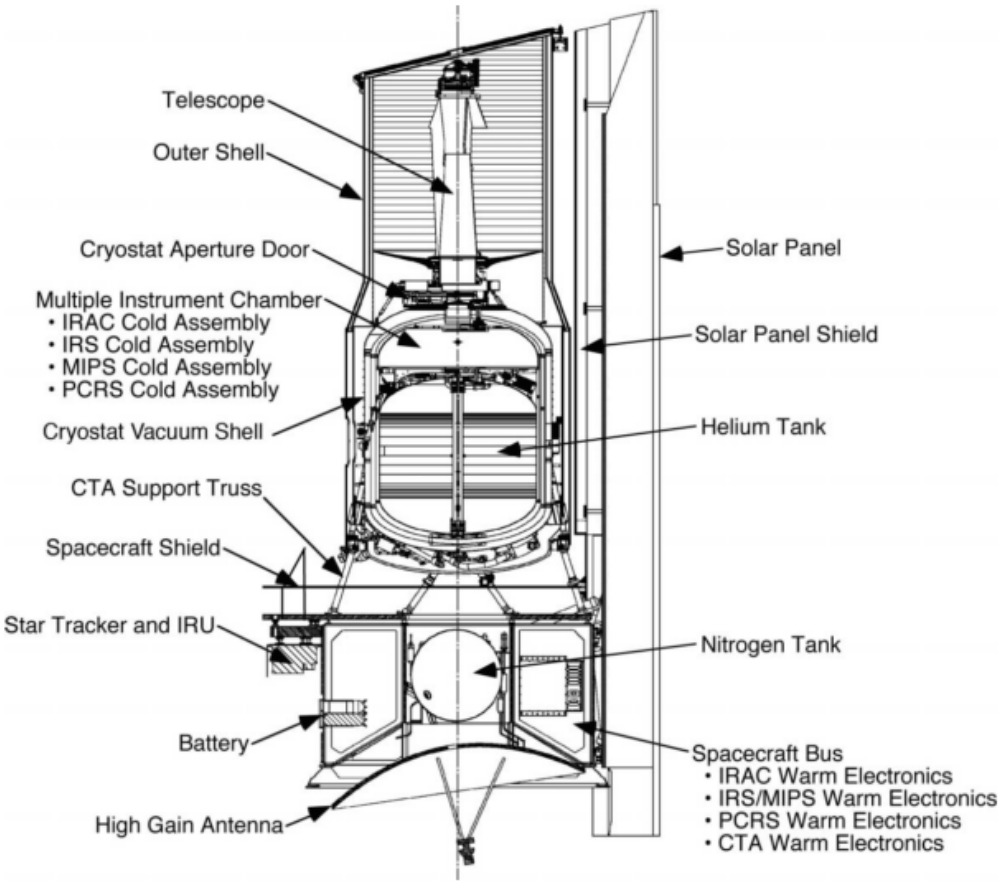

Figure 2.2: *Spitzer* configuration. Image from Werner et al. (2004).

telescope assembly (CTA) was cooled by superfluid liquid helium, helium boil-off gas and radiative cooling. The two components are thermally isolated from each other. The spacecraft provides electrical power to the instrument, stabilizes the pointing, manages the data processing, the storage and the communication with the ground. Moreover, the spacecraft structure includes sensors that are used for calibration twice a day.

The three instruments onboard, which share a common focal plane, are:

- IRS (Infrared Spectrograph) - a low- to moderate-resolution spectrometer
- IRAC (Infrared Array Camera) - a four-channel imaging photometer
- MIPS (Multiband Infrared Photometer) - an imager and spectral en-

ergy distribution photometer

More details on the telescope can be found in the *Spitzer* Observer's Manual as well as in Werner et al. (2004).

2.2.2 IRAC

The Infrared Array Camera is a four-channel camera that provides photometry at 3.6, 4.5, 5.8 and 8.0 μm. The four channels in pairs (3.6 and 4.5 μm; 5.8 and 8.0 μm) simultaneously map two adjacent 52'×52' fields of view (FOV). The full width at half maximum (FWHM) of the point spread functions (PSF) are 1.7", 1.7", 1.9" and 2" for the channels 3.6, 4.5, 5.8 and 8.0 μm, respectively. The analysis of the flux calibrator data indicates that absolute flux calibration is accurate to 3%. More details of the instrument and its performance can be found in the IRAC Instrument Handbook as well as in Fazio et al. (2004).

2.2.3 MIPS

The Multiband Imaging Photometer provides images at 24, 70 and 160 μm and SED measurements between 52 to 97 μm at low spectral resolution $R = \lambda/\Delta\lambda = 15$ - 25. The photometer contains three separated detector arrays. Their FOVs are 5'×5', 2.5'×5' and 0.5'×5' for 24, 70 and 160 μm, respectively. The FWHM of the PSFs are 6", 18" and 40" for 24, 70 and 160 μm, respectively. More details of the instrument and its performance can be found in the MIPS Instrument Handbook as well as in Rieke et al. (2004).

2.2.4 IRS

Instrument design

The Infrared Spectrograph consists of four separate spectrograph modules (Figure 2.3) covering the wavelength range 5.2-38 μm with a resolution, $R = \lambda/\Delta\lambda$, from 90 up to 600. Two are long-slit low-resolution modules, Short-Low (SL) and Long-Low (LL). IRS is limited by the zodiacal and/or Galactic background in these two modes. Each of the low-resolution modules is divided in two sub-slits, providing spectra in the first or second order (called SL1, SL2, LL1, LL2). In order to assure an overlap in wavelength between the two orders, a short list of the first-order automatically appears on the array when a source is observed in the second order. The other two modes are the high-resolution modes, Short-High (SH) and Long-High (LH). They were designed to reach the highest resolution, given the array dimensions.

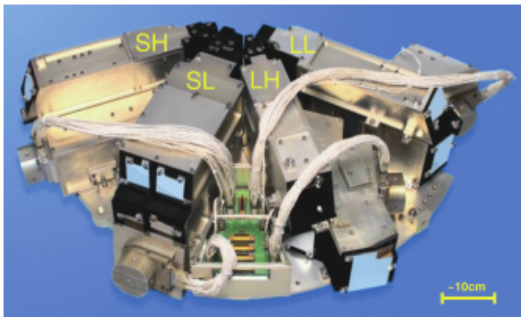

Figure 2.3: The four IRS modules, SH, SL, LH, and LL on *Spitzer* from Houck et al. (2004). They cover the wavelength range 5.2 to 38 μm. In this thesis I use observations from these four modules.

Each of the high-resolution modules has a single slit and is cross-dispersed, allowing for broad spectral coverage in one single exposure. Moreover, the IRS provides imaging in two filters, 13-19 μm and 18-26 μm. They are referred to as the blue and red peak-up (PU) arrays and are used to obtain calibrated images at 16 and 22 μm with a field of view of 54"×81". Figure 2.4 shows a schematic of the slits and the peak-up arrays and Table 2.2 provides the characteristics of each module.

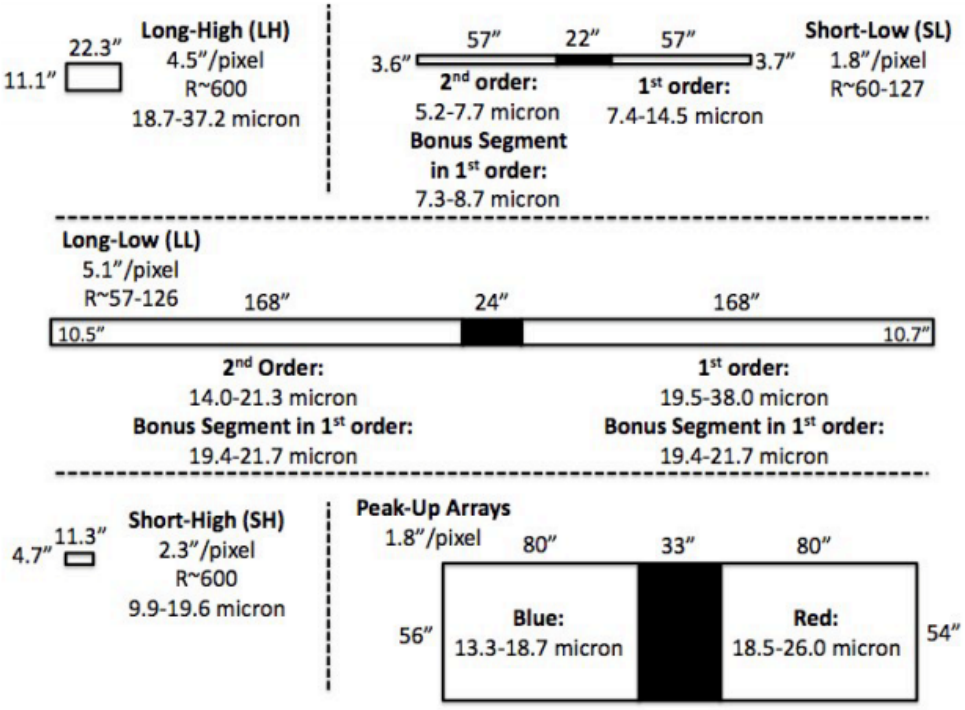

Figure 2.4: Schematic view of the slits and peak-up apertures. (From the IRS Instrument Handbook).

Capabilities

Spectral calibration is obtained via several steps. The first is a flat-field calibration, which is used to compute the response of the detector for each pixel. It requires the observation of an extended source whose response is assumed to be uniform throughout the detector. The spectrum obtained from this observation is called a spectral flat and is applied to the observed spectra to calibrate them. In order to construct the IRS spectral flats, several observations of standard stars (with a smooth, well-known spectrum) are combined, simulating an extended source. The simulated extended source is then divided by the modeled extended source to produce the protoflat (which is a flat that has not yet been corrected using zodiacal light observations) and finally the non-uniform spatial response of the protoflat is corrected using observations of the zodiacal light. The next step is the wavelength calibration, which is computed from measurements of bright Galactic sources and from bright extragalactic lines for the spectral regions that do not include bright Galactic lines. The internal cross-calibration of the IRS is re-inforced by the overlaps in wavelength coverage between the modules and the slits of each module.

The median 1-σ continuum sensitivity reached in a 512-second integration with low background for the IRS low-resolution modules is about 0.06 mJy from 6 to 15 μm (SL module) and 0.4 mJy from 14 to 38 μm (LL module). For the IRS high-resolution modules, it is about 1 mJy from 10 μm to 20 μm (SH module) and 4 mJy from 20 μm to 38 μm (LH module). The median 1-σ line sensitivity reached in a 512-second integration with low background is $2.7{\times}10^{19}$ W m^{-2} for the short-wavelength high-resolution

Table 2.2: Main properties of the IRS modules.

Module	Order	$\lambda_{min} - \lambda_{max}$ $[\mu m]$	$\lambda/\Delta\lambda$	FWHM $[arcsec]$	Slit Size $[arcsec]$	Pixel Scale $[arcsec]$
SL	SL1	$7.4 - 14.5$	$60 - 127$	3.7	3.7×57	1.85
	SL 2	$5.2 - 7.7$				
LL	LL1	$19.5 - 38.0$	$60 - 127$	10	10.7×168	5.10
	LL2	$14.0 - 21.3$				
PU-blue		$13.3 - 18.7$	~ 3	3.8	80×56	1.8
PU-red		$18.5 - 26.0$	~ 3	5.3	80×54	1.8
SH	$11 - 20$	$9.9 - 19.6$	600	4	4.7×11.3	2.3
LH	$11 - 20$	$18.7 - 37.2$	600	8	11.1×22.3	4.5

module and 8.5×10^{19} W m^{-2} for the long-wavelength high-resolution module.

Spitzer **IC 10 observations**
IC 10 has been targeted with IRS on two different occasions. The first observations with the SL module (1st and 2nd order) were performed on September 2008 mapping a region of ∼330"×290", which corresponds to ∼1.6 kpc ×1.4 kpc at the distance of IC 10. Moreover additional five individual high-resolution pointings, corresponding to the peaks of PAH emission, were observed with the SH and LH modules. On the second occasion, LL modules (1st and 2nd order) were used to map a region of 2.9'×2.4'. In both cases the sources were observed in spectroscopic mapping mode. In order to obtain the full map coverage, the observer selects a grid of map positions around a central target position. The telescope is moved in directions perpendicular to the long axis of the slit covering the area selected, then moved parallel to the slit. In order to optimize the observing time, the observations in SL mode do not fully cover the galaxy. Instead, between every perpendicular scanning position, a gap with the same width as the SL aperture was introduced. These gaps were then covered by smoothing the data to lower spatial resolution. The LL map was observed only in directions perpendicular to the long axis of the slit. Figure 2.5 shows the slit configurations of the regions covered by SL (left) and LL (right) observations. The positions of the HR pointings are shown in Figure 2.6.

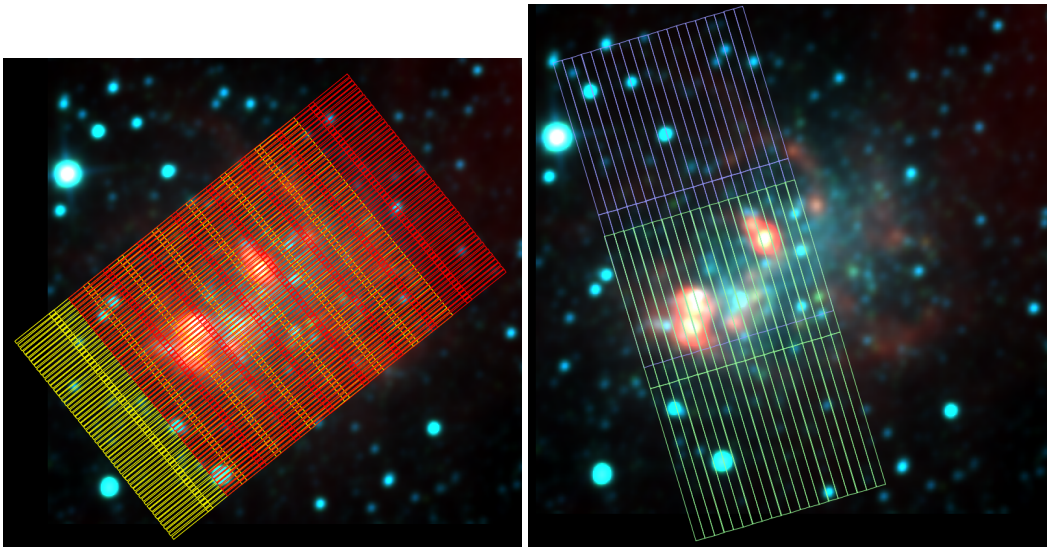

Figure 2.5: *Left*: Projection of the configuration of the slits for SL observations of IC 10 (SL1 in red and SL2 in yellow). *Right*: Projection of the configuration of the slits for LL observations (LL1 in green and LL2 in violet)

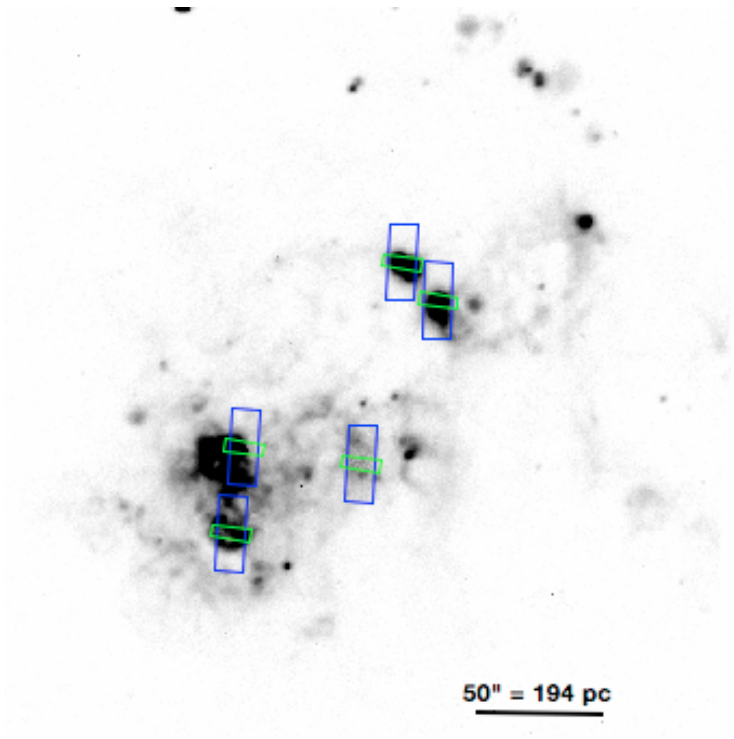

Figure 2.6: Hα map of IC10 (Hunter & Elmegreen 2004). The *Spitzer*/IRS high-resolution slits are overlaid: the long module in blue and the short module in green.

Table 2.3 provides a summary of the observations.

2.2.5 Data reduction - *Spitzer*/IRS

The IRS data used in my thesis were reduced by V. Lebouteiller, author of the CASSIS spectral database (Lebouteiller et al. 2011, http://cassis.sirtf.com/) and PACSman (Lebouteiller et al. 2012). Below I present a brief summary of the IRS data reduction process, as applied to the IC 10 observations.

- **SL and LL observations** : The basic calibrated data products are downloaded from the *Spitzer* Heritage Archive (SHA[1]). Exposures are then cleaned with IRSclean[2] and combined in Smart[3] (Higdon et al. 2004; Lebouteiller et al. 2010). The data are then imported into CUBISM[4] (Smith et al. 2007; DOI 10.1086/522634) for further cleaning (cube backtracking) and for building a data cube with pixel sizes of 1.8″ and 5.1″ for SL and LL respectively. A Monte-Carlo simulation is

[1] http://sha.ipac.caltech.edu/applications/Spitzer/SHA/
[2] http://irsa.ipac.caltech.edu/data/SPITZER/docs/dataanalysistools/tools/irsclean/
[3] http://irs.sirtf.com/IRS/SmartRelease
[4] http://irsa.ipac.caltech.edu/data/SPITZER/docs/dataanalysistools/tools/cubism/

Table 2.3: Summary of IRS observations of IC 10.

Position	*Module*	*Size*	*AORkey*
0 : 20 : 13.45 +59 : 18 : 20.0	*SL*	$330'' \times 290''$	25968384
00 : 20 : 24 +59 : 18 : 03	*LL*	$2.90' \times 2.40'$	26396672
00 : 19 : 21 +59 : 15 : 01	*LL*	*one slit*	26397184 (*background*)
0 : 20 : 27.25 +59 : 17 : 05.9	*SH* *LH*	*one slit* *one slit*	25968640
0 : 20 : 26.81 +59 : 17 : 39.6	*SH* *LH*	*one slit* *one slit*	25968896
0 : 20 : 20.84 +59 : 17 : 35.3	*SH* *LH*	*one slit* *one slit*	25969152
0 : 20 : 17.30 +59 : 18 : 40.2	*SH* *LH*	*one slit* *one slit*	25969408
0 : 20 : 19.20 +59 : 18 : 54.5	*SH* *LH*	*one slit* *one slit*	25969920
0 : 20 : 33.84 +59 : 12 : 54.3	*SH* *LH*	*one slit* *one slit*	25969664 (*background*)

then used to produce the spectral maps. First, a hypercube with 100 outcomes ("planes") is created and for each outcome: (1) The gaps in the SL map are filled using a B-spline fit in the direction perpendicular to the slits. (2) A median filtering is applied in the dispersion direction to accommodate for the lack of spatial resolution due to the incomplete sampling in that direction. These first two steps are performed only for SL because in LL there is no over-slit: the maps are covered only in one direction. (3) Each plane is convolved to a resolution of either $4''$ (SL) or $11''$ (SL and LL). (4) Each plane is resampled to a pixel size of either $4''$ (SL) or $12''$ (SL and LL). Finally, spectral lines are adjusted for each pixel in each plane and the line flux and associated uncertainties are calculated using the median and median absolute deviation of the line flux distribution among the 100 outcomes.

- **SH and LH observations** : The individual high-resolution pointings are retrieved from the CASSIS. For some pointings, the emission is extended and relatively uniform. Thus the SH and LH spectra do

not align because both modules have different slit sizes (4.7"×11.3" for SH, 11.1"×22.3" for LH). For such cases, the extended source calibration is used, and a scaling factor is applied to match SH to LH in the overlapping wavelength range of 19.0-19.5 μm band. Some pointings are dominated by a point source. In such cases, the SH and LH spectra, when calibrated with a point-source correction, align fairly well. Table 2.4 reports the fluxes obtained for four of them. The fluxes of the pointing AORkey25968896 are not presented because it is missed pointing. Thus, SH and LH did not observe the same position and the calibration is not reliable.

2.3 The *Herschel* Space Observatory

2.3.1 *Herschel* Mission

The *Herschel* Space Observatory was the fourth "cornerstore" mission in the ESA "Horizon 2000" program. Originally called "FIRST" (for Far InfraRed and Submillimetre Telescope), the name was changed to *Herschel* in honor of Sir William Herschel who discovered IR radiation. The *Herschel* Space Observatory was launched on May the 14th, 2009 (together with the *Planck* telescope). It operated at the 2nd Lagrangian point of the Sun/Earth system until April the 29th, 2014, when the helium that cooled the instruments was exhausted. With far higher spatial resolution and sensitivity than previous infrared space missions, *Herschel* was also designed to observe the cold universe, extending the wavelength coverage toward submm wavelengths. The aim of the mission was to investigate a large range of questions, from the study of the chemistry of planets to the structure of the ISM to galaxy formation and evolution processes in the early universe.

The spacecraft (Figure 2.7) has a 3.5-m mirror, a helium cryostat, a sun shade and a service module. It was fitted with three instruments cooled down to 0.3 K by the liquid helium housed in the cryostat, allowing full spectral coverage in the 60-670 μm range. The three instruments onboard *Herschel* complement each other:

- PACS (Photodetector Array Camera and Spectrometer; Poglitsch et al. 2010) - an imaging photometer and medium resolution spectrometer. The spectrometer covers the 55-210 μm wavelength range, while the photometer covers the 70-160 μm wavelength range;
- SPIRE (Spectral and Photometric Imaging Receiver; Griffin et al. 2010) - an imaging photometer and an imaging Fourier transform spectrom-

Table 2.4: Fluxes obtained with HR modules for each pointing used in this work.

Line	$Flux \pm Uncertainty$ [$\times 10^{-16}$W m^{-2}]			
	25968640 *Center c3*$^{(a)}$ *point*$^{(b)}$	25969152 *extended*$^{(c)}$	25969408 *ArcA c2*$^{(a)}$ *point*$^{(b)}$	25969920 *ArcA c1*$^{(a)}$ *point*$^{(b)}$
[SIV]	6.59 ± 0.10	$< 0.01(1\sigma)$	17.70 ± 0.23	3.25 ± 0.11
$H_2(0,0)S(2)$	0.48 ± 0.06	0.16 ± 0.06	0.12 ± 0.04	$< 0.01(1\sigma)$
Huα	0.39 ± 0.06	0.19 ± 0.05	0.53 ± 0.04	0.29 ± 0.04
[NeII]	5.98 ± 0.19	1.01 ± 0.05	5.35 ± 0.23	3.49 ± 0.13
$[NeV]_{14\mu m}$	$< 0.03(1\sigma)$	0.17 ± 0.08	$< 0.02(1\sigma)$	0.18 ± 0.06
$[NeIII]_{15\mu m}$	11.79 ± 0.44	0.81 ± 0.07	25.73 ± 1.11	7.44 ± 0.33
$H_2(0,0)S(1)$	0.80 ± 0.04	$< 0.01(1\sigma)$	0.13 ± 0.03	0.09 ± 0.02
$[SIII]_{18\mu m}$	11.00 ± 0.25	0.84 ± 0.03	17.81 ± 0.18	7.17 ± 0.03
$[FeII]_{17\mu m}$	0.19 ± 0.04	0.05 ± 0.04	$< 0.03(1\sigma)$	$< 0.02(1\sigma)$
$[FeII]_{25\mu m}$	0.35 ± 0.01	0.09 ± 0.01	0.31 ± 0.02	0.11 ± 0.02
[OIV]	0.12 ± 0.01	0.03 ± 0.01	0.07 ± 0.02	0.07 ± 0.01
$[NeIII]_{36\mu m}$	1.40 ± 0.18	$< 0.03(1\sigma)$	2.86 ± 0.40	0.91 ± 0.15
[SiII]	8.04 ± 0.26	1.41 ± 0.03	5.93 ± 0.23	2.69 ± 0.09
$[SIII]_{33\mu m}$	21.20 ± 0.52	1.78 ± 0.04	24.30 ± 0.26	10.10 ± 0.13
$H_2(0,0)S(0)$	0.44 ± 0.04	0.07 ± 0.01	0.17 ± 0.05	0.06 ± 0.02
$[NeV]_{24\mu m}$	$< 0.0175(1\sigma)$	$< 0.01(1\sigma)$	$< 0.03(1\sigma)$	$< 0.01(1\sigma)$
[ArIII]	0.19 ± 0.02	0.01 ± 0.01	0.44 ± 0.03	0.16 ± 0.02
[FeIII]	0.47 ± 0.01	0.06 ± 0.01	0.37 ± 0.03	0.14 ± 0.01

(a) ID used in this work for the clump that correspond to this pointing (Section 5.2.1).
(b) Pointings calibrated with a point-source calibration.
(c) Pointings calibrated with extended-source calibration.

eter. The spectrometer covers the 194-324 μm and 316-671 μm wavelength ranges, while the photometer covers the bands centered in 250, 350 and 500 μm;

- HIFI (Heterodyne Instrument for the Far Infrared; de Graauw et al. 2010) - a very high resolution heterodyne spectrometer, covering the 157-212 μm and 240-625 μm wavelength ranges.

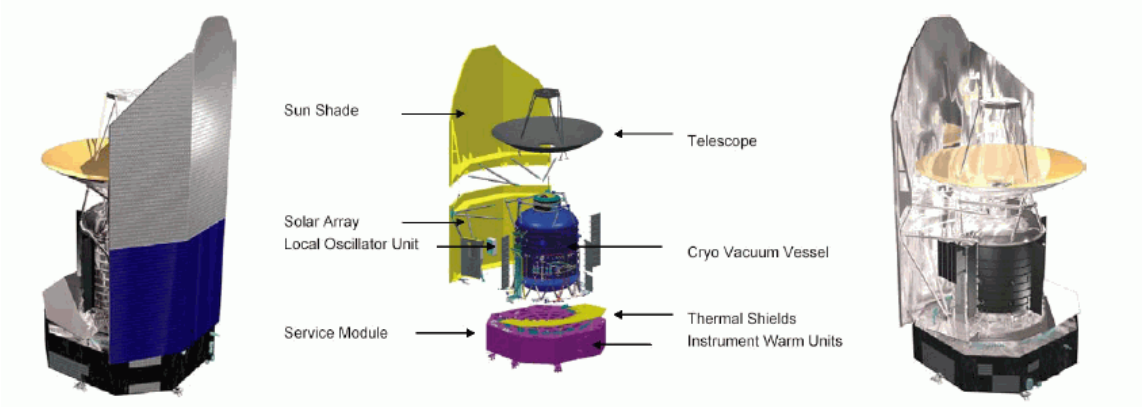

Figure 2.7: The *Herschel* spacecraft. The "warm" side on the left and the "cold" side on the right. The image in the middle shows details of the major components. (Image from *Herschel* Observer's manual).

2.3.2 SPIRE

The Spectral and Photometric Imaging Receiver (SPIRE) consists of a three-band imaging photometer that provides photometry in spectral bands centered on 250, 350 and 500 μm and an imaging Fourier Transform Spectrometer (FTS) that uses two overlapping bands to cover the wavelength range 191-671 μm. The layout of the FTS is shown on the left side of Figure 2.8, while the right side shows the layout of the photometer.

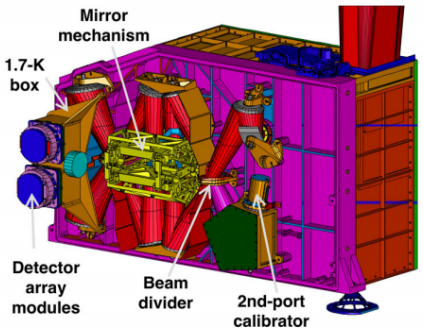

Figure 2.5: SPIRE FPU: spectrometer side layout.

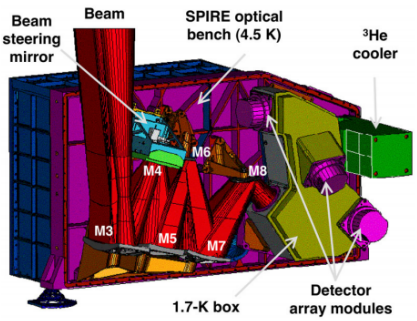

Figure 2.3: SPIRE FPU: photometer side layout.

Figure 2.8: The SPIRE focal plane unit: (*Left*) the photometer layout; (*Right*) spectrometer layout. (Images from SPIRE Observers' Manual).

Table 2.5: SPIRE spectrometer characteristics.

Band	*Range* $[\mu m]$	*Spectral resolution* $[km/s]$	*FWHM* $[arcsec]$	*Line sensitivity* $5\sigma - 1h$ $[Wm^2 \times 10^{-17}]$
SSW	$194 - 324$	$280 - 450$	$16 - 20$	$1.56 - 2.15$
SLW	$316 - 672$	$440 - 970$	$30 - 43$	$0.94 - 2.04$

Spectrometer : The FTS worked as an interferometer in a Mach-Zehnder configuration. The incident light is separated by a beam splitter into two rays that travel along different optical paths before recombining. The interferogram of the signal is created from the Optical Path Difference (OPD) of the two beams. The signal that is registered by the detectors is the Fourier component of the full spectral content rather than the integrated flux density within the passband. For this reason, the spectrum as a function of frequency is the inverse of the Fourier transform of the signal. The highest resolution available was $\Delta\sigma = 0.04$ cm^{-1}, which depends on the maximum OPD (14 cm).

The two overlapping bands are 194-324 μm covered by the SPIRE Short Wavelength spectrometer array (SSW) and 316-672 μm by the SPIRE Long Wavelength spectrometer array (SLW). These arrays contain 37 (SSW) and 19 (SLW) hexagonally arranged detectors, resulting in a FOV of 2' in diameter. The characteristics of the spectrometer bands are summarized in Table 2.5

Photometer : The SPIRE photometer observed in three broad-bands simultaneously, centered on 250, 350 and 500 μm, for the short wavelength (PSW), medium wavelength (PMW) and long wavelength (PLW) modules, respectively. The light was separated by dichroic filters and focused onto three detector arrays composed of 139 (250 μm), 88 (350 μm) and 43 (500 μm) detectors. The FOV for each of the filters is 4'×8', while the sensitivity and the PSF FWHM vary for each band, as summarized in Table 2.6. The calibration uncertainty is a combination of the absolute and relative calibration uncertainties. The absolute flux calibration from observations of Neptune is estimated to be ∼4%, while the relative calibration uncertainty, related to the ability of the instrument to reproduce a measurement of the same flux at the same time, is measured to be ∼1.5%. More details regarding SPIRE can be found in Griffin et al. (2010) and the SPIRE Observers' Manual.

Table 2.6: SPIRE photometer characteristics.

Band	*Centered wavelength* (μm)	*FWHM* ($arcsec$)	*Scan mapping sensitivity* $1\sigma - 1s$ (mJy)
PSW	250	18.1	30.6
PMW	350	24.9	36.0
PLW	500	36.4	68.5

2.3.3 PACS

Instrument design

The Photodetector Array Camera and Spectrometer (PACS, Poglitsch et al. 2010) consists of two sub-instruments, a dual-band photometer and an integral-field spectrometer. The photometer is a three-band instrument designed to observe in two bands at a time: the blue band (60-85 μm) or the green band (85-130 μm) were observed simultaneously with the red band (130-210 μm), over a field of view of 1.75'×3.5'. The spectrometer has two channels (blue: 51-105 μm; red: 102-220 μm) observing simultaneously over a field of view of 47"×47".

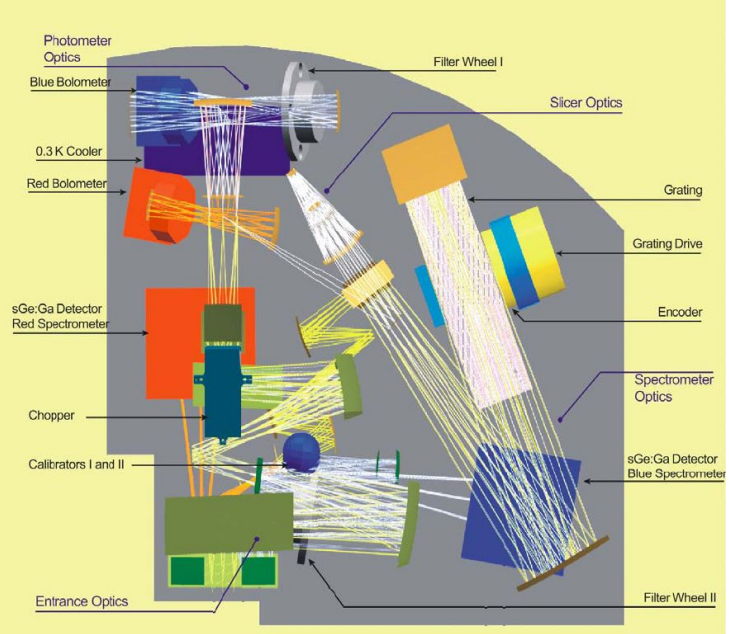

Figure 2.9: PACS layout. Beyond the common entrance optics, the light is divided into the spectrometer path and into the photometer path. In the photometer the light is separated in two channels, red and blue. In the spectrometer, the light is first split into three orders. Only two of them fall on the blue and red detectors. (Images from *Herschel* Observer's manual).

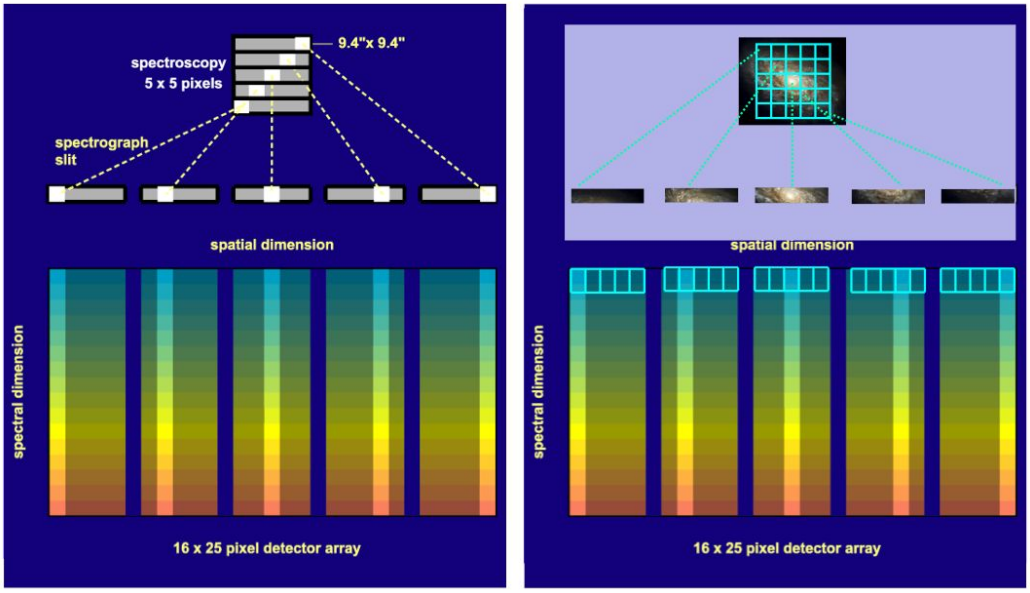

Figure 2.10: The PACS integral-field spectrometer. The optical image slicer rearranges the 2-dimensional field along the entrance slit of the grating spectrograph: a spectrum can thus be obtained simultaneously for each spatial element of the field of view. (Image from *Herschel* Observer's manual).

The light arrives at the *entrance optics*, common to both the photometer and the spectrometer. It contains the calibration sources and the chopper. The calibration sources are low emissivity gray-body sources: they provide FIR radiation loads slightly above or below the telescope background used for calibration measurements. The chopper is a small inclinable mirror that points alternatively towards the celestial sources or to the nearby sky position. This allows a full separation between the object field and the reference field. The light continues into the *photometer camera* or the *spectrometer* section (Figure 2.9).

- *photometer camera*: the light is split into the short-wavelength (blue or green) and long-wavelength (red) channels. The short-wavelength channel has a 32×64 pixel array, while the long-wavelength channel has a 16×32 pixel array. The incident infrared radiation is then absorbed, which raises the temperature of the bolometers. The small difference in temperature is then measured and registered.

- *spectrometer*: the 2D image of the 47"×47" field of view, resolved into 5×5 pixels, is converted into a 1D array of 1×25 pixels by an image slicer and directed onto a grating (Fig 2.10). The light is diffracted by

the grating into three orders: the first order covers the range 102-210 μm, the second order 71-105 μm, and the third order 51-73 μm. To be able to cover the full wavelength range of each order, the grating can move from an angle of 25° up to 70°. Afterwards, a beamsplitter separates the light of the 1st order to feed the red band detector from the light of the two other orders, while the light of the 2nd or the 3rd order fall on the blue band detector.

Capabilities

Photometer : The absolute flux calibration uncertainty is within 5% for each photometer band. The filter transmission curves are shown in Figure 2.11. The reference wavelengths for the three bands are 70, 100 and 160 μm.

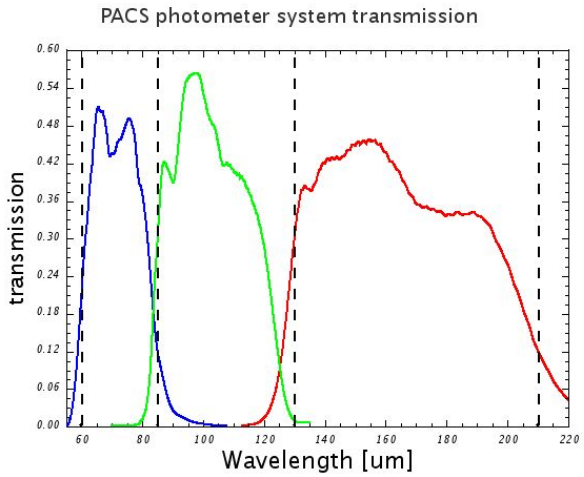

Figure 2.11: Filter transmissions of the three photometric band of PACS. The dashed lines represent the edge of each band. (Image from *Herschel* Observer's manual).

Spectrometer : The calibration is calculated at the central wavelength observed by each of the 16 pixels of the instantaneous spectrum. Rms calibration uncertainties lower than 10% are found near the center of the bands, while higher values, closer to 20%, are obtained at the borders of the bands due to leakage effects. The spectral leakage at the borders of the grating orders is due to some overlap between grating orders $n+1$ and n. Therefore, the spectral lines found at wavelengths toward the edges of the bands are associated with higher uncertainties.

The wavelength dependence of the spectrometer sensitivity and the PSF are shown in Figure 2.12. The spectral resolution also varies as a function

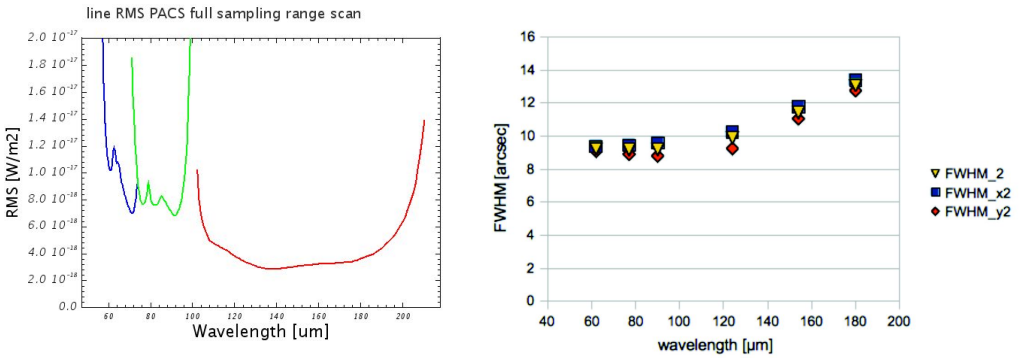

Figure 2.12: *Left*: PACS spectrometer point-source line sensitivity as a function of wavelength. *Right*: PACS spectrometer PSF as a function of wavelength. (Both images from the *Herschel* Observer's manual).

of wavelength and covers the range $c\delta\lambda/\lambda \sim$ 55-320 km/s. It is 240 km/s at 158 μm (1st order), 125 km/s at 88 μm (2nd order) and 90 km/s at 63 μm (3rd order). The instantaneous spectral coverage of the 16 pixels varies from 0.15-1.0 μm, corresponding to 600 to 2900 km/s.

Herschel IC 10 observations

IC 10, as part of the DGS (Section 1.5), has been observed with the PACS and SPIRE instruments onboard *Herschel*.

Photometer: Three observed modes are supported by the PACS photometer:

1) the point source photometry mode (which makes use of a chop-nod technique), 2) the standard scan map mode that uses a PACS/SPIRE parallel mode coveraging technique and 3) the mini scan map mode (for point-sources as well as small and large fields). For point-source observations, the "mini-scan map" configuration was often recommended over the original chop-nod mode. With this special mode the scanning was done along the two diagonals of the bolometer detectors, with 3' scan legs. In this way, the point-source sensitivity for all of the bands was increased. As described previously, all configurations performed dual-band observations, in

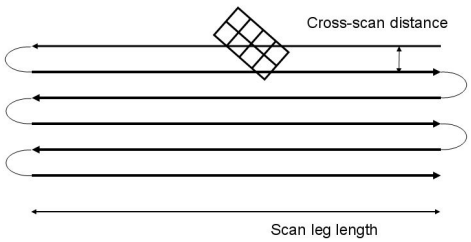

Figure 2.13: Example of how a scan map is performed by the PACS photometer.(Image from the *Herschel* Observer's manual).

which the red long wavelength band was observed together with one of the two short wavelength bands, the blue or the green band.

The scan map mode was the most frequently used with *Herschel* and was the mode used to perform the observations of IC 10 (Lianou et al., in prep.). Fig 2.13 illustrates how scan map observations were taken. The telescope was moved at a constant speed along parallel lines, with the array of detectors positioned at an angle. The scan leg length was adapted to the area observed. A combination of two orthogonal scan directions was observed: it allows a better PSF reconstruction while allowing us to remove the striping effects typically observed as a consequence of 1/f noise.

Spectrometer: Two observation schemes are available with the PACS spectrometer: line spectroscopy and range spectroscopy observing modes. The line spectroscopy mode observes a limited number of selected narrow lines with a fixed angular range scanned. The range spectroscopy, instead, is a more flexible and extended version of the previous mode and was used to observe a broader wavelength range. For our source, we used the line spectroscopy mode. IC 10 was observed in unchopped grating scan mode, a mode usually used when the source is an extended object and there is no suitable emission-free area within a radius of 6' from the source[5]. In this mode, the telescope observed the source, then an emission free area in order to eliminate the telescope background: $F_{observed}$ = [NodA_{on-off}] + [NodB_{on-off}] / 2 = [(T2+F_{source}-T1] + [(T1+F_{source}-T2] / 2 = F_{source}, where T1 and T2 are the fluxes of the telescope background at the two chopper positions. This mode was not recommended for faint sources. Figure 2.14 shows the raster projection of the [CII] 157.7 μm observations, as an example.

2.3.4 Data reduction - *Herschel*/PACS

The spectrometer data of the DGS processing is explained in Cormier et al. (2015) while the photometric data processing of the DGS is explained in Rémy-Ruyer et al. (2014), and that of IC 10 is in Lianou et al. (in prep.). Here I present a brief summery of the spectrometer data processing.

Data were reduced with the Herschel Interactive Processing Environment (HIPE) and reprocessed from the initial level (level 0) to data spectral cube (level 2) using standard pipeline scripts available with HIPE v12.0.0. Initially, the data cube consisted of 16 spectral pixels for 25 spatial pixels (spaxels) for each time frame. From level 0 to level 0.5, the signal was converted to

[5]Chopping-nodding was the standard observing PACS spectrometer mode. However it required an emission free area at 1.5', 3' or 6' from the object.

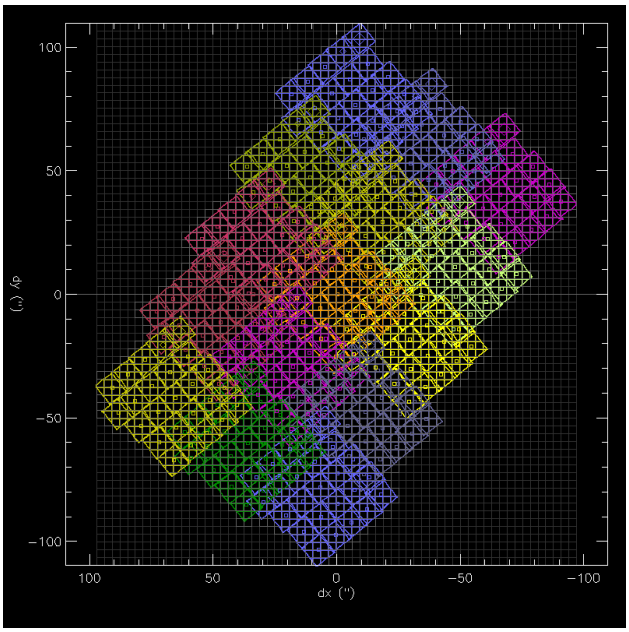

Figure 2.14: PACS raster projection of the [CII] 157.7 μm observations IC 10 into subgrid of 3" pixels. Each color represents a different footprint.

Volts/s, with the bad and noisy pixels being masked. Therefore from level 0.5 to level 1 bad pixels were flagged, the chopper position was subtracted, the calibration was applied and the cube was transformed into $5\times5\times n_\lambda$, where n_λ is the number of wavelengths. In order to improve the quality of the data at this level, we calculated a linear drift correction of the signal with the noise, a median shift correction and a linear spectral flat-field. Individual cubes were then created for each nod and each raster position and the final spectral cubes were saved as FITS files.

The FITS files were then processed by the software PACSman 3.4, described in Lebouteiller et al. (2012). For each spatial position, line-fitting were performed using a polynomial curve of order 2 for the continuum. The instrument profile was assumed to be Gaussian. The uncertainties, which are not propagated in HIPE, were estimated from the dispersion in each wavelength bin. Subsequently, the fits were projected on a new grid of subpixels of 3" to reach the best spatial resolution. If more than one spaxel fell in the same subpixel, a fraction of flux from each of them was considered.

2.4 SOFIA Telescope

2.4.1 SOFIA overview

The Stratospheric Observatory for Infrared Astronomy (SOFIA) is a 2.5 meter telescope onboard a Boeing 747-SP aircraft (Figure 2.15). It is the succes-

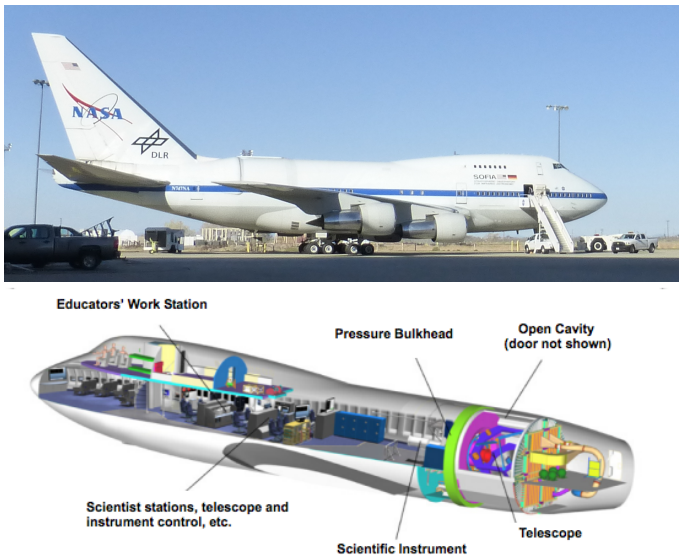

Figure 2.15: *Top*: Photo of the SOFIA Observatory a few minutes before my flight, at NASA Armstrong Flight Research Center in Palmdale, California. *Bottom*: A cutaway view of the SOFIA Observatory (Picture from *The Science Vision for the SOFIA*).

sor to the 90 cm Kuiper Airborne Observatory (KAO), which flew from 1974 to 1996 and was operated by NASA. SOFIA observes at altitudes between 37,000 and 45,000 feet, which removes 99% of the water vapor of the Earth's atmosphere. In addition to opening a window not available from the ground, it allows us access to unique ISM cooling lines, for example, [OIII] 51.8 μm, which was not covered by *Herschel* or *Spitzer*, as well as other bright FIR and MIR spectral features.

The telescope occupies an open cavity in the rear section of the aircraft. Its elevation range is +20° to +60° with the azimuthal motion restricted to ±3°. The desired azimuthal positioning is achieved through scheduling an optimized flight plan for each observing run. SOFIA offers eight instruments (spectrometers and photometers) that cover the wavelength range 0.3-1600 μm. Table 2.7 lists the general capabilities of the various instruments. I observed IC 10 with the Far Infrared Field-Imaging Line Spectrometer (FIFI-LS).

2.4.2 FIFI-LS

FIFI-LS is an integral field far-infrared spectrometer similar in design to PACS on *Herschel* (section 2.3.3), providing spectra at each point in its field of view (FOV), in contrast to a spectrometer with a slit, such as the IRS on *Spitzer*, which only provides spectra along the slit. FIFI-LS includes two independent grating spectrometers sharing a common FOV: a blue channel that observes the wavelength range from 51 to 120 μm and a red channel covering 115-203 μm. Each channel has a 5×5 pixel projection on sky and

Table 2.7: General capabilities of the instruments onboard SOFIA (from SOFIA Observer's Manual).

Instrument	Description	Wavelength coverage
EXES (Echelon-Cross-Enchelle Spectrograph)	High Resolution (R > 10^5) Enchelle Spectrometer	5-28 μm
FIFI-LS (Field Imaging Far-Infrared Line Spectrometer)	Dual channel integral field grating spectrometer	42-110 μm 100-219 μm
FLITECAM (First Light Infrared Test Experiment CAMera)	Near infrared imaging grism spectroscopy	1-5.5 μm
FORCAST (Faint Object Infrared CAmera for the SOFIA Telescope)	Mid-infrared duel channel imaging grism spectroscopy	5-25 μm 25-40 μm
FPI+ (Focal Plane Imager Plus)	Visible light high speed camera	360-1100 nm
GREAT, upGREAT (German REceiver for Astronomy at Terahertz frequencies)	High resolution (R > 10^6) heterodyne; multi-pixel spectrometer	1.25-1.52 THz 1.81-1.91 THz 4.74 THz
HAWC+ (High-resolution Airborne Wideband Camera-Plus)	Far-infrared camera and polarimeter	Five $\sim$20% bands at 53, 63, 89, 154 and 214 μm
HIPO (High-speed Imaging Photometer for Occultations)	High-speed time resolved imaging photometry at two optical wavelengths	

covers a different FOV. For the blue spectrometer, the pixel size is 6"×6", yielding a 30"×30" FOV, while for the red spectrometer the pixel size is 12"×12", yielding a 1'×1' FOV. Figure 2.16 shows the configuration of each spectrometer. Each has 25×16 photoconductors. The 5×5 pixel FOV is re-arranged to form a 25×1 array and dispersed by the diffraction grating over 16 pixels. The result is a data cube with 5×5 spaxels and 16 pixels in the spectral dimension.

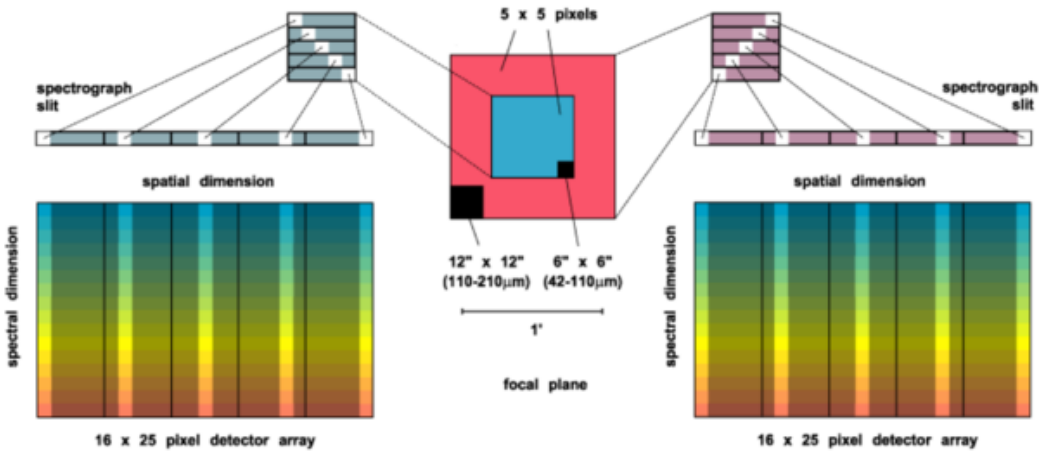

Figure 2.16: Integral-field spectrometer: the blue channel is on the left and the red channel is on the right. The 2-dimensional fields of 5×5 are re-arranged into a 25×1 array. (Picture from the *SOFIA Observer's Handbook*).

The blue channel is present in the 1st and 2nd orders, while the red channel in the 1st. The spectral resolution ($\lambda/\Delta\lambda$) ranges from 500 to 2000.

2.4.3 SOFIA IC 10 observations

I observed IC 10 on SOFIA with FIFI-LS during three flights, between February 27th to March 8th 2017, with a total of 6h (including overheads).

The two main star-forming regions of the galaxy (Figure 2.17) have been covered in [OIII] 51.8μm. These regions show excessively bright [OIII] 88.4 μm emission in the *Herschel* maps (Chapter 3), suggesting the presence of a dominant diffuse ionized phase. As complementary data, the two regions have also been observed with the red channel, in the [CII] 157.7 μm and [OI] 145.5 μm lines.

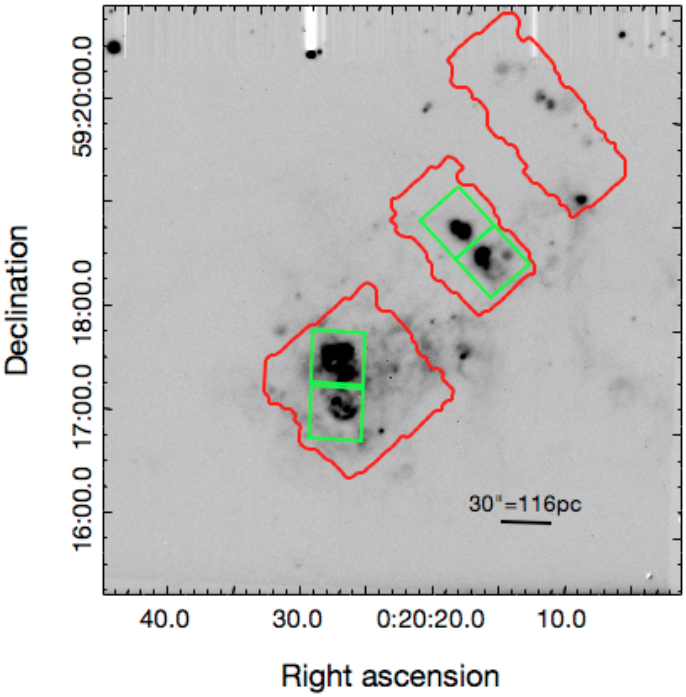

Figure 2.17: Hα image of IC10 (Hunter & Elmegreen 2004). Overlaid in red are the pointings of [OIII] 88 μm from *Herschel*. The FIFI-LS pointings are shown in green boxes, each having a size of 30 $\times$ 30 arcsec^2.

The subtraction of the sky background is done by alternatively nodding the telescope and chopping the secondary mirror. IC 10 has been observed in symmetric chop mode (recommended observing mode). Namely, the two off-source positions are symmetric to the on-source position and the source is observed 50% of the time. The *SOFIA* maps we obtained are presented in Chapter 7.

Chapter 3

Spitzer and *Herschel* Observations of IC 10

Contents

The MIR and FIR fine-structure cooling lines are powerful tracers of ISM properties as well as of the star formation activity (Section 1.2.4), and they are less affected by the gas attenuation as compared to the optical lines (Section 1.2.5). While the ISM properties have been investigated in integrated (global galaxy scale) DGS objects (Cormier et al. 2015) and in individual star-forming regions in the Magellanic Clouds (Lebouteiller et al. 2012; Chevance et al. 2016; Lee et al. 2016), the next step is to examine the spatial variations of various ISM properties in a nearby galaxy that is fully mapped. This is possible thanks to the complete MIR and FIR dataset of dust and gas tracers in the low-metallicity galaxy IC 10, which was observed with photometry and spectroscopic maps with the *Spitzer* and *Herschel* telescopes (Chapter 2). The analysis of IC 10 is thus aimed at providing a link between the small spatial scales accessible within an HII region and the global scales accessible for more distant galaxies. Such comprehensive spectroscopic maps covering most of the main body of nearby galaxies were not easily obtained for many Local Group galaxies with *Spitzer* and *Herschel*. The Magellanic Clouds, NGC6822 and M33, for example, are too close and/or too large to be fully mapped spectroscopically, and only specific regions (e.g., in M33 by Braine et al. 2012; LMC-N11 by Lebouteiller et al. 2012; LMC-N159 by Lee et al. 2016; LMC-30 Dor by Chevance et al. 2016 and Indebetouw 2015) or strips within large galaxies (e.g., Kennicutt et al. 2011; Smith et al. 2017) could be mapped.

In this chapter I present the available *Spitzer* and *Herschel* spectroscopic maps tracers I use to investigate the spatial variations of ISM properties in IC 10. In the following chapters (Chap. 5 and Chap. 6), I will use these maps to carry out the ISM modeling and analysis at various spatial scales.

3.1 Dataset

This study is based on the interpretation and modeling of the infrared cooling lines provided by *Spitzer*/IRS and *Herschel*/PACS observations (Figure 3.1), which are presented here.

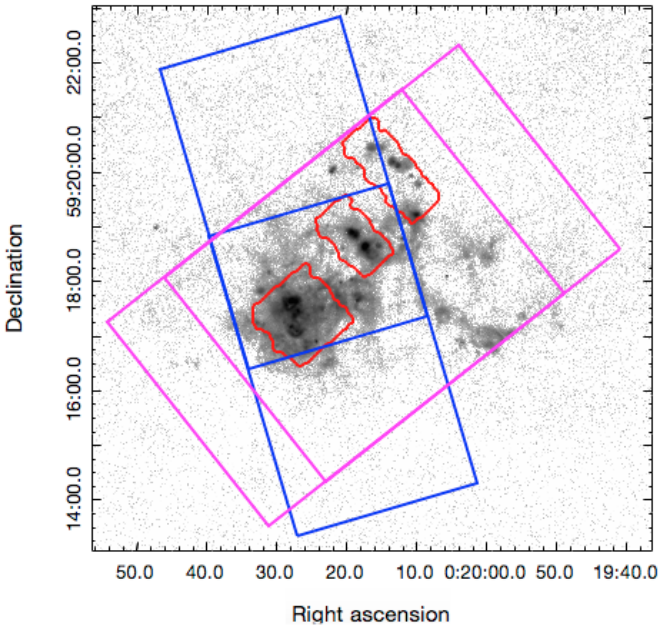

Figure 3.1: Hα map (Gil de Paz et al. 2003). Red borders show the areas covered by *Herschel*/PACS [OIII] 88.4 μm map, magenta *Spitzer*/IRS Short-Low maps and blue *Spitzer*/IRS Long-Low maps.

3.1.1 *Spitzer*/IRS maps

Spitzer/IRS observations generated a data cube of the main body of IC 10 for the wavelengths between 5.2 and 38 μm (two spatial dimensions and one dimension for the wavelength). The data reduction process is explained in Section 2.2.4. Examples of emission-line maps are presented in Figures 3.2 and 3.3. Since the maps are observed with different IRS modules (SL and LL; Chapter 2), they cover different areas of IC 10. However, all of the maps include the star-forming body of the galaxy.

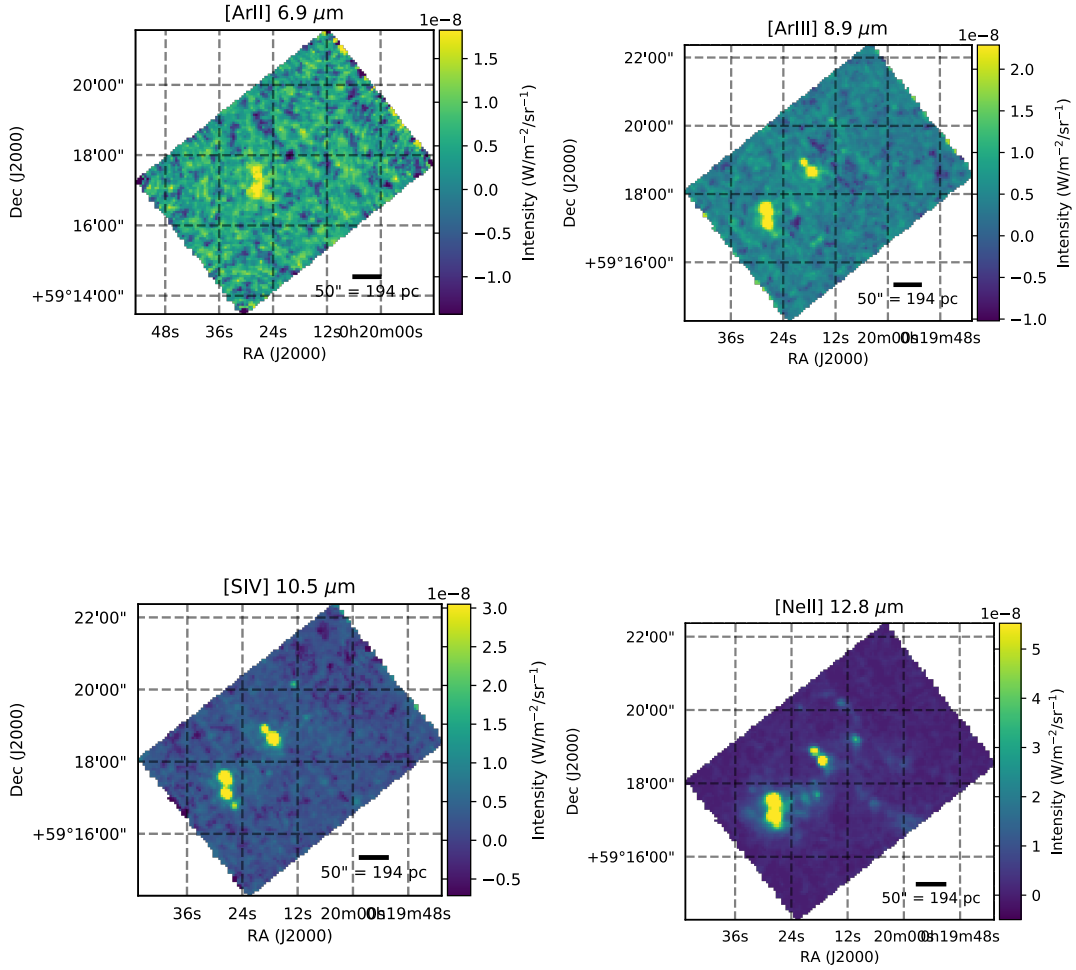

Figure 3.2: *Spitzer*/IRS SL maps: [ArII] 6.9 μm and [ArIII] 8.9 μm (*top*), [SIV] 10.5 μm and [NeII] 12.8 μm (*bottom*) in W m^{-2} sr^{-1}. The spatial resolution is 4″ ($\approx$ 14.5 pc).

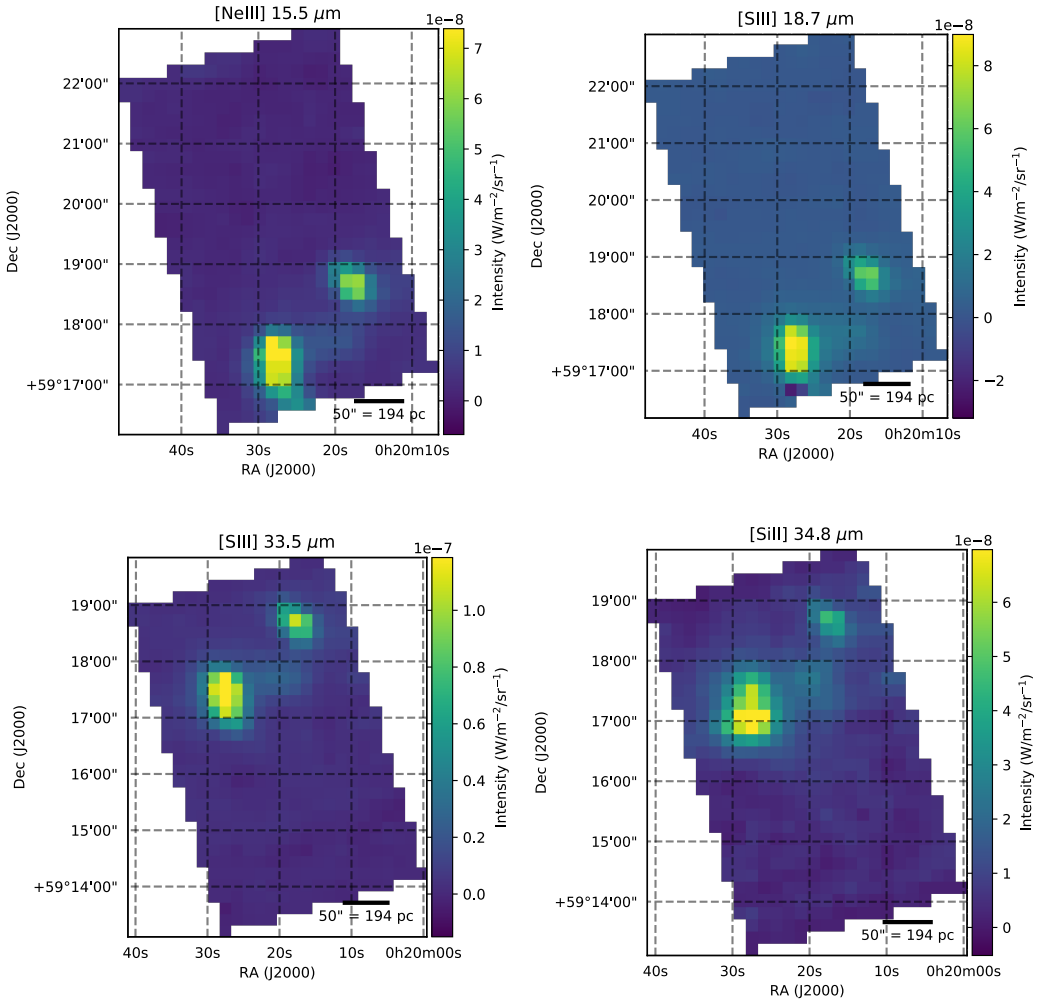

Figure 3.3: *Spitzer*/IRS LL maps: [NeIII] 15.5 μm and [SIII] 18.7 μm (*top*), [SIII] 33.5 μm and [SiII] 34.8 μm (*bottom*), in W m^{-2} sr^{-1}. The spatial resolution is 12$''$ ($\approx$ 43 pc).

3.1.2 *Herschel* maps

IC10 was observed with the PACS and SPIRE instruments onboard *Herschel* in both photometry and spectroscopy as part of the DGS program (Madden et al. 2013; Rémy-Ruyer et al. 2015). Five maps have been obtained: [OIII] 88.4 μm , [NII] 121.9 μm , [CII] 157.7 μm , [OI] 63.2 μm and [OI] 145.5 μm. The maps are shown in Figure 3.4. The observations were designed independently for each line, according to their expected brightness. For this reason, the map coverage is not the same for all lines, with only the brightest regions being observed in the faintest lines (e.g., [NII] 121.9 μm and [OI] 145.5 μm).

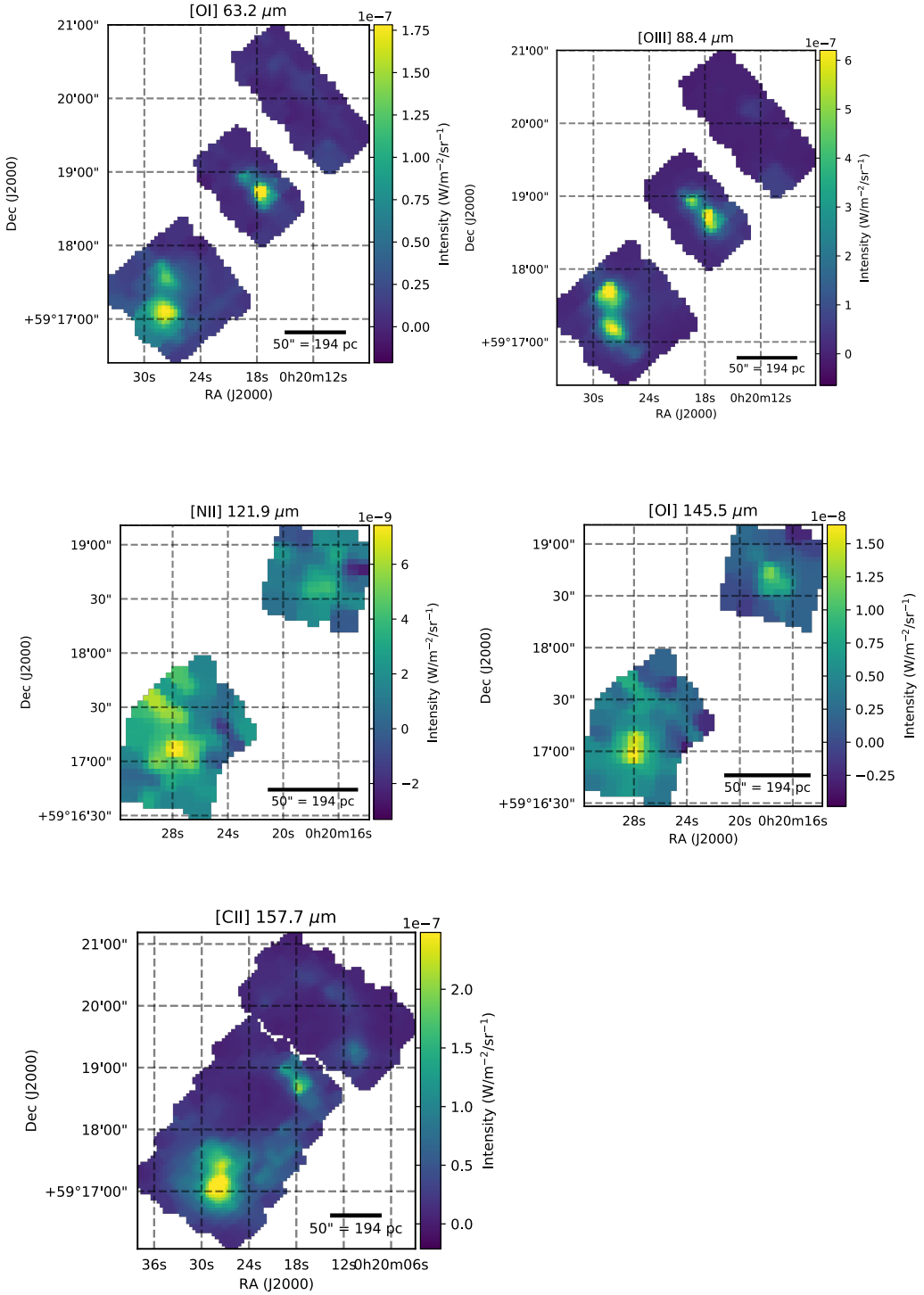

Figure 3.4: *Herschel*/PACS maps: [OI] 63.2 μm and [OIII] 88.4 μm (*top*), [NII] 121.9 μm and [OI] 145.5 μm (*middle*), and [CII] 157.7 μm (*bottom*) in W m^{-2} sr^{-1}. The maps are shown with their original spatial resolution (ranging between $\approx 9.5''$ at $\approx 60\mu$m to $\approx 12''$ at $\approx 150\mu$m).

3.2 Spatial distribution of ISM tracers

3.2.1 Available tracers

The maps of MIR and FIR emission lines show bright compact clumps distributed in the main star-forming region on the south and in two arcs. Some tracers also show prominent extended emission (e.g., [NeII], [CII]), which seems to arise in relatively more diffuse medium.

In addition to the IR tracers mapped with *Spitzer* and *Herschel*, IC 10 was also mapped in Hα with the 1.8m Perkins Telescope at Lowell Observatory, with a spatial resolution of 2.3" (Figure 3.5). The map has been corrected for the temperature band-pass shift of the filter, the integration time of the image, the airmass of the observation and the contribution of [NII]. The Hα emission was calibrated using the Hα flux from the HII regions NGC2363 and NGC604 and from spectrophotometric standard stars. More details can be found in Hunter & Elmegreen 2004. A preliminary investigation of the maps shows that the spatial distribution in the MIR and FIR tracers follows closely that of Hα (the emission peaks in the same clumps). The Hα data are calibrated but not corrected for extinction by dust. While extinction measurements toward individual stars or toward integrated star-forming regions exist (Chapter 6), the spatial variations of the extinction *seen by the gas* are unknown. For this reason, I do not use Hα as a constraint to the models. Instead, however, I compare the observed line flux to the model prediction in order to infer a posteriori, the extinction seen by the gas (Section 6.1.2).

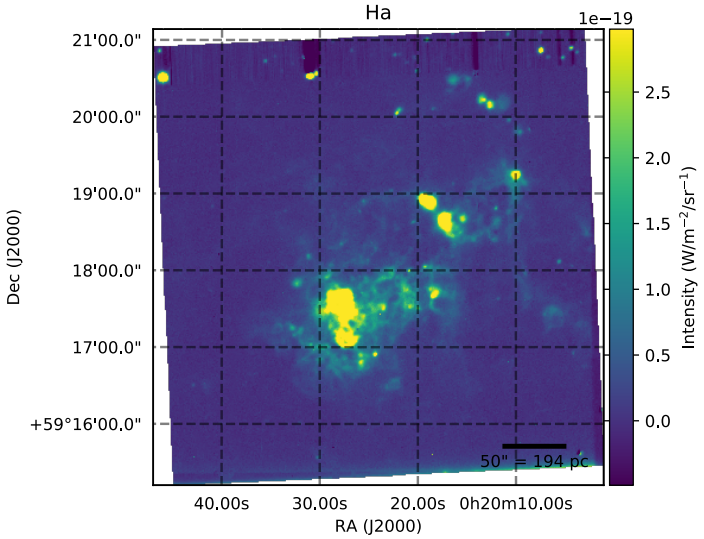

Figure 3.5: Hα map of IC 10 (Hunter & Elmegreen 2004), with a spatial resolution of 2.3″ ($\approx$ 9 pc).

In addition to the spectroscopic maps, I also use a map of the integrated infrared luminosity, which traces the dust emission. The infrared luminosity is used to provide a constraint for the photodissociation region models (Chapter 7). The FIR luminosity (L_{FIR}; Figure 3.6) map was created from a combination of the *Spitzer*/MIPS 24μm and *Herschel*/PACS 70, 100 and 160 μm photometry maps, following Galametz et al. (2013). Improved maps, using a model of the dust spectral energy distribution (model from Galliano 2017, in prep.), applied to the six PACS and SPIRE photometric bands, will be available in the future (Lianou et al., in prep.). The dust luminosity peaks toward the prominent star-forming regions seen in Hα and in the infrared fine-structure lines. The dust emission also shows an extended component.

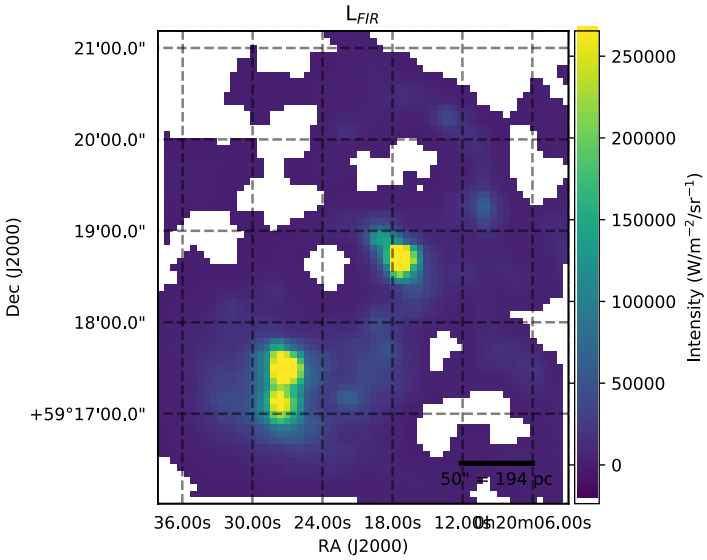

Figure 3.6: L_{FIR} map of IC 10. The spatial resolution is 12″ (≈ 43 pc). The white areas correspond to pixels with a signal-to-noise ratio less than 3 in at least one of the maps used in the calculation of L_{FIR} (Galametz et al. (2013); i.e., among MIPS 24μm and PACS 70, 100 and 160 μm maps).

3.2.2 MIR and FIR ratios

The various tracers observed in IC 10 (Section 3.1) correspond to different ISM phases (ionized, neutral) and/or to the same phase but with different gas densities or different extinctions. While most of this study revolves around the modeling of the ISM in IC 10 in order to infer the ISM physical conditions, some diagnostics involving particular line ratios can already be investigated. In this section I examine the spatial variations of a few such line ratios. Some preliminary work was necessary in order to compare the maps of tracers observed with different instruments/module/wavelength. I convolved the maps to the same and lowest spatial resolution, i.e., the resolution of PACS at 160μm and of IRS/LL (12″ ≈ 47 pc at the distance of IC 10), using the

kernels from Aniano et al. (2011) for PACS and Gaussian kernels for the IRS (Section 2.2.4).

The low-metallicity ISM structure: [OIII] 88.4 μm & [CII] 157.7 μm [OIII] 88.4 μm is the brightest FIR line in IC 10, with emission distributed beyond the immediate compact HII regions. This at first seems surprising since [CII] 157.7 μm is usually the brightest infrared line in galaxies, at least in relatively more metal-rich sources (Brauher et al. 2008), since high-energy photons (35 eV) are required to create O^{2+}. Several studies have already highlighted this effect, noting that [OIII] 88.4 μm is often the brightest FIR line in low-metallicity environments, at the scale of HII regions (Chevance et al. 2016; Lebouteiller et al. 2012) as well as at global galaxy scales (Hunter 2001; Madden et al. 2013; Cormier et al. 2015). [OIII] 88.4 μm is also shown to extend over surprisingly large spatial scales in nearby giant HII regions in the Magellanic Clouds, suggesting low-density channels that allow high-energy photons to travel far from the young clusters (Lebouteiller et al. 2012; Kawada et al. 2011).

Figure 3.7 shows the spatial variation of the [OIII] 88.4 μm /[CII] 157.7 μm ratio throughout the star-forming body of IC 10. Although the emission of [OIII] 88.4 μm shows an extended component, [CII] 157.7 μm is comparatively brighter in regions between the star-forming clumps. [CII] 157.7 μm is more extended than any of the MIR and FIR lines. The [OIII] 88.4 μm /[CII] 157.7 μm ratio varies from 0.6 toward the more diffuse regions up to 4.5 toward the brightest HII regions. Furthermore, [OIII] 88.4 μm /[CII] 157.7 μm varies significantly between HII regions, with larger values in regions that are bright in Hα. Since [CII] 157.7 μm originates mostly in photodissociation regions (PDRs) around molecular clouds illuminated by young stellar clusters, one could have expected in principle to observe a relatively constant [OIII] 88.4 μm /[CII] 157.7 μm ratio toward all the star-forming regions. Such variations of [OIII] 88.4 μm /[CII] 157.7 μm suggest that the environment around the stellar clusters in IC 10 is quite different (e.g., covering factor of dense clouds around the clusters and clouds with different densities) and/or that the stellar clusters have different properties (e.g., age). One of the objectives of the detailed modeling in the next chapters is to investigate this aspect.

The IC 10 dataset may provide some insight into the fact that [OIII] 88.4 μm is brighter than [CII] 157.7 μm in integrated low-metallicity galaxies. Since [CII]/TIR is at least as large in metal-poor galaxies as in metal-rich sources and sometimes larger (Cormier et al. 2015), this suggests that the large [OIII] 88.4 μm /[CII] 157.7 μm ratio observed in low-metallicity galaxies is due to enhanced [OIII] 88.4 μm emission rather than to a lower heating

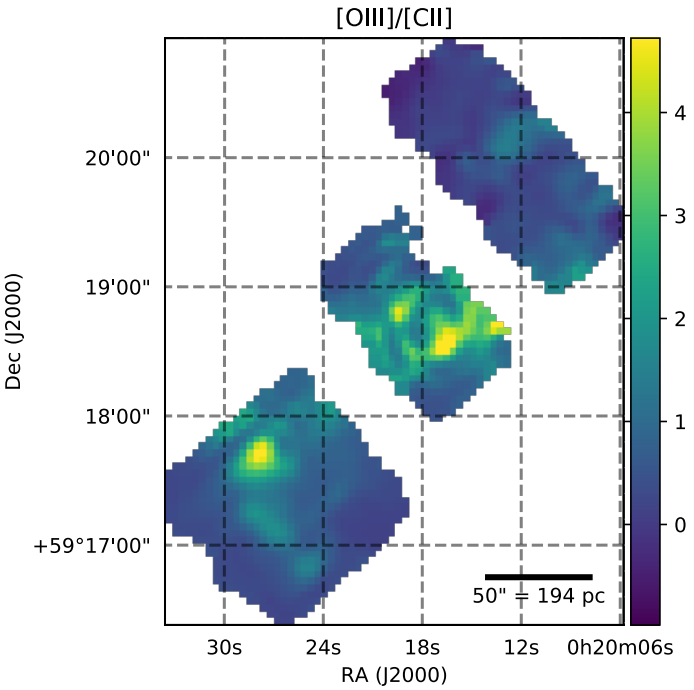

Figure 3.7: Observed [OIII] 88.4 μm/[CII] 157.7 μm ratio throughout the star-forming body of IC 10. The map size is limited by the [OIII] 88.4 μm map.

efficiency in PDRs. It is possible that the [OIII] 88.4 μm emission is relatively more spatially extended in metal-poor galaxies, with a high filling factor of diffuse highly-ionized gas[1] due (1) to the lower abundance of dust and (2) to an enhanced disruption of the natal molecular cloud resulting in a lower covering factor of dense clouds around young stellar clusters (see also Chapter 6).

Ionized gas density: [SIII] 33.5 μm/[SIII] 18.7 μm The ratio of lines emitted by two electronic levels of the same ion, with different critical densities, are valuable density tracers (Section 1.2.4). In the MIR wavelength range, the [SIII] 33.5 μm/[SIII] 18.7 μm ratio can be used to estimate the density of the ionized gas where the [SIII] lines emit. Considering the critical densities of these lines (e.g., Dudik et al. 2007), the [SIII] 33.5 μm/[SIII] 18.7 μm ratio is sensitive to densities of a few thousands cm^{-3}. With enough signal-to-noise ratio and assuming that the temperature is around 10^4 K, one can estimate densities as low as $\sim 100\,\mathrm{cm}^{-3}$.

Figure 1.4 shows the map of the densities inferred from the observed [SIII] line ratio. The density ranges from $\sim 10^2$ to $\sim 10^3$ cm^{-3}, with no obvious structure. The models presented in Chapter 5 include the [SIII] line ratio as

[1] [OIII] 88.4 μm emission line has a low critical density of $5 \times 10^2\,\mathrm{cm}^{-2}$.

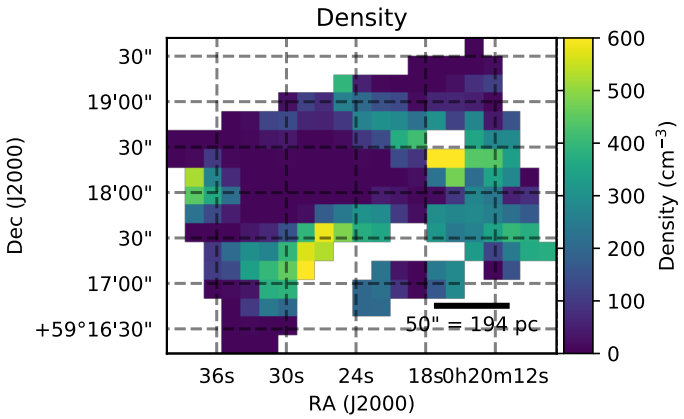

Figure 3.8: Density map inferred from the observed [SIII] 33.5 μm/[SIII] 18.7 μm ratio. The white pixels have signal-to-noise less than 3. The size of the map is given by the region where the two [SIII] maps overlap.

a constraint for the density, which is determined consistently (e.g., with the gas temperature as predicted by the model).

Other ratios are in principle available to estimate the gas density. The use of other tracers, with different critical densities or from species with different ionization potentials, enables the determination of several density values, effectively corresponding to different regions or layers (e.g., density in matter-bounded regions vs. density in radiation-bounded shells). In the MIR, it is possible to use the [NeIII] 36/15 μm ratio as an additional density tracer, but the [NeIII] 36 μm is unfortunately too faint in IC 10. In the FIR, the [NII] 205/122 μm is a valuable diagnostic for the density of the rather diffuse phases, but once again, the [NII] 205 μm is too faint. Finally, spectral maps in the optical would allow the determination of the density not only from the [OIII] lines but also from the [SII] lines, the latter tracing the relatively denser shells.

The origin of [CII] 157.7 μm emission: [NII] 121.9 μm & [CII] 157.7 μm Since C^0 has a low ionization potential of 11.3 eV, [CII] 157.7 μm can a priori arise from the ionized gas (with electrons as collision partners and a critical density of $\approx 50\,\mathrm{cm}^{-3}$) and from the neutral phase (with H^0 and H_2 as collision partners and a critical density $\approx 3000\,\mathrm{cm}^{-3}$ and $\approx 5000\,\mathrm{cm}^{-3}$

respectively; Goldsmith et al. 2012). On the other hand, [NII] 121.9 μm, is found only in the ionized phase (ionization potential of 14.5 eV for N^0), with e^- as collision partners and a critical density of 300 cm^{-3}. The [NII] 205 μm transition has an even lower critical density (180 cm^{-3}).

Since the [NII] far-infrared transitions have low critical densities, they are useful tracers of the ionized gas where C^+ is able to exist and where the integrated [CII] 157.7 μm emission partly originates from. The [NII] 205 μm line was too faint to be observed in IC 10, but the [NII] 121.9 μm line was detected (Section 3.1). For the regions observed with [NII] 121.9 μm we determined the observed ratio [NII] 121.9 μm /[CII] 157.7 μm (Figure 3.9) and compared it with the theoretical value in the ionized gas. Since the carbon abundance is not well known in IC 10, we use elemental abundances from the LMC[2]. According to photoinization grids (e.g., MAPPINGS III; Allen et al. 2008), the ionization fractions C^+/C and N^+/N follow each other well, yielding a uniform ratio [(C^+/C) / (N^+/N)]. The theoretical [CII]/[NII] ratio is then a function of gas density and temperature, but in practice depends mostly on density. Hence, from the observed [CII]/[NII] ratio one can determine the additional [CII] emission from the neutral phase, as a function of density.

Figure 3.10 shows the theoretical [CII]/[NII] as a function of density for different temperature values and the comparison with the range of observed [CII]/[NII] values. One can see that the observed ratios are much larger than the theoretical values, for any density and temperature. From this I can conclude that most of the [CII] emission (at least 98 %) does not arise from the ionized gas, but instead arises from the neutral gas. Considering the area mapped in [NII], this result holds for the bright star-forming clumps as well as for the more diffuse regions. This result is in agreement with those obtained by Chevance et al. (2016) and Lebouteiller et al. (2012) in two star-forming regions of the LMC (30 Dor and N 11).

Since [CII] mostly arises from the neutral phase, this obviously implies that [CII] cannot be used as a constraint to the models of the photoionized gas (Chapter 5). However, [CII] is an important constraint to the future PDR models, and our result suggests that the correction for [CII] in the ionized gas is not significant.

Properties of the neutral gas: [CII] 157.7 μm & [OI] 63.2 μm , [OI] 145.5 μm [OI] 63.2 μm is one of the brightest cooling lines in the PDR along with [CII]. Since the observed [CII] 157.7 μm emission in IC 10 has been demonstrated to originate from PDRs, the [OI] 63.2 μm/[CII] 157.7 μm ratio

[2]LMC has metallicity of 1/2 $Z_\odot$, which is similar to that of IC 10

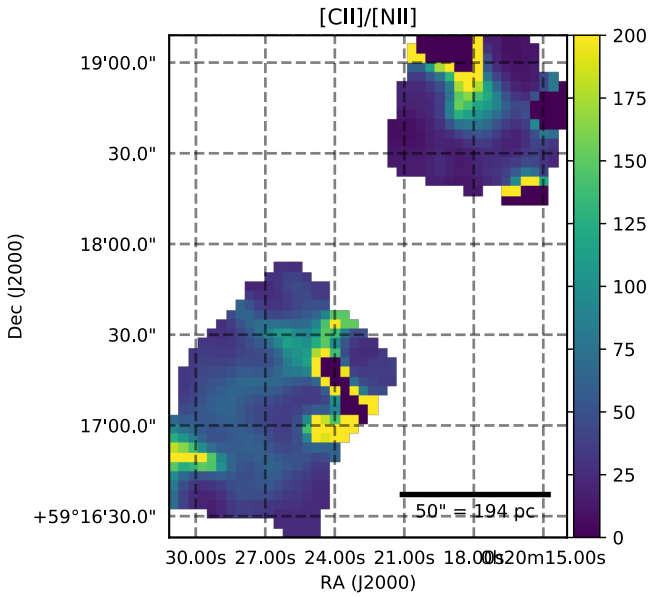

Figure 3.9: Observed [CII] 157.7 μm /[NII] 121.9 μm ratio throughout the star-forming body of the galaxy (the two maps are in intensity unit [W/m^{-2}/sr^{-1}]). The size of the ratio map is limited by the observed [NII] 121.9 μm map.

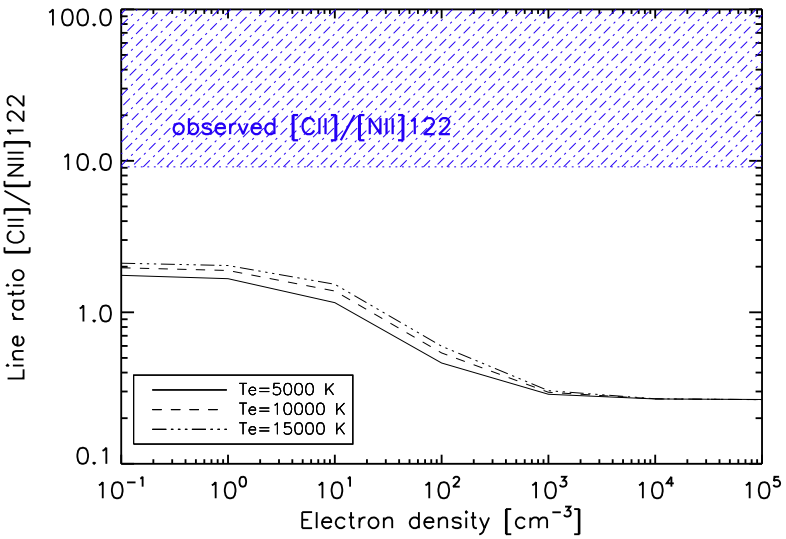

Figure 3.10: The theoretical [NII] 121.9 μm /[CII] 157.7 μm ratio is plotted as a function of density and for several temperatures. The blue area indicates the range of observed ratios in IC 10.

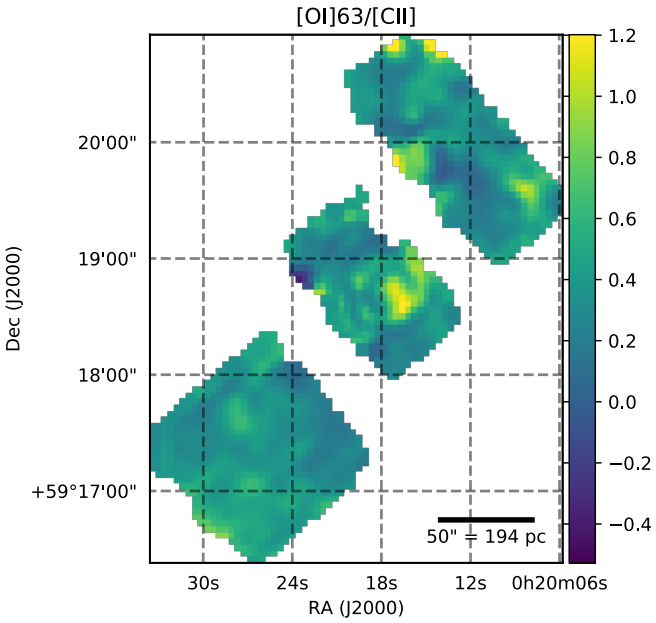

Figure 3.11: Observed [OI] 63.2 μm/[CII] 157.7 μm ratio throughout the star-forming body of IC 10. The size of the ratio map is limited by the [OI] 63.2 μm map.

can be used to investigate the properties of the neutral phase throughout IC 10. The [OI] 63.2 μm/[CII] 157.7 μm ratio increases with increasing density and radiation field (Kaufman et al. 2006). This is due to the difference in critical densities ($\approx 10^5\,\mathrm{cm}^{-3}$ for [OI] vs. $\approx 10^3\mathrm{cm}^{-3}$ for [CII]) and to the difference in excitation temperatures (228 K vs. 91 K respectively).

The observed [OI] 63.2 μm/[CII] 157.7 μm is below 1 everywhere in IC 10 (Figure 3.11), with an average value ≈ 0.6. This value is compatible with the average values of the DGS sample, found on global galaxy-wide scales (median value of ≈ 0.64; Cormier et al. 2015). The [OI] 63.2 μm/[CII] 157.7 μm ratio is fairly uniform toward the main star-forming region in the south, suggesting relatively uniform physical conditions in PDRs. It is important, however, to recall that [OI] 63.2 μm can suffer optical depth effects, much more so than [CII] (Tielens & Hollenbach 1985; Abel et al. 2007; Chevance et al. 2016).

Another useful line to examine the PDR properties is [OI] 145.5 μm, which is much less affected by optical depth as compared to [OI] 63.2 μm. However, the [OI] 145.5 μm line can be as faint as two orders of magnitude lower than [CII] 157.7 μm, and could be detected only toward the brightest star-forming regions. Unfortunately, this prevents the study of the spatial distribution of this ratio. Hence, in order to provide a satisfactory analysis of the properties of the PDRs, modeling the suite of lines is crucial.

3.2.3 Conclusion

In this chapter I presented the spatial distribution of the MIR and FIR tracers throughout the main star-forming body of IC 10, and some diagnostics enabled by specific line ratios. In summary, the brightest infrared line in IC 10 is not [CII] 157.7 μm , such as for the metal rich galaxies, but it is [OIII] 88.4 μm, which is somewhat extended beyond the compact HII regions, suggesting a high filling factor of diffuse ionized gas. The low-metallicity ISM seems to be very porous, allowing hard photons, such as those creating the O^{2+} ion, to penetrate over large distances across the body of the galaxy. The second brightest infrared cooling line is [CII] 157.7 μm , which has substantial extended emission and has been shown to originate in the neutral PDRs. Hence, in our study, [CII] 157.7 μm , [OI] 63.2 μm and [OI] 145.5 μm are tracers of the neutral gas and will be used in the future PDR modeling effort. Finally, the ratio [SIII] 33.5 μm/[SIII] 18.7 μm reveals that the density of the ionized gas is $\sim$500 cm^{-3}. In the following chapters a quantitative analysis of the ionized gas is performed, modeling the emission of these MIR and FIR diagnostic tracers.

Chapter 4

Modeling the ISM physical properties with Cloudy

Contents

The different physical and chemical processes occurring in the ISM all leave their imprint on the observed spectra. Thus, the comparison of the observations with models, computed with theoretical calculations based on robust physics, can help us extract physical properties of the local radiation source, gas and dust properties (e.g. electron density, temperature) as well as physical processes taking place (e.g. photoionization, photodissociation). In order to reproduce an observed spectrum, the codes consider a cloud of gas and dust, where the geometry is generally spherical or a plane-parallel slab, and divide this cloud into several zones as a function of depth. Then, the radiation striking the cloud is propagated through those zones and, at each step, physical processes such as the radiative transfer, chemical reactions, level populations, etc. are treated.

In this Chapter, I start with an overview of the radiative transfer notions and on the state-of-the-art modeling codes (Section 4.1). Since the thesis project is mostly focused on the analysis of the ionized gas, the description is directed in that direction. Then, I present the photoionization and photodissociation code CLOUDY (Section 4.2) and how I used it in my project (Section 4.3).

4.1 State-of-the-art modelling

4.1.1 Radiative transfer theory and energy balance

The radiation emitted by the stars is continuously absorbed, re-emitted and scattered by dust and gas along the way. Given the intensity I_ν, its propagation through the cloud surrounding the source, measured by the optical path length s, is described by the radiative transfer equation:

$$\frac{dI_\nu}{ds} = -(\alpha_\nu + \sigma_\nu)I_\nu + j_\nu + \sigma_\nu J_\nu \tag{4.1}$$

where:

- j_ν is the emission coefficient
- α_ν is the absorption coefficient
- σ_ν is the scattering coefficient
- $J_\nu = \frac{1}{4\pi}\int I_\nu d\Omega$ is the mean intensity of the radiation. Hence $4\pi J_\nu = \frac{L_\nu}{4\pi\, r^2}$, where L_ν is the luminosity of the source per unit frequency interval.

Given the optical depth $\tau_\nu = \int \alpha_\nu ds$ and considering only the gas ($\sigma_\nu = 0$), the radiative transfer equation can be rewritten as:

$$\frac{dI_\nu}{d\tau_\nu} = -I_\nu + S_\nu \tag{4.2}$$

combining the emission and the absorption coefficients in $S_\nu = j_\nu/\alpha_\nu$, the source function. The solution to the equation takes the form:

$$I_\nu = I_\nu(0)e^{-\tau_\nu} + \int S_\nu(\tau_\nu^{'})e^{-(\tau_\nu - \tau_\nu^{'})}d\tau_\nu^{'} \tag{4.3}$$

where $I_\nu(0)$ is the background radiation.

The predicted line emission depends on the processes of excitation and de-excitation of atomic and molecular levels due to the energy transfer. In order to simplify the complexity of the radiative transfer problem, some assumptions can be made. In the following, I detail the energy balance in a static, pure hydrogen nebula heated by photoionization.

Ionization equilibrium
Considering the simplest case of a pure hydrogen cloud irradiated by stellar radiation, the ionization equilibrium equation is:

$$n(H^0)\int_{\nu_0}^{\infty} \frac{4\pi J_\nu}{h\nu} a_\nu d\nu = n_p n_e \alpha(H^0, T) \tag{4.4}$$

where:

- $\frac{4\pi J_\nu}{h\nu}$ is the number of incident photons per unit area, per unit time and unit frequency interval
- a_ν: ionization cross section for H by photons with energy $h\nu > h\nu_0$, where $h\nu_0$ is the energy necessary to ionize the neutral H atom

$\Rightarrow$ the integral on the left side of the equation represents the number of photoionizations per H atom per unit time.

- $n(H^0)$, n_p and n_e: the neutral, electron and proton densities per unit volume
- $\alpha(H^0, T)$: recombination coefficient for H^0 that depend on the excitation temperature

$\Rightarrow$ the right side of the equation gives the number of recombinations per unit volume per unit time.

Thermal equilibrium

Under the assumption of thermal equilibrium, the temperature at each zone of the cloud is fixed by the equilibrium between heating by photoionization and cooling by radiation from the medium and by recombinations. The difference between the mean energy of the new photoelectrons, i.e. electrons produced by the photoionization of H, and the mean energy of recombining electrons, is lost mainly by radiation.

At any specific point in the cloud, the energy input by photoionization is:

$$G(H) = n(H^0) \int_{\nu_0}^{\infty} \frac{4\pi J_\nu}{h\nu} h(\nu - \nu_0) a_\nu(H^0) d\nu \tag{4.5}$$

Since the medium is in ionization equilibrium, the equation can by written as:

$$G(H) = n_p n_e \alpha(H^0, T) \frac{\int_{\nu_0}^{\infty} \frac{4\pi J_\nu}{h\nu} h(\nu - \nu_0) a_\nu(H^0) d\nu}{\int_{\nu_0}^{\infty} \frac{4\pi J_\nu}{h\nu} a_\nu d\nu} = n_p n_e \alpha(H^0, T) \frac{3}{2} k T_i \tag{4.6}$$

where T_i is the initial temperature of the new photons produced by photoionization. In thermal equilibrium $G(H) = L_R + L_{FF} + L_C$, with L_R the kinetic energy lost by electrons in recombination, L_{FF} the energy lost by free-free radiation and L_C the energy loss by collisionally excited line radiation. Of the three processes, L_C is the most important radiative cooling process in galaxies.

For the simple case of a two-level system, for which ions in the lower level 1 are excited to the upper level 2 by collisions with electrons, we have:

$$N_e N_1 v_1 \sigma_{12}(v_1) f(v_1) dv_1 = N_e N_2 v_2 \sigma_{21}(v_2) f(v_2) dv_2 \tag{4.7}$$

where

- $\sigma_{12}(v_1)$ and $\sigma_{21}(v_2)$ are the cross sections for excitation and for de-excitation, respectively, as a function of electron velocity v_1 (before collision) and v_2 (after collision).
- N_e, N_1 and N_2 are the electron density and the density of the ion population at the lower lever 1 and at the excited level 2, respectively. The populations at the two levels are related to each other by the Boltzmann equation of thermodynamic equilibrium:

$$\frac{N_2}{N_1} = \frac{w_2}{w_1} e^{-h\nu_{21}/kT} \tag{4.8}$$

with

- T: the excitation temperature
- h and k: the Planck constant and the Boltzmann constant, respectively
- w_2 and w_1 : the degeneracies of the upper and lower levels

The same relation relates the total collisional excitation rate per unit volume per unit time, $N_e N_1 q_{12}$, and the total collisional de-excitation rate per unit volume per unit time, $N_e N_2 q_{21}$:

$$\frac{q_{12}}{q_{21}} = \frac{w_2}{w_1} e^{-h\nu_{21}/kT} \tag{4.9}$$

where $q_{12} = \int_0^\infty \sigma_{12}(v_1) f(v_1) dv_1$ and $q_{21} = \int_0^\infty \sigma_{21}(v_2) f(v_2) dv_2$ are, respectively, the collisional excitation and de-excitation coefficients.

Thus, equation 4.7 becomes, in general:

$$N_e N_1 q_{12} = N_e N_2 q_{21} + N_2 A_{21} \tag{4.10}$$

where A_{21} is the Einstein A_{ul} (l=lower, u=upper) coefficient of spontaneous emission and absorption. Hence, the cooling rate L_c is:

$$L_c = N_2 A_{21} h\nu_{21} = N_e N_1 q_{12} h\nu_{21} \left(\frac{1}{1 + \frac{N_e q_{21}}{A_{21}}} \right) \tag{4.11}$$

The previous calculations give an overview of the main contributions to the energy balance by making several approximations, such as a single temperature, a pure H nebula, or a two-level system. With more sophisticated methods, such as radiative transfer codes, those approximations can be dropped as the codes consider more levels, more elements, and solve for quantities as a function of cloud depth.

4.1.2 Photoionization models

The art of photoionization modeling consists of moving from a multidimensional parameter space to a multidimensional observational space, as shown schematically in Figure 4.1. In order to compute the transport of radiation through the interstellar matter and predict the emitted spectrum, model calculations start from the characteristics of the radiation sources and the material exposed to the radiation field (parameter space). The equations of chemical and thermal equilibrium and the radiative transfer equation are solved by making use of libraries on atomic and molecular data (e.g. model

atoms, chemical reactions, recombination coefficients, collisional excitation rate coefficients). This allows the code to calculate, at each radial step, the propagation of the radiation into the cloud and the physical properties of the material such as the pressure, density and temperature, etc. of the gas and dust. The model calculations can then provide, as output, for example, the observed line emission, dust continuum, as well as heating and cooling balance and cloud properties (observational space).

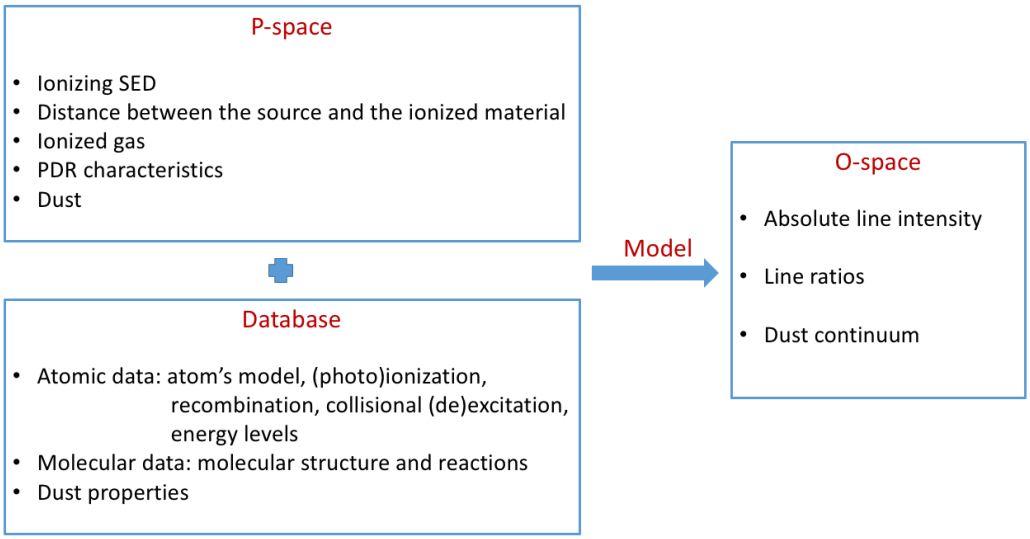

Figure 4.1: Schematic view of the configuration of an ionization code. *Left*: Model calculations start from: 1. *Top*: Parameter space (P-space), which is the set of input parameters (provided by the user), that describes the radiation source and the initial conditions of the surrounding matter. 2. *Bottom*: database (atomic, molecular and dust physics). *Right*: as output the calculations provide the physical properties of the material (observational space: O-space) that can be compared with the observations (adapted from C. Morriset).

In my case, the goal of the modeling is to derive the characteristics of the ISM and of the energy sources from the observations. Hence we want to move in the opposite direction of the code, from the observational space to the parameter space (Figure 4.2), and compare the predicted observations given by the models with the observed data. For this reason, the common approach is to build a grid of models by varying the parameter space and find the parameters or range of parameters that better reproduces the observations. However, this process is not straightforward. For instance, degeneracies in the parameter space imply numerous solutions in the multidimensional parameter space (e.g. Morisset et al. 2016).

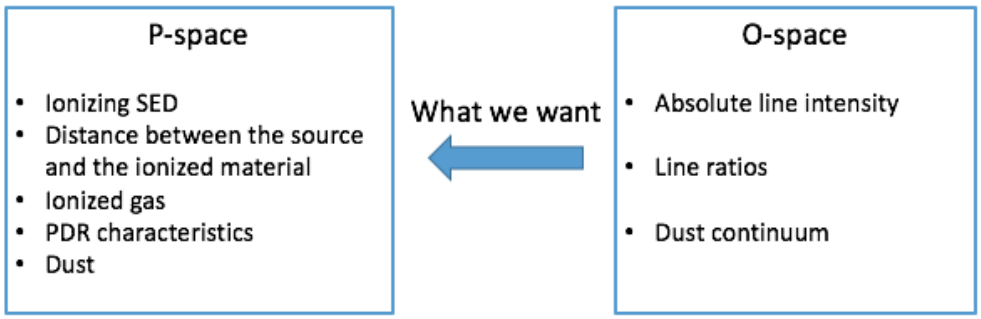

Figure 4.2: The modeling technique is used to compare the observations, such as observed line emission, with that predicted by the models, observational space (*right*), in order to derive the physical properties of the medium and the source, parameter space (*left*).

Since the first photoionization code, from Hjellming (1966) and Rubin (1968), several codes had been developed. Some of the most widely used are Cloudy (Ferland & Truran 1981) and MAPPINGS-III (Allen et al. 2008). While overlapping in some physics, each of them has some specific applications. MAPPINGS-III is a shock and photoionisation code, while Cloudy is a photoionisation and photodissociation code.

4.2 Photoionization and photodissociation code: CLOUDY

4.2.1 Overview

In my thesis project I used the spectral synthesis code Cloudy. It blends physical processes from first principles to reproduce the ionization, chemical and thermal state of material that is exposed to an external source of heating and predicts observables such as line intensities. It is a physical code that solves plasma equations to calculate all parameters (ionization, level populations, kinetic temperature, etc.) at each step, by balancing recombination, radiative cooling and ionization processes, as radiation propagates through the surrounding material. For these reasons, it can be used to model very different astrophysical objects: very low densities such as in the hot ionized phase of the ISM, where thermodynamical equilibrium is not reached, as well as dense clouds surrounding an accretion disk or a supermassive black hole.

The core of the code was presented in "*An X-ray model for the nebula of*

nova DQ Herculis 1934", Ferland & Truran (1981), while the first full description of the code, as a photoionization code, was presented in Ferland et al. (1998). This is also the first paper in which the code is named CLOUDY and is made publicly available for download. Since 1998, CLOUDY has been improved in terms of programming language (from Fortran to C++) as well as in complexity of the physical processes and chemistry taken into account. Inclusion of grain physics (van Hoof et al. 2004), H_2 treatment (Shaw et al. 2005) and more complete molecular network are particularly important for the applicability of CLOUDY to other ISM phases than HII regions. All of the versions are open sources available for download at `http://www.nublado.org/`. I used version c13.03 described in Ferland et al. (2013) and Abel et al. (2005). Together with the code, the manuals Hazy1, Hazy2, and Quick start are available.

The CLOUDY models consist of a central source surrounded by a cloud of gas and dust (Figure 4.3), which has a 1D spherical geometry. When the illuminated cloud of material is at a relatively large radius from the source, compared to the thickness of the cloud, the geometry is equivalent to a plane-parallel slab. For the sphere, the illumination is internal and isotropic. The source ionizes the inner edge of the cloud, where the HII region begins, and the propagation of the radiation is computed step by step into the medium.

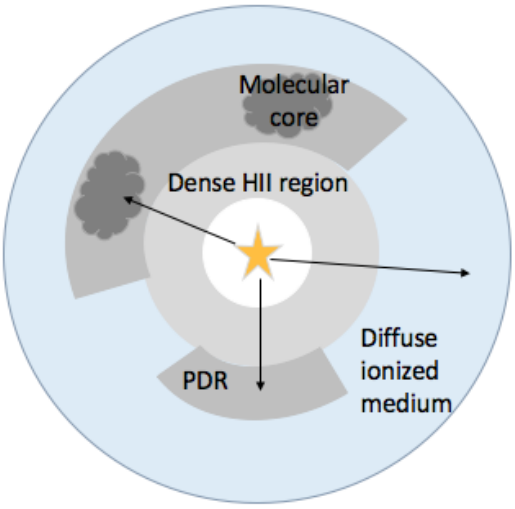

Figure 4.3: Scheme of the multi-phase ISM structure modeled by Cloudy. The star represents the ionization source surrounded by a multi-phase cloud: dense HII regions (light grey), PDRs (grey), molecular core (dark grey) and diffuse ionized gas (light blue).

The main power of CLOUDY is the self-consistent calculation of the thermal and chemical structure of HII regions and PDR regions in pressure equilibrium. Indeed, the common approach is to consider the two regions separately. However, these two regions are linked by dynamical processes (Henney et al. 2005). The physical properties of the PDRs are a conse-

quence of the transport of radiation and gas through the HII region. It can be difficult to match the boundary conditions between HII regions and PDRs, self-consistently, when these regions are modeled completely separately, and without continuity. Unlike codes that treat only HII regions or only PDRs, CLOUDY allows the treatment of the ionized, neutral and molecular gas and the radiative transfer between the phases with a self-consistent approach. In this way, the temperature, density, and ionization are calculated self-consistently from the beginning of the HII region through the PDR. Another problem related to the separate treatment of the phases is the assumption that the emission lines originate only from one of the phases, while some emission lines, such as [CII] 157.7 μm and [SiII] 34.8 μm can arise from both HII and PDR regions (Sec. 1.2.4). Hence, computations which do not take into account multiple gas phases will not correctly account for the observations, bringing incorrect interpretation to the phase properties.

In order to create models with CLOUDY, the main inputs of the parameter space to set are:

1. the shape and the strength of the radiation field striking the cloud (age of the burst, t_{burst})
2. the initial hydrogen density (n_H)
3. the gas and dust chemical composition
4. the cloud geometry

The following subsection describes each input parameter in a generic way and the choice of input parameters for the study of IC 10 is described in Section 4.3.

4.2.2 Input parameters

Shape and strength of the radiation field

Several radiation fields can be included as part of the total field irradiating the cloud and for each of them both the shape and the intensity must be specified.

1) Shape of the external source: Starburst99

The shape of the external radiation source describes the amount of energy as a function of frequency or wavelength. It can be either an AGN (Active galactic nucleus) continuum, a stellar spectrum from a stellar library or from STARBURST99 (Leitherer et al. 2010), a user-defined spectrum, etc. The

SED of the source must be fully specified. For my project, I investigated the properties of the ISM illuminated by stellar clusters for which I generated stellar ionizing continuum using STARBURST99. The construction of a simple stellar population (SSP) requires three inputs: stellar evolution theory, stellar spectra libraries, and the initial mass function. These components are typically combined in the following way:

$$L_\nu = \int_M \Phi(M)_{t,Z} L_\nu(M, t, Z) \tag{4.12}$$

where:

- L_ν is the emitted light (per unit frequency per unit mass) of a SSP of mass M, age t, and metallicity Z. Thus L_ν is the sum of the luminosity of the individual stars and the emitted light is dominated by the most massive and luminous stars. The determination of the SED $L_\nu(M, t, Z)$ requires the computation of stellar evolutionary tracks. The track determines where a star of given stellar parameters lies in the Hertzsprung-Russel diagram and builds up the stellar "isochrone". The stellar evolutionary tracks are used to compute or to build empirically a stellar library of $L_\nu(M, t, Z)$ with full coverage of bolometric luminosity, temperature, and Z, in order to determine what the resulting spectrum of such a star is. Isochrones are constructed from stellar evolution calculations for stars from the hydrogen burning limit ($\approx 0.1\ M_\odot$), to the maximum stellar mass ($\approx 100\ M_\odot$). A number of widely-used isochrone tables exist in the literature. The most popular models span a wide range in ages (masses), chemical compositions, and cover the most relevant evolutionary phases. Models in this category that are widely used include the Padova models (Bertelli et al. 1994; Girardi et al. 2000; Marigo et al. 2008), Geneva models (Schaller et al. 1992) and Charlot & Bruzual (1991).

- IMF: the initial mass function describes the distribution in mass of a putative zero-age main sequence stellar population. The IMF is usually limited between a minimum and a maximum stellar mass, where the lower limit is often taken as the hydrogen burning limit (either 0.08 or 0.1 $M_\odot$) and the upper limit is 100-150 $M_\odot$. Three empirical forms are most commonly used: a simple power-law model (Salpeter 1955) $dN/dM \propto M^x$ where $x = 2.35$, a broken power-law (Kroupa 2001), or a log normal form (Chabrier 2001).

- $\Phi(M)_{t,Z}$: the stellar mass function is computed from an IMF ($\Phi_0(M)$) and stellar evolution. It describes when and which stars stop contribut-

ing to the SSP spectra because their lives end either as supernovae or as white dwarfs.

The spectral synthesis code STARBURST99 assumes a particular star formation law, specific IMF and the evolution of the stellar population using stellar evolution models. All of these ingredients can be chosen by the user. It is an open source available for download at http://www.stsci.edu/science/starburst99/. Alternatively, instead of installing the code, our own simulations can be run remotely at http://www.stsci.edu/science/starburst99/docs/parameters.html. STARBURST99 considers two cases for the star formation law: 1) an instantaneous burst of star formation and 2) star formation proceeding continuously at a constant rate. In the case of an instantaneous burst, the user can choose the stellar age and the total mass. The choice of the stellar age sets the hardness of the radiation field, modifying the shape of the spectrum. The choice of the total mass, instead, scales the intensity of the radiation. Figure 4.4 (left) shows the stellar spectra at different ages, in the case of an instantaneous burst of star formation with a fixed mass of 10^5 $M_\odot$. For ages above 6 Myr, the spectra have fewer high-energy photons, hence the hardness decreases. Figure 4.4 (right) shows the stellar spectra, for different total masses, in the case of an instantaneous burst at a fixed age of 5.5 Myr.

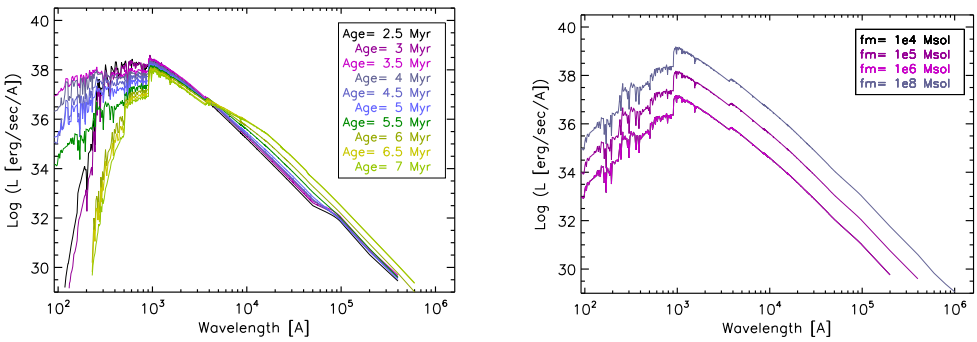

Figure 4.4: Stellar population spectra for a single burst. *Left*: Spectra for fixed total mass of 10^5 $M_\odot$. The different colors show the spectra at different ages, between 2.5 Myr and 7 Myr. *Right*: Spectra for a fixed age of 5.5 Myr. The different colors show the spectra for different total stellar masses, between 10^4 $M_\odot$ and 10^8 $M_\odot$.

In the case of continuous star formation, the parameters that can be set by the user are the stellar age and the SFR. The first parameter (stellar age) changes the shape of the spectrum at wavelength longer than 912Å (i.e. non-ionizing radiation), while the second parameter (SFR) scales the intensity of

the radiation. Figure 4.5 (left) shows the stellar spectra, at different ages, in the continuous star formation case for a SFR of 0.01 $M_{\odot}\,\mathrm{yr}^{-1}$. Figure 4.5 (right) shows the stellar spectra, for different SFRs, in the continuous star formation case at fixed age 500 Myr.

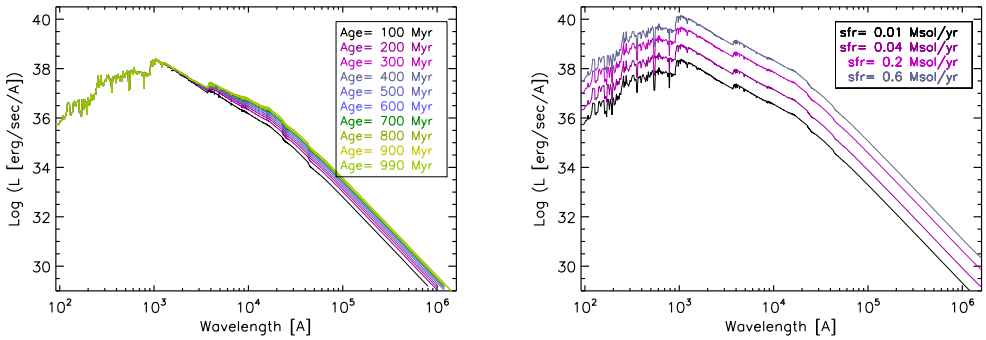

Figure 4.5: Stellar population spectra for continuous star formation. *Left*: Spectra for a fixed SFR of 0.01 $M_{\odot}\,\mathrm{yr}^{-1}$. The different colors show the spectra at different ages, between 100 Myr and 990 Myr. *Right*: Spectra for fixed age of 500 Myr. The different colors show the spectra for different SFRs, between 0.01 $M_{\odot}\,\mathrm{yr}^{-1}$ and 0.6 $M_{\odot}\,\mathrm{yr}^{-1}$.

Moreover, STARBURST99 offers different possibilities for the IMF. The user can choose a simple or a multi power-law IMF and specify for each of them the exponent α and the mass boundaries (the maximum of mass intervals is 10). Thus, in order to approximate a Kroupa IMF, for example, it is enough to indicate a multi power-law IMF with two IMF exponents, $\alpha 1 = 1.3$ and $\alpha 2 = 2.3$, and three IMF boundaries, M = 0.1, 0.5, 100 $\mathrm{M}_{\odot}$. Instead, for a classical Salpeter IMF, which is a single power-law, the combination of a single exponent $\alpha = 2.35$ and a single high mass $M_{up} = 100\ M_{\odot}$ is required.

Regarding the stellar evolution models, the code offers the choice between several evolutionary tracks and metallicity values. The evolutionary tracks available are specific versions of two main families: the *Padova* tracks (Bertelli et al. 1994) and the *Geneva* tracks (Schaller et al. 1992,Meynet et al. 1994). The main differences between them are the lowest mass included (0.15 $\mathrm{M}_{\odot}$ for *Padova* and 0.8 $\mathrm{M}_{\odot}$ for *Geneva*); consideration of thermally pulsing AGB stars (*Padova* tracks with AGB stars) or the rotation of the stars (*Geneva* tracks with or without rotation) For any evolutionary track selected, there are five metallicity values available: Z = 0.040, 0.020 ($\mathrm{Z}_{\odot}$), 0.008, 0.004, and 0.001. These values permit the creation of models covering a range of metallicities.

2) Brightness of the external source
The brightness of the radiation field irradiating the cloud can be described either by the luminosity or by the intensity. For the luminosity case, the luminosity emitted by the central source and the distance between the source and the illuminated face of the cloud must be specified. For the intensity case, it is not necessary to specify the inner radius, which is assumed to be 10^{30} cm (by default) with a plane-parallel geometry. However, when using the source intensity the radius is specified and the geometry of the cloud can be spherical, plane-parallel or a thick shell. For both cases, there are several parameters that can be used to indicate the strength of the external source. In particular, one intensity parameter that is used when either the luminosity of the source or the radius are not available, is the **ionization parameter** (U). The ionization parameter is the dimensionless ratio of hydrogen-ionizing photon to total-hydrogen densities. It is defined as:

$$U = \frac{Q(H)}{4\pi r_0^2 n_H c} = \frac{\Phi(H)}{n_H c} \tag{4.13}$$

where:

- n_H is the total hydrogen density
- c is the speed of light
- r_0 is the inner radius
- $Q(H)$ is the number of hydrogen-ionizing photons emitted by the central source
- $\Phi(H)$ is the surface flux of ionizing photons.

For a given model, several input spectra can be combined, such an AGN with a starburst. The shape and brightness of each individual input spectrum must be specified.

Initial hydrogen density

The initial hydrogen density (n_H) is the total hydrogen density at the illuminated face of the cloud:

$$n(H) = n(H^0) + n(H^+) + 2n(H_2) + \sum_{other} n(H_{other}) \tag{4.14}$$

where the sum includes H in the ionized, molecular and neutral atomic forms. The hydrogen density can be considered to be constant throughout the cloud (default) or the total pressure can be chosen to be constant.

Chemical composition and grain properties

There are various choices for the chemical composition in Cloudy. By default, grains are not included in the structure of the cloud and the elemental abundances are set to a solar chemical composition that is summarized in Table 7.1 of the manual Hazy1. It is also possible to: (1) choose a different set of abundances among those pre-defined by Cloudy to better represent the medium that is investigated, e.g. a planetary nebula; (2) scale all the abundances to a specific metallicity; (3) enter as input the abundance of one or several elements, if known, by giving the number of atoms of the element relative to hydrogen, e.g. n(C)/n(H)$\approx 2\times10^{-4}$. The abundance sets pre-defined in Cloudy are the following:

- Crab nebula: abundances are from Pequignot & Dennefeld (1983) and grains are not included;
- Nova: abundances are for the classical nova V1500 Cygni, from Ferland & Shields (1978);
- HII region: abundances are mainly those of Orion Nebula determined by Rubin et al. (1991), Baldwin et al. (1991), Osterbrock et al. (1992) and Rubin et al. (1993). Choosing this chemical composition, grains are included with properties from Baldwin et al. (1991) and van Hoof et al. (2004);
- Planetary nebula: abundances are from Aller & Czyzak (1983) and Khromov (1989). This set includes grains;
- ISM: the abundances are coming mostly from Cowie & Songaila (1986) and Savage & Sembach (1996), while the interstellar medium grains are those defined by Mathis et al. (1977), for the Galaxy;
- old solar 84: is the chemical solar composition used in version 84 - 94 of Cloudy. The values are taken from Grevesse & Anders (1989) and Grevesse et al. (1993);
- GASS10: is the chemical solar composition updated from Grevesse et al. (2010).

Grains and PAHs can be added if they are not included in the selected set of abundances. There are default files for the grain distribution, composition, opacities, which can also be specified by the user. For more details on the elemental abundances and grain commands, we refer the reader to the manual Hazy1.

Geometry

The geometry of the model can be open, with a plane-parallel cloud, or closed, with a spherical cloud. For both cases, the computation of the radiation transfer and equilibrium functions starts at the illuminated face of the cloud, which is the edge of the cloud facing the source and located at a distance of the inner radius to the source. The calculation stops on the opposite side of the cloud, at the outer radius. The two possibilities are shown in Figure 4.6. More complex geometries to calculate a 3D propagation of the radiation, such as Cloudy-3D, are described in Morisset (2006) and available from `http://sites.google.com/site/cloudy3d/`.

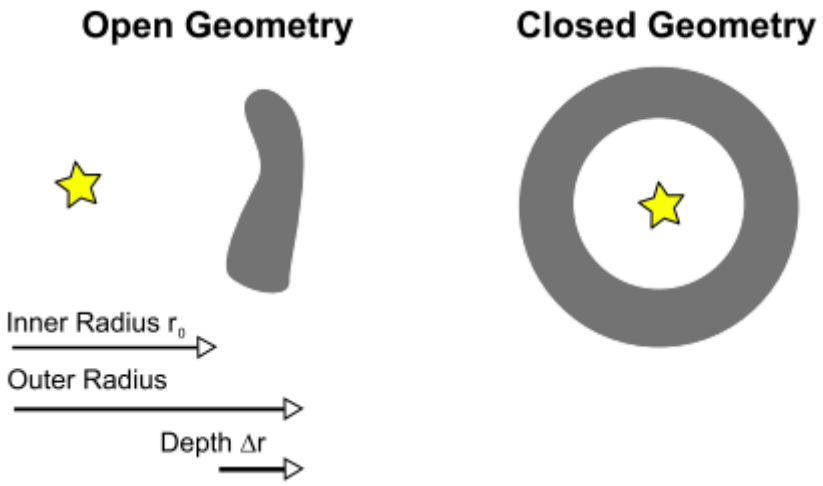

Figure 4.6: Two possible geometry cases that can be assumed by CLOUDY (Figure from the manual Hazy1). *Left*: open geometry. *Right*: spherical geometry. The stars represent the radiation sources and the gray shapes are the clouds irradiated by the ionization field.

4.3 Cloudy models applied to IC 10

In this section, I present the choices of initial conditions and strategy adopted to build the grid of CLOUDY models necessary for my project. The methods used to compare the model predictions to the MIR and FIR observations are presented in Chapter 5, while the results are discussed in Chapter 6.

4.3.1 Setting the input parameters

The main inputs of the parameter space that I used to build our grid of models are:

1. the shape of the radiation field source, age of the burst (t_{burst}), which is varied
2. the ionization parameter ($\log U$), which is varied
3. the initial hydrogen density (n_H), which is varied
4. the gas and dust chemical composition, which is fixed
5. the depth of the cloud, which is varied

Shape of the source spectrum: age of the burst (t_{burst}) As explained previously, I used the spectral synthesis code Starburst99 (Leitherer et al. 2010) to create the stellar ionizing continuum that serves as input for the models. In particular, I chose a Salpeter IMF ($\alpha = 2.35$) with an upper mass limit of 100 $M_\odot$ as done, for example, in the optical study of IC 10 from López-Sánchez et al. (2011) and Padova asymptotic giant branch tracks with Z = 0.008. I assumed a single-burst star formation event with a fixed mass of 10^5 $M_\odot$. However, since Cloudy uses only the shape information from the source spectrum, it is not important which fixed mass is chosen. Motivated by studies of the stellar population of IC 10 (e.g. Sanna et al. 2009; Yin et al. 2010; Vacca et al. 2007), the age of the cluster is varied within the range 2.5 to 7 Myr (steps of 0.1 Myr between 2.5 to 3.5 Myr and between 5 to 6 Myr, and steps of 0.5 Myr between 3.5 to 5 Myr and between 6 to 7 Myr).

Intensity of the radiation field: ionization parameter
The geometry of the gas and the luminosity of the source are not known. Hence, I used the ionization parameter to constrain the source brightness. In our grid, $\log U$ is varied from -4 to -1 with steps of 0.2.

Hydrogen density
The models are run in pressure equilibrium, i.e. the total pressure is kept constant. As a consequence, the density of the models varies with depth in the cloud to satisfy the equation of state. The initial value of the hydrogen density (at the inner radius) is set to cover the range of 10 - 10^4 cm^{-3} with steps of 0.2 in logarithmic scale.

Chemical composition
Based on the literature, I set the elemental abundances of oxygen, nitrogen, neon, argon and sulphur to observed values. Since the elemental abundances are not constant across the galaxy, I used different sets of elemental abundances for the different HII regions of IC 10 analyzed (Figure 5.1). The abundances were measured in Magrini & Gonçalves (2009) and López-Sánchez et al. (2011). I adopted those values as reported in Table 4.1, in order to consider the difference between the two studies as well as the solar ratio (e.g. (O/Ar)) from Asplund et al. (2009). For the analysis at larger scales, we considered the values reported for the central region[1]. The uncertainties on these measured abundances bring uncertainties on the line intensities predicted by the models, of a factor of 2-4, depending on the element. These uncertainties will be taken into account in the modeling (Sect. 5.3). The values adopted for each star-forming region are presented in Table 4.1. For the other elements, I chose the solar abundances scaled to the metallicity of IC 10, $Z = 0.3\ Z_{\odot}$.

For the grains, I used the grain size distribution presented in Abel et al. (2005), which is based on the work of Weingartner & Draine (2001) and consists of graphites and silicates. The grain properties of IC 10 are not well known hence I have used files that exist in CLOUDY to describe the grain properties of the Small Magellanic Cloud (SMC). The abundances are also scaled to the metallicity of IC 10.

Table 4.1: Elemental abundances used to model the HII regions of IC 10 with CLOUDY.

Element	Central	ArcA c1	ArcA c2
12 + log(O/H)	8.26±0.15	8.19±0.15	8.45±0.15
12 + log(N/H)	6.90±0.20	6.95±0.20	7.21±0.20
12 + log(Ne/H)	7.60±0.20	7.40±0.20	7.71±0.20
12 + log(Ar/H)	6.25±0.30	6.10±0.30	6.32±0.30
12 + log(S/H)	6.75±0.30	6.60±0.30	6.60±0.30

4.3.2 Stopping criteria

CLOUDY has several stopping criteria already set, e.g. the default lowest temperature of 4 000 K. If one of the stopping criteria is reached, the computation of the model stops. Hence, in order to proceed deeper into the cloud,

[1]For each element, the different values are all inside 1 σ.

it is important to either modify or turn off the default criteria and select your own criteria. The user can indicate many different stopping criteria (e.g. A_V, column density, depth) and the code stops when the first of the specified criteria is reached. Since I want to investigate first the ionized gas and, at a later time, propagate the analysis into the PDR and molecular phases, I chose to stop the models at the ionization front. The ionization front is defined as the location in the cloud when the ratio of $n(H^+)/n(H_{tot})$ falls below 1%. Since at the ionization front most of the recombination have occurred, the temperature is lower than 4 000K (∼1 500K in our models). Hence, the default lowest temperature must be turned off. Subsequently, the properties identified for the HII regions are used as input characteristics to investigate the following phases with a self-consistent approach.

Depth of the cloud

Since the models are stopped at the ionization front, the HII region surrounding the stellar source is assumed to be radiation-bounded, which means that the region is optically thick to the ionizing radiation. However, the HII region could be matter-bounded or density-bounded, in which case there is not enough matter to absorb all the ionizing radiation and the HII region is limited by the size of the gas cloud. A matter-bounded region, hence, is optically thin to the radiation field and the ionizing photons can escape the region. The regions investigated in this work, in particular those corresponding to small spatial scales (*clump*; see Section 5.2.1), have sizes lower than 30 × 30 pc, thus, in principle, it is possible that a fraction of the ionizing photons escape from the region. In order to consider that possibility, the depth of the cloud is a free parameter. I did not create a model for each depth. However, for each model (stopped at the ionization front), I saved the output values at each depth of the cloud, from the illuminated front to the ionization front. If the region is radiation-bounded, the observed lines will be better reproduced at a depth, normalized to the location of the ionization front, of 1. Otherwise, if the HII region is matter-bounded, the model that better represents all of the observed line intensities will have a depth lower than 1. This criterion affects mostly the emission of lines with low excitation potentials, such as [ArII] 6.9 μm and [NII] 121.9 μm which have excitation potentials of 15.7 eV and 14.5 eV respectively. These two species reach their maximum of emission at the edge of the ionized phase, as shown in Figure 4.7. If in some regions of IC 10 there is really a fraction of ionizing photons that escapes, a radiation-bounded model will over-predict the line intensities of [ArII] 6.9 μm and [NII] 121.9 μm in those regions. In that case, the modeled cloud should be matter-bounded instead of radiation-bounded, i.e. it should stop before the ionization front, in order to reproduce correctly

all the tracers.

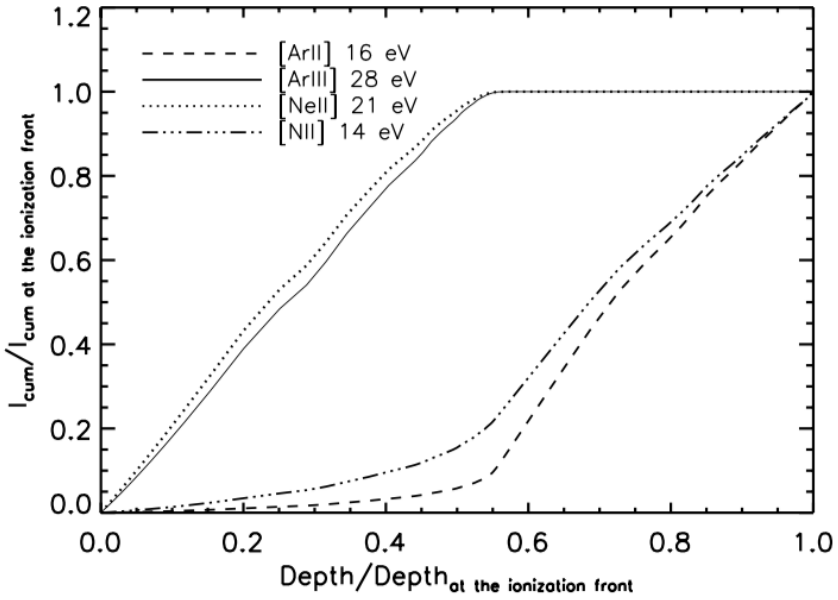

Figure 4.7: Cumulative intensity (I_{cum}) of the lowest excitation potential lines used in the study of the HII regions as a function of the depth of the cloud for a model with log U = -2, n_H = 2.2 cm^{-3} and t$_{burst}$ = 5.5 Myr. The intensities and the depths are normalized to the values reached at the ionization front. Both [NeII] 12.8 μm and [ArIII] 8.9 μm achieve the maximum emission at 50% of the depth of the cloud, while [NII] 121.9 μm and [ArII] 6.9 μm reach the total emission at the ionization front.

Chapter 5

Modeling the ionized gas at different spatial scales

Contents

The ISM incorporates the clues of galaxy evolution from primordial environments to present-day galaxies. As described in Chapter 1, the ISM is at the same time the site of stellar birth and the receptacle of products from dying stars (e.g., winds, SNe). The ISM therefore hosts the signatures of metal enrichment over a galaxy's history, and it provides environmental details and constraints on processes that drive star formation. Star formation is a mechanism that depends on many parameters related to dynamical instabilities (e.g., Ostriker et al. 2010) and to the amount and structure of molecular gas (e.g., Krumholz & McKee 2005). In the latter case, metallicity is an important parameter to account for the presence of dust grains (which in turn affect the formation of molecular gas, provide gas heating through the photoelectric effect, and provide shielding from UV photons) and for the gas cooling (e.g., through the C^+ fine-structure line). The ISM structure and phases (in particular their relative filling factor) seems to be a strong function of metallicity. In low-metallicity environments, ionizing photons can penetrate deeper into the molecular cloud (because of the lower dust abundance) and dissociate molecules that are not efficient in self-shielding, such as CO (Chapter 1). Moreover, those photons can propagate on large spatial scales, ionizing a large volume filling factor (Chapter 1 and Chapter 3). Cormier et al. (2012) used combinations of observations from tracers of different ISM phases and state-of-the-art models to show that the ionized gas of the low-metallicity galaxy Haro 11 (unresolved with *Spitzer* and *Herschel*) fills a relatively larger volume of the ISM as compared to more metal-rich galaxies. It was also shown that the ionized gas is likely distributed in a dense phase related to the star formation sites (e.g., HII regions) and a more diffuse phase that pervades the galaxy scale. These kinds of studies remain sparse and require careful analysis as there is no single, well-established method to model a multi-phase ISM. The modelling depends on what tracers are available and whether the scientific objectives require a complex ISM model. Hence the work presented in this chapter is an important part of my project. While the results for Haro 11 were inferred from integrated measurements of the entire galaxy (Cormier et al. 2012), the proximity of the galaxy IC 10 ($\sim$700 kpc; Sakai et al. 1999; Sanna et al. 2009; Kim et al. 2009; see source description in Section 1.6) makes it possible to examine the ISM phases and their tracers at various spatial scales − from individual star-forming regions to the whole body of the galaxy − in a similarly low-metallicity environment. The objectives are numerous. We first seek to characterize the physical conditions in the ionized gas in a low-metallicity environment by providing access to relatively high spatial resolution and establishing a modeling strategy. We then wish to understand which combinations of ionized gas emission lines provide useful diagnostics as a function of the methodology choices and *as*

a function of the spatial scale used and the potential corresponding biases. Finally, we need to set a reference model of the ionized gas distribution and characteristics that can be used to further model the connected HI shells and the molecular gas.

In the next two sections, I describe the various spatial scales used in the study of IC 10, which tracers are used for each spatial scale, and how the models account for the choice of available tracers. In the remainder I explore two different methods to compare the observations with the model predictions.

5.1 Tracers used

All the emission lines seen with *Spitzer* and *Herschel*, expected to arise from the ionized gas, are used. This includes lines from all species with an ionization potential larger than that of H^0 (13.6 eV), particularly N^+, O^{2+}, Ne^+, Ne^{++}, S^{++}, S^{3+}, Ar^+, and Ar^{++}. Collisionally-excited emission lines from these species (with e^- as collision partners) can be used as constraints to derive the physical conditions of the ionized gas (Table 1.2). On the other hand, species with lower ionization potential than 13.6 eV may become ionized while hydrogen is still in the form of H^0; this includes C^+, Si^+, or Fe^+ and the corresponding prominent emission lines in the infrared, [CII] 157.7 μm , [FeII] 25.9 μm , [FeII] 17.9 μm and [SiII] 34.8 μm. These emission lines cannot immediately be used as constraints for modeling the ionized gas because a fraction of the emission, sometimes dominant, arises in the neutral gas instead (with H^0 or H_2 as collision partners). Since such lines are potentially important constraints for the neutral atomic and molecular gas in PDRs (Chapter 7), it is, however, important to estimate the fraction arising in the ionized vs. neutral gas. This fraction will come as a by product of my models, since the latter predict intensities of [CII], [FeII] and [SiII] in the ionized gas, which I can then simply compare to the observed values (Section 6.1.4).

The Hα line in the optical is potentially a useful tracer of the ionized gas because it traces the ionized hydrogen. However, Hα suffers from significant extinction from dust in the Milky Way, especially for IC 10 (Galactic latitude of IC 10 = $-3.3°$) and from dust internal to IC 10. Unless the extinction is known with accuracy, it is thus difficult to use Hα as an additional constraint. Instead, I will use the model predictions for Hα and compare to the observed value in order to estimate the extinction (Section 6.1.2).

5.2 Spatial decomposition

5.2.1 Description of the spatial scales used

One of the objectives is to compare the physical conditions inferred from ionized gas tracers observed at various spatial scales. For this reason, I chose three spatial scales:

1. "Clumps": The smallest spatial scale accessible is limited by the spatial resolution of the instruments. The best resolution is achieved with the *Spitzer*/IRS SL observations, with 4″, corresponding to ~ 14 pc at the distance of IC 10. With this resolution I can disentangle the compact regions, *clumps*, from the more extended gas components. Although many clumps could in principle be investigated, I restrict myself to the brightest clumps of the galaxy in MIR and FIR lines that are accessible in the *Spitzer* and *Herschel* maps. I identified five such *clumps* in the body of IC 10: three in the *central main star-forming region* (*Central main zone*; labeled *Center c*1, *Center c*2 and *Center c*3), and two in the *first star-forming arc* (*ArcA c*1 and *ArcA c*2). Figure 5.1 shows the clump locations. The method used to disentangle the clumps and measure their fluxes and errors is described in Sect. 5.2.2. As explained in that section, the *Spitzer*/IRS LL and *Herschel* maps, with their lower spatial resolution, require additional constraints on the clump decomposition.

2. "Zones": I selected large areas of the galaxy (few kpc), that are expected to exhibit different local physical conditions (Figure 5.2). Some *zones* enclose the *clumps* described above (*Central main zone* and *ArcA*) and structures visible in Hα (*ArcB*, *Intermediate*, *Central north* and *West*) while the *Diffuse* zone was selected in order to examine the most diffuse phase possible (with an area large enough for integrated lines to have the best signal-to-noise ratio possible). Each *zone* spreads across many pixels in the IRS data cube and a single spectrum was produced by stacking spectra in the cube from the relevant spatial pixels. Line fluxes and errors are propagated through a Monte-Carlo simulation. For each Monte-Carlo iteration one spectrum is produced and one set of line fluxes is calculated. The fluxes and the associated errors are calculated using the median and the standard deviation of the flux distribution. The procedure for the *Herschel* PACS maps is slightly different as the HIPE pipeline does not provide uncertainties on the measurements. Empirical errors are calculated from the dispersion of the data cloud at every wavelength bin, and the line flux and errors are

then inferred from each projected pixel (see Lebouteiller et al. 2012). For each PACS line we thus simply summed the flux over the pixels in each *zone*, and propagated errors accordingly. Table 5.1 presents the fluxes and errors measured for each *zone*. Figure 5.3 shows an example of a set of lines corresponding to the integrated *Central main zone*, region (∼200 pc × 250 pc).

3. "Body": The largest scale corresponds to most of the star-forming body of the galaxy, encompassing a zone of 608 pc × 855 pc and includes most of the zones examined individually and described above (*Body* in Figure 5.2). It is the largest region available accessible with the *Spitzer* spectroscopic observations. The integrated fluxes of this area are calculated with the same method used for the other *zones*. Unfortunately, the PACS spectral maps do not cover the entire *Body* zone.

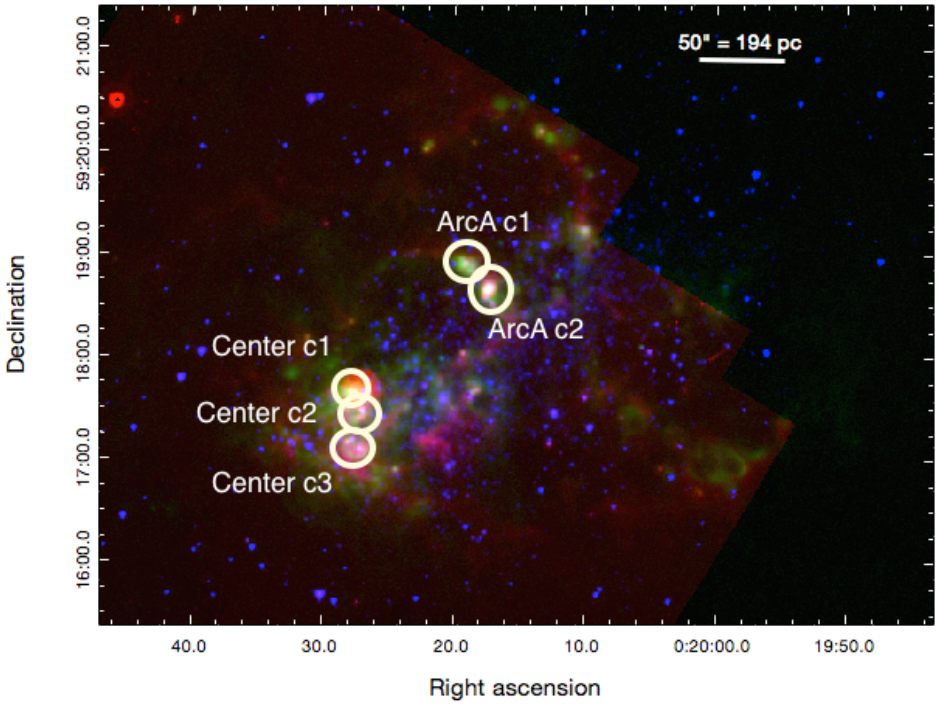

Figure 5.1: Three-color image of IC 10 with PAH emission (Spitzer/IRAC4; 8.0μm) in red, Hα (Hunter & Elmegreen 2004) in green, and stars (Spitzer/IRAC1; 3.6μm) in blue. The smallest scale used to infer physical conditions in the ionized gas are what I define as "clumps" in the *Central main zone* ($c1$, $c2$, $c3$) and the *ArcA* region ($c1$, $c2$).

Table 5.1: Integrated fluxes (×1e-16 W m^{-2}) for the defined zone and body regions (Figure 5.2).

	Central main	Central north	ArcA	Intermediate
$[SIII]33$	$45.99^{\pm 1.29}$	$4.50^{\pm 0.41}$	$18.53^{\pm 1.67}$	$13.96^{\pm 0.92}$
$[SIII]18$	$31.94^{\pm 1.08}$	$2.75^{\pm 0.34}$	$11.39^{\pm 0.71}$	$8.71^{\pm 0.53}$
$[SiII]$	$27.30^{\pm 1.67}$	$3.46^{\pm 0.78}$	$9.24^{\pm 1.23}$	$12.16^{\pm 1.08}$
$[NeIII]$	$27.70^{\pm 0.82}$	$2.02^{\pm 0.43}$	$12.18^{\pm 0.55}$	$8.87^{\pm 0.49}$
$[NeII]$	$22.61^{\pm 0.19}$	$1.66^{\pm 0.09}$	$7.12^{\pm 0.12}$	$6.89^{\pm 0.15}$
$[ArIII]$	$8.29^{\pm 0.54}$	$0.73^{\pm 0.13}$	$4.81^{\pm 0.26}$	$3.40^{\pm 0.27}$
$[ArII]$	$5.14^{\pm 0.98}$	$0.82^{\pm 0.65}$	$1.37^{\pm 1.06}$	$1.51^{\pm 0.65}$
$[SIV]$	$10.51^{\pm 0.39}$	$0.65^{\pm 0.16}$	$8.86^{\pm 0.31}$	$3.79^{\pm 0.26}$
$[OIII]$	$126.30^{\pm 2.40}$	-	$91.03^{\pm 2.25}$	-

	ArcB	West	Diffuse	Body.
$[SIII]33$	-	-	$2.10^{\pm 0.70}$	$135.40^{\pm 3.30}$
$[SIII]18$	-	-	$0.99^{\pm 0.35}$	$86.96^{\pm 3.23}$
$[SiII]$	-	-	$2.52^{0.70}$	$105.90^{6.00}$
$[NeIII]$	-	-	$1.64^{\pm 0.43}$	$86.35^{3.55}$
$[NeII]$	$2.74^{\pm 0.09}$	$4.17^{\pm 0.20}$	$0.59^{\pm 0.14}$	$56.25^{\pm 0.63}$
$[ArIII]$	$2.63^{\pm 0.37}$	$2.24^{\pm 0.32}$	$1.56^{\pm 0.20}$	$28.66^{\pm 1.14}$
$[ArII]$	$1.72^{\pm 5.07}$	$2.60^{\pm 2.28}$	$81.36^{\pm 121.63}$	$21.44^{\pm 3.97}$
$[SIV]$	$1.24^{\pm 0.28}$	$1.20^{\pm 0.32}$	$0.29^{\pm 0.43}$	$32.76^{\pm 1.87}$
$[OIII]$	$15.19^{\pm 2.15}$	-	-	-

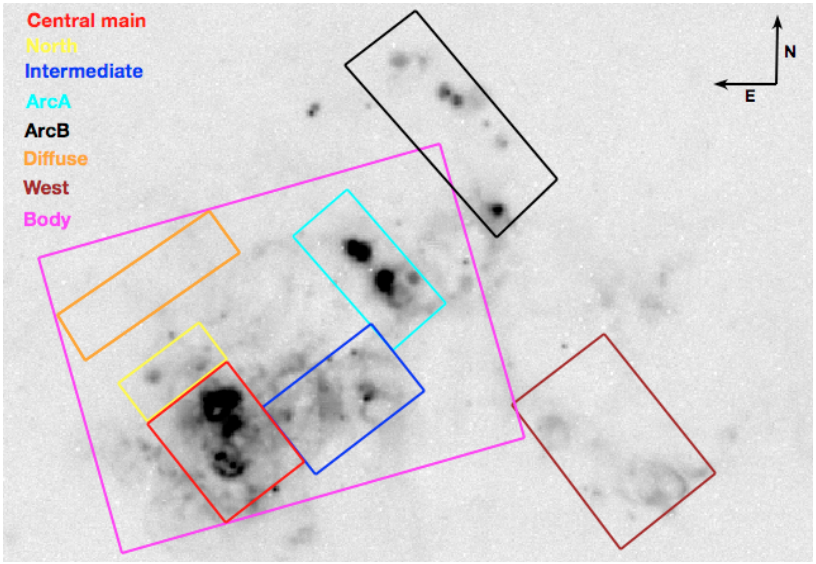

Figure 5.2: The outlines of the various *zones* investigated are overlaid on the Hα background image. The *Body* zone corresponds to the largest area that we investigated.

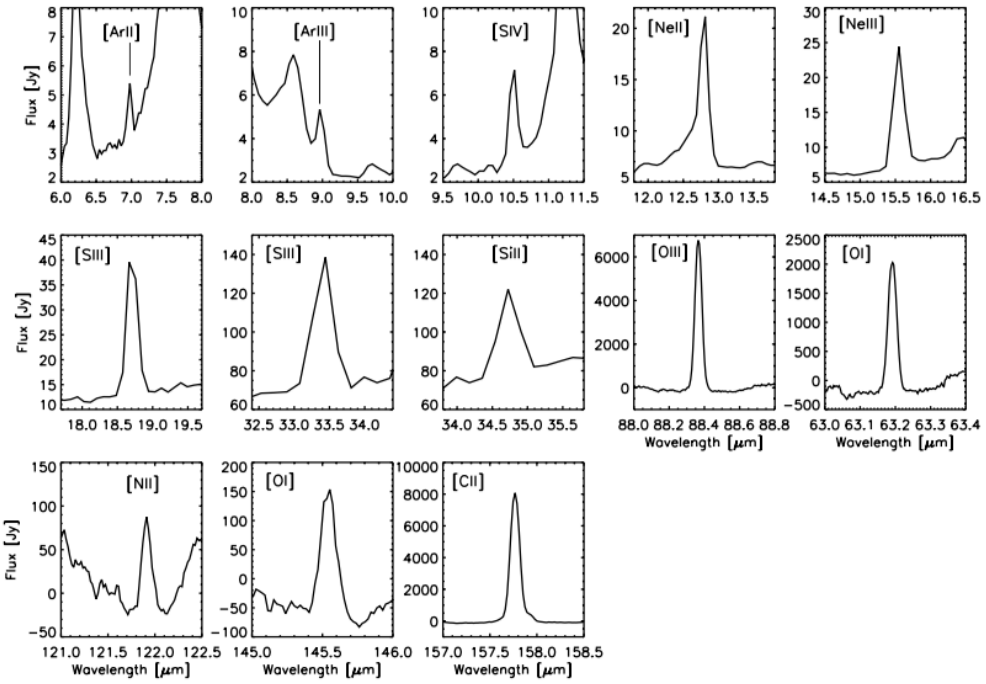

Figure 5.3: The *Spitzer*/IRS and *Herschel*/PACS lines for the *Central main zone* (see location of zone in Figure 5.2).

5.2.2 Disentangling the "clumps"

To disentangle the clumps and derive the fluxes of each line, I used the IDL package *MPFIT* (Markwardt 2009), which is a set of routines for robust least-squares minimization.

At the spatial resolution of *Spitzer*, three clumps are identified in the *Central main zone* and two clumps in the *ArcA* region (i.e., the first arc; Figure 5.1). Since the clumps are spatially blended with *Spitzer*, a simultaneous decomposition is necessary. For each set of clumps, I used an asymmetric 2D Gaussian decomposition to simultaneously adjust the profiles of the clumps as well as the underlying extended component. Various constraints on the position, size, and asymmetry of the clumps can be used to improve the decomposition, as explained in the following. For all tracers, the minimum Gaussian width is given by the resolution of the instrument, $\sigma^2_{res} = (FWHM/2.354)^2$. The quadratic difference between the clump size measured in each tracer and the spatial resolution element provides the intrinsic clump size. In all cases, the flux uncertainties were calculated using a Monte-Carlo simulation. For tracers with spatial resolution better than $12''$ (SL-IRS maps: [ArII] 6.9 μm, [ArIII] 8.9 μm, [SIV] 10.5 μm and [NeII] 12.8 μm; PACS maps: [OIII] 88.4 μm and [NII] 121.9 μm), some degree of freedom on the position, (maximum) size, and asymmetry was allowed.

For all tracers, I tested three different methods to disentangle the *clumps*.

1. *Rxy*: The asymmetry of the Gaussian, described by the parameter Rxy $= \sigma_x/\sigma_y$ (with σ_x and σ_y measured in the two axes of the Gaussian) is constrained to be between 0.5 and 2.

2. *Free*: No constraints on the Gaussian asymmetry. The weight provided to MPFIT is 1/err, where err is the error derived for each pixel.

3. *err2*: No constraints on the Gaussian asymmetry. The weight provided to MPFIT is $1/\mathrm{err}^2$.

An illustration of the decomposition is shown in Figure 5.4 for the clumps in the *Central main zone*. The fluxes calculated with the three methods are reported in Table 5.2 and compared in Figures 5.5 to 5.8. It can be seen that the methods provide similar fluxes for each clump within errors, except for [NeII] 12.8 μm in the central region. The [NeII] decomposition of the clumps in the central region is particularly difficult because of a bright extended component that is not uniform. In addition, there are several satisfactory solutions (in terms of χ^2) for different *Rxy* values. While the *sum* of $c1$+$c2$ in [NeII] is the same for all methods, the *Rxy* method distributes the flux differently between the clumps $c1$ and $c2$. I attribute the difference observed

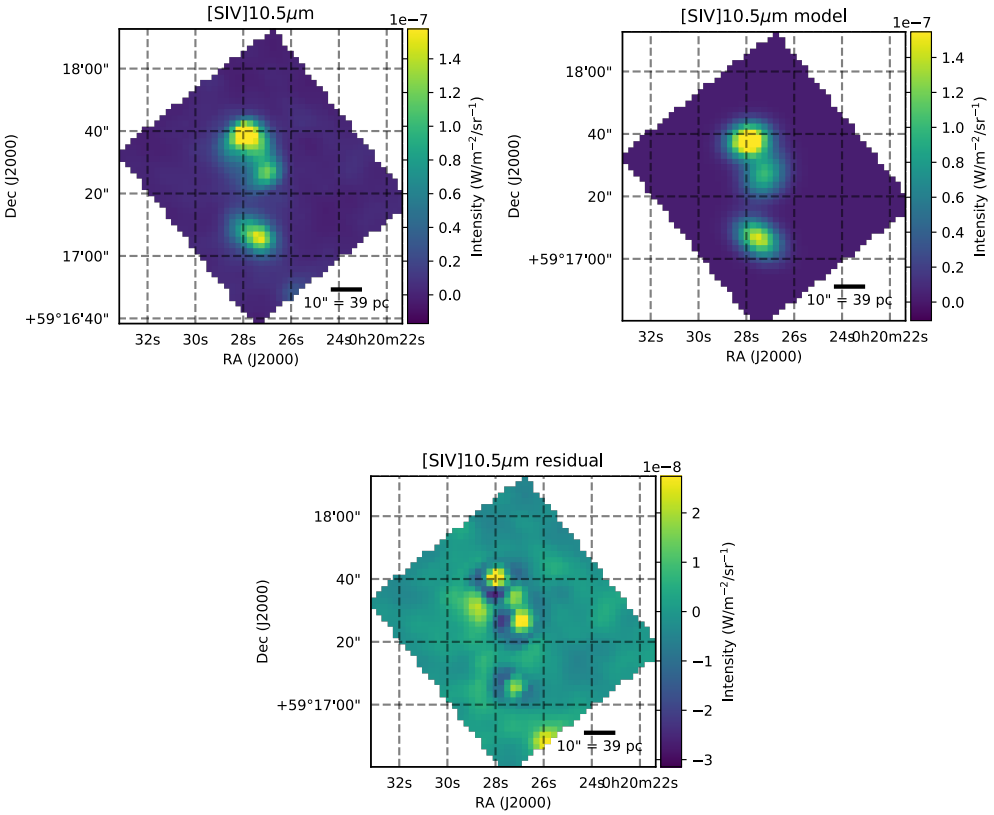

Figure 5.4: Example of the decomposition obtained with the *Rxy* method for the clumps in the *Central main zone*. *Top left*: Observed [SIV] 10.5 μm map; *Top right*: clump model; *Bottom*: residuals. The residual is calculated as (observed - model)

for [NeII] to an unrealistic asymmetry of the 2D Gaussian if the Gaussian size parameters are left free. Hence, for all of the tracers I used the fluxes calculated with *Rxy* method.

Table 5.2: Fluxes (×1e-16 W m^{-2}) for each clump using the different decomposition methods.

	FWHM [arcsec]	Center c1	Center c2	Center c3	ArcA c1	ArcA c2
$[ArII]_{free}$	3.7	$0.91^{\pm0.41}$	$0.72^{\pm0.52}$	$2.04^{\pm0.68}$	$0.60^{\pm0.23}$	$1.07^{\pm0.44}$
$[ArII]_{err2}$		$0.92^{\pm0.26}$	$0.67^{\pm0.44}$	$1.83^{\pm0.62}$	$0.52^{\pm0.29}$	$1.06^{\pm0.59}$
$[ArII]_{Rxy}$		$1.09^{\pm0.59}$	$0.57^{\pm0.51}$	$2.59^{\pm1.38}$	$0.48^{\pm0.29}$	$1.07^{\pm0.60}$
$[ArIII]_{free}$	3.7	$2.50^{\pm0.83}$	$2.17^{\pm0.81}$	$2.85^{\pm0.31}$	$1.26^{\pm0.32}$	$3.27^{\pm0.22}$
$[ArIII]_{err2}$		$2.17^{\pm0.55}$	$2.17^{\pm0.73}$	$2.87^{\pm0.41}$	$1.21^{\pm0.34}$	$3.22^{\pm0.27}$
$[ArIII]_{Rxy}$		$2.50^{\pm0.92}$	$2.17^{\pm0.80}$	$2.85^{\pm0.34}$	$1.26^{\pm0.32}$	$3.27^{\pm0.22}$
$[SIV]_{free}$	3.7	$4.08^{\pm0.36}$	$3.44^{\pm0.40}$	$3.51^{\pm0.26}$	$1.96^{\pm0.16}$	$9.48^{\pm0.25}$
$[SIV]_{err2}$		$4.27^{\pm0.58}$	$3.07^{\pm0.51}$	$3.56^{\pm0.32}$	$1.89^{\pm0.14}$	$9.36^{\pm0.39}$
$[SIV]_{Rxy}$		$4.08^{\pm0.36}$	$3.44^{\pm0.40}$	$3.51^{\pm0.26}$	$1.96^{\pm0.16}$	$9.48^{\pm0.25}$
$[NeII]_{free}$	3.7	$3.53^{\pm0.70}$	$7.04^{\pm1.25}$	$11.15^{\pm0.43}$	$2.63^{\pm0.14}$	$4.77^{\pm0.13}$
$[NeII_{err2}$		$3.38^{\pm0.48}$	$7.41^{\pm0.94}$	$11.45^{\pm0.88}$	$2.61^{\pm0.10}$	$4.95^{\pm0.15}$
$[NeII]_{Rxy}$		$4.86^{\pm0.53}$	$4.84^{\pm0.69}$	$11.13^{\pm0.61}$	$2.63^{\pm0.14}$	$4.77^{\pm0.13}$
$[OIII]_{free}$	9.5	$16.09^{\pm0.36}$	$10.69^{\pm0.256}$	$15.78^{\pm0.22}$	$6.27^{\pm0.14}$	$16.16^{\pm0.15}$
$[OIII]_{[err2]}$		$17.74^{\pm0.27}$	$0.0^{\pm0.26}$	$17.02^{\pm0.42}$	$17.14^{\pm0.09}$	$44.44^{\pm0.10}$
$[OIII]_{[Rxy]}$		$17.96^{\pm0.24}$	$13.37^{\pm0.14}$	$15.70^{\pm0.21}$	$16.41^{\pm0.48}$	$45.23^{\pm0.82}$
$[NII]_{free}$	9.8	-	-	$0.79^{\pm0.02}$	$0.05^{\pm0.01}$	$0.41^{\pm0.03}$
$[NII]_{[err2]}$		-	-	$0.81^{\pm0.04}$	$0.05^{\pm0.02}$	$0.42^{\pm0.05}$
$[NII]_{[Rxy]}$		-	-	$0.79^{\pm0.03}$	$0.05^{\pm0.03}$	$0.41^{\pm0.06}$

The decomposition methods are described in Section 5.2.2.

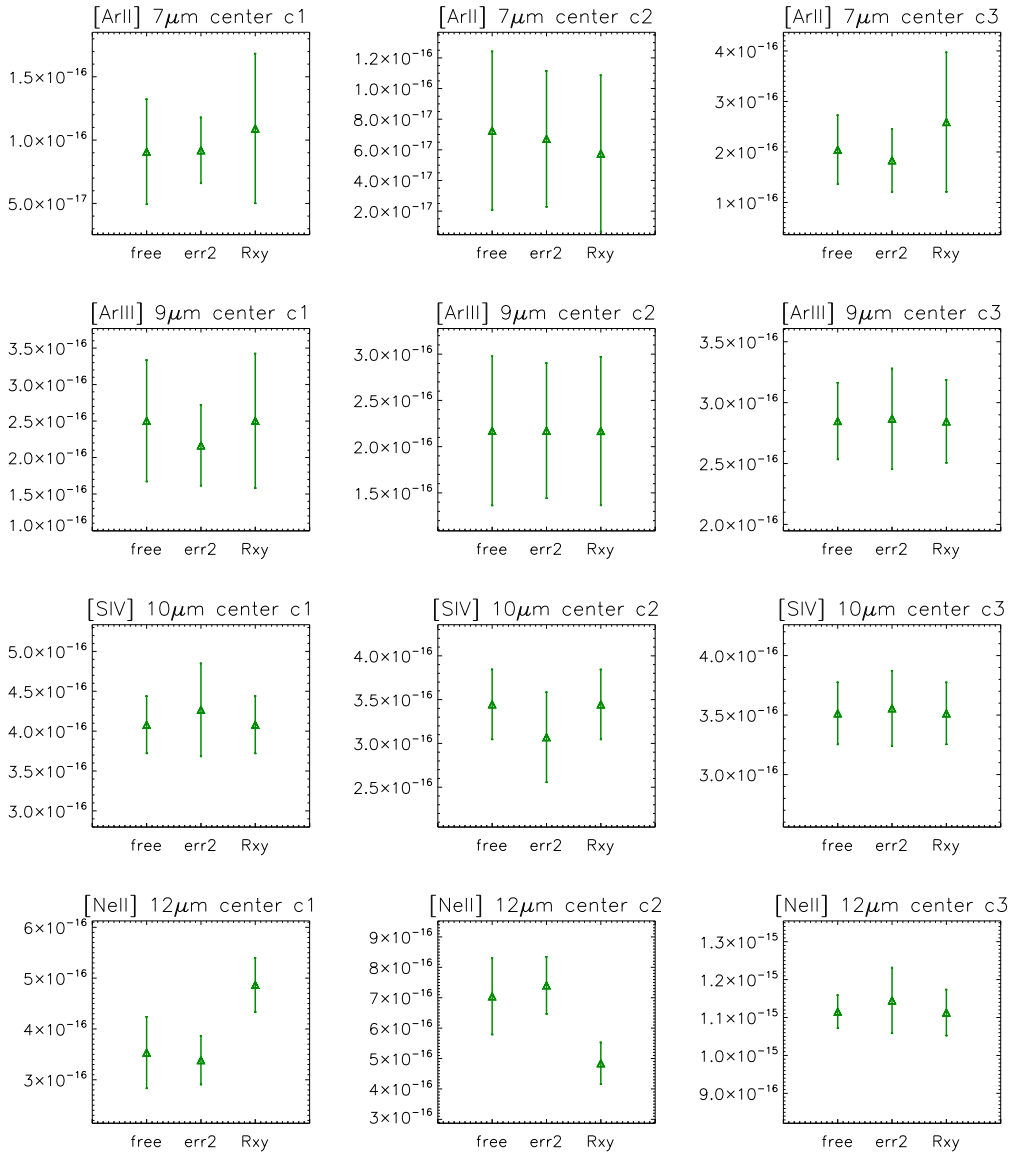

Figure 5.5: Comparison of the *Spitzer* line fluxes determined for the three clumps (from left to right : $c1$, $c2$ and $c3$) in the *Central main zone*, using the different decomposition methods (labeled on x-axis; see Section 5.2.2 for explanation of the methods used).

For the tracers with low spatial resolution ($> 12''$; [SIII] 18.7 μm, [SIII] 33.5 μm and [NeIII] 15.5 μm), I fixed the reference positions based on the Hα peaks (convolved to the *Spitzer* resolution; Hunter & Elmegreen 2004). For the Gaussian width, I could assume that the clumps were not spatially

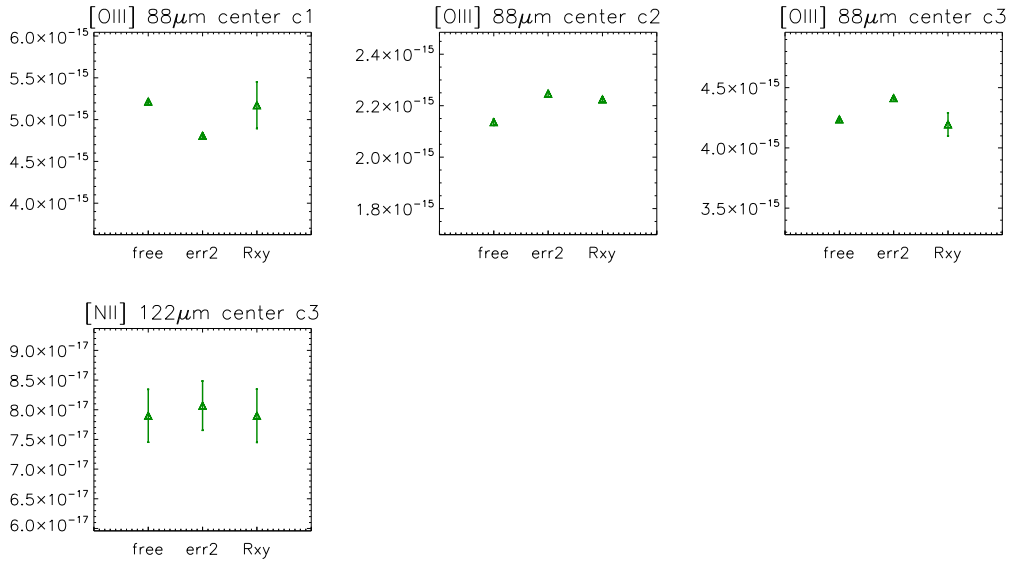

Figure 5.6: Comparison of the PACS line fluxes determined for the three clumps in the *Central main zone*. See Figure 5.5 for the plot description.

resolved. This comes from the relatively small intrinsic clump size ($\ll 11''$) measured from the IRS SL decomposition described above, which is performed at higher spatial resolution.

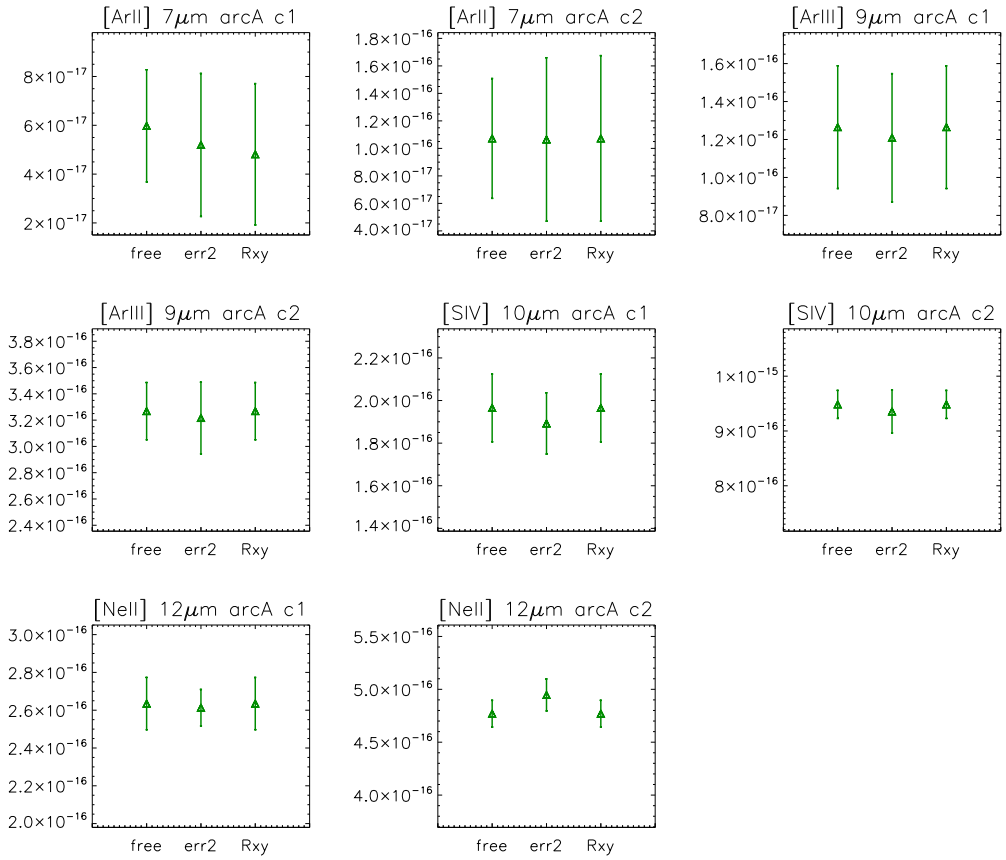

Figure 5.7: Comparison of the *Spitzer* line fluxes determined for the two clumps in the *ArcA* region. See Figure 5.5 for the plot description.

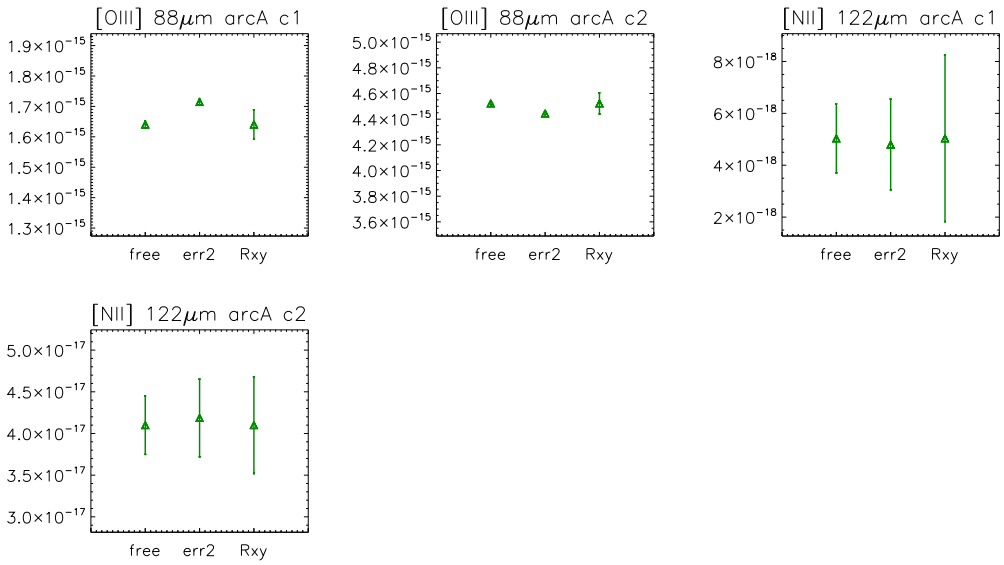

Figure 5.8: Comparison of the PACS line fluxes determined for the two clumps in the *ArcA* region. See Figure 5.5 for the plot description.

5.3 Building a set of observational constraints for the models

In order to derive the physical properties of the ionized gas, I compare the fluxes calculated at various spatial scales (Section 5.2) with the grid of models presented in Section 4.3. In this section, I describe two methods that use our measured line fluxes in two different ways, either as **line ratios** or as **absolute line fluxes**.

5.3.1 Foreword on the available methods

The first method, **line ratios** (Section 5.3.2), is suggested by Abel et al. (2005) to infer physical conditions in ionized nebulae and it is indeed frequently used in the modeling of various galaxy types or HII regions (e.g. Morisset et al. 2016; Spinoglio et al. 2015). Using line ratios presents a priori several advantages. First, it is possible to measure accurate ratios with lines arising from the same instrument/grating/detector (thereby ignoring relative calibration errors) or lines from the same atomic element (thereby ignoring uncertainties on relative elemental abundances). Furthermore, we may be able to choose ratios that trace a given physical parameter (e.g., the [SIII] line ratio for the electron density).

The second method, **absolute fluxes** (Section 5.3.3), instead uses the comparison of the predicted vs. observed line absolute fluxes (or luminosities). This is the method used by, e.g., Cormier et al. (2012) and Dimaratos et al. (2015), to infer physical conditions from galaxy-integrated *Spitzer* and *Herschel* lines. For this method, there is no a priori selection of tracers based on parameters to constrain, and all of the tracers are used. Correlated uncertainties are accounted for by building a covariance matrix between all tracers.

A fundamental difference between the two methods is the way in which the constraints are able to probe the parameter space used in the models, and the biases related to the fact that any given model parameter can be "over-represented" (i.e., providing too much weight when finding the best model). Ideally, the model solution should not depend on the selection of lines used or the way they are used as constraints (ratios or absolute fluxes). However, biases may occur if the model, by design, is not able to reproduce all of the observations. This can be due, for instance, to the hypotheses in the model configuration (e.g., assuming a single phase, a constant density...), to the atomic data used in the model (e.g., collisional rates), or to systematic uncertainties that are unaccounted for in the observations. While the

best efforts have been made to ensure that the atomic data, the measured line fluxes and related uncertainties are as reliable as possible, the hypotheses in the model configuration do not necessarily imply that we can find a model solution that reproduces all of the observations used as constraints. In particular, since we are limited by the spatial resolution of our observations and by the relatively small number of constraints, we are forced to assume a relatively naive model topology with uniform physical conditions over the region or zone we wish to examine. As the spatial scales that we consider get larger and larger, it becomes more and more problematic to reproduce all of the observations simultaneously. One of the objectives of this study is, in fact, to understand how the spatial scale over which the observations and models are performed "dictate" the derived "physical" conditions and their applicability to describe, in effect, the actual state of the nebula.

The two methods described above are somewhat different from what is usually done with the optical (or near-UV to NIR) spectra. Many past studies deal with the combination of optical emission lines that are already known to trace unambiguously, or at least convincingly, some given physical parameter (electron temperature, electron density, metallicity, starburst age...; e.g. Morisset et al. 2016). The use of MIR and FIR ionized gas emission lines to infer such parameters is, however, much less explored and less straightforward. Useful recipes and diagnostic ratios that use infrared lines and that are particularly relevant to extract physical conditions in a metal-poor environment have not yet been provided. Furthermore, we seek to constrain some parameters that are little studied, such as the fraction of matter-bounded vs. radiation-bounded ionized clouds (which is indirectly related to the "depth" parameter described in Section 4.3). In practice, few infrared line ratios are known to probe any single physical parameter, apart from the [SIII] line ratio, which strictly traces the electron density (to be more rigorous: the density in regions where sulfur exists as S^{++}). Other line ratios, such as [NeIII]/[NeII] or [ArIII]/[ArII] show expected degeneracies between the ionization parameter and the starburst age, but they also depend on the matter- vs. radiation-bounded nature of the clouds (because [NeII] and [ArII] emit at or near the photoionization front). Another important difference with optical line ratios is the wide range of critical densities of the transitions observed in the MIR and FIR (as low as a few $100\,\mathrm{cm}^{-3}$). Almost any given ratio shows some dependency with the density, which is especially important considering that the typical densities we expect in the ISM lie precisely around $100 - 1000\,\mathrm{cm}^{-3}$. For all of these reasons, whether using line ratios or absolute fluxes, the observational constraints probe the parameter space in a way that we cannot control a priori, and the selection of lines used or the way lines are combined as ratios to provide a constraint,

have both a significant impact on the process of finding a model solution.

5.3.2 Line Ratio Method

The performance of the models is evaluated via a χ^2 calculation and the "best" models are defined as those with a minimum χ^2 value. For each model of the grid (presented in Section 4.3), I calculated the χ^2 by comparing the observed line ratio, R_j, to the ratio predicted by the model, M_j:

$$\chi^2 = \sum_{j=0}^{N} \left(\frac{R_j - M_j}{\sigma_j} \right)^2 , \tag{5.1}$$

where σ_j is the uncertainty on the line ratio (accounting for correlated errors due to the instrument calibration and/or to uncertainties on the elemental abundance used) and N is the number of models in the grid.

For each observed line, several uncertainties are considered: the calibration error (σ_c; 5% for the IRS and 12% for PACS), the error on the line flux measurement (σ_f; see Table 5.2 for the clumps and Table 5.1 for the zones), the uncertainty on the elemental abundance (σ_e; Table 4.1), and an additional systematic uncertainty describing possible issues with atomic data (σ_s; 10%). Note that the uncertainty on the elemental abundance is assigned to the observations and not to the models. We did not produce several models with varying chemical abundances, but we verified that the line fluxes vary linearly with the respective elemental abundance for the uncertainty ranges considered here. Thus the final uncertainty for each line is:

$$\sigma_{line} = \sqrt{\sigma_c^2 + \sigma_f^2 + \sigma_s^2 + \sigma_e^2} \tag{5.2}$$

Regarding the zones, they have dimensions much larger than 12″ (i.e., the resolution of the IRS LL maps), so that we can simply integrate the flux in the SL and LL cubes in each zone without decomposing the spatial components. The SL and LL data cubes are projected independently, however, with different map parameters (number and overlap of parallel and perpendicular steps; Section 2.2.4), which can result in some discrepancy in the continuum flux level for a given spatial region. This discrepancy is estimated by calculating the stitching factor between the SL and LL continuum for the overlap wavelength window around $14 - 15\mu$m. The standard deviation of the ratio LL14μm/SL14μm, σ_{st}, is about 15%. Thus, the final uncertainty of LL-lines is given by:

$$\sigma_{LL-line} = \sqrt{\sigma_c^2 + \sigma_f^2 + \sigma_s^2 + \sigma_e^2 + \sigma_{st}^2}, \tag{5.3}$$

Testing different combinations of line ratios

While using absolute line fluxes as constraints does not require combining the constraints in any particular way, using line ratios instead implies that lines are combined two by two in an arbitrary way. Part of the numerous tests I performed during my work was to understand how the model solutions depend on the choice of line ratios used, and whether an optimal set of line ratios can be found.

In general, in order to tie the ratios together, some lines need to be used in more than one ratio. The selection of lines for each ratio was thus optimized to avoid giving too much importance to any one line (i.e., by having one line used in too many ratios), but also, when possible, to combine lines that were observed with the same instrument (in order to minimize uncertainties due to instrumental effects) or that belong to the same element (in order to minimize uncertainties due to the elemental abundance).

In order to illustrate the effect that choosing different sets of line ratios has on finding the model solutions, I use the *Central main zone* because of the large signal-to-noise ratio and because all of the MIR and FIR tracers are available (except [NII] 121.9 μm due to incomplete maps). In the following I compare the solutions obtained with two sets of line ratios:

1.
   - [ArIII] 8.9 μm/[ArII] 6.9 μm ,
   - [NeIII] 15.5 μm/[NeII] 12.8 μm ,
   - [SIV] 10.5 μm/[SIII] 33.5 μm ,
   - [SIII] 33.5 μm/[NeII] 12.8 μm ,
   - [SIII] 33.5 μm/[SIII] 18.7 μm ,
   - [NeIII] 15.5 μm/[OIII] 88.4 μm ,
   - [SIV] 10.5 μm/[OIII] 88.4 μm ,
   - and [SIII] 18.7 μm/[ArIII] 8.9 μm .
2.
   - [ArIII] 8.9 μm/[ArII] 6.9 μm ,
   - [ArIII] 8.9 μm/[NeII] 12.8 μm ,
   - [SIV] 10.5 μm/[NeII] 12.8 μm ,
   - [NeII] 12.8 μm/[OIII] 88.4 μm ,
   - [NeIII] 15.5 μm/[NeII] 12.8 μm ,
   - [SIII] 33.5 μm/[SIII] 18.7 μm ,
   - [SIII] 33.5 μm/[NeIII] 15.5 μm ,

- [SIII] 18.7 μm/[SIV] 10.5 μm ,
- and [ArIII] 8.9 μm/[SIV] 10.5 μm .

In set number 1, three line ratios depend mostly on the ionization parameter and four depend mostly on the density. Hence, we hope to avoid over-representing one specific parameter although the way in which the constraints should be chosen to probe the parameter space in an optimal way is extremely difficult to set up. However this set does not include the subset of line ratios available for the clump analysis. The set number 2 includes some of the same ratios either because they have small uncertainties or because they are known to trace a physical parameter (e.g., the [SIII] line ratio, the [ArIII]/[ArII]) and it includes the subset of line ratios available for the clump analysis, thus the results at the different scales can be comparable. In order to compare the model solutions found with the different sets of ratios, I used probability distribution function (PDF), which, for each physical parameter, is calculated as:

$$PDF(p) = \sum_{i,p} e^{-\frac{\chi^2_{i,p}}{2}}, \tag{5.4}$$

where the sum is performed over all of the models for which the parameter value is p. Figures 5.9 and 5.10 show the PDFs of each parameter individually and the 2D PDFs for each pair of parameters. The 2D PDFs are useful in that they may highlight a degeneracy between parameters, and also because it is possible to identify other solutions (i.e., other local χ^2 minima) in the parameter space.

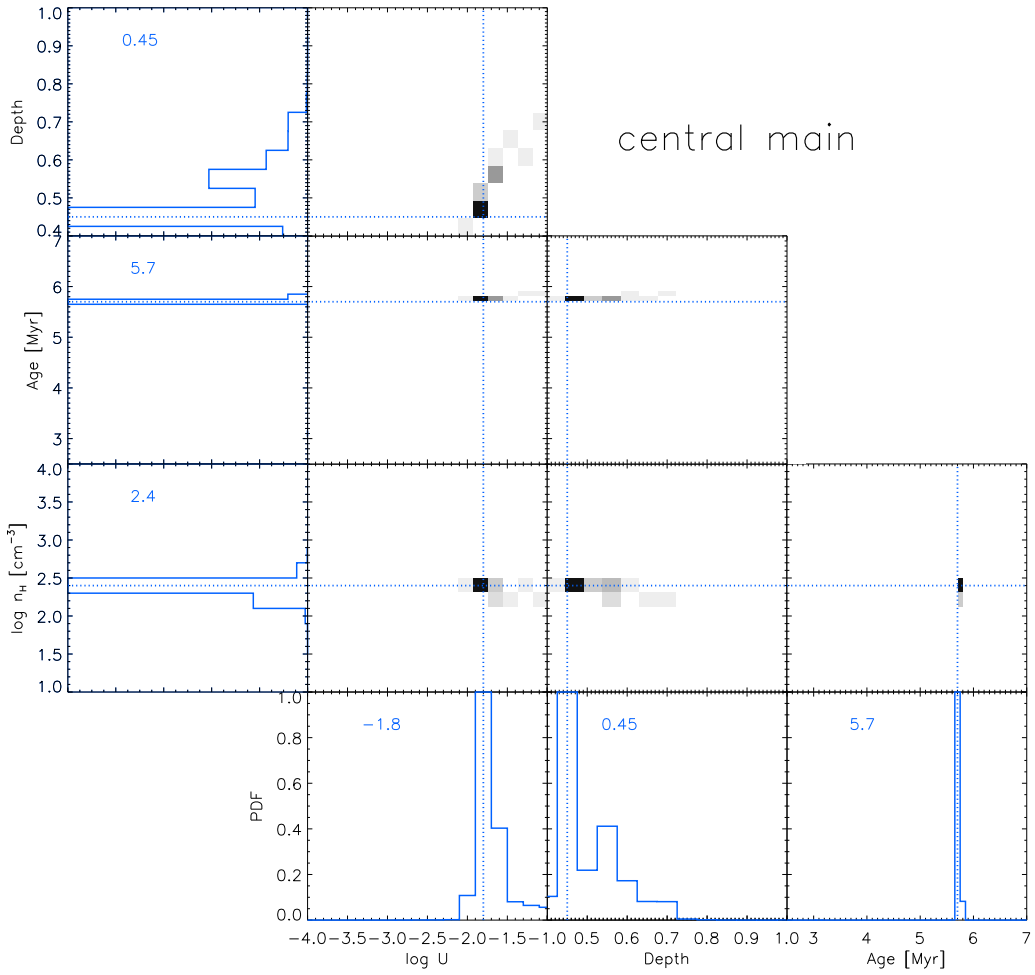

Figure 5.9: PDFs for n_H, log U, t_{burst} (age), and physical depth for the *Central main zone* with the line ratio method, set number 1. The blue histograms show the PDF for each single parameter. The 2D PDFs are shown as density plots (black ∼1, to white ∼0) at the intersection between two parameters. The blue horizontal and vertical lines indicate the parameter value corresponding to the best model solution, with the corresponding parameter value given in blue.

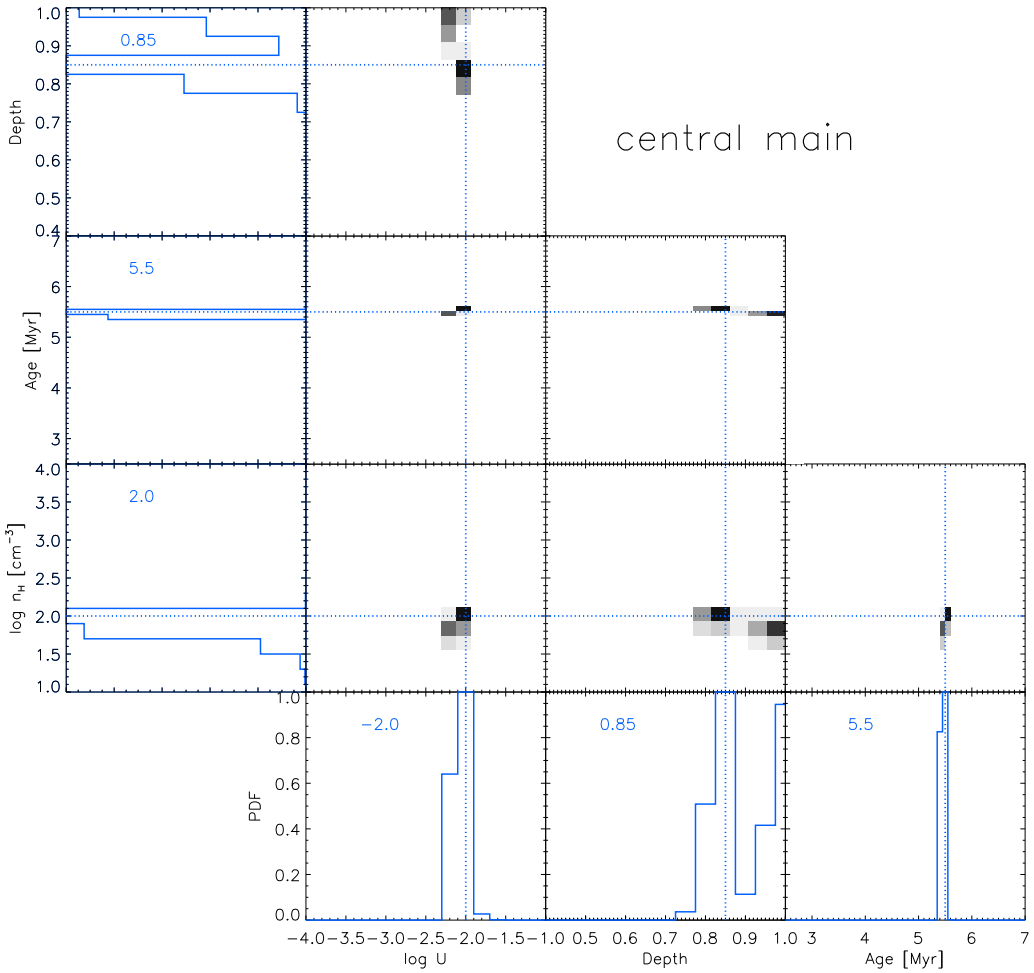

Figure 5.10: PDFs for the *Central main zone* with the line ratio method, set number 2. See Figure 5.9 for the plot description.

Although the same lines are used in the two sets of line ratios, they are combined in different ways. This results in a different χ^2 distribution, as can be seen in Figures 5.9 and 5.10. In both cases, a well-defined peak is shown, corresponding to the lowest χ^2 value. However, the best solution found for all parameters differs significantly based on which set of line ratios

was used. Even the density parameter shows a discrepancy, despite the fact that the density-sensitive [SIII] line ratio is used in both sets. Hence, one can see that a bias is being induced simply through the choice of line combinations as constraints. As explained in Section 5.3.3, the other method, using absolute line fluxes, circumvents the arbitrary choice of combining the lines and simply considers the available list of lines as possible constraints. This does not mean that a bias does not exist for the absolute line fluxes method, since the contribution of each line may skew or even shift the χ^2 distribution in the parameter space. However, this is the most straighforward way to use the available observational constraints if the parameters cannot be determined using specific line combinations (Section 5.3.1). It is possible that an iterative process may provide better results, with the following steps (1) the available line fluxes are used as constraints, (2) the way each parameter depends on each constraint is examined, (3) the constraints are given more or less weight in order to constrain simultaneously and evenly all the parameters, i.e., without one parameter dominating the χ^2 variations. Investigating such a process was beyond the scope of my present work.

Despite my tests showing that the **line ratio method** induces significant biases in the model solution, this method is often used and it seems natural to look for the best possible application. In other words, there may be an optimal choice of line ratios to probe the parameter space. In the following I present the solutions obtained with the line ratio method, with sets of line ratios that were optimized. Later on in Section 5.3.3, I will compare results obtained this way to the results with the **absolute flux method**.

Clump analysis

For the investigation of the clump properties (clumps defined in Section 5.2.1), [NII] 121.9 μm was not considered because of the incomplete PACS maps (Section 3.1). In a first iteration, I also omitted the lines observed in the IRS LL module ([SIII] 18.7 μm,[SIII] 33.5 μm and [NeIII] 15.5 μm) because the spatial resolution is too low to reliably decompose the clumps unless the clump position and size are fixed (Section 5.2.2). Hence, based on the available tracers, I chose the following ratios as constraints:

- [ArIII] 8.9 μm/[OIII] 88.4 μm,
- [ArIII] 8.9 μm/[SIV] 10.5 μm,
- [SIV] 10.5 μm/[NeII] 12.8 μm,
- [NeII] 12.8 μm/[OIII] 88.4 μm

- and [ArIII] 8.9 μm/[ArII] 6.9 μm.

This makes 5 line ratios (not independent) to constrain 4 physical parameters. These ratios all depend on more than one physical parameter in the model (Section 5.3). However, among these ratios, [ArIII] 8.9 μm/[ArII] 6.9 μm is the only constraint on the fraction of the ionized gas that is matter- vs. radiation-bounded (which we trace indirectly with the depth parameter in our models). This is because [ArII] 6.9 μm is the best available tracer of the ionization front (Section 4.3.2). I performed some tests with the additional constraints provided by the [SIII] line ratio but the results were not changed, mostly because of the large uncertainties in the clump decomposition in the LL maps (Section 5.2.2).

Overall, we find that the models have trouble to reproduce all of the line ratios of the clumps within their 1σ uncertainty and the minimum χ^2 values are accordingly quite large (see Table 5.3). As an illustration, Figure 5.11 shows the behavior of the selected line ratios (left panel) and the χ^2 distribution (right panel), in the parameter space $\log U$ vs. $\log n_H$ for the clump in the *Central* $c2$. As discussed previously (Section 5.3.1), this could be due to nu-

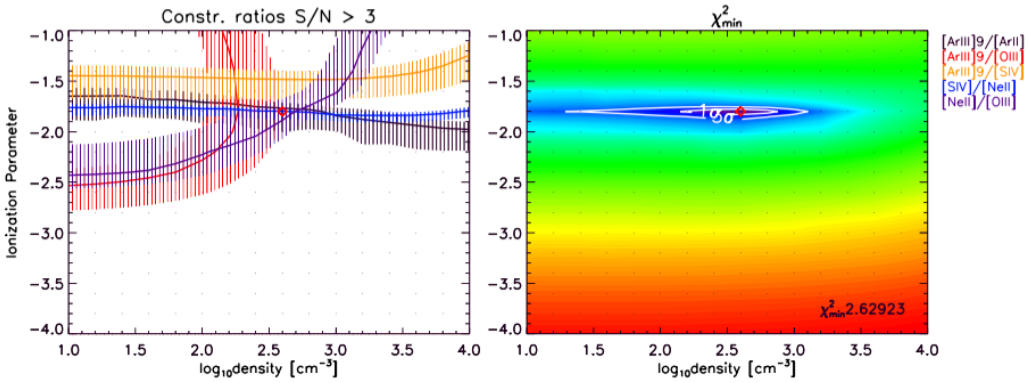

Figure 5.11: *Left*: The observed line ratios (solid lines) are plotted in the model parameter space $\log U$ vs. $\log n_H$ for the clump *Central* $c2$ with the line ratio method. The filled area represents the 1σ uncertainties. All of the line ratios have a signal-to-noise ratio (S/N) larger than 3. Many such plots exist for each set of physical depth and starburst age parameters, but for clarity we only show here the plot for the best solution. *Right*: χ^2 distribution in the parameter space. The white contours indicate 1σ and 3σ error bars, while the number on the bottom right is the minimum χ^2 across the entire model grid. For both plots, the red diamond shows the best solution and the small black dots represent the grid of model parameters.

merous caveats related to the atomic data, to the observations, to the model

hypotheses or to the set of line ratios selected to explore the parameter space. For instance, it is natural to question whether the model should consist of a single ionized gas phase with a given density, rather than by a combination of at least two phases (e.g., a dense phase associated with ionized gas filaments in HII regions and a more diffuse gas pervading over large scales). Indeed, Cormier et al. (2012) have demonstrated that an additional low-ionization component is necessary to reproduce the observed [NeII] 12.8 μm emission in the global study of the starburst galaxy Haro 11. This seems to be consistent with the morphology of the [NeII] 12.8 μm emission in IC 10 compared to the other tracers (Section 3), with [NeII] 12.8 μm showing more prominent extended components. In our suite of lines, [OIII] 88.4 μm is another line that may arise from a highly-ionized low-density ($10 - 100\,\mathrm{cm}^{-3}$) gas, as observed in several HII regions in the Large Magellanic Clouds (Lebouteiller et al. 2012 and Kawada et al. 2011). Note that a large-scale underlying emission component, presumably relatively more diffuse, was subtracted when disentangling the clumps (Section 5.2.2). The clouds that I modeled should therefore correspond to the denser structures associated with the HII regions in the central and arc regions. Nevertheless, it is plausible that several phases or one phase with a distribution of its parameters around their mean value (e.g., a probability distribution function of densities) should be considered, even at the spatial scale of clumps and even with the large-scale underlying emission component subtracted. In practice, implementing two phases or more complex parameter distributions was not possible for the clump analysis because of the limited number of constraints and increasing number of model parameters to fit.

Overall, the PDFs show well-defined peaks and there is good agreement between the best model parameters (lowest χ^2; shown as blue lines in the PDFs) and the peaks of the PDFs. This is an interesting finding, considering that the best models may not have been deemed satisfactory, notably because of the large χ^2 (Table 5.3) and the inability to reproduce all of the line ratios at once.

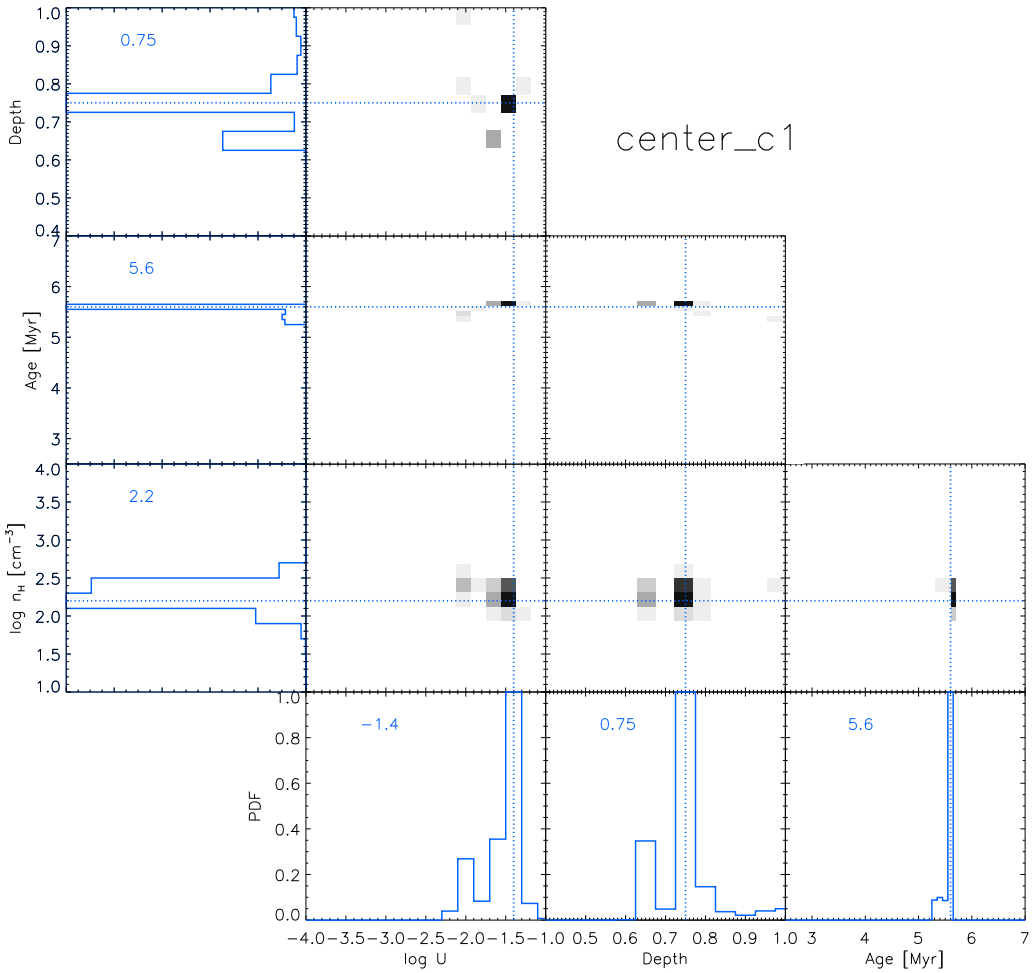

Figure 5.12: PDFs for the clump *Center c*1 with the line ratio method. See Figure 5.9 for the plot description.

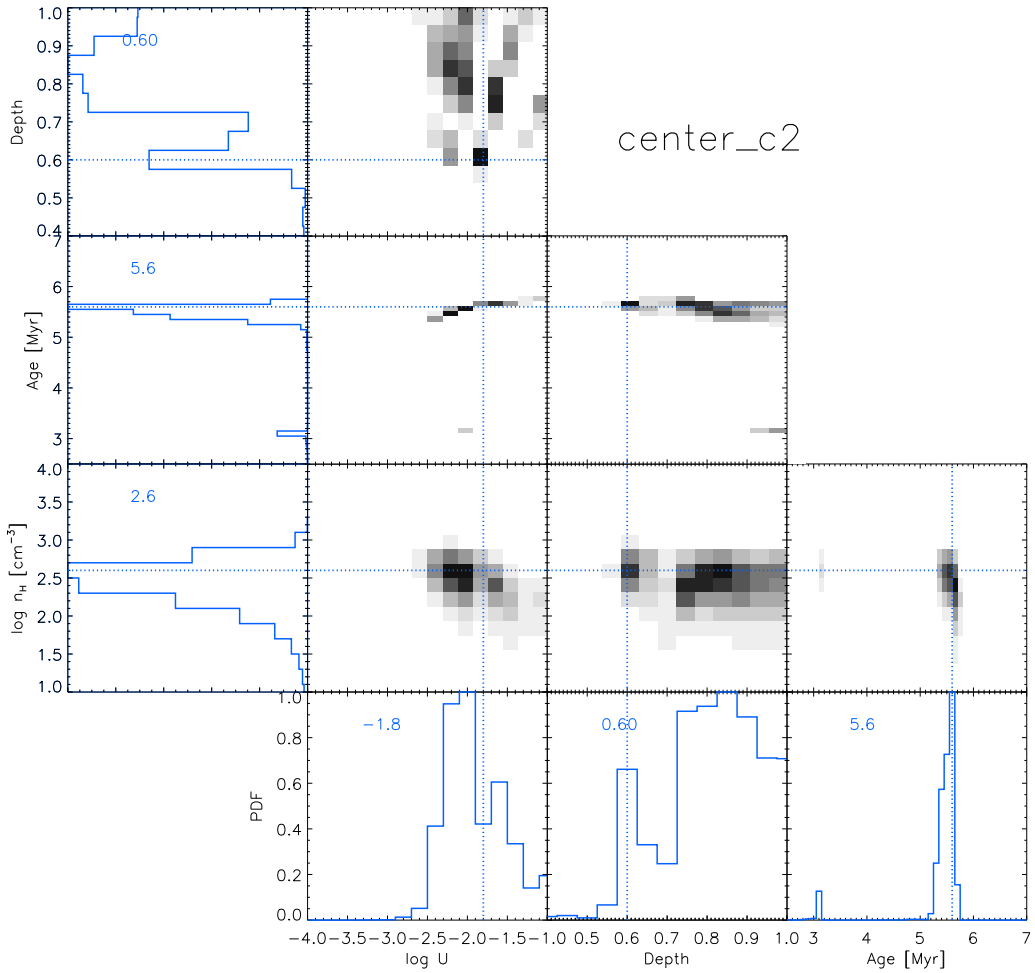

Figure 5.13: PDFs for the clump *Center c2* with the line ratio method. See Figure 5.9 for the plot description.

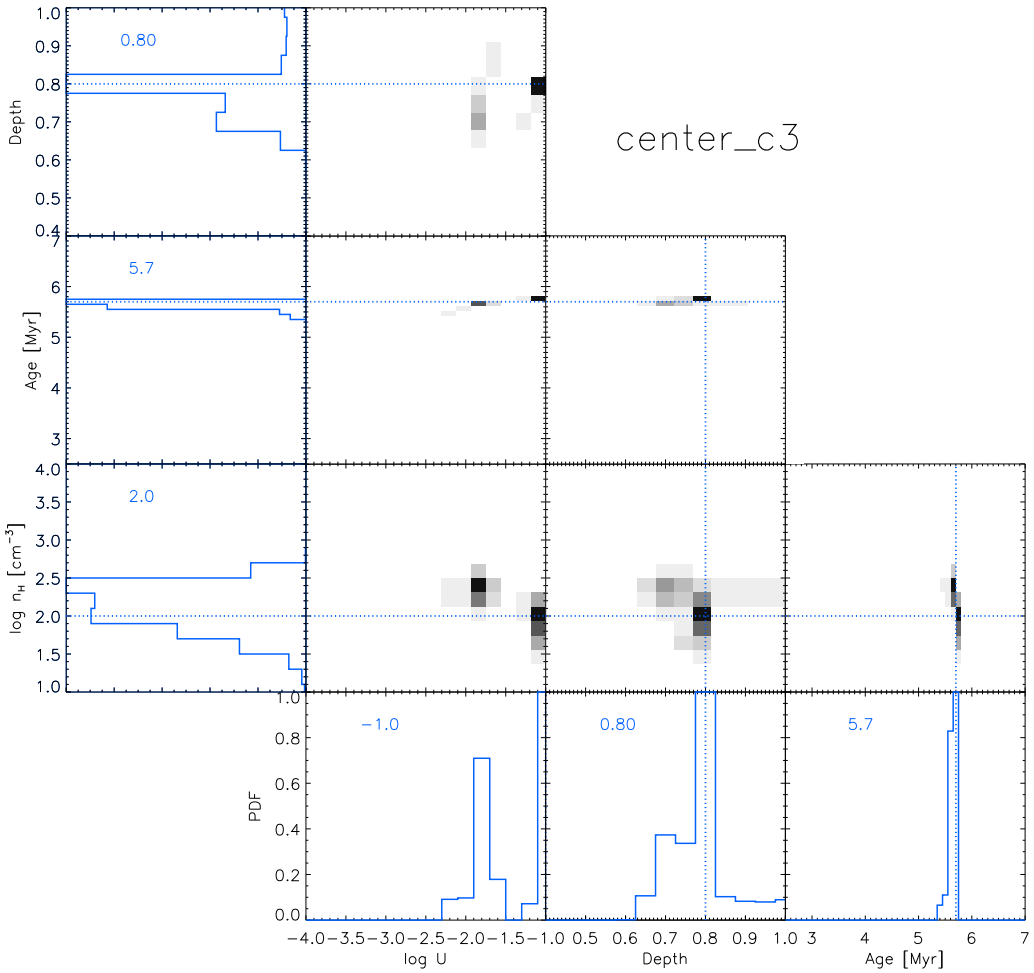

Figure 5.14: PDFs for the clump *Center c*3 with the line ratio method. See Figure 5.9 for the plot description.

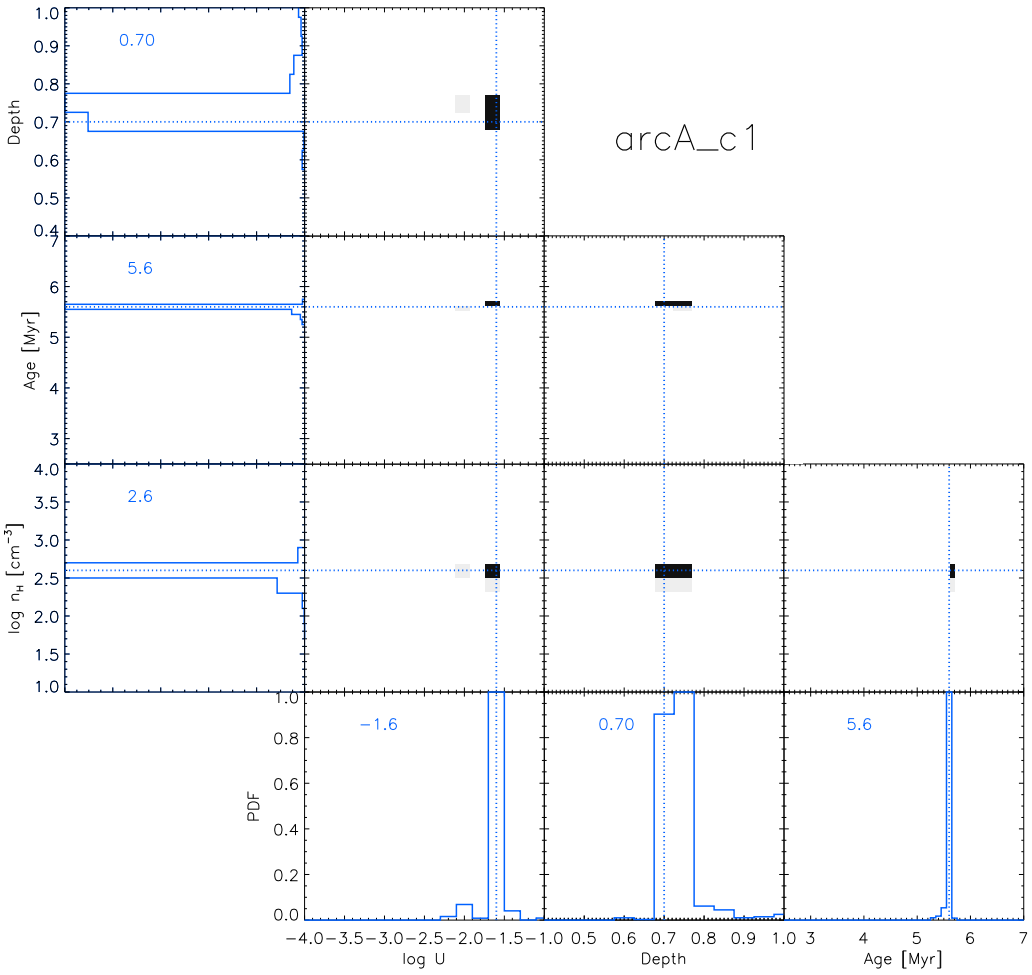

Figure 5.15: PDFs for the clump *ArcA c*1 with the line ratio method. See Figure 5.9 for the plot description.

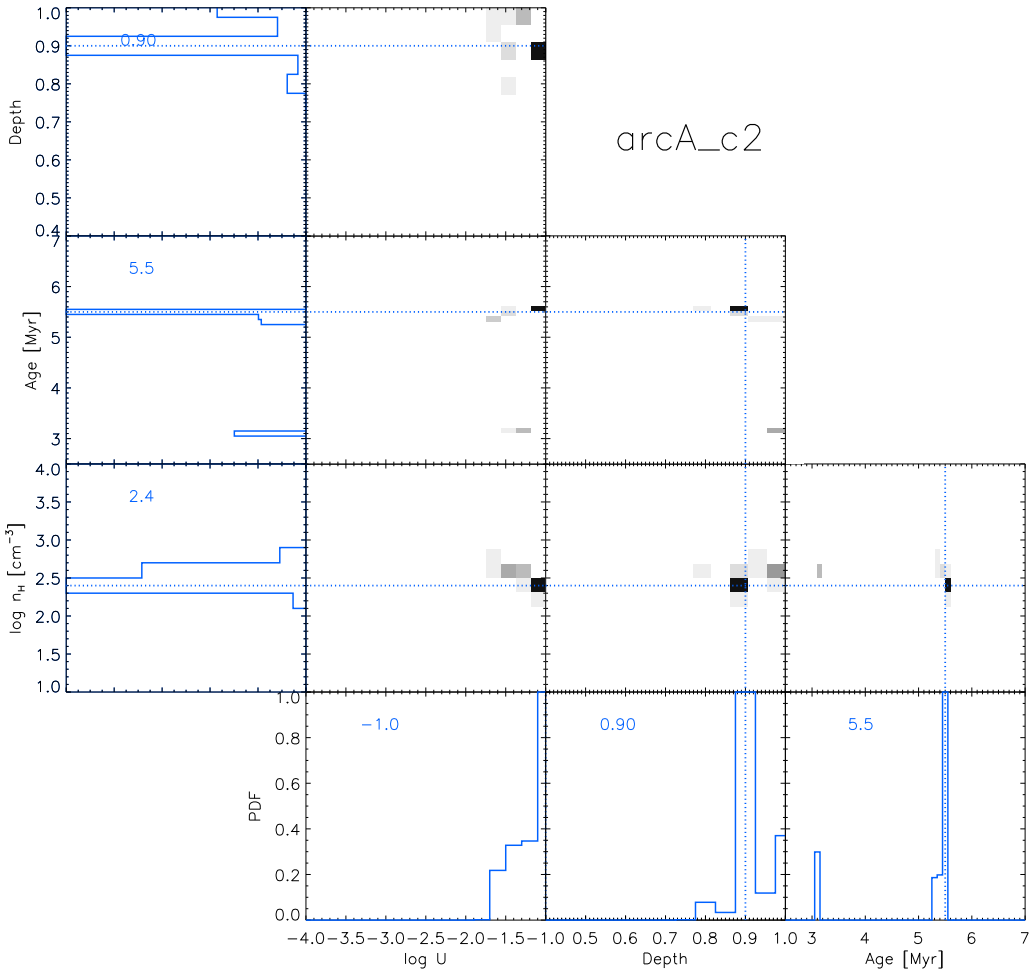

Figure 5.16: PDFs for the clump *ArcA c2* with the line ratio method. See Figure 5.9 for the plot description.

A more detailed analysis of the PDFs reveals a certain level of degeneracy between some parameters, especially between $t_{\rm burst}$ and the ionization parameter U, in particular for the clump *Center c2* (Figure 5.13). For clump *Center c2*, the PDFs are rather broad, which is probably due to the fact that it is a relatively faint clump lies between two brighter ones. The PDFs for clump *ArcA c2* are particularly narrow. However, the large χ^2 values (even for the best solution; Table 5.3), suggests that the results for this clump should be regarded with caution.

To estimate the uncertainties on the parameters for the best solution, I considered all models with a χ^2 below the threshold given by $\chi^2_{\rm min} + \Delta\chi^2$, where $\Delta\chi^2 = 4.7$ is the 1σ confidence interval with four free parameters (Press et al. 1992), i.e., n_H, log U, t_{burst}, and physical depth. The uncertainties are given by the lower and upper bounds of the 1σ confidence distributions. The histograms of the parameter distributions are shown in Figure 5.17 and in Figure 5.18, while Table 5.3 summarizes the solutions. Note that the corresponding histograms are not PDFs but simply statistical histograms of the number of models below the χ^2 threshold for each parameter.

Table 5.3: Results of the best model parameters with 1σ uncertainties for each clump for the line ratio method.

Clump	t_{burst} [Myr]	log U	log n_H [cm^{-3}]	depth	$\chi^2_{min,red}$
Cent. c1	$5.6^{+0.0}_{-0.0}$	$-1.4^{+0.2}_{-0.0}$	$2.2^{+0.2}_{-0.2}$	$0.75^{+0.00}_{-0.10}$	7.7
Cent. c2	$5.6^{+0.1}_{-2.5}$	$-1.8^{+0.8}_{-0.6}$	$2.6^{+0.2}_{-1.0}$	$0.60^{+0.40}_{-0.00}$	2.6
Cent. c3	$5.7^{+0.0}_{-0.1}$	$-1.0^{+0.0}_{-0.8}$	$2.0^{+0.6}_{-0.4}$	$0.80^{+0.00}_{-0.15}$	13.7
ArcA c1	$5.6^{+0.0}_{-0.0}$	$-1.6^{+0.0}_{-0.0}$	$2.6^{+0.0}_{-0.2}$	$0.70^{+0.10}_{-0.00}$	20.1
ArcA c2	$5.5^{+0.0}_{-2.4}$	$-1.0^{+0.0}_{-0.4}$	$2.4^{+0.2}_{-0.0}$	$0.90^{+0.10}_{-0.00}$	45.3

In some cases, no error bar is reported because the error is lower than the step in the parameter grid.

Overall, the histograms indicate that the density is fairly well constrained, with values between 100 to 400 cm^{-3}. Values are in agreement with the results obtained by López-Sánchez et al. (2011) on their analysis of the area that correspond to *Center c1* of this work. As an additional estimate of the density, independent from the modeling, I used the high spectral resolution IRS pointings that give us access to the ratio [SIII] 33.5 μm/[SIII] 18.7 μm (Section 2.2.4). Since the high-resolution observations are pointings with relatively small apertures, there is no spatial information. Hence, I could use these observations only for those clumps that coincide with the positions of the pointings: *Central c3*, *ArcA c1*, and *ArcA c2*, with estimated densities of

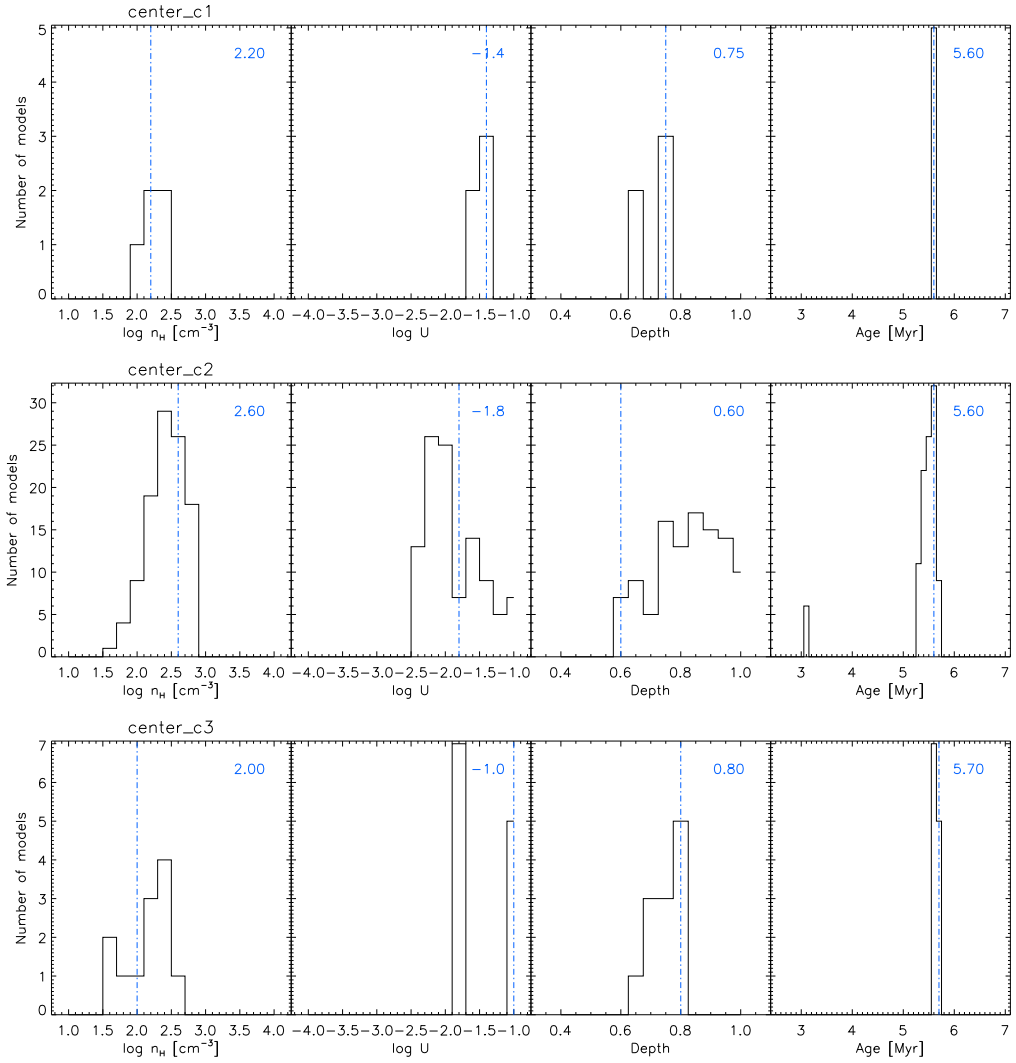

Figure 5.17: Histograms of the distribution of the parameters for the clumps *Center c*1, *Center c*2 and *Center c*3 with the line ratio method. The blue vertical line represents the parameter value corresponding to the best model solution, with the corresponding parameter value given in the top-right corner.

$10^{2.1}$, $10^{2.5}$ and $10^{2.5}$ cm^{-3}, respectively. These results are compatible, within the uncertainties, with the values that I found with the model grids using IRS SL and [OIII] as constraints. This confirms independently that at least some parameters (in this case the density) can be well constrained by our method even though the best solutions have large χ^2 values. It is likely that large χ^2 values are driven by line ratios that probe other parameters, or, in

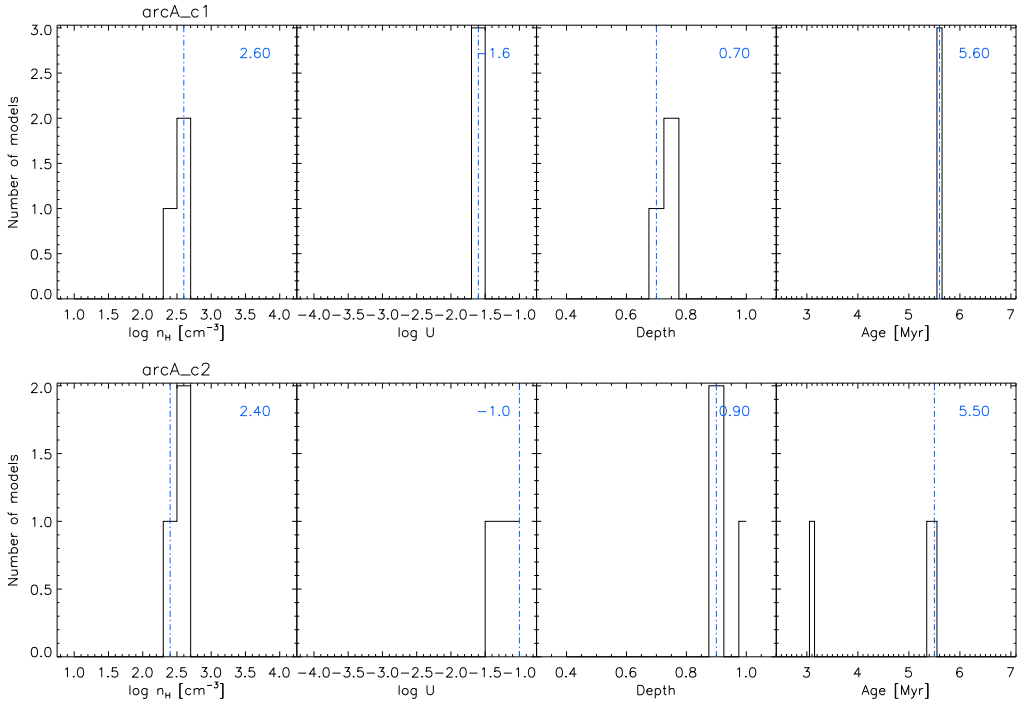

Figure 5.18: Histograms of the distribution of the parameters for the clumps *ArcA c*1 and *ArcA c*2 with the line ratio method. See Figure 5.17 for the plot description.

general, a different zone in the parameter space, with little impact on the density parameter determination.

The starburst age is globally well constrained and found identical for all clumps ($\approx$ 5.6 Myr). Recall that the hypothesis of an instantaneous burst was assumed, and the mere fact that we do observe bright HII region tracers already suggested that the burst age should be between 3 and 6 Myr because younger clusters are still embedded and older clusters have fewer ionizing photons (see Chapter 6 for a discussion).

The log of the ionization parameters, log U, ranges between -1.8 and -1, which are exceptionally large values. This parameter is less well constrained, for some of the clumps, and the degeneracy between the ionization parameter and other parameters (in particular the depth and the starburst age) is investigated in the following. A lower ionization parameter can be found for a younger age and/or a smaller depth parameter.

The physical depth is calculated as a fraction of the total depth of a radiation-bounded cloud (i.e., 1 corresponds to the ionization front). The

results show that most clumps are not completely radiation-bounded, which can be seen either as one cloud around the stellar cluster being matter-bounded (with a depth between 0.6 and 1), or some fraction of the clouds covering the stellar cluster being matter-bounded and some fraction being radiation-bounded (the calculation of the corresponding fraction is not trivial; see Chapter 6).

Zone analysis

I use the following line ratios:

- [ArIII] 8.9 μm/[ArII] 6.9 μm ,
- [ArIII] 8.9 μm/[NeII] 12.8 μm ,
- [SIV] 10.5 μm/[NeII] 12.8 μm ,
- [NeII] 12.8 μm/[OIII] 88.4 μm ,
- [NeIII] 15.5 μm/[NeII] 12.8 μm ,
- [SIII] 33.5 μm/[SIII] 18.7 μm ,
- [SIII] 33.5 μm/[NeIII] 15.5 μm ,
- [SIII] 18.7 μm/[SIV] 10.5 μm ,
- and [ArIII] 8.9 μm/[SIV] 10.5 μm .

This makes 9 line ratios (not independent) for 4 free model parameters. Not only do I have more line ratios than for the clump analysis (which was limited to [OIII] 88.4 μm and the IRS SL tracers), but I am now able to use the [SIII] line ratio directly, which traces the gas density, in the calculation of the best model. For the zone analysis, some line ratios have a S/N<3 (Table 5.1), I decided to exclude them for the calculation of the best model. The results of the zone analysis are reported in Table 5.4.

For the *Central main zone* , I could use all line ratios because their S/N is >3. However, it was not possible to find a unique solution that agrees with all of the line ratios with their 1σ uncertainties, and the best model shows a large χ^2 value. This result is similar to what is obtained with the clump analysis, and it is even exaggerated. Adding more constraints simply increases the problem in finding a satisfactory solution. As for the clump analysis, it seems natural to attribute this inability to find a good solution in the overall parameter space to the restricted model hypotheses. In other words, the tracers used imply a more complex topology or distribution of physical conditions (e.g., assumption of a single density) than what the model initially assumes. Most importantly, I am now using the emission of zones that are much larger than the clumps: while I was able to isolate the clump emission from the large-scale underlying emission component, the zones measurements integrate regions with a variety of physical properties.

Despite these considerations, and as for the clump analysis, we can examine individual parameters using the PDFs and the histograms of the best

solutions in terms of $\Delta\chi^2$. The PDFs and histograms of the parameter distributions for the *Central main zone* are shown in Figure 5.19. In this figure one can see that all of the model parameters are well constrained. The density is about 100 cm^{-3}, which is a few times lower than the densities measured in the individual clumps within this zone ($\geq 100\,\mathrm{cm}^{-3}$). Similarly, the ionization parameter value is lower than for the clumps. These results seem to indicate that in low-metallicity environment the solution, *when using the line ratio method* and when integrating the measurement over a large spatial scale, tend to favor a more diffuse gas located further away from the ionizing sources. The emission from this diffuse gas is significant enough to change the solution from the clumps to the region, indicating that the emission from the clumps does not outshine completely that of the diffuse gas.

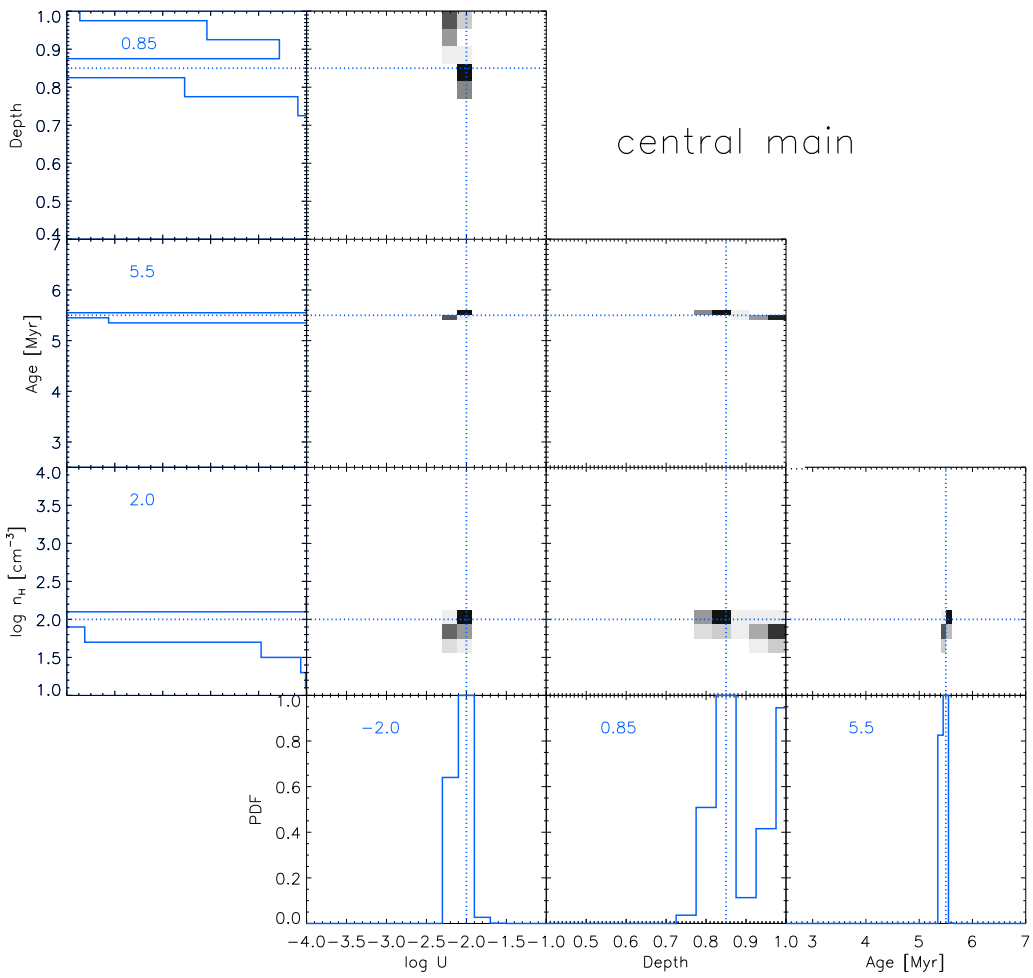

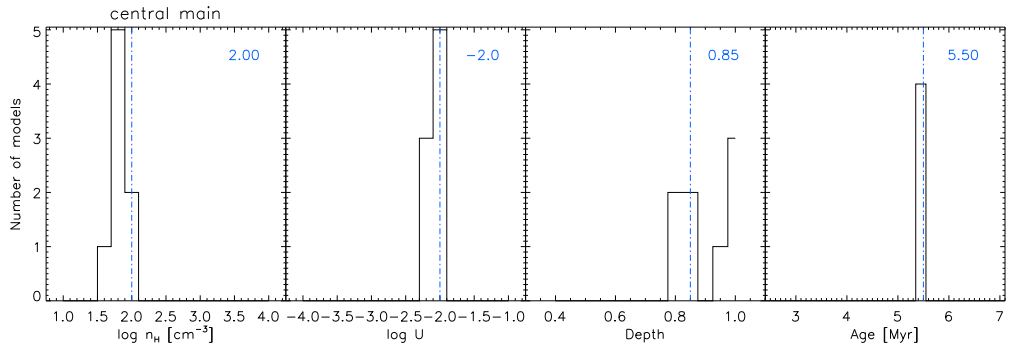

Figure 5.19: Results for the *Central main zone* with the line ratio method. *Top*: PDFs, see Figure 5.9 for the plot description. *Bottom*: Histograms of parameter distributions for the best models (see text for details).

The results for the other zones are shown in Figures 5.20 to 5.26. In the case of the *Central north* zone, the density is not well determined, despite the use of various density-sensitive ratios. This result is also seen, to a lesser extent, for a few other zones. This suggests that such zones may benefit from more complex modeling with different ionized gas components. For the *ArcB* and *West* zones, only a few ratios are available with sufficient S/N, and these ratios mostly trace the ionization parameter and the starburst age. Accordingly, other parameters (density, physical depth) are not well determined. The degeneracy in some parameters is evident in the faintest zone (in particular, ionization parameter vs. starburst age; e.g., Figure 5.25).

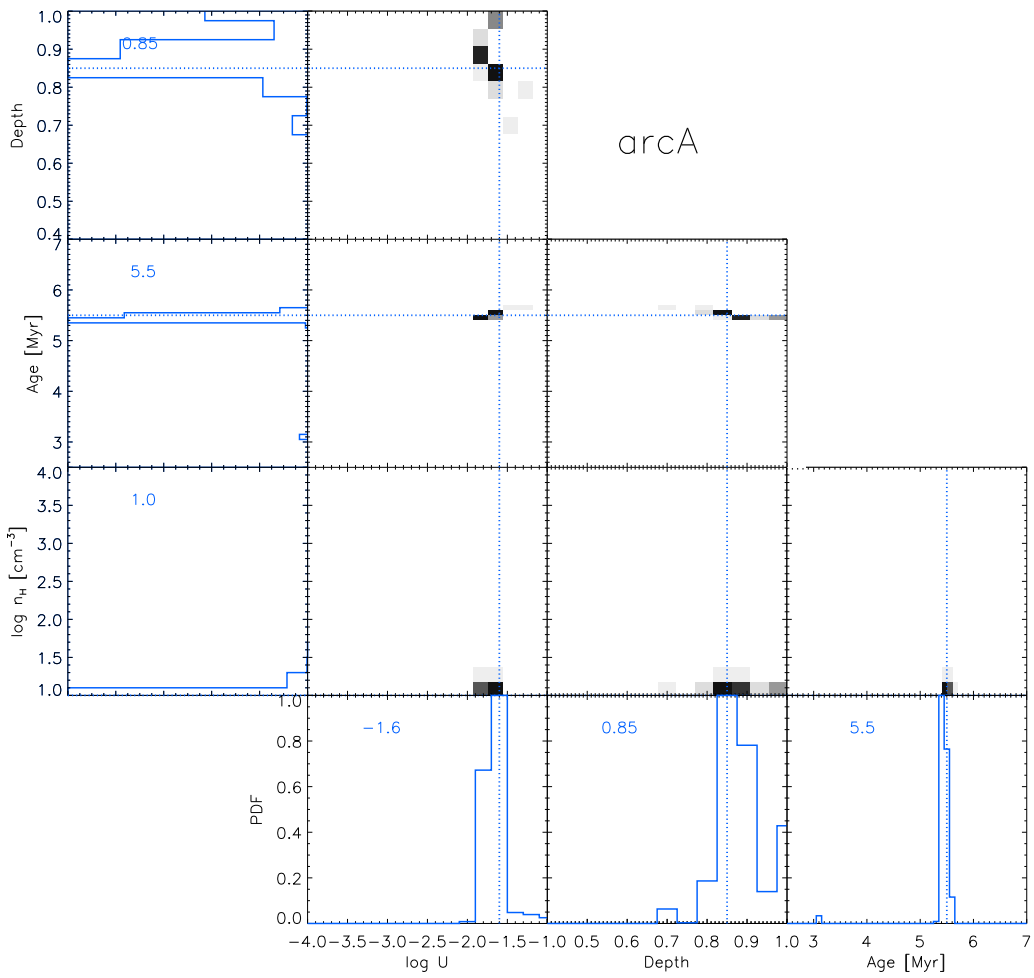

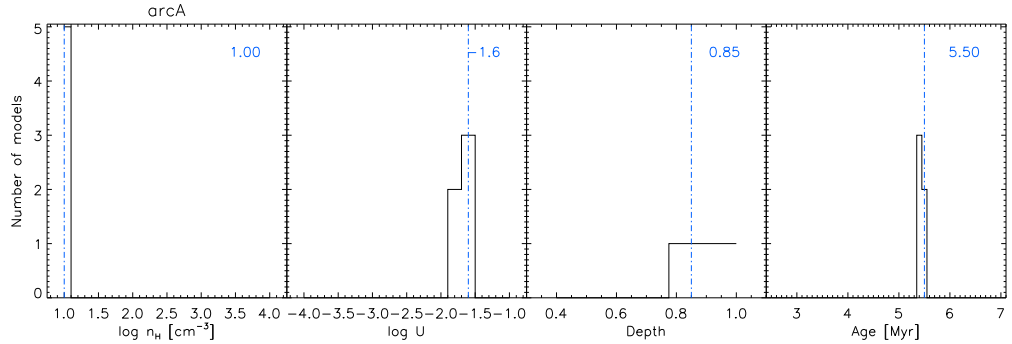

Figure 5.20: Results for the *ArcA* zone with the line ratio method. *Top*: PDFs, see Figure 5.9 for the plot description. *Bottom*: Histograms of parameter distributions for the best models (see text for details).

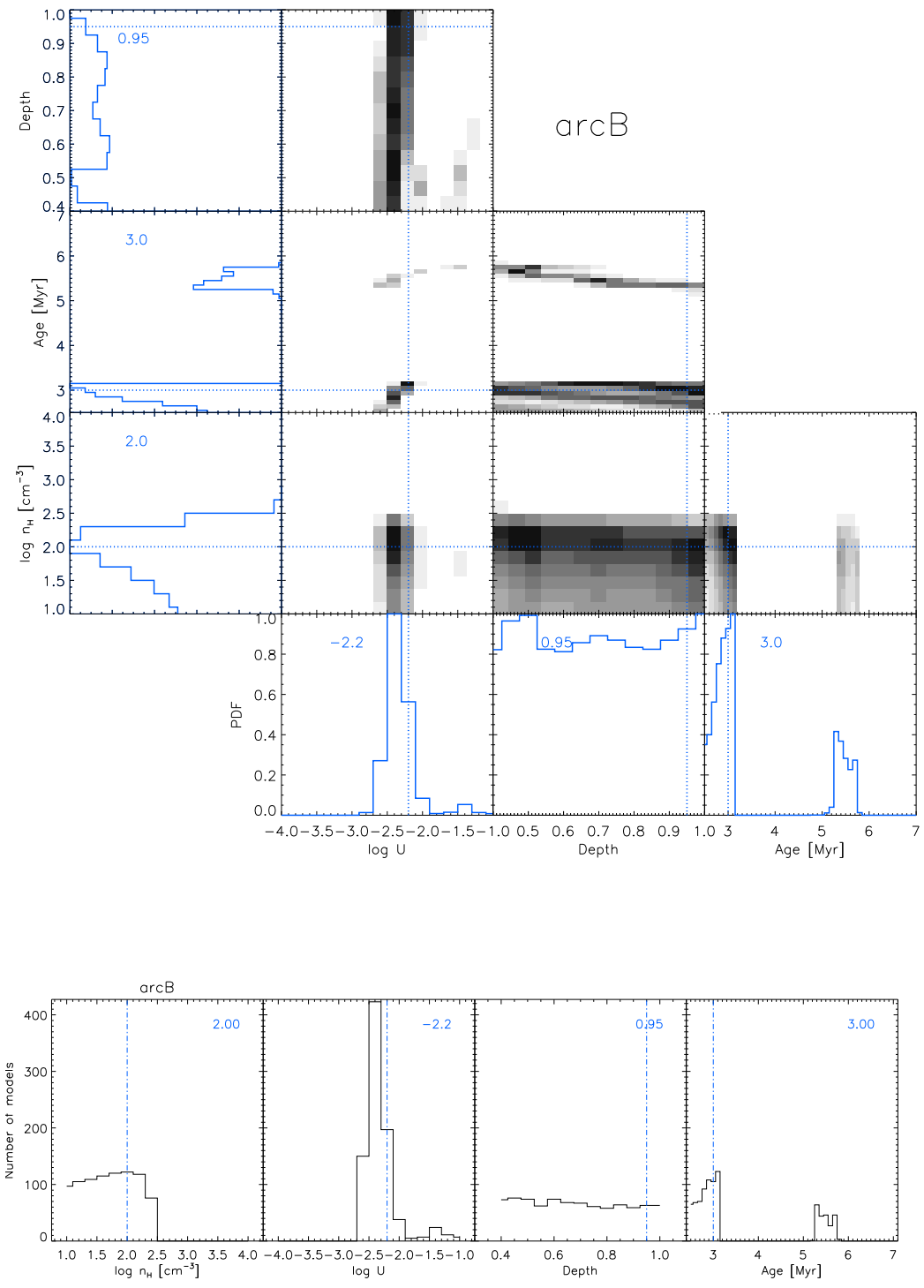

Figure 5.21: Results for the *ArcB* zone with the line ratio method. *Top*: PDFs, see Figure 5.9 for the plot description. *Bottom*: Histograms of parameter distributions for the best models (see text for details).

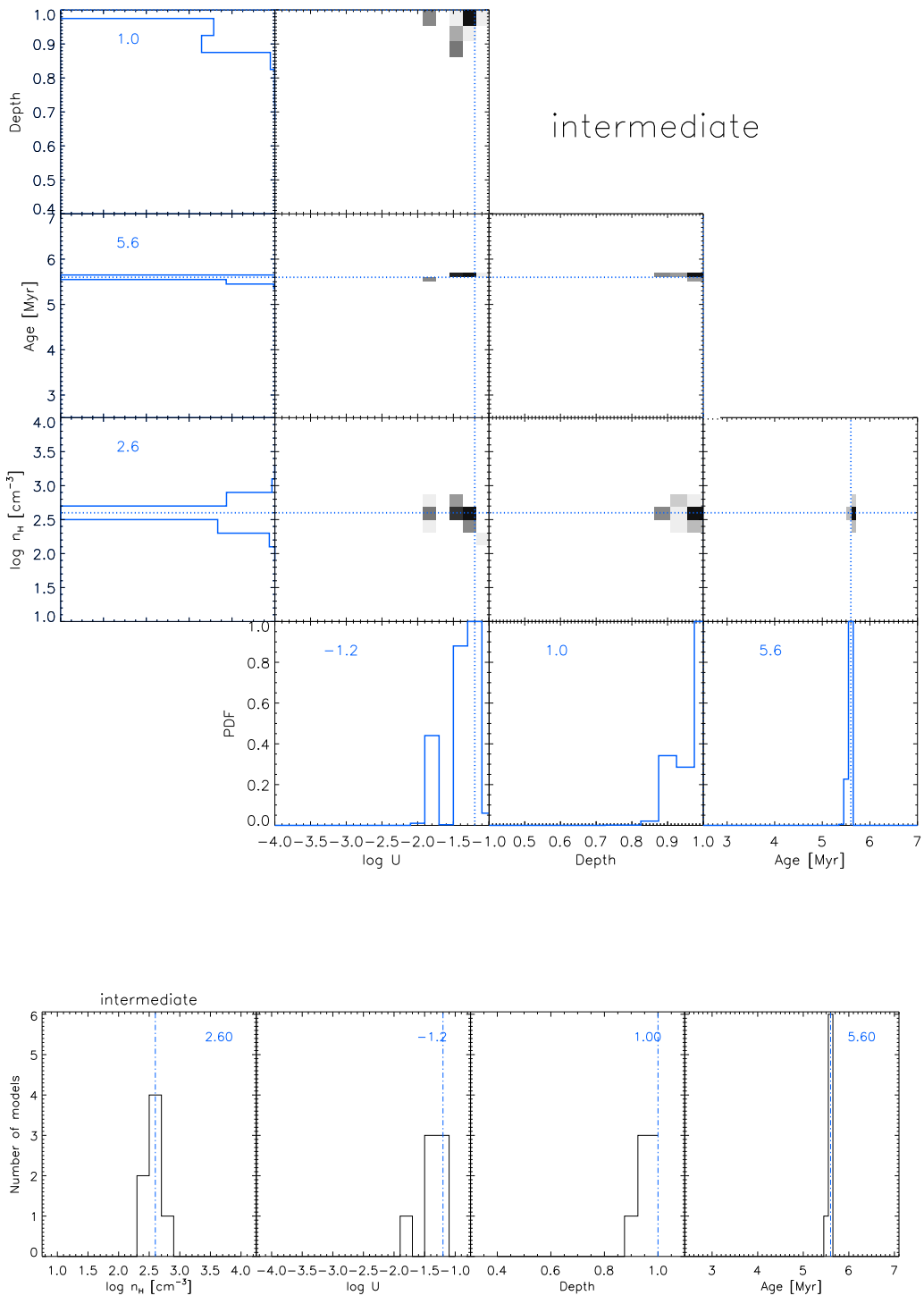

Figure 5.22: Results for the *Intermediate* zone with the line ratio method. *Top*: PDFs, see Figure 5.9 for the plot description. *Bottom*: Histograms of parameter distributions for the best models (see text for details).

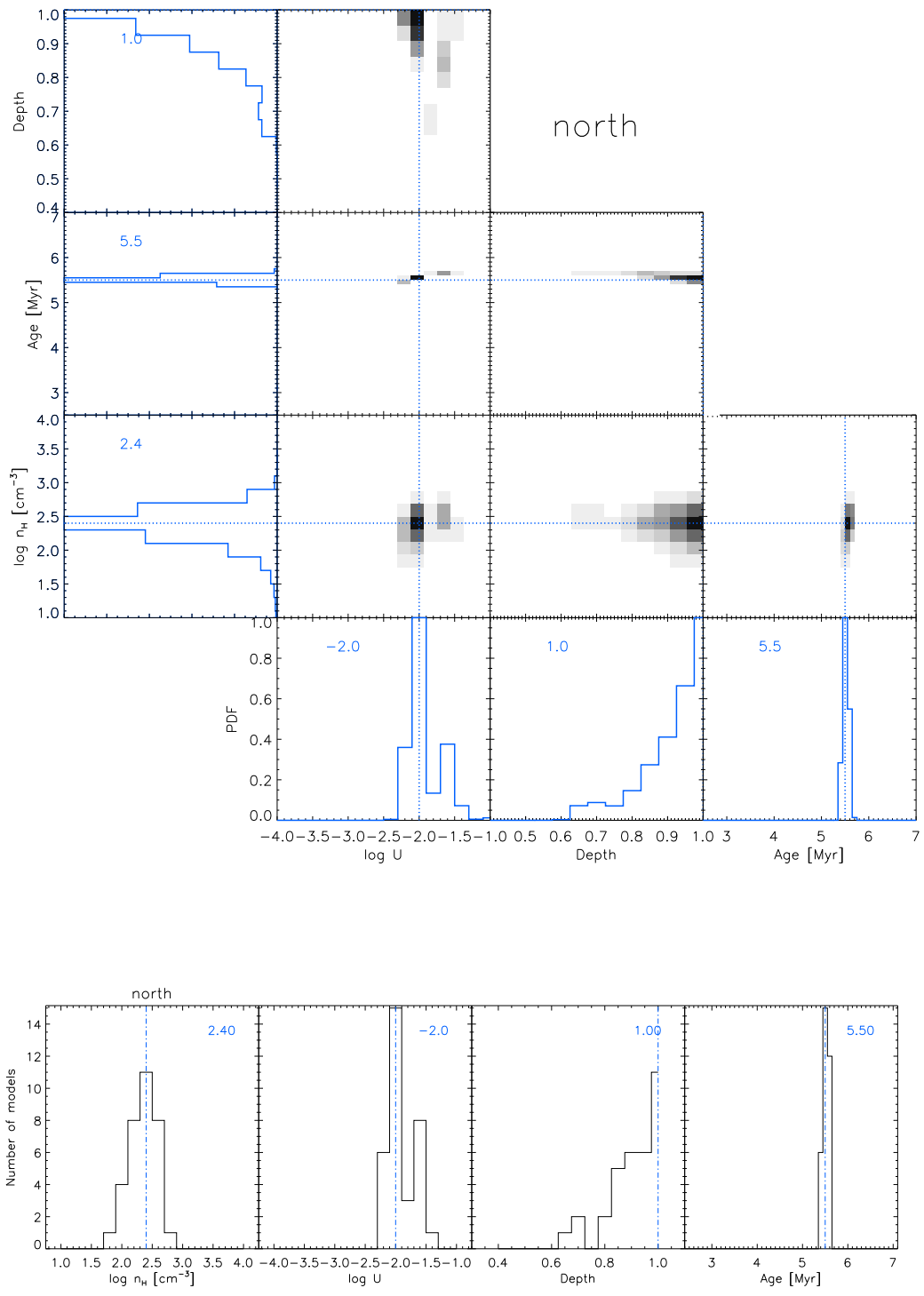

Figure 5.23: Results for the *Central north* zone with the line ratio method. *Top*: PDFs, see Figure 5.9 for the plot description. *Bottom*: Histograms of parameter distributions for the best models (see text for details).

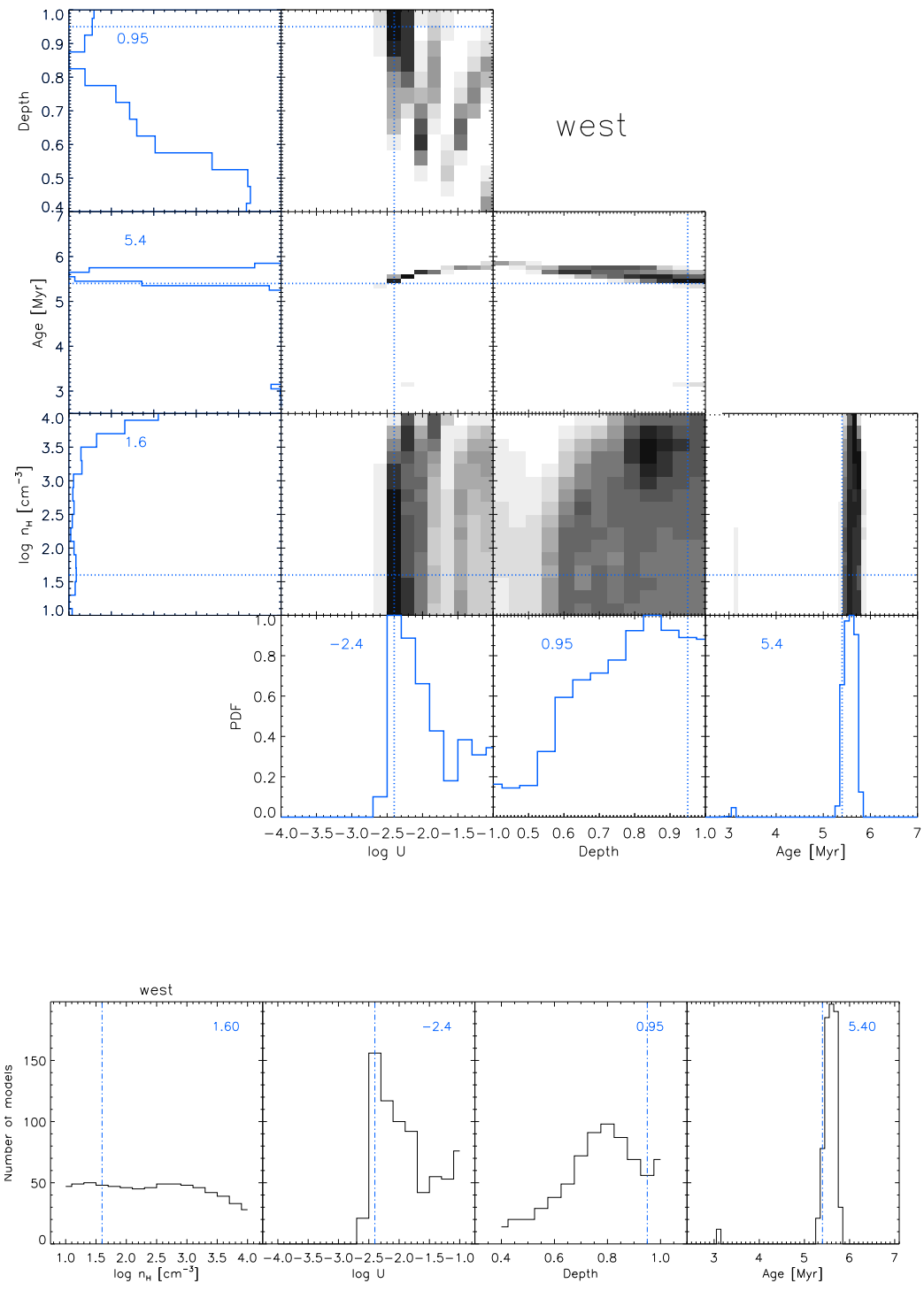

Figure 5.24: Results for the *West* zone with the line ratio method. *Top*: PDFs, see Figure 5.9 for the plot description. *Bottom*: Histograms of parameter distributions for the best models (see text for details).

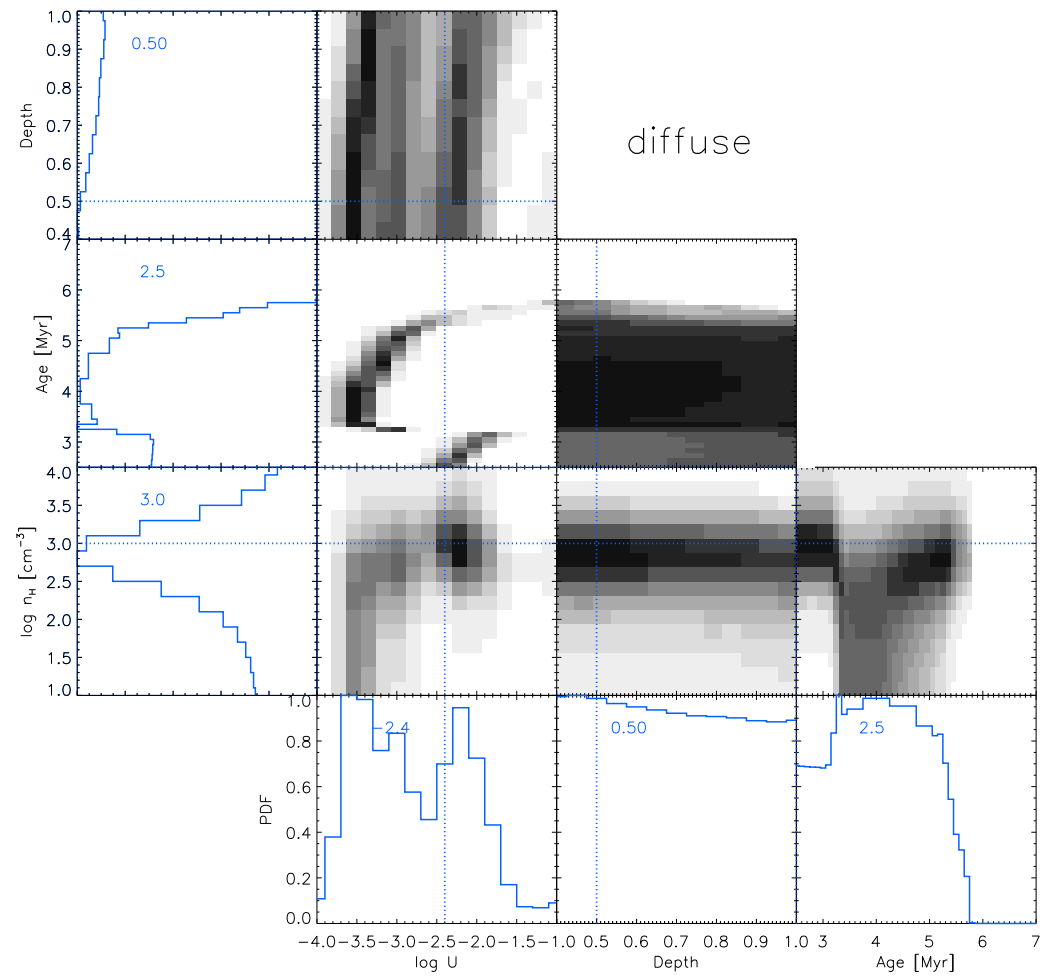

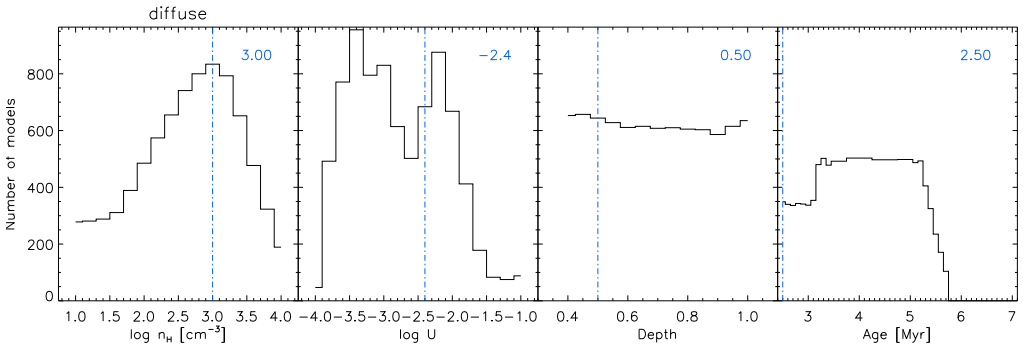

Figure 5.25: Results for the *Diffuse* zone with the line ratio method. *Top*: PDFs, see Figure 5.9 for the plot description. *Bottom*: Histograms of parameter distributions for the best models (see text for details).

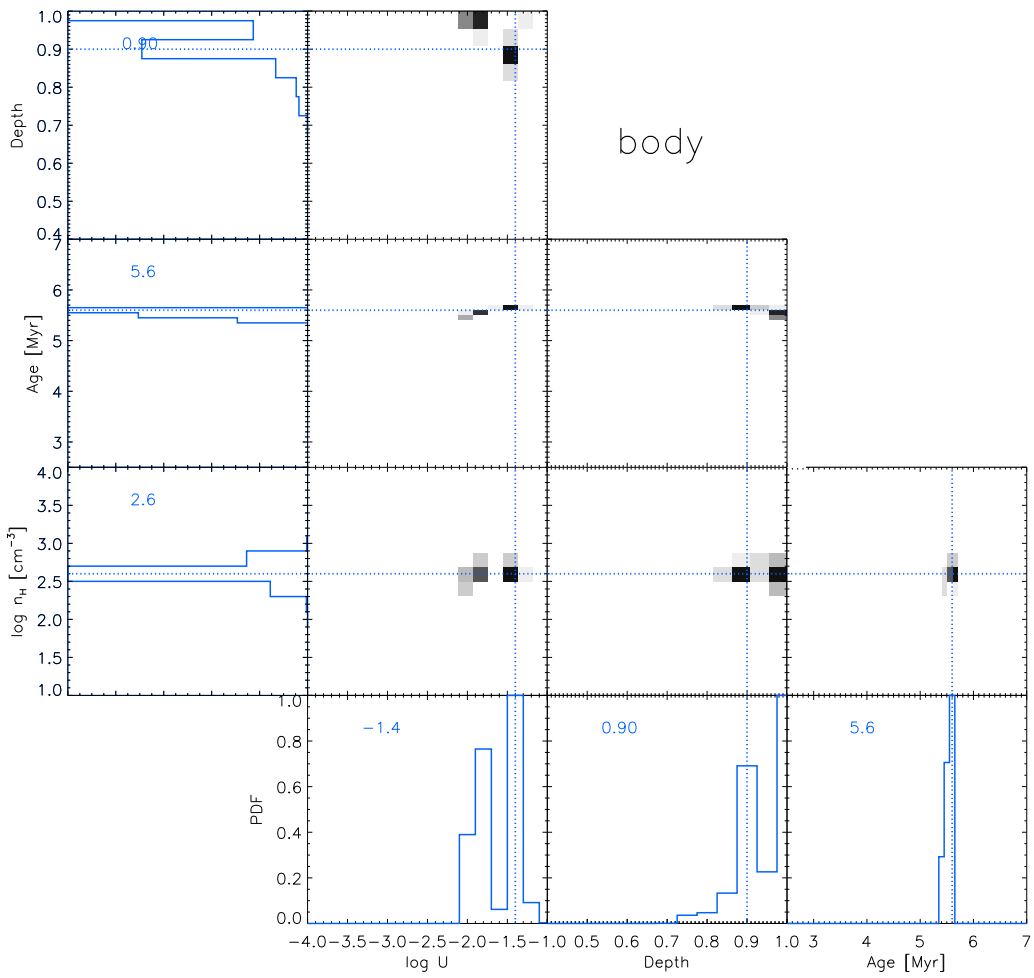

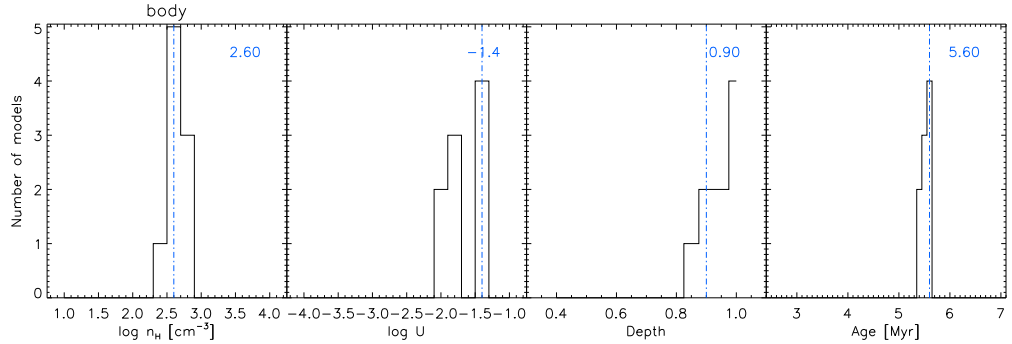

Figure 5.26: Results for the *Body* zone with the line ratio method. *Top*: PDFs, see Figure 5.9 for the plot description. *Bottom*: Histograms of parameter distributions for the best models (see text for details).

Table 5.4 summarizes the solutions obtained for the *zone scale* with the **line ratio method**. In general, the density derived for the zones that include the clumps previously examined (*Central main zone* and *ArcA*), seems to be lower than that derived for the individual clumps, while the ionization parameter is either lower than or equal to the clumps. Even larger scales (i.e., the *Body* zone) show unexpected behaviors, with a rather large ionization parameter and density determined (-1.4 and $10^{2.6}$ cm^{-3}, respectively). Based on the previous results, one could have expected the solution for the largest scale to be dominated by the most diffuse regions filling a larger volume of the galaxy. Interestingly, two other zones, *Intermediate* and *Central north* also show surprisingly high densities while the inspection of available optical and infrared images suggests instead a rather diffuse component. Among the selected line ratios, only two of them trace the density, [SIII] 33.5 μm/[NeIII] 15.5 μm and [SIII] 33.5 μm/ [SIII] 18.7 μm , and only [SIII] does not depend on the other parameters. Using the [SIII] ratio to trace the density independently from the model grid, i.e., comparing to the theoretical values assuming the gas temperature, provides $\sim 10^{2.4\pm0.2}$cm^{-3}. Hence, it seems that the zones that include HII regions, are characterized by a rather high density, comparable to that of the clumps. Thus, the density values obtained modeling the different zones, could be driven by the other ratios that are not *direct* tracers of the density. In principle one could rearrange the lines in order to use the same number of ratios that are sensitive to the density as the number of ratios that are sensitive to the ionization parameter (for example the set number 1: [ArIII] 8.9 μm/[ArII] 6.9 μm , [NeIII] 15.5 μm/[NeII] 12.8 μm and [SIV] 10.5 μm/[SIII] 33.5 μm as tracers of the density and [SIII] 33.5 μm/[NeII] 12.8 μm , [SIII] 33.5 μm/[SIII] 18.7 μm , [NeIII] 15.5 μm/[OIII] 88.4 μm and [SIV] 10.5 μm/[OIII] 88.4 μm as tracers of U). In practice the solutions were not "better" (i.e., it was not possible to find a model that reproduces all of the line ratios within their 1σ uncertainty) than the ones presented here. As we will see in Section 5.3.3, the solution found with absolute line fluxes is different (in particular with a lower density) for the three regions, *Body* , *Intermediate* , and *Central north* compared to the solution with line ratios.

The case of the *Central north* zone is also interesting. The model solution is rather well defined (Table 5.4 and also Figures 5.23). For this zone, the line ratios agree with a single ionization parameter value, and the density is also well determined. In the infrared images, no bright clump can be seen in this zone, which suggests that a single component with uniform properties may be dominating the emission and therefore the model solution.

Finally, the physical depth parameter, with values > 0.85 is globally larger for the zones than for the clump analysis. This is expected as the

fraction of ionizing photons absorbed by the gas should be close to 1 on large scales, based on the observations of low fraction of escaping Lyman continuum photons from galaxies (Leitet et al. 2013; see also discussion in Chapter 6).

Table 5.4: Results for each zone using the line ratio method.

Zone	t_{burst} [Myr]	log U	log n_H [cm^{-3}]	depth	χ^2_{min}	N$^{(a)}$	$\chi^2_{min,red}$ $^{(b)}$
Central Main	$5.5^{+0.0}_{-0.1}$	$-2.0^{+0.0}_{-0.2}$	$2.0^{+0.0}_{-0.4}$	$0.85^{+0.15}_{-0.05}$	103.0	9	20.6
ArcA	$5.5^{+0.0}_{-0.1}$	$-1.6^{+0.0}_{-0.2}$	$1.0^{+0.0}_{-0.0}$	$0.85^{+0.15}_{-0.05}$	95.0	8	2.3
ArcB	$3.0^{+2.7}_{-0.5}$	$-2.2^{+1.2}_{-0.4}$	$2.0^{0.5}_{-1.0}$	$0.95^{+0.05}_{-0.40}$	0.1	4	-
Intermediate	$5.6^{+0.0}_{-0.1}$	$-1.2^{+0.0}_{-0.6}$	$2.6^{0.2}_{-0.2}$	$1.00^{+0.0}_{-0.10}$	31.0	7	10.3
Central North	$5.5^{+0.1}_{-0.1}$	$-2.0^{+0.6}_{-0.2}$	$2.4^{+0.6}_{-0.6}$	$1.00^{+0.00}_{-0.45}$	4.0	7	1.3
West	-	-	-	-	-	3	-
Diffuse	-	-	-	-	-	3	-
Body	$5.6^{+0.0}_{-0.2}$	$-1.4^{+0.0}_{-0.6}$	$2.6^{+0.2}_{-0.2}$	$0.90^{+0.10}_{-0.05}$	90.0	8	2.2

$^{(a)}$ Number of line ratios available to constrain the model. $^{(b)}$ $\chi^2_{min,red}$ is the reduced χ^2.

Summary

In most cases and at any spatial scale considered (clumps or zones), the modeling performed with the **line ratio method** could not reproduce all of the line ratios at a better than 1σ level and unexpectedly, the *Body* solution shows a dense emission component. Despite this result, some individual parameters seem to be relatively well determined. The clump analysis reveals rather matter-bounded clouds, while the solutions for larger spatial scales tend to favor components that are globally radiation-bounded or almost radiation-bounded. The inability of the models to reproduce all of the observed line ratios is probably due in part to the model hypotheses that assume a single ionized gas component while multiple components may be at work within each of our different modeled regions. I also notice that the choice of the line ratio set, especially for the largest scale possible in our study, drives the way in which the parameter space is probed, suggesting that the method (using line ratios or absolute line fluxes) may have a significant impact in the derivation of the physical conditions.

5.3.3 Absolute Flux Method

Apart from line ratios, another possibility to compare the observations with model predictions is the **absolute flux method**. By using absolute line fluxes as constraints instead of line ratios (Section 5.3.2), I expect to be able to isolate more easily the lines that may require another component (e.g., [NeII]). While I previously used ratios in order to minimize the uncertainties due to instrumental effects or elemental abundances, here I consider each line individually with the corresponding uncertainties. As explained in the following, particular attention will be given to the correlation between the various types of uncertainties. While the choice of line ratios "dictated" the way in which the model parameter space was probed, the absolute flux method is simpler in that, it is the actual list of lines that controls the parameter space. Therefore, I also hope to minimize potential biases in the process of finding the best solutions with multiple tracers.

For the absolute flux method, we wish to compare the observed line *luminosities* to the values predicted in CLOUDY. However, since the CLOUDY calculations are performed in the intensity-case (Section 4.3), I need to convert the model predictions to a luminosity quantity. For this, I introduced a scaling factor parameter (sl) which is the ratio between the observed line *luminosity*, O, and the modeled line *intensity*, M: $sl = O/M$. Instead of using a reference line that would be used to normalize the models to the observations, we decided to calculate a global scaling factor $sl_{\rm global}$ that is applicable for all the lines. This global scaling factor[1] is left free to vary between a minimum and maximum value given by the extreme values of $sl(\text{line}_i)$ calculated for each individual line separately.

For each model, the goodness of the fit was calculated with the χ^2 as:

$$\chi^2 = X^T V^{-1} X$$

where X is a N-dimensional vector (N is the total number of the lines),

[1]The scaling factor implies a transformation of intensities to absolute luminosities for the model and is a free parameter because the absolute luminosity of the ionizing sources are not known. Ideally, I would like to use the observed line-to-bolometric luminosity ratio as a constraint in the models, but this proved difficult since I only had access to the *infrared* luminosity with the *Herschel* and *Spitzer* photometry measurements and not to the bolometric luminosity. In any case, I assumed typical values for the infrared-to-bolometric conversion factor in star-forming galaxies of the Herschel Reference Survey (Boselli et al. 2010 and Ciesla et al. private communication), and computed the expected value of the line-to-bolometric luminosity. The line-to-bolometric luminosity values obtained from the model are in good agreement with the expected values, definitely within the errors related to the uncertainty in the infrared-to-bolometric conversion factor.

individually noted as j with $X_j = O_j - (M_j * sl_{\rm global})$. O_j is the observed emission of line j, M_j is the predicted emission and $sl_{\rm global}$ is the global scaling factor described above. V is the covariance matrix ($N \times N$) with $V_{ij} = \rho_{ij}\,\sigma_i\,\sigma_j$, where σ_i and σ_j are the uncertainties related to the lines i and j, respectively, and ρ_{ij} is the correlation coefficient between σ_i and σ_j. The uncertainties taken into account to calculate the matrix were the calibration uncertainties (5% for IRS and 12% for PACS), the uncertainties on the line fit (Table 5.2 for the clumps and Table 5.1 for the zones), the uncertainties on the elemental abundances (Table 4.1), and the uncertainties due to the SL/LL stitching (15% for IRS LL; see zone analysis in Section 5.3.2). I populated the covariance terms (uncertainties and correlation coefficient) using a Monte Carlo simulation with 10^6 iterations. Similar to the method using line ratios, the best model was found by minimizing the χ^2 value.

Clump analysis

As for the line ratio method (Section 5.3.2), the LL tracers are not used at first for the clump analysis, due to the low spatial resolution available in LL. However, I included [NII] 121.9 μm for those clumps covered with PACS. The reason why [NII] 121.9 μm was included despite its low S/N is related to the number of degrees of freedom for the models. By using absolute line fluxes instead of ratios, I added an extra free parameter, the scaling factor, requiring an additional observational constraint. Hence, the available constrains are:

- [ArII] 6.9 μm
- [ArIII] 8.9 μm
- [SIV] 10.5 μm
- [NeII] 12.8 μm
- [OIII] 88.4 μm
- [NII] 121.9 μm only for the clumps *Center* $c3$, *ArcA* $c1$ and *ArcA* $c2$.

As for the line ratio method, I use probability distribution functions (PDFs) to display the model solutions.

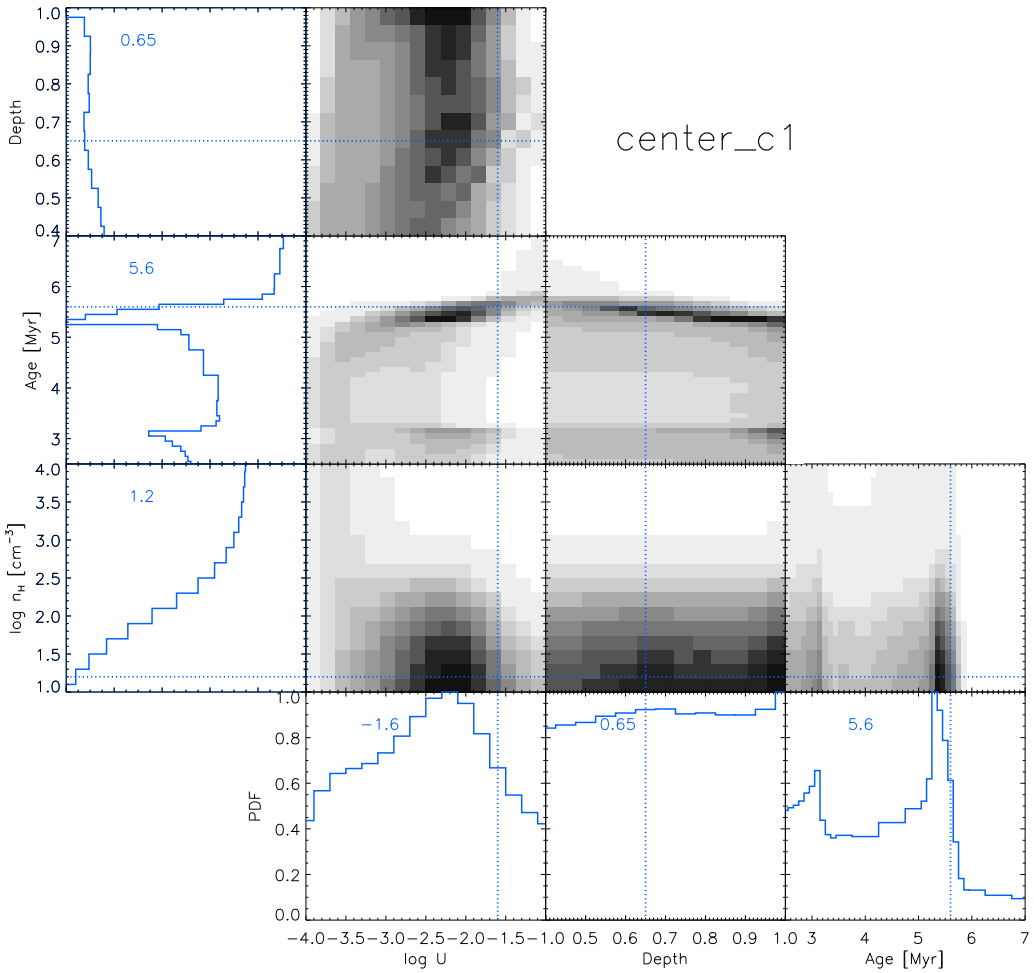

Figure 5.27: PDFs for the clump *Center c*1 with the absolute line flux method. See Figure 5.9 for the plot description.

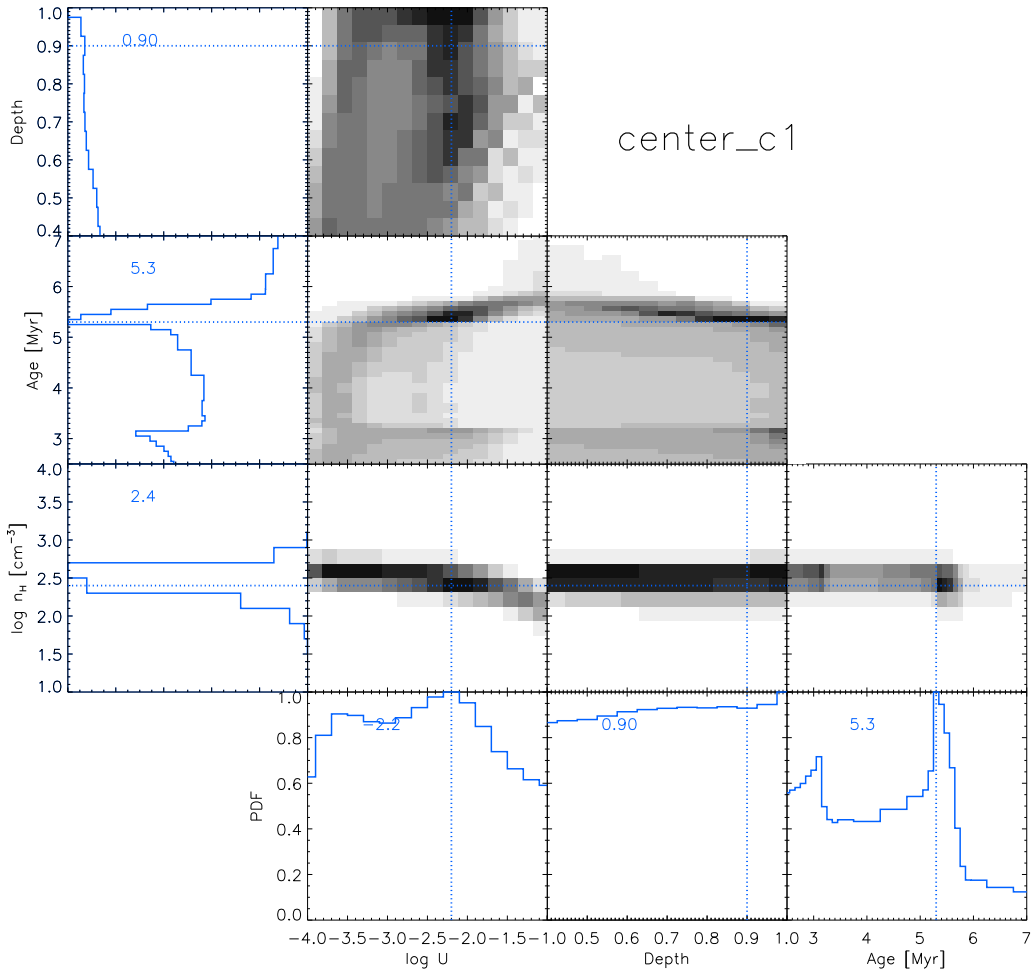

Figure 5.28: PDFs for the clump *Center c*1 with the absolute line flux method, including [SIII] line ratio as constraint. See Figure 5.9 for the plot description.

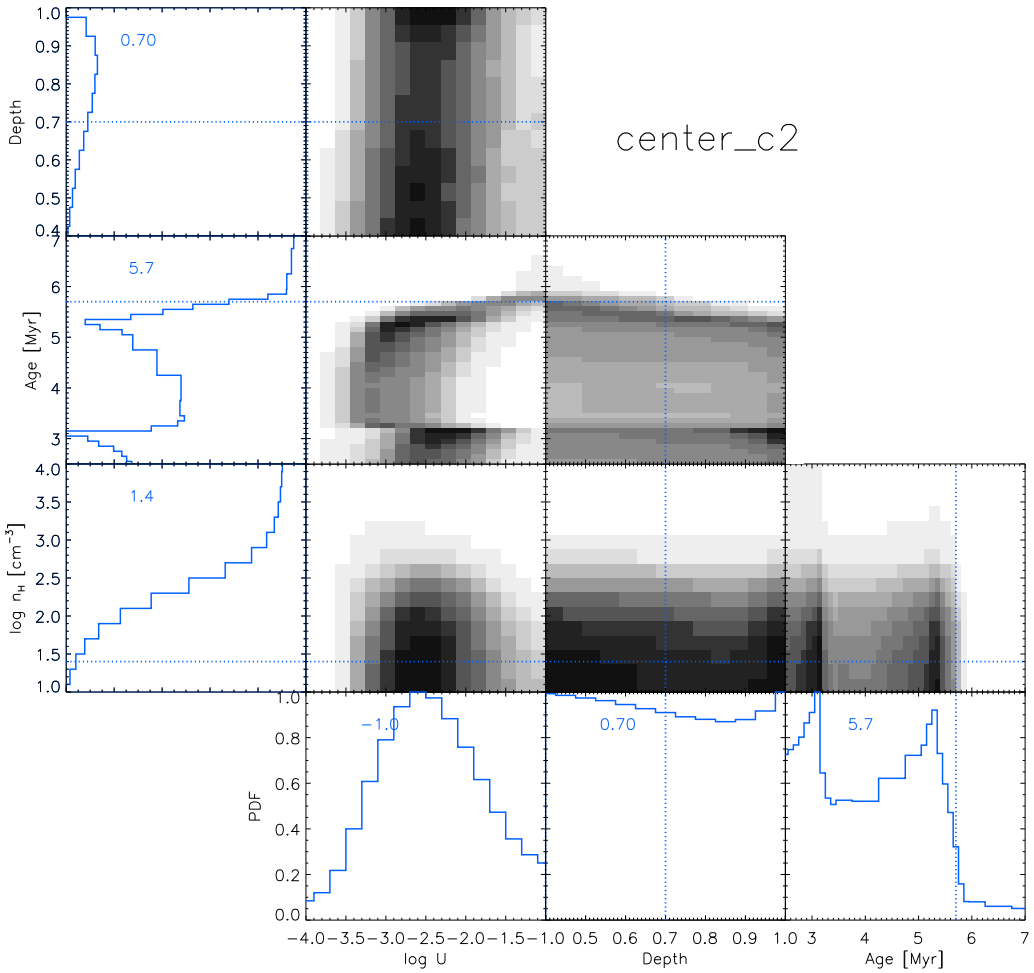

Figure 5.29: PDFs for the clump *Center c*2 with the absolute line flux method. See Figure 5.9 for the plot description.

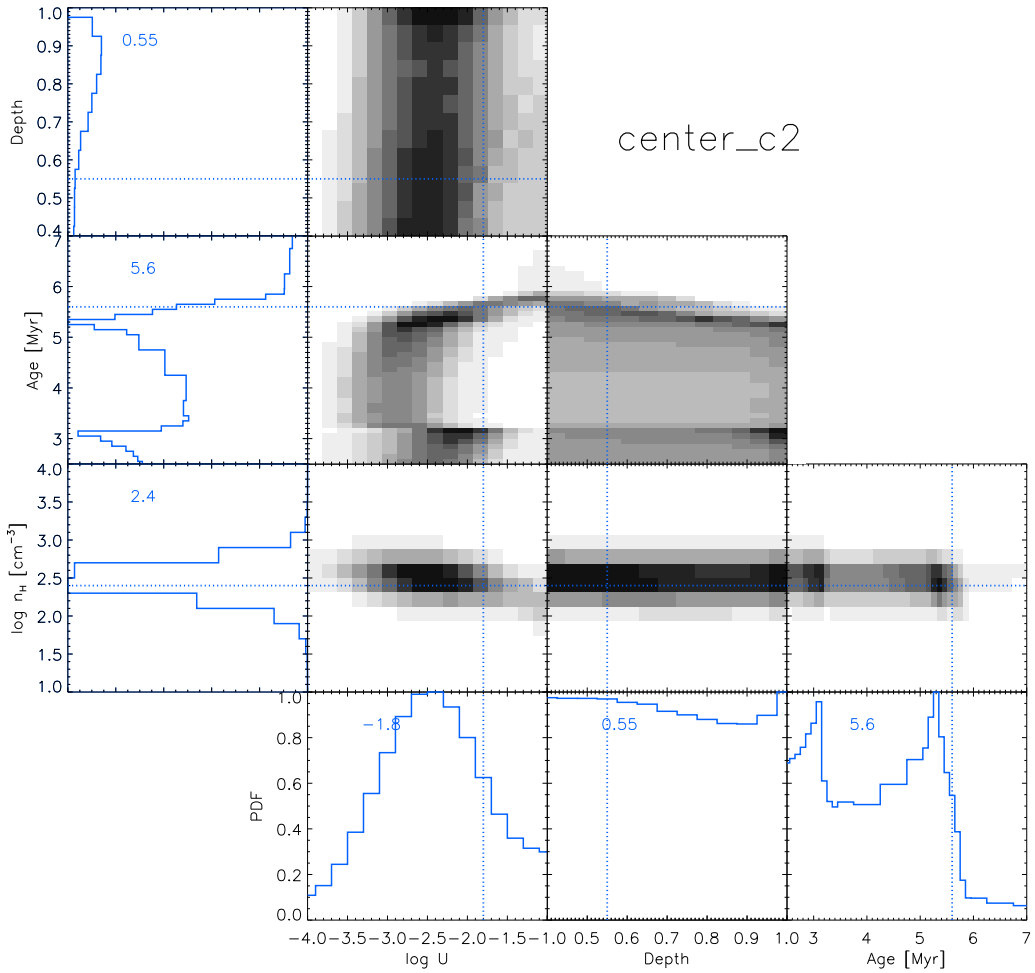

Figure 5.30: PDFs for the clump *Center c*2 with the absolute line flux method, including [SIII] lines as constraint. See Figure 5.9 for the plot description.

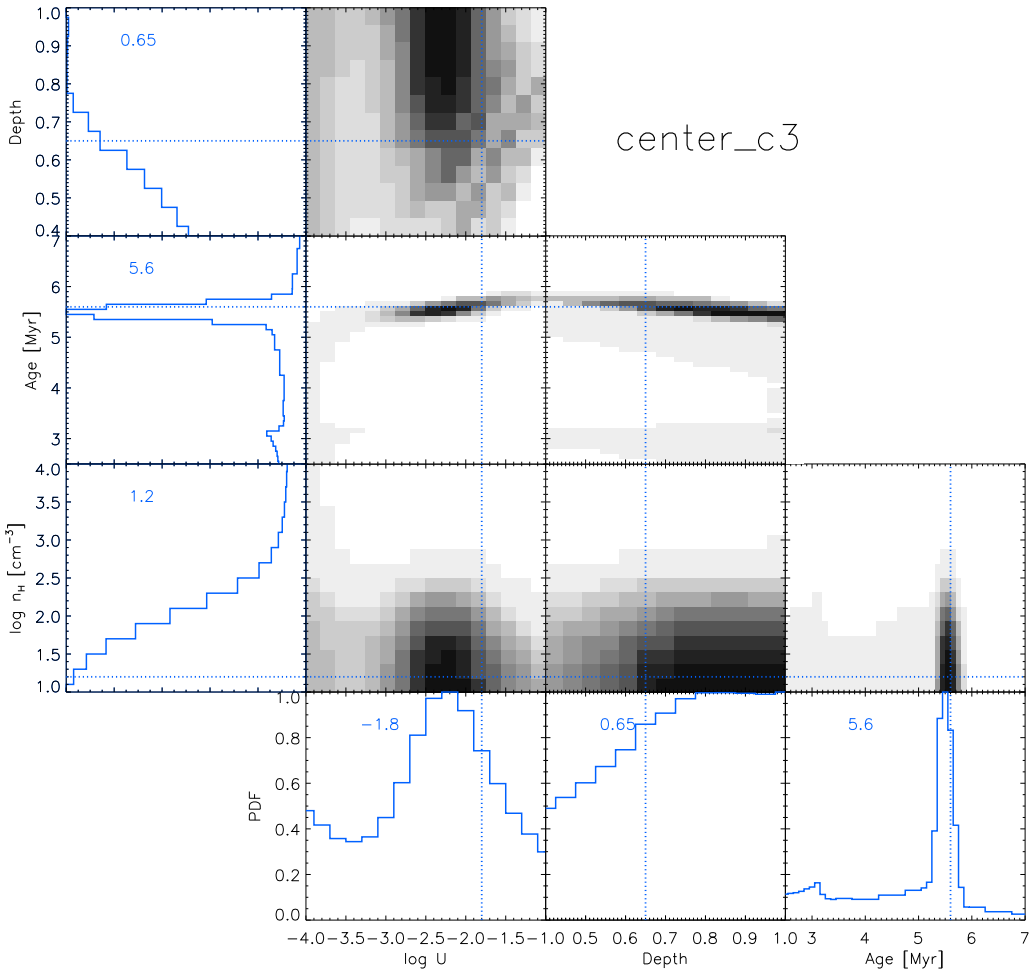

Figure 5.31: PDFs for the clump *Center c3* with the absolute line flux method. See Figure 5.9 for the plot description.

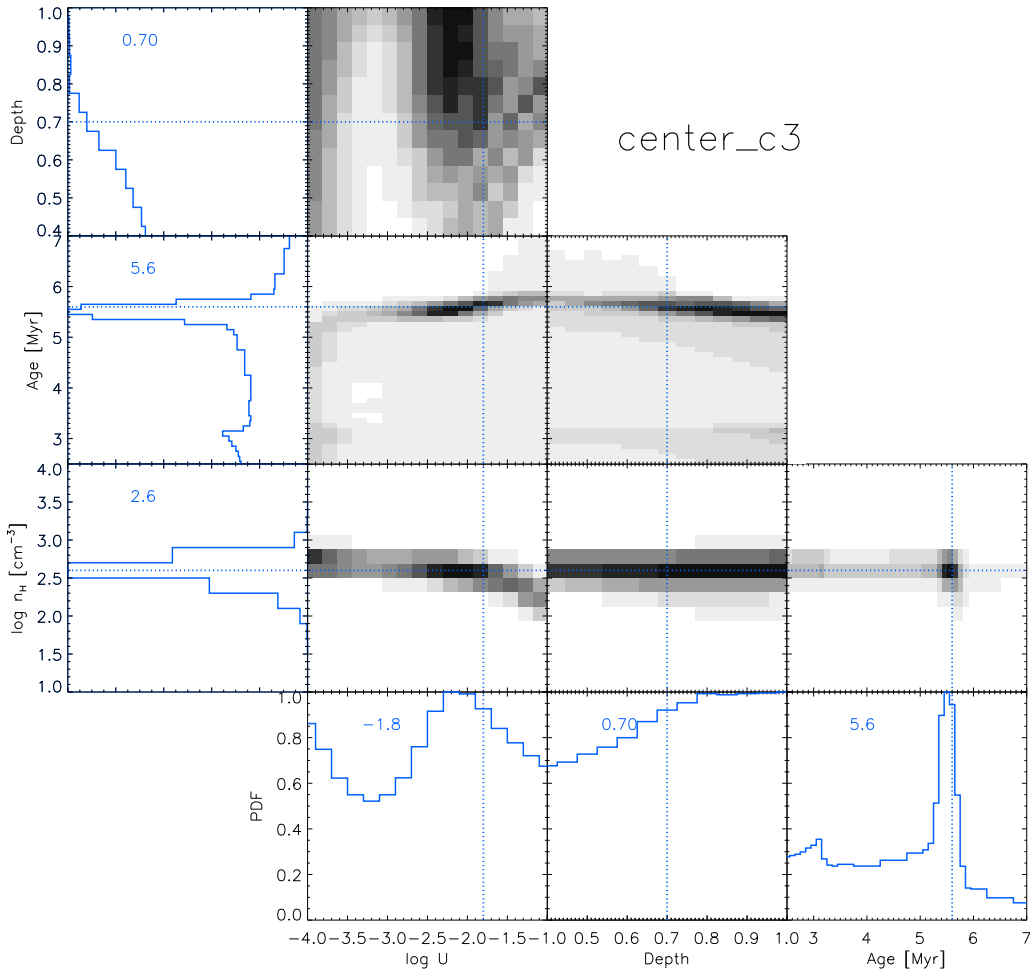

Figure 5.32: PDFs for the clump *Center c*3 with the absolute line flux method, including [SIII] lines as constraint. See Figure 5.9 for the plot description.

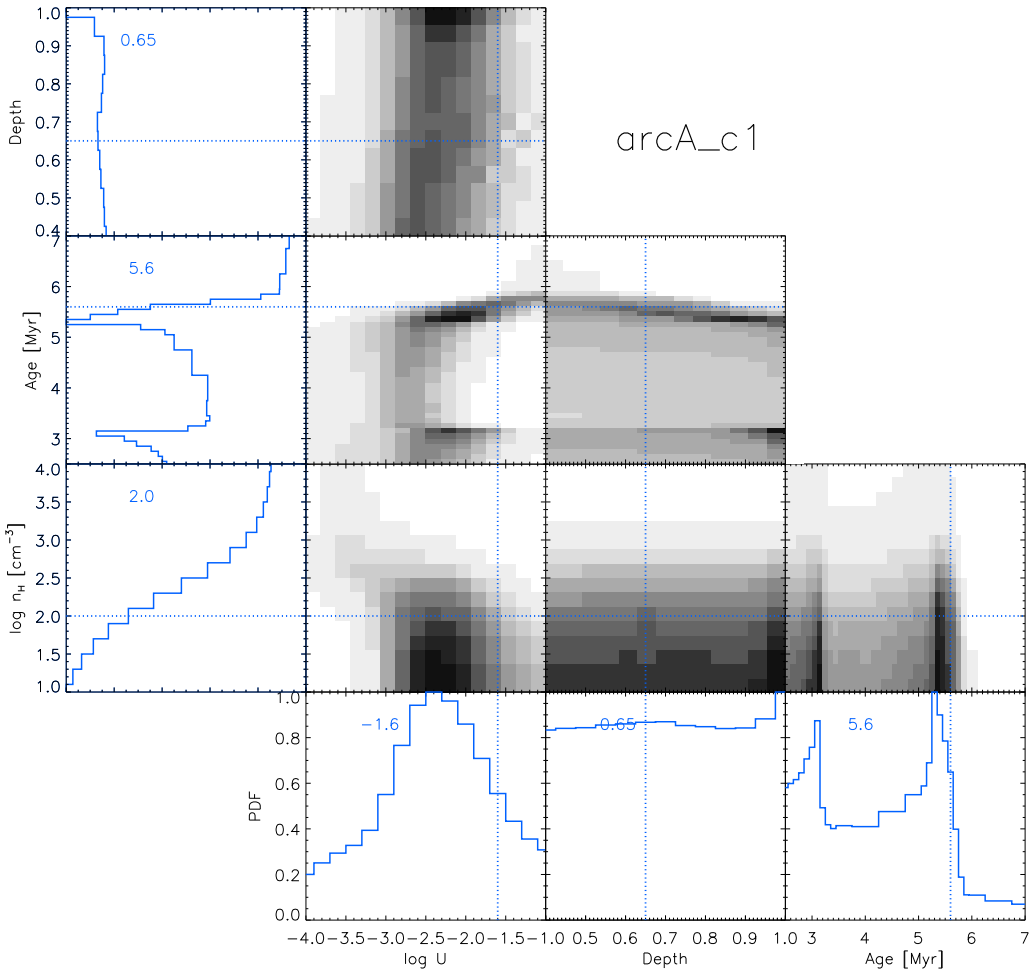

Figure 5.33: PDFs for the clump *ArcA c*1 with the absolute line flux method. See Figure 5.9 for the plot description.

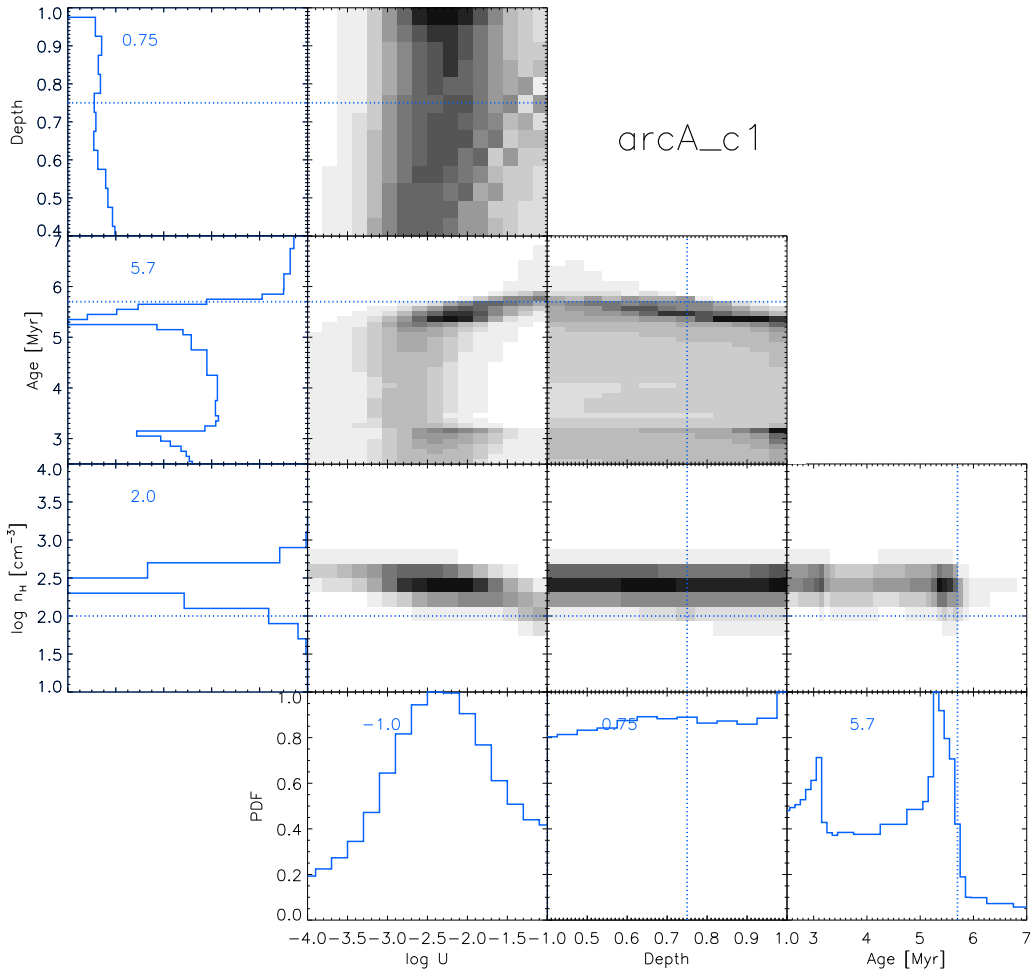

Figure 5.34: PDFs for the clump *ArcA c*1 with the absolute line flux method, including [SIII] lines as constraint. See Figure 5.9 for the plot description.

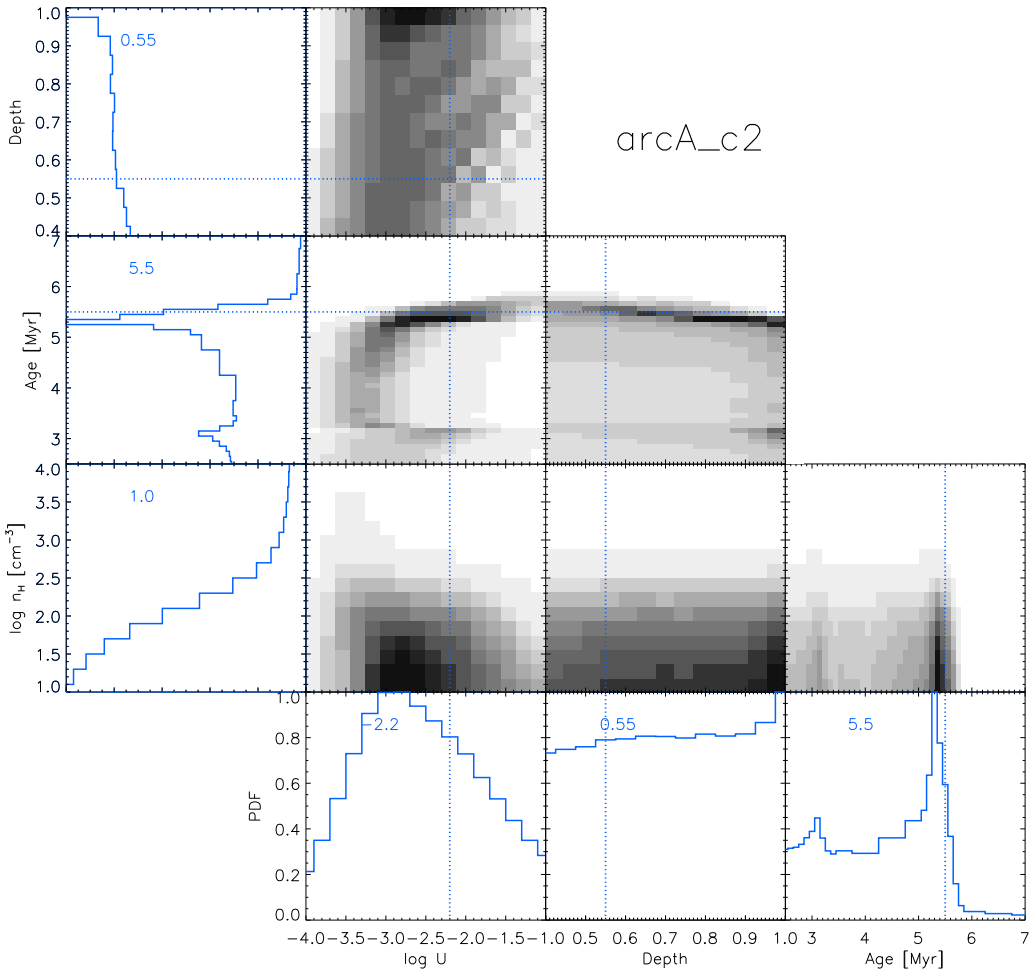

Figure 5.35: PDFs for the clump *ArcA c2* with the absolute line flux method. See Figure 5.9 for the plot description.

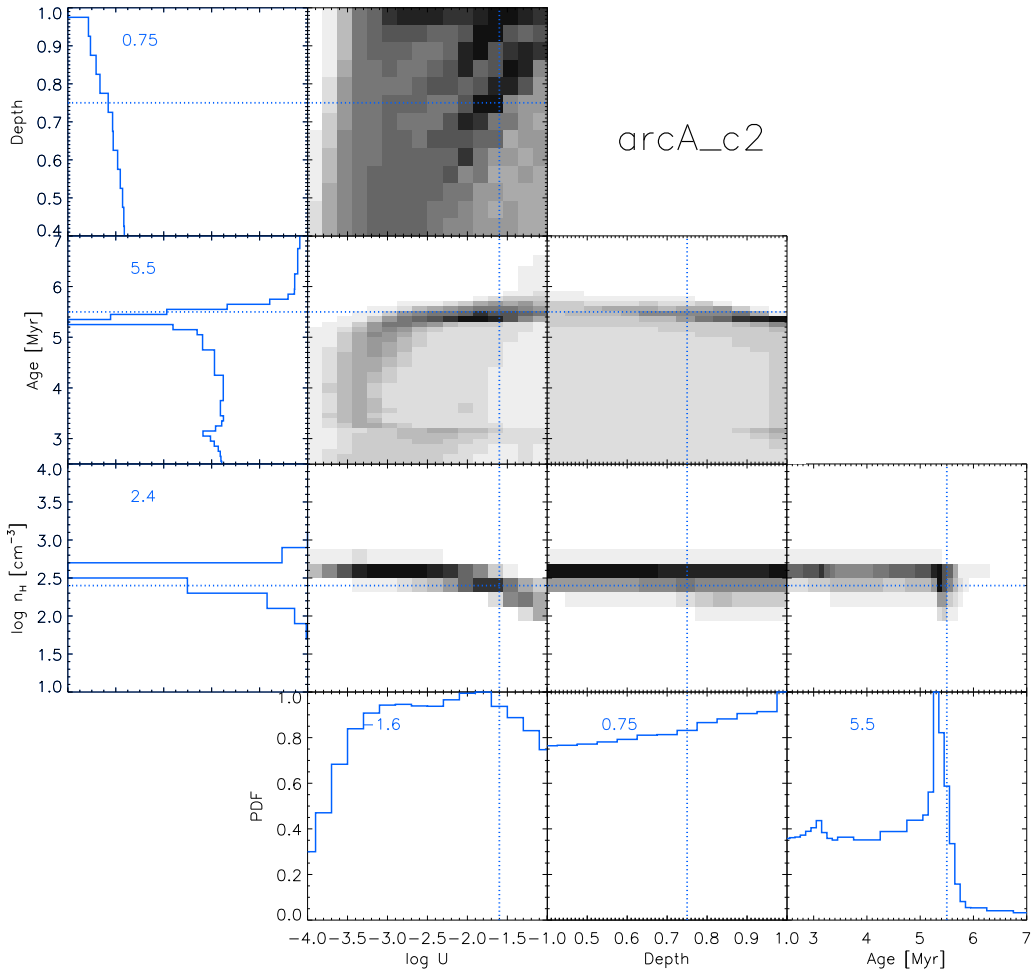

Figure 5.36: PDFs for the clump *ArcA c2* with the absolute line flux method, including [SIII] lines as constraint. See Figure 5.9 for the plot description.

Figures 5.27, 5.29, 5.31, 5.33, and 5.35 show the PDFs and the best model solutions (lowest χ^2; vertical line in the figure) for each clump. One can see that the density and the depth are not well constrained. Indeed, a well-defined peak is not visible in the PDFs and the 2D PDFs show extended black/grey areas instead of a well-defined spot. Furthermore, the best solution is not always in agreement with the PDF peak, in particular for the ionization parameter. This led me to introducing again the ratio [SIII] 33.5 μm/[SIII] 18.7 μm as a constraint to the models, because this ratio traces the gas density unambiguously. Although the [SIII] lines were already accounted for in the list of lines used to constrain the model with the previous method, these two lines arise in the IRS LL module for which the low spatial resolution prevents an accurate clump decomposition, thus resulting in large error bars on the *absolute* fluxes. Nevertheless, the [SIII] line *ratio* is much better behaved. Thus we combine here the lessons learned from both methods, i.e., using line ratios *and* absolute line fluxes. Figures 5.28, 5.30, 5.32, 5.34, and 5.36 show the PDFs for each clump, with the χ^2 calculation that includes the [SIII] line ratio as a constraint. As expected, the change is dramatic for the density parameter, which is now quite well constrained in each clump. The density values are close to those found with the line ratios method (Section 5.3.2). The PDFs for the other parameters are somewhat changed, but the general shape is the same.

For a more detailed analysis, I also computed the statistical histograms of each parameter for the best models only. The best models are defined by these models with a χ^2 value lower than χ^2_{min}+5.89, where 5.89 is the 1σ confidence interval with five free parameters (Press et al. 1992), i.e., n_H , log U, t_{burst}, physical depth, and *sl*. The corresponding statistical histograms of the four physical properties are shown in Figures 5.37 and 5.38. One can see that only the density is well constrained by the available tracers with a 1σ error bar smaller than the full parameter range. On the other hand, for all the other parameters, the best models in terms of χ^2 provide parameter values distributed over the entire parameter range used in the model grid. In other words one cannot derive an error bar.

We note in particular the large uncertainties in the depth parameter. This parameter is mostly constrained by two lines that arise near or at the photoionization front, [ArII] 6.9 μm and [NII] 121.9 μm. Unfortunately, both lines have large error bars as compared to most of the other tracers. Indeed, the [ArII] 6.9 μm S/N is overall lower than 2 while [NII] 121.9 μm is not only faint but it also carries a relatively large calibration uncertainty because it is observed with a different instrument than most of the other lines. The large uncertainties on the ionization parameter and the starburst age are related to the degeneracy between these two parameters: a model

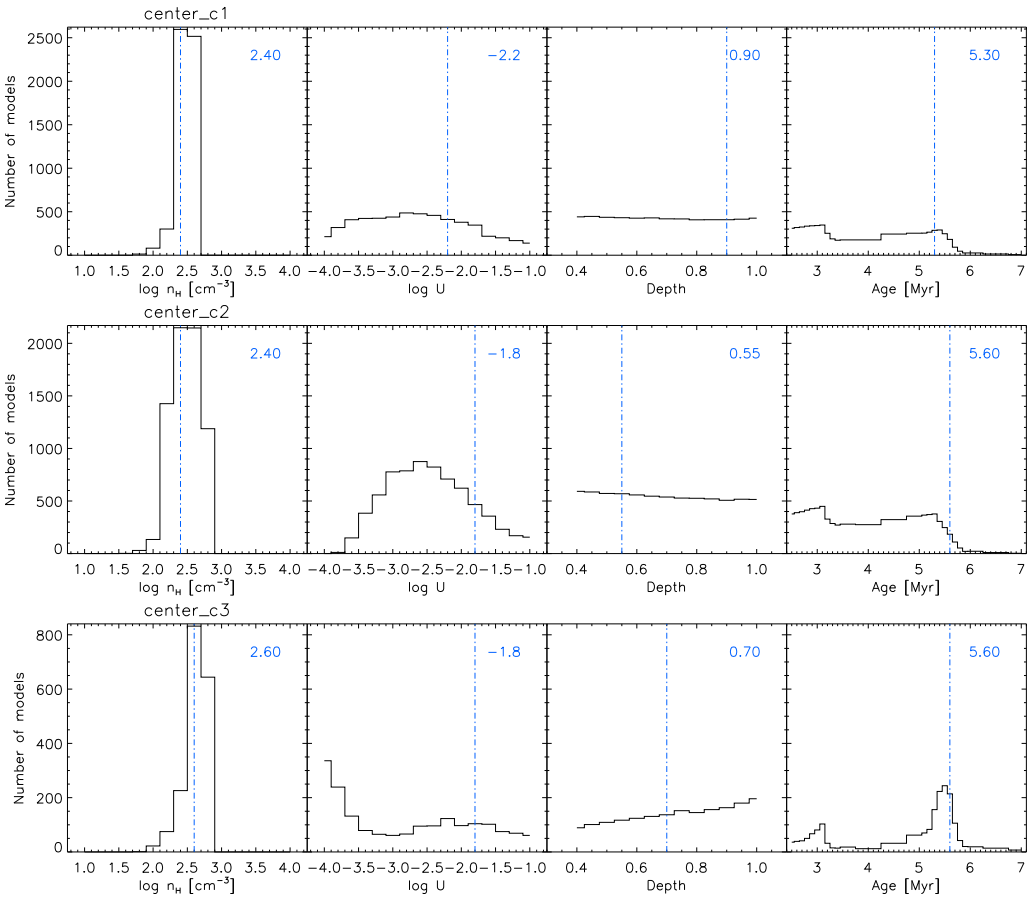

Figure 5.37: Histograms of parameter distributions for the best models for the clumps *Center c*1, *Center c*2, and *Center c*3 with the absolute line flux method (see text for details).

with a young stellar population combined with a low ionization parameter produces a similar spectrum as a model with a high ionization parameter and older starburst. This degeneracy is evident in the 2D PDFs related to these two parameters.

Looking back at the PDFs, the t_{burst} parameter shows two peaks, at ≈ 3 and ≈ 5.5 Myr. Since I do not have enough information on the age of the stellar population, I explored the effect of restricting the starburst age to either one of the two peaks, in order to witness the effect on the PDFs of the other parameters. Figures 5.39 and 5.40 show the PDFs when constraining t_{burst} between 2.8 and 3.3 Myr (i.e., the Wolf-Rayet stage), while Figures 5.41 and 5.42 show the PDFs for constraining t_{burst} between 5.2 and

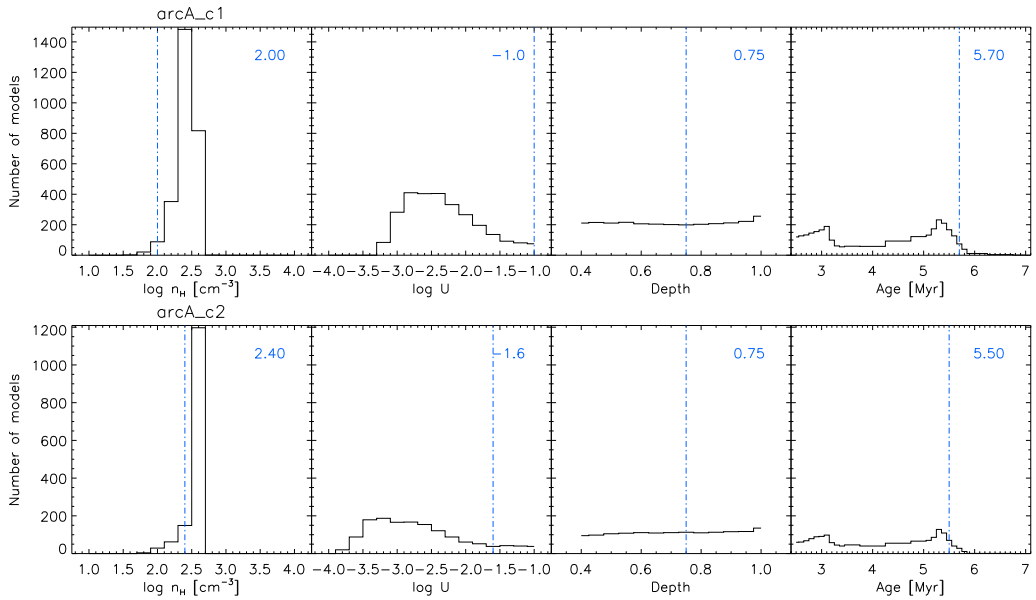

Figure 5.38: Histograms of parameter distributions for the best models for the clumps *ArcA c*1 and *ArcA c*2 with the absolute line flux method.

5.8 Myr (i.e., the typical HII region age for an instantaneous burst hypothesis; Section 5.3.2). Globally, the density parameter is not affected by the choice of starburst age: I find nearly identical densities in both cases. As expected, the PDFs for the ionization parameter change. This is due to the well known degeneracy described above that we witness here directly. The PDFs for the physical depth also change, which is easily understood since the ionization parameter, the starburst age, and the physical depth all depend on the relative intensity of high- vs. low-ionization tracers. In the case of the ionization parameter and of the starburst age, this is simply related to the input radiation field, but in the case of the physical depth, this is because higher ionization species are located closer to the ionizing sources.

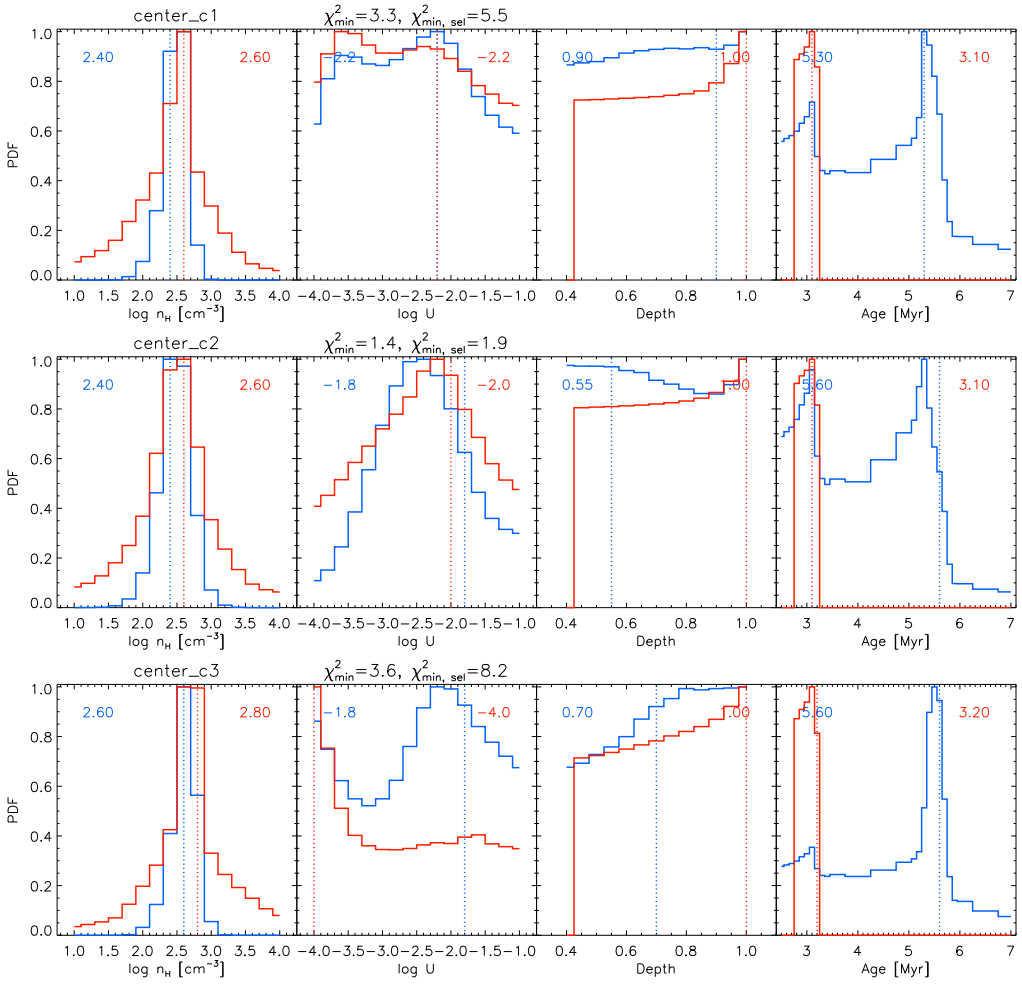

Figure 5.39: PDFs for the clumps *Center c*1, *Center c*2 and *Center c*3 from top to bottom with the absolute line flux method. The blue histograms show the PDFs from Figures 5.28, 5.30 and 5.32, with the best model ($\chi^2_{\rm min}$) shown by the vertical blue line and the best model parameter values given by the blue number on the top left corner. The PDFs overplotted in red are for the subset of the models with t_{burst} (Age) constrained between 2.8-3.3 Myr. For each subset PDF, the vertical red line and the red number on the right corner indicate the best model ($\chi^2_{\rm min,sel}$) in that particular subset.

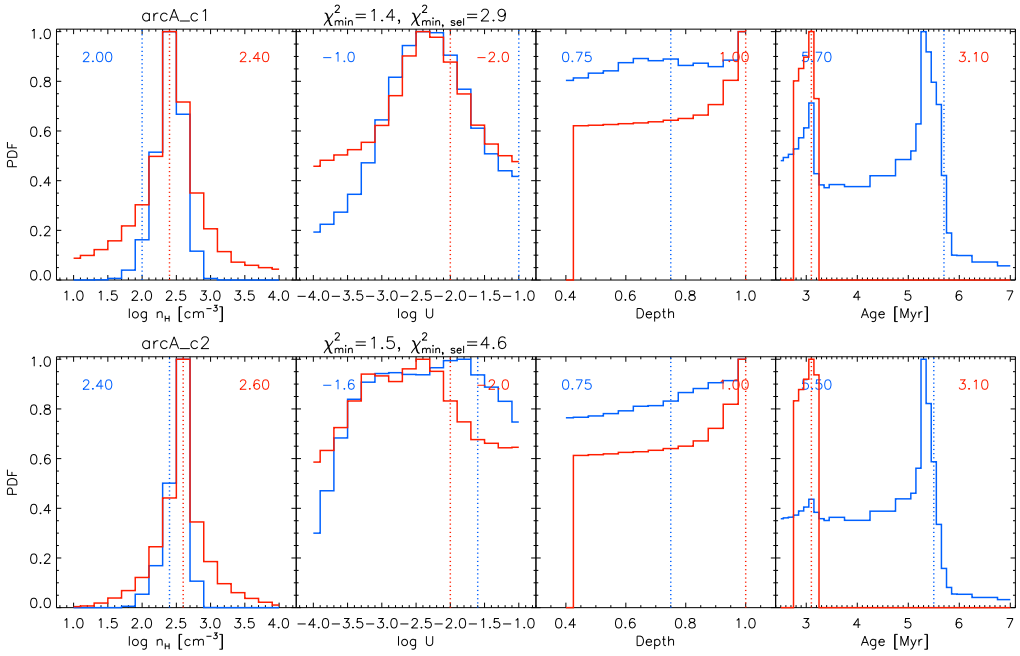

Figure 5.40: PDFs for the clumps *ArcA c*1 and *ArcA c*2 from top to bottom with the absolute line flux method. The PDFs overplotted in red are for the subset of the models with t_{burst} (Age) constrained between 2.8-3.3 Myr. See Figure 5.39 for the plot description.

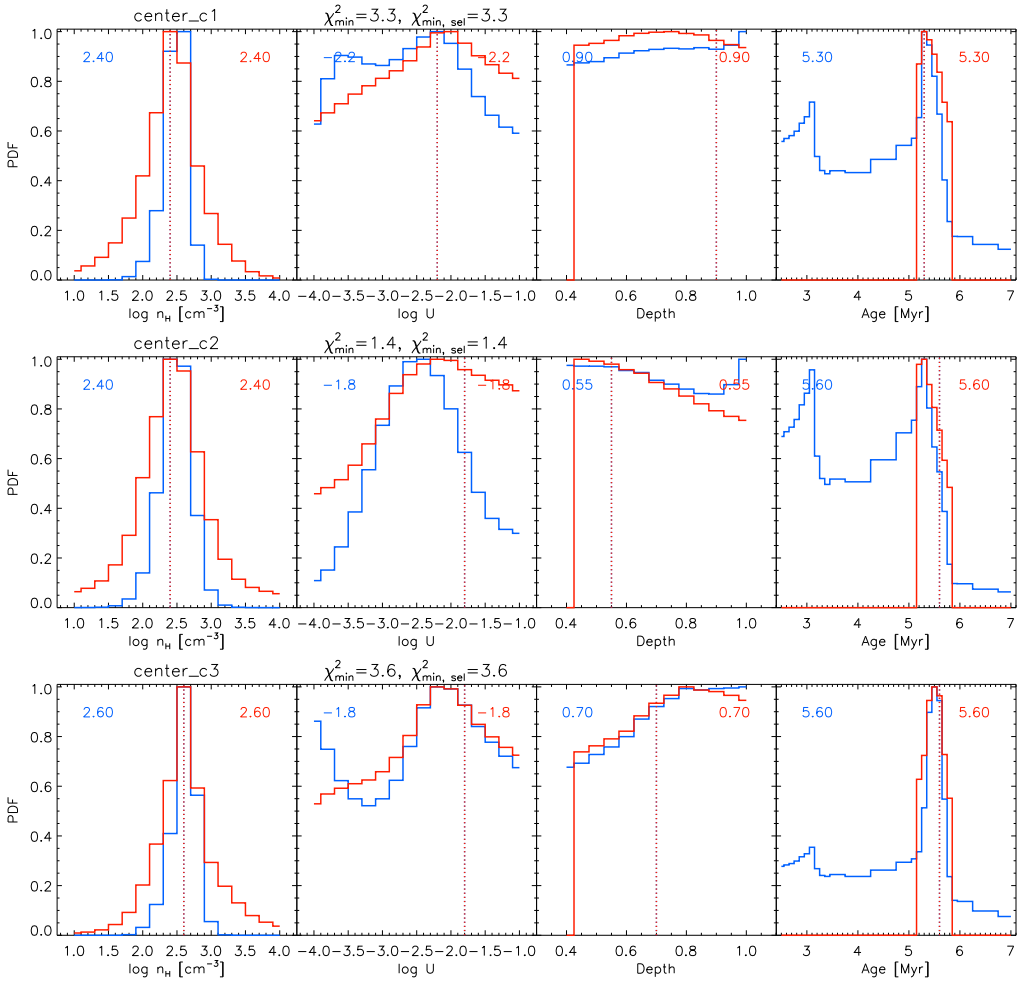

Figure 5.41: PDFs for the clumps *Center c*1, *Center c*2 and *Center c*3 from top to bottom. The PDF overplotted in red is for the subset of the models with t_{burst} (Age) contained between 5.2-5.8 Myr. See Figure 5.39 for the plot description.

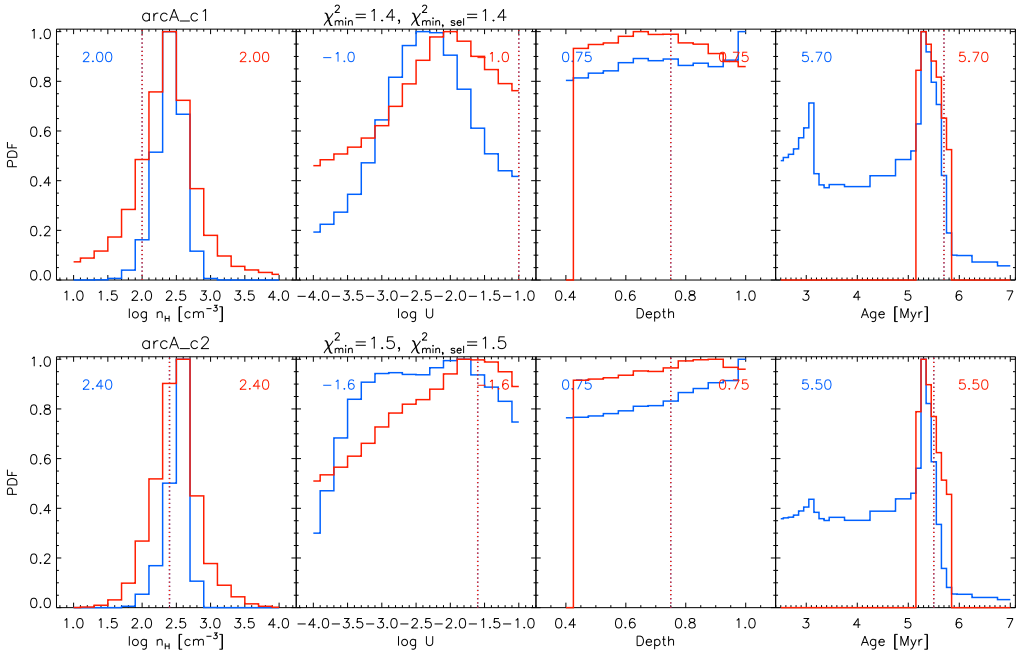

Figure 5.42: PDFs for the clumps *ArcA c*1 and *ArcA c*2 from top to bottom with the absolute line flux method. The PDF overplotted in red is for the subset of the models with t_{burst} (Age) constrained between 5.2-5.8 Myr. See Figure 5.39 for the plot description.

For all of the clumps, the starburst age around 5.5 Myr is preferred by the models (higher peak in the PDFs). The line ratio method (Section 5.3.2) already hinted that such an age was indeed to be favored, which is also compatible with the expectation that we are mostly observing HII regions and not compact HII regions or ultracompact HII regions that are still embedded. If we thus consider the subset of the models with an age around 5.5 Myr (Figures 5.41 and 5.42), this implies that the physical depth parameter for the clumps is relatively low (0.5-0.8), that the ionization parameter is between -2.5 and -1, while the density is consistently around $\sim 250\,\mathrm{cm}^{-3}$ except for the *ArcA c1* clump with a somewhat lower density around $100\,\mathrm{cm}^{-3}$.

Hence, these experiments show that reasonable solutions can be found if the degeneracy between U, the starburst age, and the physical depth parameters can be lifted, for instance by forcing the age around 5.5 Myr. Unfortunately, we cannot use a line ratio to directly constrain any of these parameters, in the way that we used [SIII] 33.5 μm/[SIII] 18.7 μm to trace the density.

By using absolute line fluxes, one can easily examine individual lines in order to reveal whether any given line is significantly under- or overestimated by the models. For this I computed the PDFs of the ratios between observed and predicted line emission. Results are shown in Figures 5.43, 5.44, 5.45, 5.46, and 5.47. Most PDFs peak around 0 (in log scale), implying that the observations (either as an absolute line flux or as a ratio) are well reproduced, most often within a factor of $2-3$. There are some exceptions: [OIII] 88.4 μm in *Center c*1, and [OIII] 88.4 μm & [NII] 121.9 μm in both *Center c*3 and *ArcA c*2. It seems that the constraint provided by [NII] 121.9 μm has no influence on the best solution because of its low S/N and also because of the additional calibration uncertainty (this line was observed with PACS while most of the other lines were observed with the IRS). Interestingly, [OIII] 88.4 μm, which is also observed with PACS, is also not well reproduced, suggesting that PACS tracers have in general little impact on the model solution.

I also notice some systematic biases: [ArII] 6.9 μm and [ArIII] 8.9 μm are always overestimated by the models by a factor of about two. Since these two lines were both observed in the same instrument module as other IRS lines that are comparatively better reproduced ([NeII], [SIV]), this result may indicate that the argon elemental abundance has been overestimated in the models. Considering the lack of constraints on the argon abundance (Table 4.1), this seems a reasonable assumption. Finally, as far as *clumps* are concerned, there is no obvious need for another ionized gas component with a different density and/or ionization parameter, since all of the lines (including [NeII]) are relatively well reproduced. The cases for which the

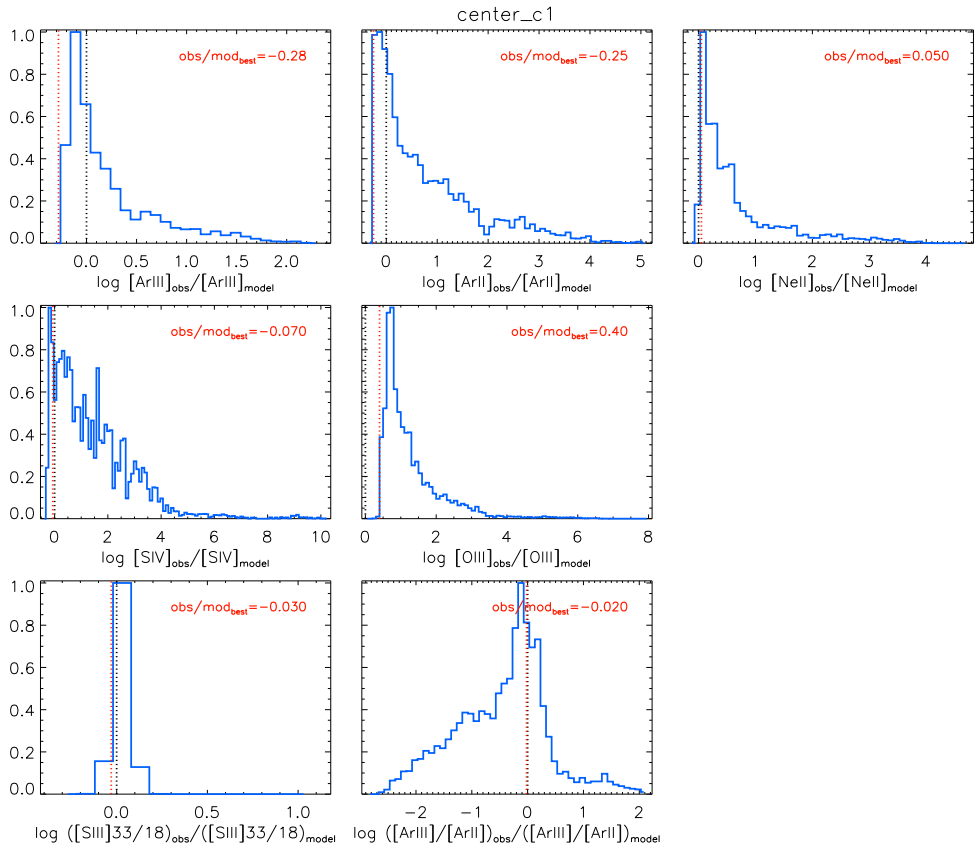

Figure 5.43: PDFs of observed vs. predicted constraint values (absolute line fluxes and the [SIII] line ratio) for the clump *Center c*1. We show also the PDF for [ArIII] 8.9 μm/[ArII] 6.9 μm as an a posteriori check. The vertical lines indicate the observed vs. predicted values for the best model (lowest χ^2), with the corresponding value shown in the right corner.

predicted [OIII] 88.4 μm and [NII] 121.9 μm fluxes are several factors away from the observed value would need to be investigated in more detail to find out whether another ionized gas component would solve the issue.

The best solutions for each clump are listed in Table 5.5. The density estimates are in good agreement with those found with the line ratio method (Table 5.3), with values between $\sim$ 100 and $\sim$ 400 cm^{-3}. The physical depth is significantly lower than 1 of the ionization front, implying that the clumps are at least partially matter-bounded. Again, this confirms the result obtained with the line ratio method and it suggests that looking at the smallest spatial scales accessible with our tracers, we are able to constrain indirectly the fraction of escaping ionizing photons. The log of the ionization parameter

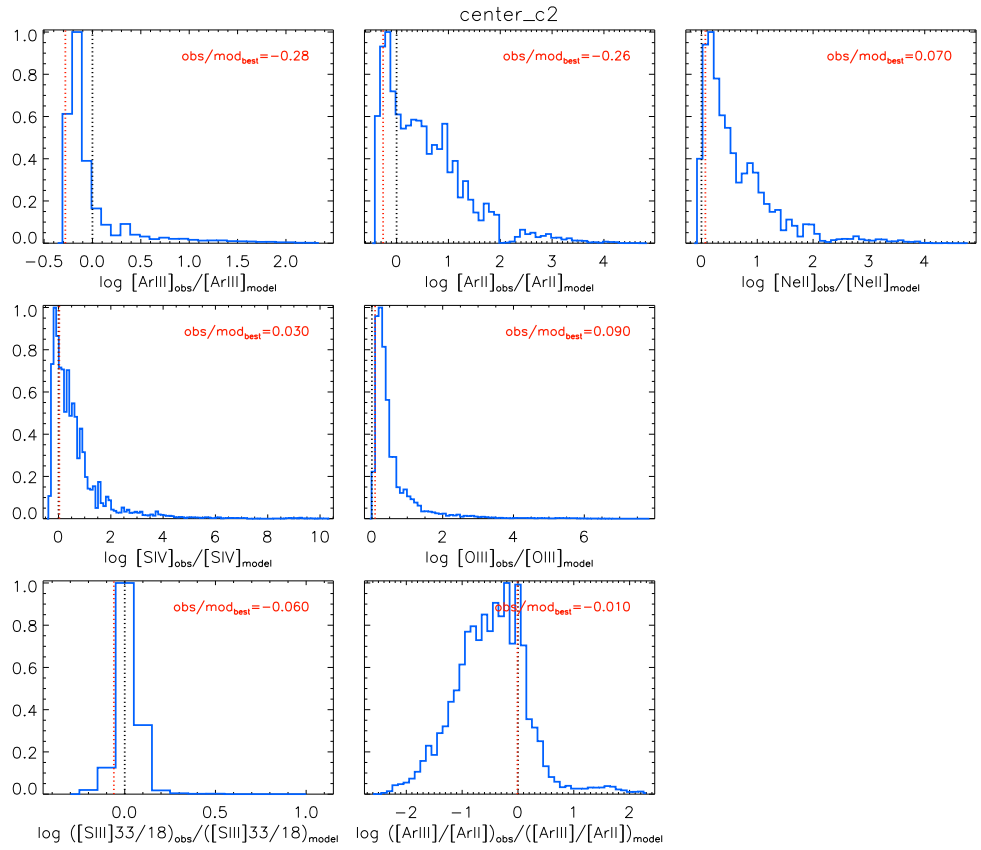

Figure 5.44: PDFs of observed vs. predicted constraint values for the clump *Center c2*. See Figure 5.43 for the plot description.

lies between −2.2 and −1.6. Most clumps have nearly identical properties except *ArcA c1*, which seems more diffuse and with a larger ionization potential, although the error bars are too large to conclude.

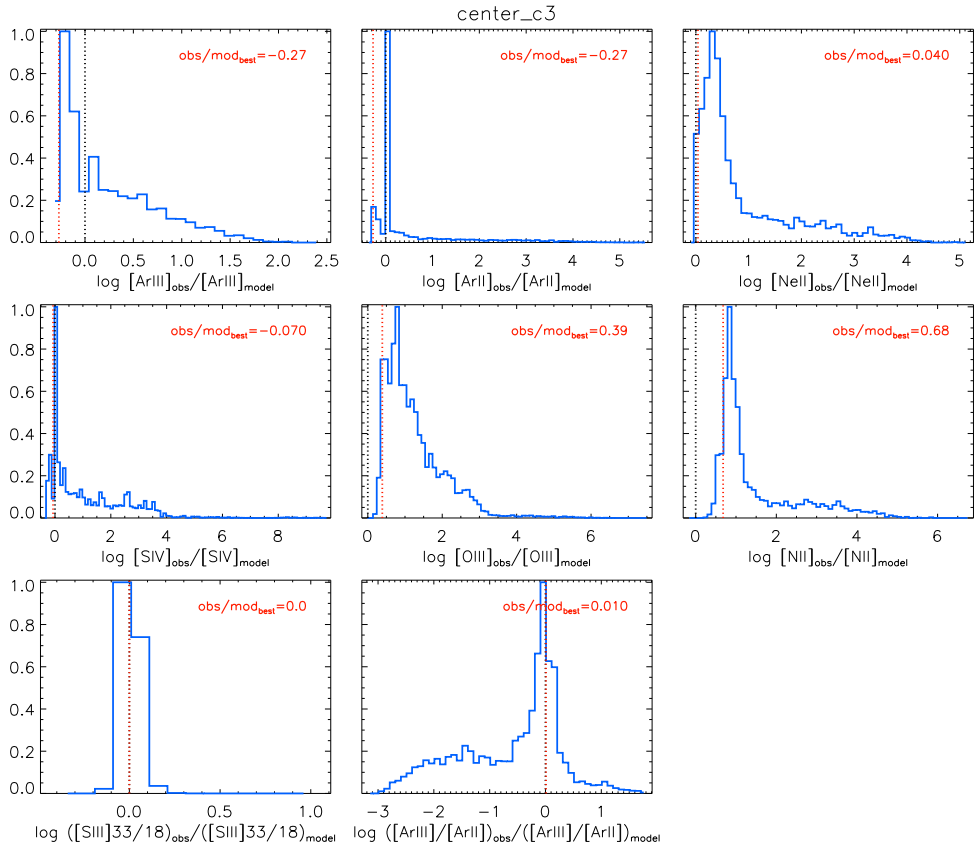

Figure 5.45: PDFs of observed vs. predicted constraint values for clump *Center c*3. For this clump [NII] 121.9 μm is an available constraint. See Figure 5.43 for the plot description.

Table 5.5: Results of the best model parameters with 1σ uncertainties, obtained with the **absolute flux method**.

Region	t_{burst} [Myr]	log U	log n_H [cm^{-3}]	Depth	χ^2_{min}
Cent. c1	$5.3^{+0.4}_{-2.8}$	$-2.2^{+1.2}_{-1.8}$	$2.4^{+0.2}_{-0.4}$	$0.90^{+0.10}_{-0.50}$	3.35
Cent. c2	$5.6^{+0.1}_{-3.1}$	$-1.8^{+0.8}_{-2.5}$	$2.4^{+0.4}_{-0.6}$	$0.55^{+0.45}_{-0.50}$	1.48
Cent. c3	$5.6^{+0.4}_{-2.6}$	$-1.8^{+0.8}_{-2.2}$	$2.6^{+0.2}_{-0.4}$	$0.70^{+0.30}_{-0.30}$	3.63
ArcA c1	$5.7^{+0.1}_{-3.2}$	$-1.0^{+0.0}_{-2.4}$	$2.0^{+0.6}_{-0.2}$	$0.75^{+0.25}_{-0.35}$	1.48
ArcA c2	$5.5^{+0.2}_{-3.0}$	$-1.6^{+0.6}_{-2.4}$	$2.4^{+0.2}_{-0.4}$	$0.75^{+0.25}_{-0.35}$	1.57

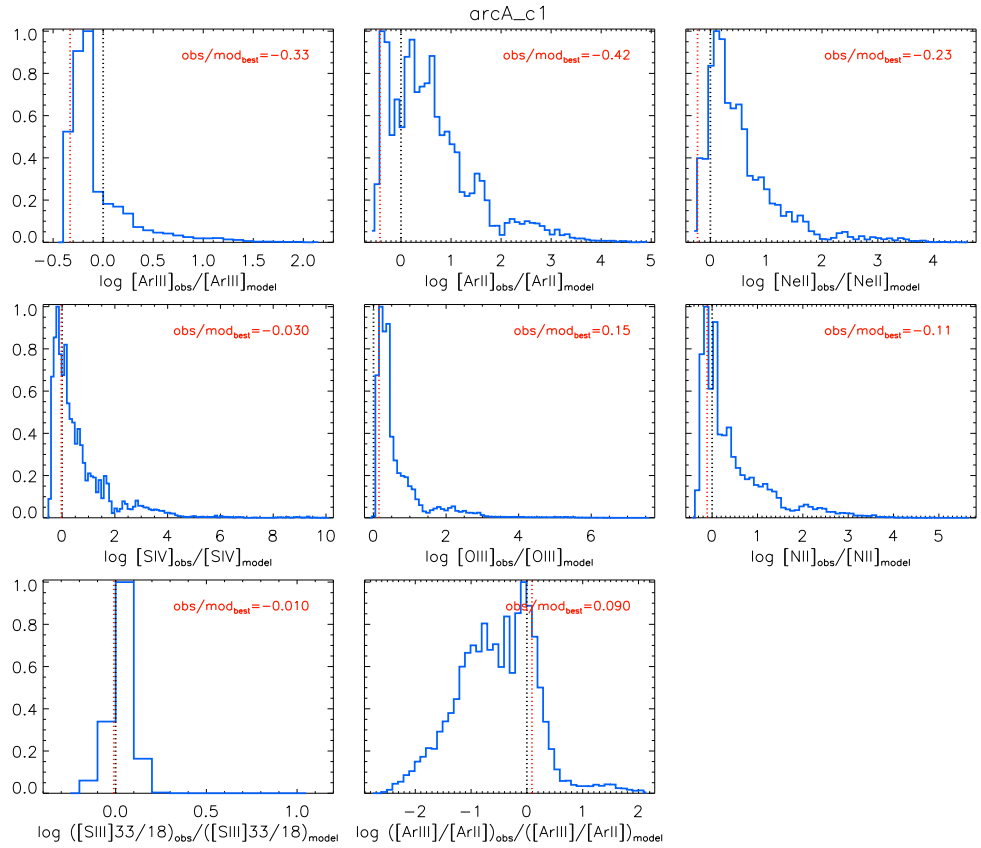

Figure 5.46: PDFs of observed vs. predicted constraint values for the clump *ArcA c*1. For this clump [NII] 121.9 μm is an available constraint. See Figure 5.43 for the plot description.

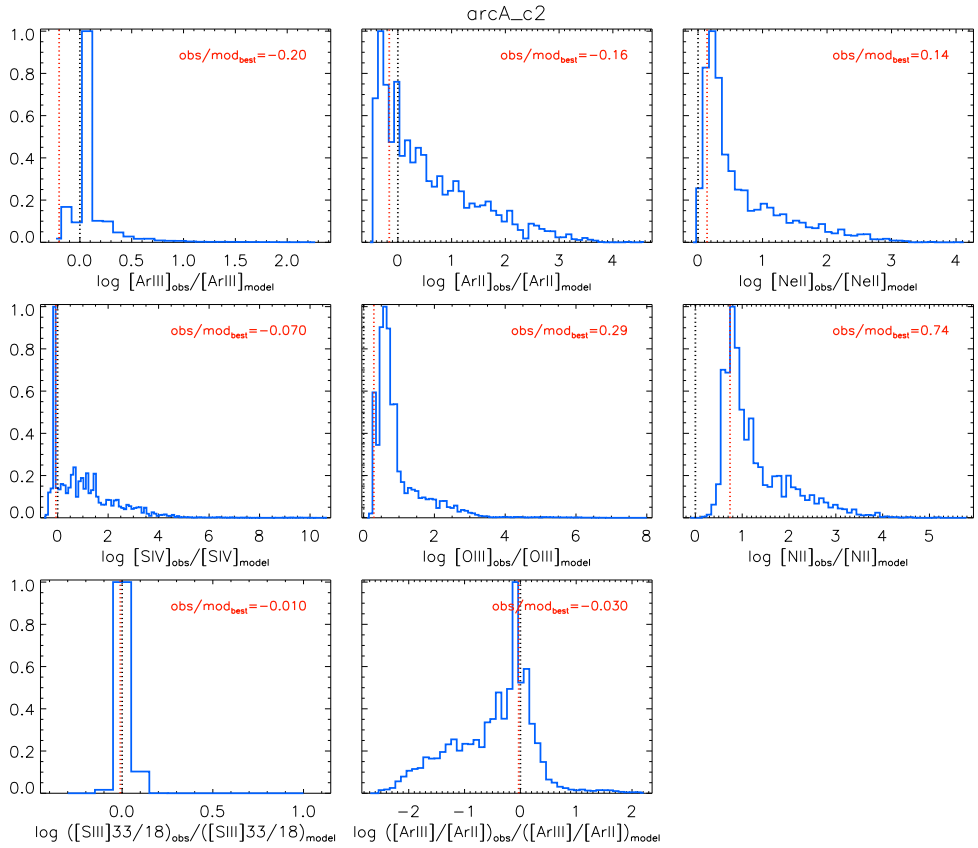

Figure 5.47: PDFs of observed vs. predicted constraint values for the clump *ArcA c*2. For this clump [NII] 121.9 μm is an available constraint. See Figure 5.43 for the plot description.

Zone analysis

By increasing the spatial scale from clumps to zones (few kpc), as we did before with the line ratio method, we are able to include more observational constraints. Hence for the *zone scale*, I was able to include the absolute fluxes of all of the tracers, even the IRS LL tracers that were not included for the clump analysis.

As for the clump analysis, I show in Figures 5.48 the PDFs (top) and statistical histograms (bottom) of the best models (defined by the $\Delta\chi^2$) for the *Central main zone*. The solution for the *Central main zone* is relatively well constrained, with each parameter showing a well-defined peak in the PDF. Furthermore, the histograms of the best models show relatively narrow ranges in each parameter, implying that an error bar can be reliably estimated. This shows that with a suite of well-detected lines from different species with a range of critical densities and ionization potential, and with an adequate method for finding the best model, one can derive all of the physical parameters at once and break the well-known degeneracies between, for instance, the starburst age and the ionization parameter. Even the depth parameter is well constrained (to $\approx$0.8) due to the good detection of [ArII] when integrating over the *Central main zone*.

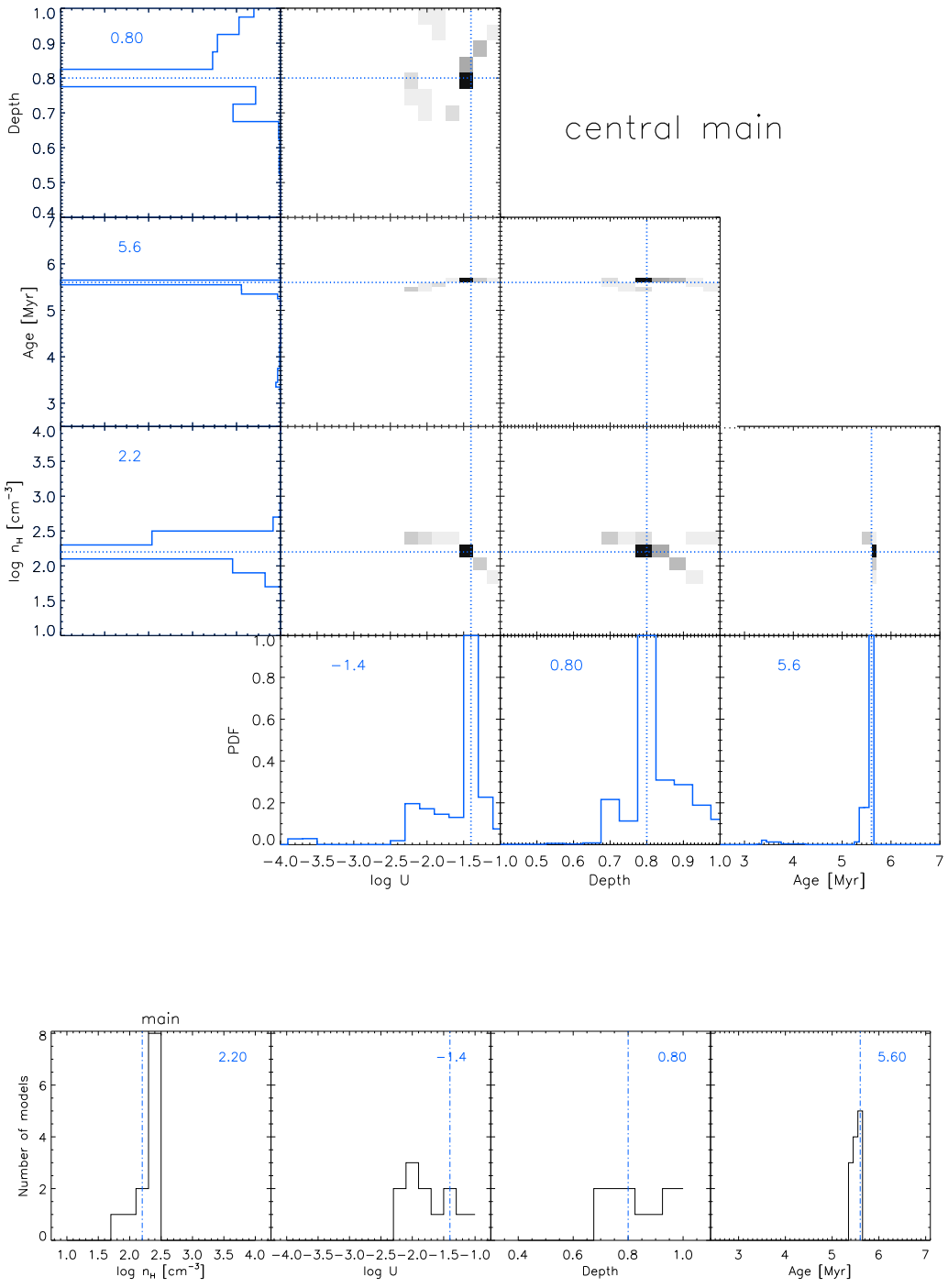

Figure 5.48: Results for the *Central main zone* with the absolute line flux method. *Top*: PDFs, see Figure 5.9 for the plot description. *Bottom*: Histograms of parameter distributions for the best models (see text for details).

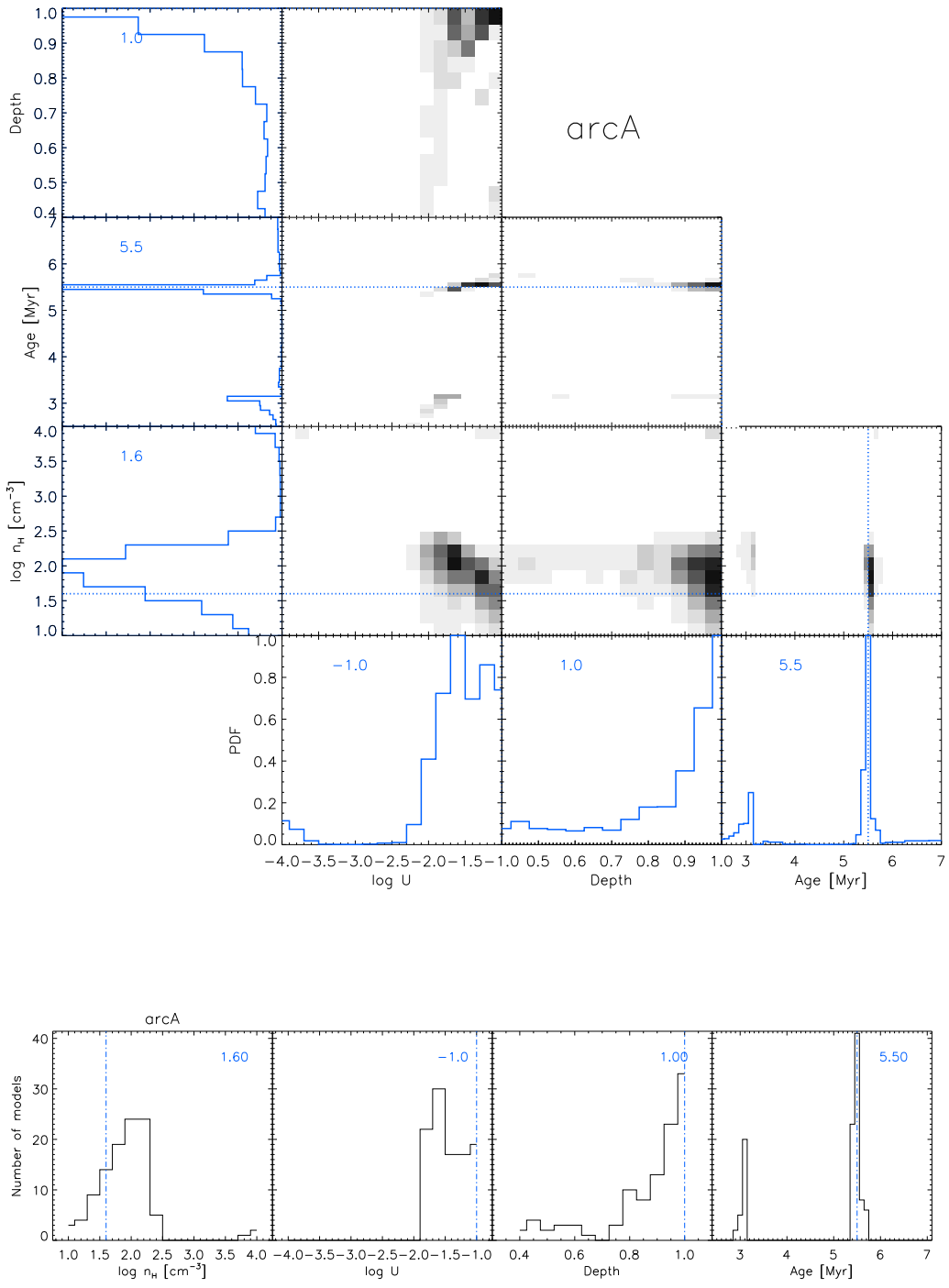

Figure 5.49: Results for the *ArcA* zone with the absolute line flux method. *Top*: PDFs, see Figure 5.9 for the plot description. *Bottom*: Histograms of parameter distributions for the best models (see text for details).

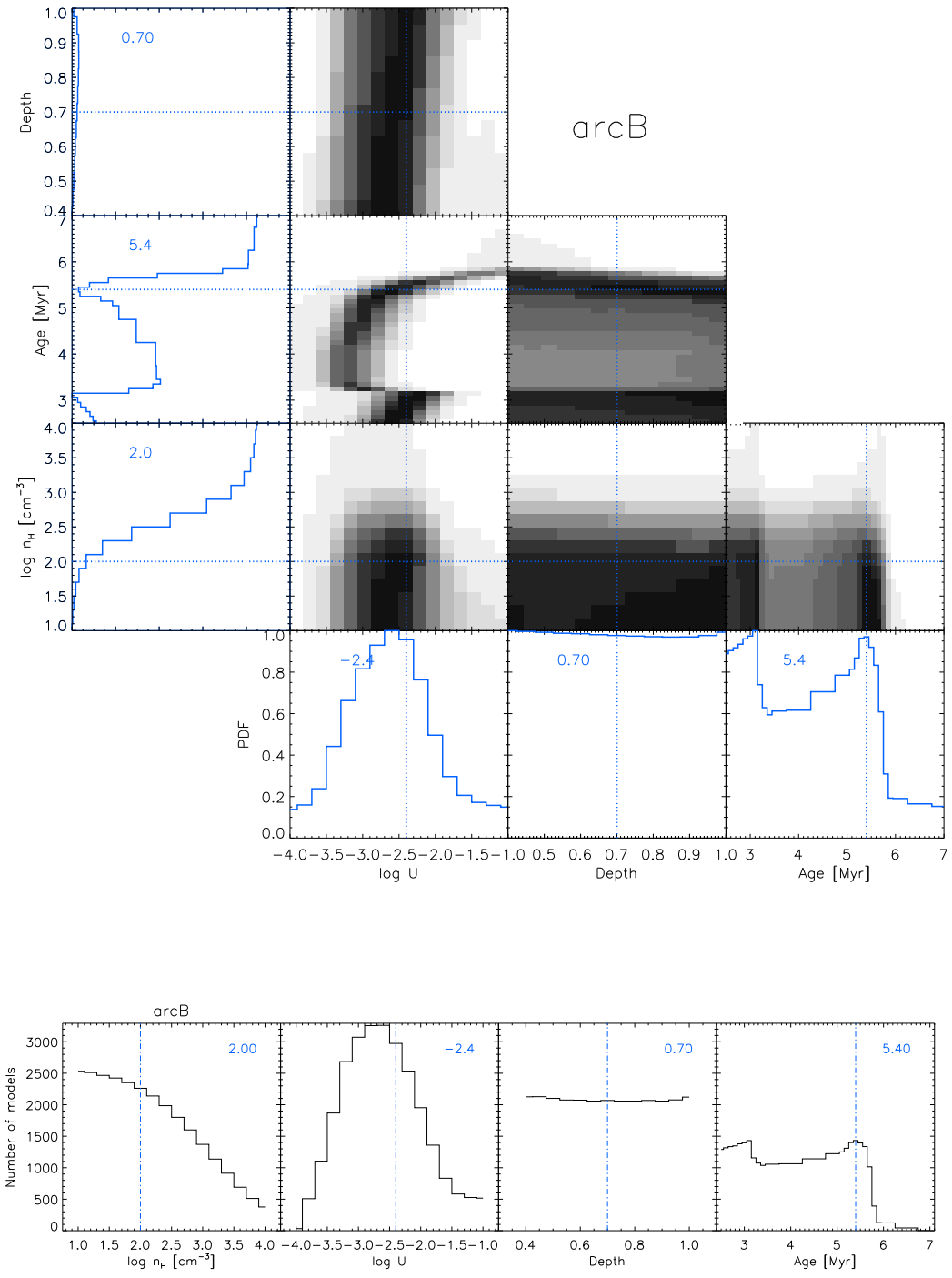

Figure 5.50: Results for the *ArcB* zone with the absolute line flux method. *Top*: PDFs, see Figure 5.9 for the plot description. *Bottom*: Histograms of parameter distributions for the best models (see text for details).

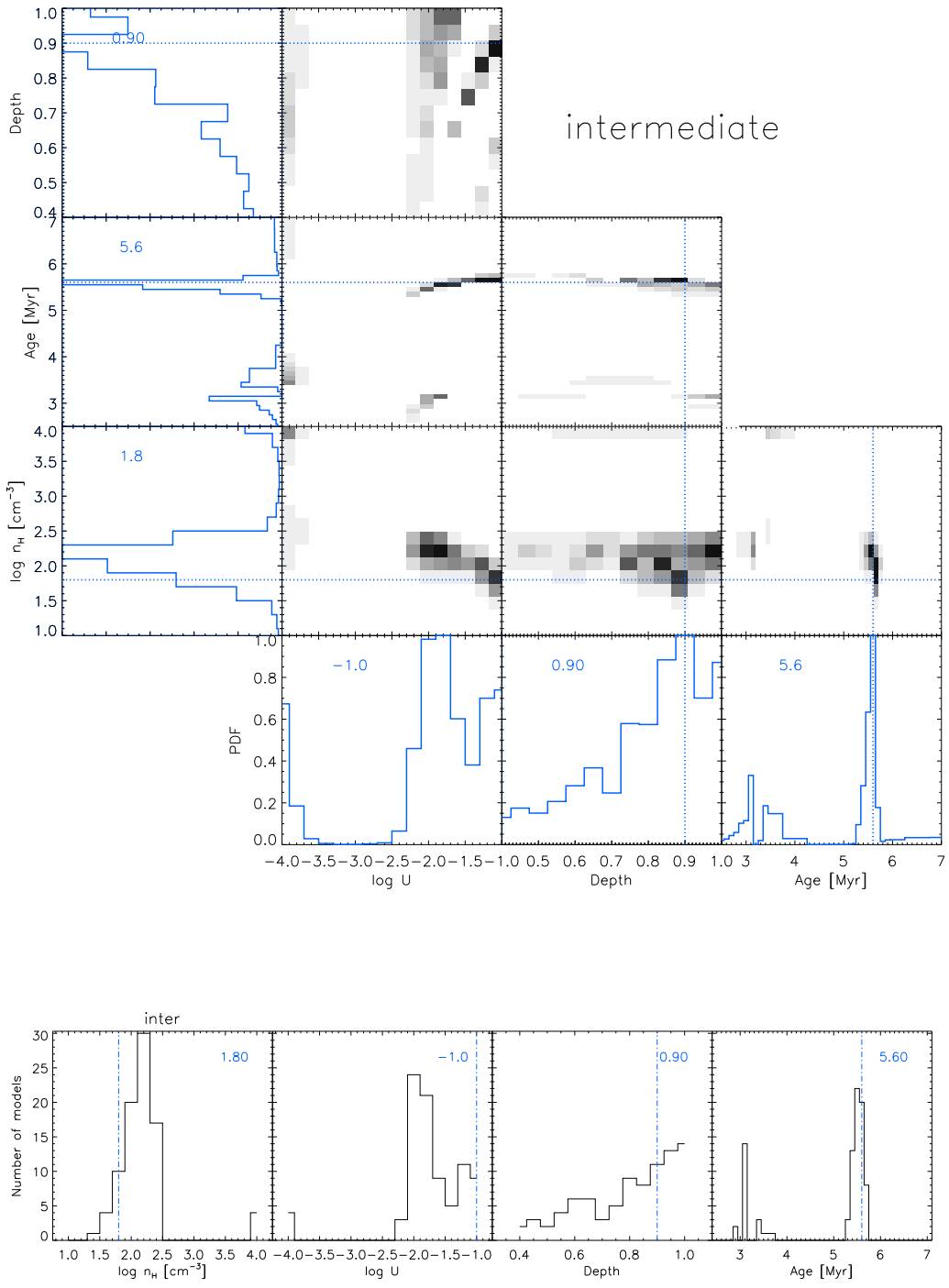

Figure 5.51: Results for the *Intermediate* zone with the absolute line flux method. *Top*: PDFs, see Figure 5.9 for the plot description. *Bottom*: Histograms of parameter distributions for the best models (see text for details).

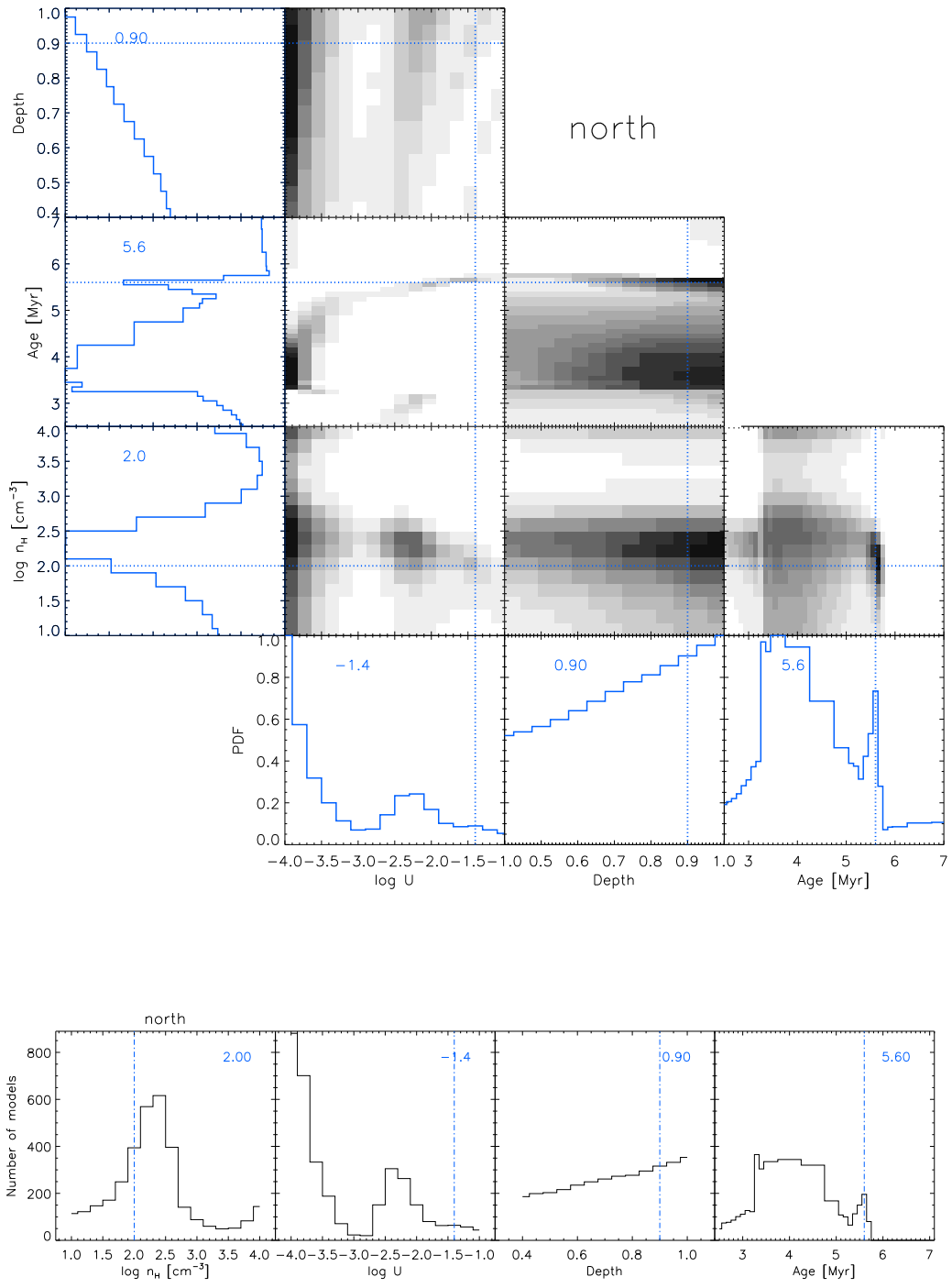

Figure 5.52: Results for the *Central north* zone with the absolute line flux method. *Top*: PDFs, see Figure 5.9 for the plot description. *Bottom*: Histograms of parameter distributions for the best models (see text for details).

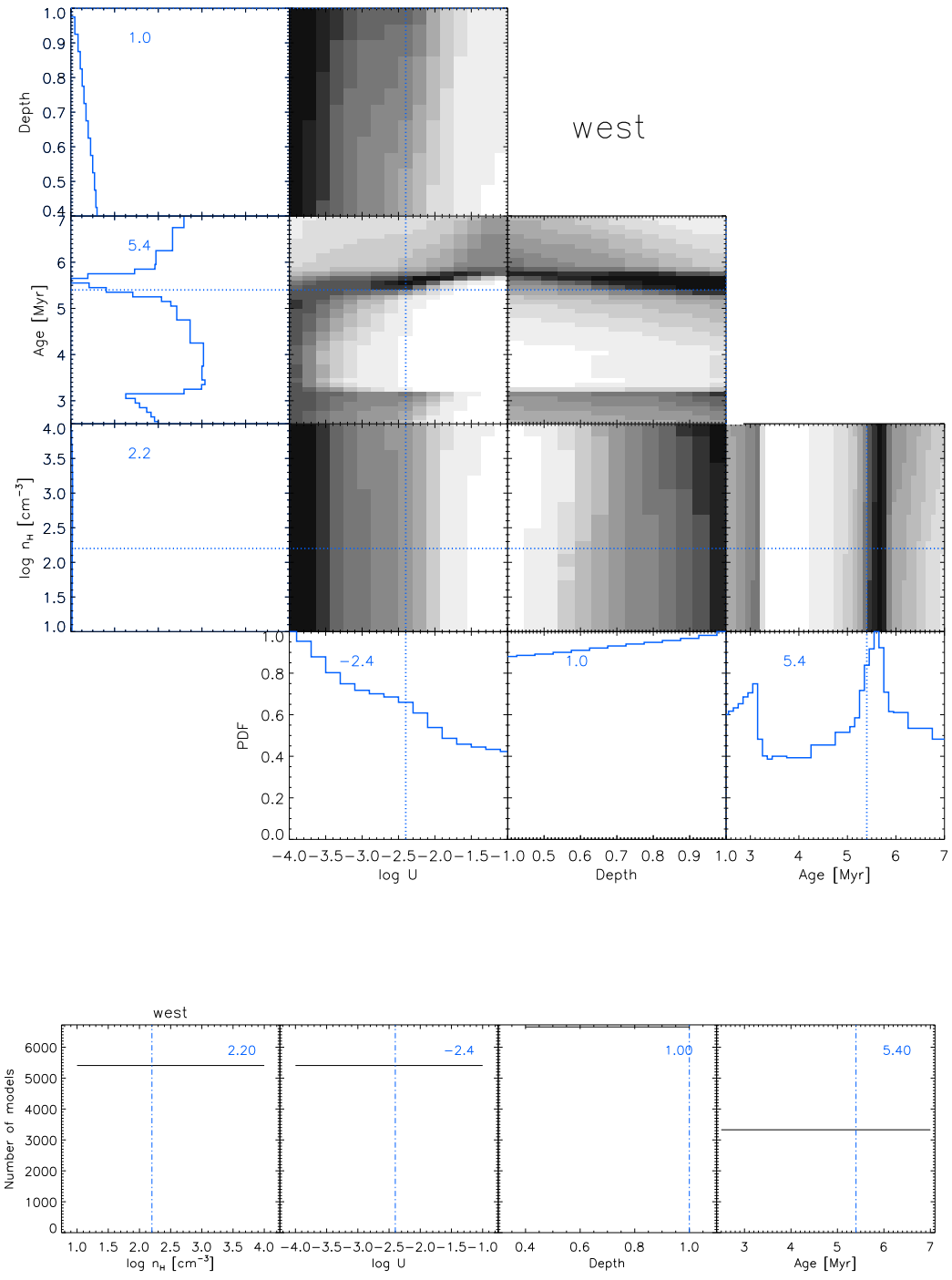

Figure 5.53: Results for the *West* zone with the absolute line flux method. *Top*: PDFs, see Figure 5.9 for the plot description. *Bottom*: Histograms of parameter distributions for the best models (see text for details).

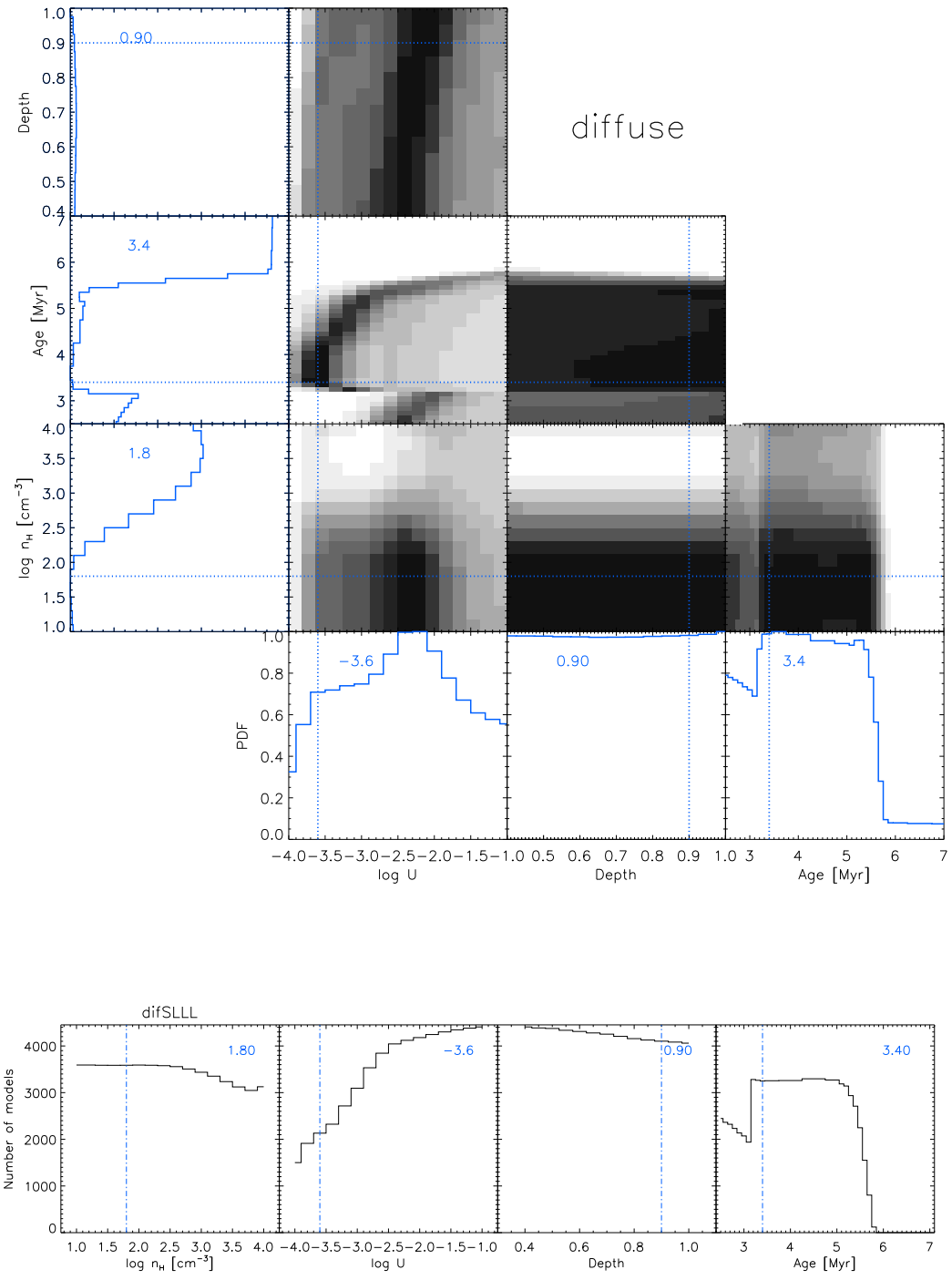

Figure 5.54: Results for the *Diffuse* zone with the absolute line flux method. *Top*: PDFs, see Figure 5.9 for the plot description. *Bottom*: Histograms of parameter distributions for the best models (see text for details).

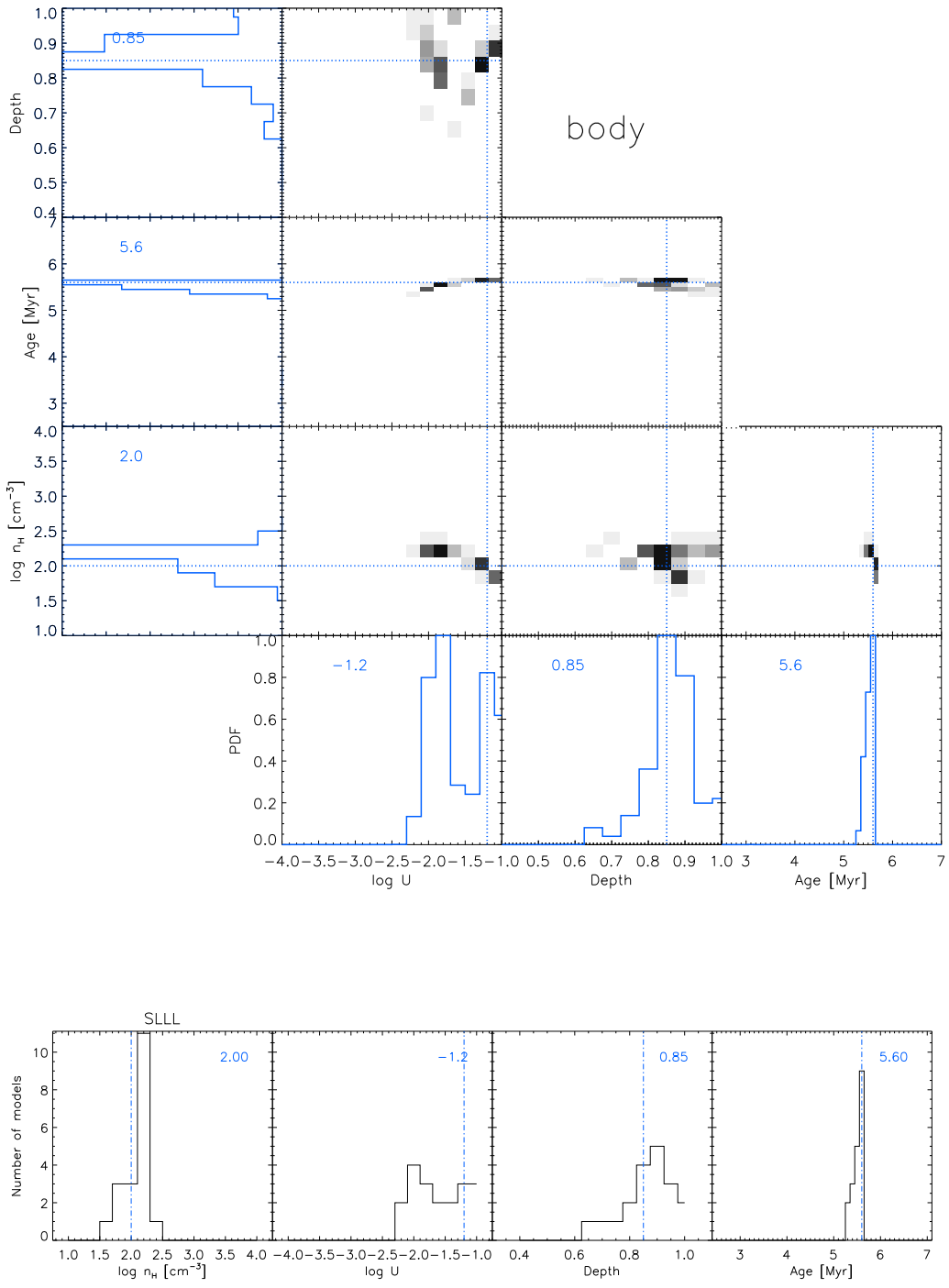

Figure 5.55: Results for the *Body* zone with the absolute line flux method. *Top*: PDFs, see Figure 5.9 for the plot description. *Bottom*: Histograms of parameter distributions for the best models (see text for details).

The PDFs and the statistical histograms for the other zones are presented in Figures 5.49 to 5.54. One can see that depending on the S/N of the tracers used, it becomes impossible to constrain some parameters (in particular the physical depth because of [ArII] and the density because of [SIII] 33μm). The *Intermediate* zone is a star-forming region not as luminous as the *Central main zone* or *ArcA* and it is not covered by the [OIII] 88.4 μm line. The ionization potential in the *Intermediate* zone is somewhat lower than in *Central main zone*. Unfortunately the low S/N of the [ArII] 6.9 μm line prevents a reliable determination of the physical depth for *Intermediate*, although high values (> 0.85) seem to be preferred. The *Diffuse* zone is the most diffuse region observed in all the *Spitzer*/IRS tracers. Since some of the lines ([ArII] 6.9 μm, [SIV] 10.5 μm, and [SIII] 18.7 μm) were not detected, there were not enough constraints to solve for the free parameters. The low S/N of [ArII] 6.9 μm has a direct impact on the depth determination, while the low S/N of [SIII] 18.7 μm has a direct impact on the density determination. Even the starburst age or the ionization parameter cannot be determined, which is in part due to the non detection of [SIV] 10.5 μm.

The largest scale accessible is *Body*, which corresponds to the main body of the galaxy. All tracers are available for this zone except [OIII] 88.4 μm, whose spatial coverage over the main body is incomplete. Results are shown in Figure 5.55. The S/N of each line is larger due to the integration of the flux in a larger area. The various parameters are relatively well constrained, with a density around $100\,\mathrm{cm}^{-3}$ and a large ionization parameter (> -2). This result is significantly different from the result obtained for the *Body* zone with the line ratio method. We attribute this difference to biases in the line ratio method (Section 5.3.2). Interestingly, the depth does not peak at 1, which suggests that even on the scale of the entire body, a significant fraction ($\sim 10\%$) of ionizing radiation may escape. One would need the observations of the MIR and FIR ionized gas lines over the entire IC 10 galaxy scale (as defined by its immense HI halo) to infer whether the fraction becomes close to 0% or not.

As for the clump analysis, I computed the PDFs of the constraints (observation/model), which are shown in Figure 5.56 for the *Central main zone* for illustration. Although we saw that the model parameters were well constrained, with well-defined peaks in the PDFs of each parameter, it is surprising to see that some lines, like [NeII] and [OIII] are reproduced only within a factor of $3-4$. Since these two lines are likely to arise in the relatively diffuse ionized gas ([OIII] because of its low critical density, $\sim 500\,\mathrm{cm}^{-3}$, [NeII] because Ne^+ exists for a large range of relatively low photon energies: 22-41 eV) that can pervade over several kpc and between individual star-forming regions, this result may indicate that another ionized gas component may be

necessary to improve the model.

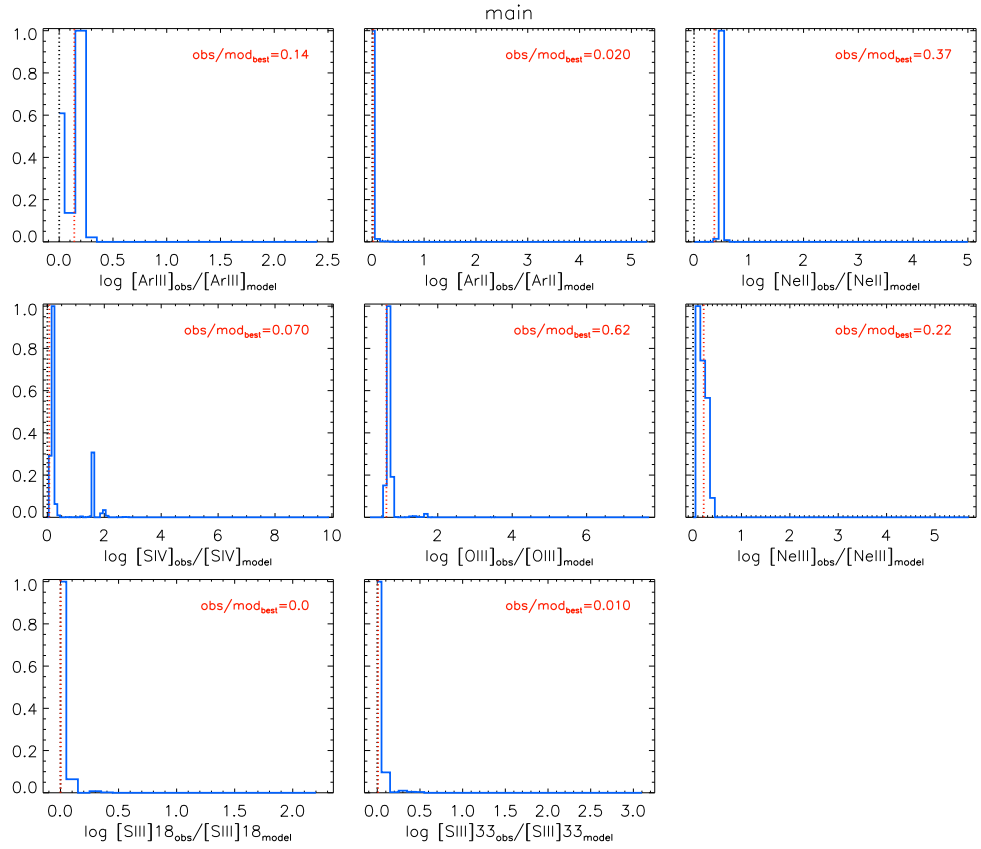

Figure 5.56: PDFs of the observed vs. predicted constraint values for the *Central main zone*. See Figure 5.43 for the plot description.

Table 5.6 summarizes the model solutions with 1σ uncertainty. Overall, the physical depth parameter is larger for the zones as compared to the individual clumps. As stated before, this could indicate that as the spatial scale increases, a larger fraction of ionizing photons is absorbed by the gas and the ionized gas component is globally almost radiation-bounded. The results concerning the ionization parameter and the density suggest important differences between the regions in IC 10, which could be due to the propagation of star formation in the main body of IC 10 and to ongoing sites of star formation where stellar clusters may still be somewhat embedded.

Table 5.6: Summary of the results for each zone.

Zone	age [Myr]	log U	log n_H [cm^{-3}]	depth	χ^2_{min}	N$^{(a)}$	$\chi^2_{min,red}$ $^{(b)}$
Central Main	$5.6^{+0.1}_{-0.3}$	$-1.4^{+0.4}_{-1.0}$	$2.2^{+0.2}_{-0.6}$	$0.80^{+0.20}_{-0.10}$	8.05	8	2.68
ArcA	$5.5^{+0.2}_{-0.2}$	$-1.0^{+0.0}_{-0.8}$	$1.6^{+2.4}_{-0.6}$	$1.00^{+0.15}_{-0.60}$	8.90	7	4.02
ArcB	$5.4^{+1.6}_{-2.9}$	$-2.4^{+1.4}_{-1.6}$	$2.0^{+2.0}_{-1.0}$	$0.70^{+0.30}_{-0.30}$	0.02	4	-
Intermediate	$5.6^{+0.1}_{-3.0}$	$-1.0^{+0.0}_{-1.4}$	$1.8^{+0.8}_{-0.4}$	$0.90^{+0.10}_{-0.50}$	4.11	6	4.11
Central North	$5.6^{+0.2}_{-3.1}$	$-1.4^{+0.4}_{-2.6}$	$2.0^{+2.0}_{-1.0}$	$0.90^{+0.10}_{-0.50}$	0.33	6	0.33
West	$5.4^{+1.6}_{-2.9}$	$-2.4^{+1.4}_{-1.6}$	$2.2^{+1.6}_{-1.2}$	$1.00^{+0.00}_{-0.60}$	0.01	2	-
Diffuse	$3.4^{+2.4}_{-1.0}$	$-3.6^{+3.6}_{-0.4}$	$1.8^{+2.2}_{-0.8}$	$0.90^{+0.10}_{-0.50}$	0.76	4	-
Body	$5.6^{+0.0}_{-0.4}$	$-1.2^{+0.2}_{-0.6}$	$2.0^{+0.4}_{-0.4}$	$0.85^{+0.15}_{-0.25}$	3.71	8	1.24

$^{(a)}$ Number of lines available to constrain the model. $^{(b)}$ The last column shows the reduced χ^2 for those zones with degree of freedom more than 0.

Summary

In the case of the clumps, the **absolute flux method** seems to fail in constraining well the model parameters and I had to include additional constraints ([SIII] line ratio or fixing the age of the starburst) to narrow down the range of parameters. But this does not necessarily imply that the line ratio method is performs better in this case. The range of valid models (within 1σ) around the best models are much larger for the absolute flux method because the χ^2 values of the clumps are lower for this method than for the line ratio method. When all the tracers are available and the S/N is good enough, the absolute line flux method provides satisfactory solutions with reasonable reduced χ^2 values, with few biases and with the possibility of breaking degeneracies between parameters. The investigation of the *Central main zone*, the largest scale accessible with all of the tracers, reveals that another ionized gas component may be necessary.

5.4 Conclusion

In this chapter, I investigated the two methods to compare the observations with model predictions: **line ratios** and **absolute fluxes**. It is well known that some line ratios can unambiguously trace some physical parameters, e.g., the [SIII] line ratio for the density. However, we currently lack specific recipes to access other parameters (starburst age, ionization parameter, physical depth) in a reliable way with infrared emission lines, especially in low-metallicity environments. Cormier et al. (2012) has paved the way by

investigating the global characteristics of the dwarf galaxy Haro 11. Here I examine IC 10 in order to infer the physical conditions using various tracers in different ways, and integrated over different spatial scales.

The **line ratio method** provides different solutions for different sets of line ratios considered. Since this choice is arbitrary, this induces a bias in the best solution found and used for interpretation. Nevertheless I combine the lines in an optimal way, with the smallest uncertainties possible and with an effort to provide similar "constraining power" per parameter (which is a loosely-defined term to describe that many constraints are available for one parameter and/or that the constraints have high S/N). This method allows determination of some properties of the individual clumps, for which the underlying extended emission was removed. However, the high χ^2_{min} values obtained highlighted the impossibility to reproduce all of the line ratios within their 1σ uncertainty. This suggests either that the uncertainties have to be better handled in the calculation (for instance applying the covariance matrix) or that our model may lack some components or that the method is inherently flawed, in the way that the parameter space is probed by the constraints we use. Moving to the *zone scale* with the line ratio method, there is more evidence for a missing ionized gas component with different properties (in particular U and density). I also identify some biases related to the choice of tracers, especially for the largest scales.

The second method, using **absolute line fluxes**, implies an additional free parameter to scale all of the predicted lines, which were computed initially as intensities and not luminosities. This second strategy allows us to treat each tracer without combining them in any way, which bears some advantages (e.g., avoiding difficult-to-choose combinations of lines) and some inconveniences (the lines with the best S/N may be sensitive to only one or two parameters, i.e., not probing sufficiently well the parameter space). In practice, we had to supplement the absolute line fluxes with the [SIII] line ratio, which traces strictly the gas density. The method is able to break degeneracies between the three parameters U, physical depth, and t_{burst} if enough constraints with good S/N are available and providing additional information on the age of the source. Although satisfactory solutions can be found, some discrepancies remain for [NeII] 12.8 μm and [OIII] 88.4 μm , suggesting that our model may be incomplete. Building a true multi-component model that can use spatially-resolved constraints is an approach I envision for the future.

Overall, I find that the [SIII] lines are an important constraint for the density. Without these lines, the density cannot be determined reliably, even if several constraints (in the considered set of lines) are available. The argon lines, instead, are important for the physical depth. In the set of lines used,

we have no good/unique tracer of the starburst age. Moreover, a degree of freedom greater than 1 is also necessary to achieve good results. One major difficulty that I have encountered in this analysis is to identify the best model or a set of good models. There are obviously biases in the choices made, such as selecting models based on a χ^2 threshold. The use of PDFs and histograms provides a good overview of the model results, though. Based on these, on the χ^2, minimum χ^2 values and the PDFs, and on the detailed description of the biases induced by each method/scale, I conclude that the absolute line flux method, supplemented by a few additional constraints, provides the best results in satisfactorily reproducing the observations and constraining the model parameters well.

In the next section, I will discuss the physical conditions derived for each region in IC 10 with results from this method.

Chapter 6

Properties of the ionized gas at different spatial scales

Contents

In the previous chapter, I investigated several star-forming clumps and several zones within IC 10 in order to infer the physical conditions. Particular attention was given to the choice of available tracers and how they can be used to constrain the parameters we wish to derive, i.e., gas density, ionization parameter, starburst age, and the matter- vs. radiation bounded of the ionized gas cloud (traced by the physical depth of the ionized gas cloud with respect to the ionization front). Depending on the method used (line ratios or absolute line fluxes) and spatial scale examined, some biases in the model solution seem to emerge, either related to the way in which the model parameter space is probed by the constraints (bias related to the method) or to the incompleteness of the model considered (with some evidence of a missing ionized gas component with a different density for large integrated regions).

In this chapter, I use the model solutions found with the absolute line flux method, which is preferred over the line ratio method for various reasons explained in the previous chapter. In short, there are few line ratios or combination of lines that can trace unambiguously any given physical parameter, and the selection of lines used as ratios has a significant influence on the model solution. Using absolute line fluxes provides a more stable solution, even though one line may not be usable (for instance because the corresponding S/N is too low). In general, I found that the absolute line flux method is relatively superior in constraining the physical parameters and it is not introducing bias related to the choice of the combination of the constraints.

6.1 Analysis of modeling results

6.1.1 Star formation activity

Most of the star formation activity in IC 10 is concentrated in the optical body, in particular in the compact region to the south (coinciding with several giant molecular clouds) and within the two arcs that extend to the north (Figure 1.14). The optical body is embedded in an extended HI envelope. The complex HI morphology and kinematics likely result from a past merger episode or from accretion of gas in the intergalactic medium (Wilcots & Miller 1998; Ashley et al. 2014).

Our models, using the hypothesis of an instantaneous burst, showed that the stellar population that illuminates the ionized gas seen in the mid- and far-infrared lines ([NII], [SIII], [SIV], [OIII], [NeII], [NeIII], [ArII], [ArIII]) is ~ 5.5 Myr for all the regions we have examined, i.e., the bright compact

clumps and also the large integrated zones (see Figure 5.2). The same age is also found for the largest scale possible in our study, which encompasses most of the optical body.

This result, which may seem surprising at first, is simply due to the detection of appreciable amounts of highly-ionized species such as Ne^{++} together with the hypothesis of an instantaneous burst. Indeed, such highly-ionized species as Ne^{++} are produced by energetic photons from short-lived stars ($\lesssim 6$ Myr). Therefore, the emission of [NeIII] (or [SIV]) drops rapidly after ≈ 6 Myr and becomes negligible compared to [NeII] (or [SIII]). In other words, for ages much larger than ≈ 6 Myr, we should not be able to detect [NeIII] (or [SIV]) anymore, contrary to what we observe. Similarly, the fact that I determined the same young age for the stellar population when examining the entire optical body is due to the integration of regions that are bright in [NeIII]. Even though such a large-scale region likely includes gas with a lower ionization degree, the fact that a ratio like [NeIII]/[NeII] reaches appreciable values is enough to constrain the burst age to about ≈ 6 Myr. In summary, we are bound to find ≈ 6 Myr because (1) a model with instantaneous burst is used, and (2) young stellar clusters contribute to the region we wish to examine. The "dilution" by regions illuminated by older stellar populations does not modify significantly the age determination.

On the other hand, the model results show a second, lower, peak in the PDFs of the starburst age, at around 3 Myr, corresponding to the Wolf-Rayet stage (i.e., when the stellar cluster is more likely to be embedded in the progenitor cloud). In most cases the probability of this solution is much lower than that for ~ 5.5 Myr.

A continuous star formation could also be considered as an alternative to the instantaneous burst. However, the shape of the UV spectrum below 10^3 Å (i.e., for energies above 13.6 eV) is almost independent of the age for a continuous star formation, so we cannot constrain the age based on the use of ionized gas tracers alone. Follow-up studies investigating species in the neutral gas and in the ionized gas may be able to constrain an age under the hypothesis of continuous star formation, due to the relatively wider energy range probed.

Despite these caveats, the fact that [NeIII] and other high-ionization lines are always detected in appreciable amounts in the bright clumps across IC 10 implies that a young stellar population exists throughout the optical body. This suggests that star formation has been triggered on large spatial scales. Interestingly, the HII regions we have analyzed, which are located inside the *Central main zone*, the *ArcA* zone, and the *intermediate* zone, are all distributed along the edge of a large HI and Hα hole. This hole is probably the result of the combined effect of stellar winds or supernovae over several Myrs.

Wilcots & Miller (1998) estimated that the amount of energy necessary to create this hole of gas is 10^{50} ergs, suggesting that it has been produced by strong stellar winds less than $\sim 10^7$ yr ago. Moreover, Wilcots & Miller (1998) also calculated that the expanding bubble shell ought to become gravitationally unstable within 10^7 yr, implying that a second star formation event is likely to be triggered.

Several giant molecular clouds (GMCs) have also been identified around this bubble (Leroy et al. 2006), as well as around the other HI holes distributed throughout IC 10. This is reminiscent of studies of Milky Way GMCs, which are often formed at the overlapping interface between several Galactic HI supershells produced by previous episodes of stellar feedback, such as stellar winds or supernovae (Dawson et al. 2015; Inutsuka et al. 2015). There is growing evidence that such a scenario may explain the location of GMCs in IC 10 and the ongoing star formation episode over kpc scales. This is also supported by the observations of two different populations of stars with ages $\sim$1 Gyr and of $\leq$ 10 Myr (Hunter 2001; Vacca et al. 2007).

6.1.2 Extinction

The observed line emission is affected by extinction due to dust present along the line of sight (Section 1.2.5). IC 10 lies close to the galactic plane (Galactic latitude b = -3.3°), which implies a significant foreground reddening in addiction to the internal reddening. Figure 6.1 shows several extinction curve shapes. The attenuation factor decreases rapidly with wavelength, with very little absorption above $\sim 10\mu$m or so.

Silicate absorption

Silicate absorption bands exist at $\approx$ 10 and $\approx$ 20 μm, possibly with significant extinction around these particular wavelengths. The silicate absorption optical depth at 10μm in IC 10 is about $\tau \approx 0.2$ on average across the main body, with peaks around 0.4 toward the clumps (as measured from the *Spitzer* IRS data cube; Lebouteiller et al. 2012). From τ we calculate an upper limit on the extinction $A_{10\mu m} < 1.086 \times 0.4 \sim 0.4$ mag.

The [ArIII] and [SIV] lines, located at 9.0 and 10.5 μm respectively are the most likely to suffer from extinction issues due to the silicate dust (the silicate absorption band at $\approx$ 20 μm is comparatively weaker). If we wish to calculate the attenuation of the [ArIII] and [SIV] lines, we need to assume a geometry, i.e., either "screen" (assuming that the gas is located behind the dust) or "mixed" (assuming the gas is mixed with the dust). For a screen geometry, we have $I_\nu / I_\nu^{inc} = e^{-\tau}$ as a solution of the transfer of radiation through dust, where I_ν is the observed intensity and I_ν^{inc} is the incident intensity. For an

homogeneous mixture of gas and dust, the equation becomes $I_\nu / I_\nu^{inc} = \frac{1-e^{-\tau}}{\tau}$ (Mathis 1972).

If we assume that the gas and dust are well mixed, the silicate absorption measured toward IC 10 clumps corresponds to an attenuation of less than 50% with lower values expected for the large zones. This value is an upper limit, since our line measurements correspond to spatial scales larger than those used for which the silicate absorption optical depth peaks were determined. Overall, we consider that the infrared lines are little affected by extinction.

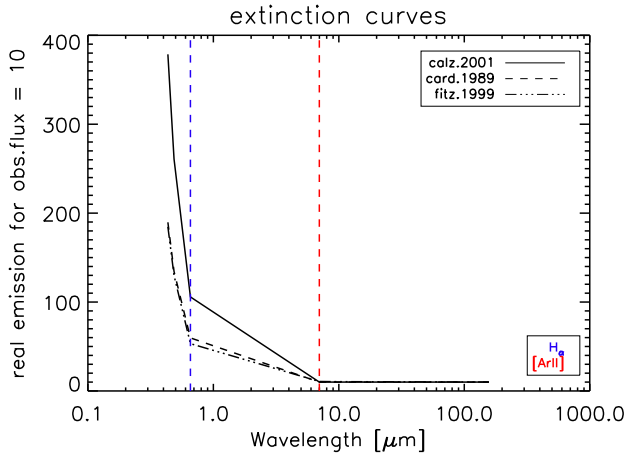

Figure 6.1: Examples of extinction curves used for the Milky Way. The blue and the red lines show the Hα and [ArII] 6.9 μm wavelengths.

Total reddening

Since we do not have a spatial map of the visual extinction seen by the gas modeled in this study, I was not able to use Hα as a constraint to the models. However, assuming the models are well constrained by the suite of infrared lines (that are little affected by extinction; see Section 1.2.5 and Figure 6.1), I can compare the predicted Hα emission to the observed value (not corrected for extinction from Hunter & Elmegreen 2004; Chapter 3) and directly infer the extinction from this comparison. The values obtained with this method using the extinction curve from Cardelli et al. (1989) are presented in Table 6.1. The values found are rather large, with total extinction E(B-V)$>$ 2.

For an independent estimate, I calculated the extinction using the HI recombination line Huα 12.3 μm observed with the *Spitzer* IRS high-resolution pointings (Chapter 2.2.4). From Hummer & Storey (1987) I estimated the theoretical ratio Huα(7-6)/Hα(3-2) expected for case B recombination, assuming a temperature 10 000 K and density of 100 cm^{-3}, resulting in a value of $\approx$294. From the observed Huα I thus compute the expected Hα, which I

Table 6.1: Comparison of the extinction E(B-V) determined toward the clumps in IC 10.

Clump	*Cloudy* prediction	Huα/Hα method	Borissova et al. (2000)[a]
Center c1	2.15	-	1.82
Center c2	2.33	-	1.88
Center c3	2.72	2.55±0.07	2.18 - 1.45 [a]
Arc c1	2.35	2.41±0.06	1.72
Arc c2	2.50	2.57±0.04	1.81

(*a*) Borissova et al. (2000) estimated the extinction values using the ratio Brγ/Hα. The error estimated is 10-15% and the clump center c3 is resolved in two HII regions.

then compare to the observed value in order to infer the extinction using the extinction curve from Cardelli et al. (1989). Results can be found in Table 6.1 (third column). I find E(B-V) values around $2.4 - 2.6$, i.e., quite similar to the values obtained from the Cloudy model predictions.

Table 6.2: E(B-V) from previous works.

Reference	E(B-V) mag	method
Sandage & Tammann (1974)	0.87	HII regions
Ciardullo et al. (1989)	0.47	PN
Massey & Armandroff (1995)	0.75 - 0.80	Wolf-Rayet stars
Sakai et al. (1999)	1.16	Cepheids variable stars
Borissova et al. (2000)	1.05±0.10	Comparing the red supergiants of IC 10 and IC 1613
	1.8±0.2 mag	Hα emission from the star forming regions
Richer et al. (2001)	0.77±0.07	Optical spectroscopy of HII regions
Hunter (2001)		TRGB
Kim et al. (2009)	0.98±0.06	*UBV* photometry

How do our values compare to measurements in the literature? For the reddening, previous studies report values between 0.7 mag to 1.0 mag, depending on the method used. Using Cepheids variable stars, for example, Sakai et al. (1999) calculated E(B-V) = 1.16 mag, while Massey & Armandroff (1995) estimated E(B-V) = 0.75 - 0.80 mag based on Wolf-Rayet stars

and the blue stellar population. Table 6.2 summarizes the reddening values from the literature[1]. These measurements correspond to various regions and various spatial scales, so the comparison with my estimates toward the clumps are not trivial. Borissova et al. (2000) investigated, however, several regions used in my study (Table 6.1; fourth column). While the two independent methods I used (Cloudy prediction and Huα) provide consistent values for E(B-V), the values I find are significantly larger (by a factor of a few) than those measured by Borissova et al. (2000). A possible explanation for these discrepancies lies in the selection of the tracers used to estimate E(B-V). Borissova et al. (2000) used the line ratio Brγ/Hα while I used longer wavelengths lines (either the metallic species used for the Cloudy predictions or the HI recombination line Huα). With infrared lines, we are able to peer through the dust more than at optical wavelengths. If we reason in terms of a single dense cloud, optical lines are able to probe the outer layers of the cloud, while infrared lines probe deeper, to larger dust column densities. Hence it seems natural that a larger extinction be measured with infrared tracers.

The measurement of the visual extinction seen by the photons in the gas enables the use of many optical lines as constraints to the models. These new constraints complement the infrared tracers, by giving access to lines of different species, with different critical densities. Some degeneracies that still exist between the physical parameters may be lifted this way. This is an interesting new prospect that optical and infrared lines can be used in a consistent study, in which extinction is not assumed but inferred.

6.1.3 Porosity of the ISM

The Cloudy models include a free parameter that corresponds to the physical depth of the cloud, measured relatively with respect to the ionization front. The main tracers for this parameter are the fluxes of [ArII] 6.9 μm and [NII] 121.9 μm relative to the other emission lines, as both [ArII] 6.9 μm and [NII] 121.9 μm emit near or at the ionization front (Figure 4.7; see also explanation in Section 4.3.2). A depth of 1 implies a radiation-bounded cloud, while a lower depth value implies a matter-bounded cloud. In the previous Chapter, I found that the depth is always lower than 1 and that the depth value increases with the size of the region considered, from values as low as 0.5 for the clumps, to about 0.9 for large integrated zones (e.g., *Central main zone* and *Body*).

Before interpreting these values further, the physical meaning of the phys-

[1]For more references see Demers et al. (2004).

ical depth parameter should be discussed. Our models consider a single central ionizing source and a single ionized gas cloud (Chapter 4.3). Therefore, the depth parameter corresponds to the depth of the modelled cloud. In reality, many clouds contribute to the observed emission-lines used as tracers, with a total covering factor that may be lower than 1 (i.e., some radiation may escape completely) and/or with a combination of matter- and radiation-bounded clouds. Therefore, the physical depth parameter represents some kind of average property (this is no different from the other parameters, in particular density and ionization parameter). Nevertheless, it should be kept in mind that the depth parameter (or fraction of escaping ionizing photons) calculated for a single cloud may also be interpreted in a fraction of matter- vs. radiation-bounded clouds around the ionizing source.

Our results imply that a significant fraction of ionizing photons is able to escape the clumps. Such results are compatible with the investigation performed by Hidalgo-Gámez (2005). They suggest, in fact, that the photons leaking from HII, in addition to the ionization provided by the WR stars, are the ionizing source of the diffuse ionized gas. This could lead to some important constraints for the models of the PDRs, as such regions obviously require a radiation-bounded cloud. In other words, the estimated fraction of escaping ionizing photons may be used to infer a covering factor of radiation-bounded clouds around the ionizing source, which, in turn, sets important constraints when comparing PDR model predictions with the observations.

The depth parameter is larger when larger zones are considered, with values reaching almost 1, implying that the modelled cloud is almost radiation-bounded. Unfortunately we are not able to measure the depth parameter for a spatial scale larger than the optical body. IC 10 shows extended HI structures, and it is likely that the fraction of escaping ionizing photons should be close to zero when considering the entire galaxy. Such a result would be compatible with the direct measurements of the Lyman continuum in external galaxies, which suggest a small fraction of escaping ionizing photons (e.g. Leitet et al. 2013; Cowie et al. 2009; Bridge et al. 2010).

Overall, the fact that the ISM is porous over large spatial scales is also related to the abundance of dust in the galaxy, and therefore to the metallicity. Several studies already suggested that the ISM at low metallicity is relatively more porous than more metal-rich environments (e.g. Madden et al. 2006; Cormier et al. 2015; Lebouteiller et al. 2012; Kawada et al. 2011). The ISM porosity is, however, a relatively loosely defined term. The porosity is often indirectly witnessed through the [OIII] 88.4 μm emission line with its low critical density, as it is the brightest infrared lines in low-metallicity galaxies (while [CII] is relatively brighter in more metal-rich environments, see Section 3.2.2, Cormier et al. (2015)). Furthermore, the [OIII] 88.4 μm emission

is distributed over surprisingly large spatial scales in IC 10 and other region in the Magellanic Clouds (Lebouteiller et al. 2012; Kawada et al. 2011). The results obtained here for IC 10 suggest that the porosity issue can be addressed in a more quantitative way. This requires that similar models, such as those I performed for IC 10, be adapted to other spatially-resolved objects with various metallicities.

6.1.4 Origin of [CII], [FeII] & [SiII]: ionized vs. neutral gas

The C^+, Fe^+ and Si^+ ions have ionization potentials lower than that of hydrogen (11.3 eV for C^+, 7.9 eV for Fe^+ and 8.2 eV Si^+; see Figure 1.5), while the potential of the next ionization stage is above 13.6 eV. Therefore, C^+, Fe^+ and Si^+ may exist in the neutral gas (i.e., where H is into H^0) and in the ionized gas (where H is into H^+; Chapter 1.2.4). In the neutral gas, the collision partners are mostly H^0, H_2, and free electrons (coming from the ionization of species with ionization potentials below 13.6 eV and from cosmic ray and soft X-ray photoionization of H). In the ionized gas, the collision partners are e^- (and protons, though the collision strength with e^- is comparatively much larger) coming from the ionization of H by FUV photons. Observationally, C^+ has been observed in the surface layers of PDRs illuminated by the radiation field of massive stars (Negishi et al. 2001), but it is also observed in the ionized gas phase (Madden et al. 1993; Abel et al. 2005; Cormier et al. 2012).

Since the origin of C^+ (and Fe^+ and Si^+) is ambiguous, the use of [CII] 157.7 μm (and [FeII] 25.9μm and [SiII] 34.8μm) to constrain the physical conditions of the ionized gas in our models is not straightforward. Instead of assuming a correction factor accounting for the fraction of the line emission arising in the neutral gas, I calculate the [CII] (and [FeII] and [SiII]) emission predicted by the models in the ionized gas, which I then compare to the observed values. Since the clump decomposition is difficult in [CII] because of the low spatial resolution of *Herschel* PACS as well as difficult in [FeII] and [SiII] (observed with *Spitzer* IRS) because of the low S/N, I could make this comparison for the integrated zones only. For each zone, the line fluxes have been integrated using the methods presented in Section 5.2. Table 6.3 shows the observed values for each *zone*. The lines are not detected toward the *West* zone, so we exclude this zone from the following discussion.

Using the observed values, I was then able to compare to the CLOUDY predictions *for the ionized gas*. Since the models I have been using contain a single component, the modeled ionized gas effectively corresponds to the HII

Table 6.3: Integrated fluxes of [CII]157.7μm, [FeII] 25.9μm and [SiII] 34.8 μm for each zone.

Zone	[CII]157.7μm	[FeII] 25.9μm	[SiII] 34.8 μm
Central Main	$1.070^{\pm 0.011}$e-14	-	$2.730^{\pm 0.167}$e-15
Central North	-	$8.867^{\pm 3.500}$e-17	$3.457^{\pm 0.784}$e-16
ArcA	$3.428^{\pm 0.067}$e-15	-	$9.238^{\pm 1.233}$e-16
Intermediate	-	-	$1.216^{0.108}$e-15
ArcB	$2.269^{0.104}$e-15	-	-
Dif.SLLL	-	-	$2.525^{\pm 0.698}$e-16
Body	-	-	$1.060^{\pm 0.060}$e-14

regions and not to the diffuse ionized gas. This implies that the difference observed between the model predictions and the observed values for [CII], [SiII], and [FeII] can either be due to the PDR (neutral) component or to a potential diffuse ionized gas component.

Figure 6.2 shows the PDFs of the observed over predicted line intensity ratio for [SiII] 34.8 μm ($[SiII]_{obs}/[SiII]_{mod}$) and [CII] 157.7 μm ($[CII]_{obs}/[CII]_{mod}$) for the three zones: *Central main zone*, *ArcA* and *ArcB*, which are the only zones fully covered by the [CII] 157.7 μm map. These PDFs show a Gaussian distribution, with the peak indicating the ratio of the observed [CII] 157.7 μm over the best model solution, and with the width representing the uncertainties related to the solutions of the model (see Section 5.3.3).

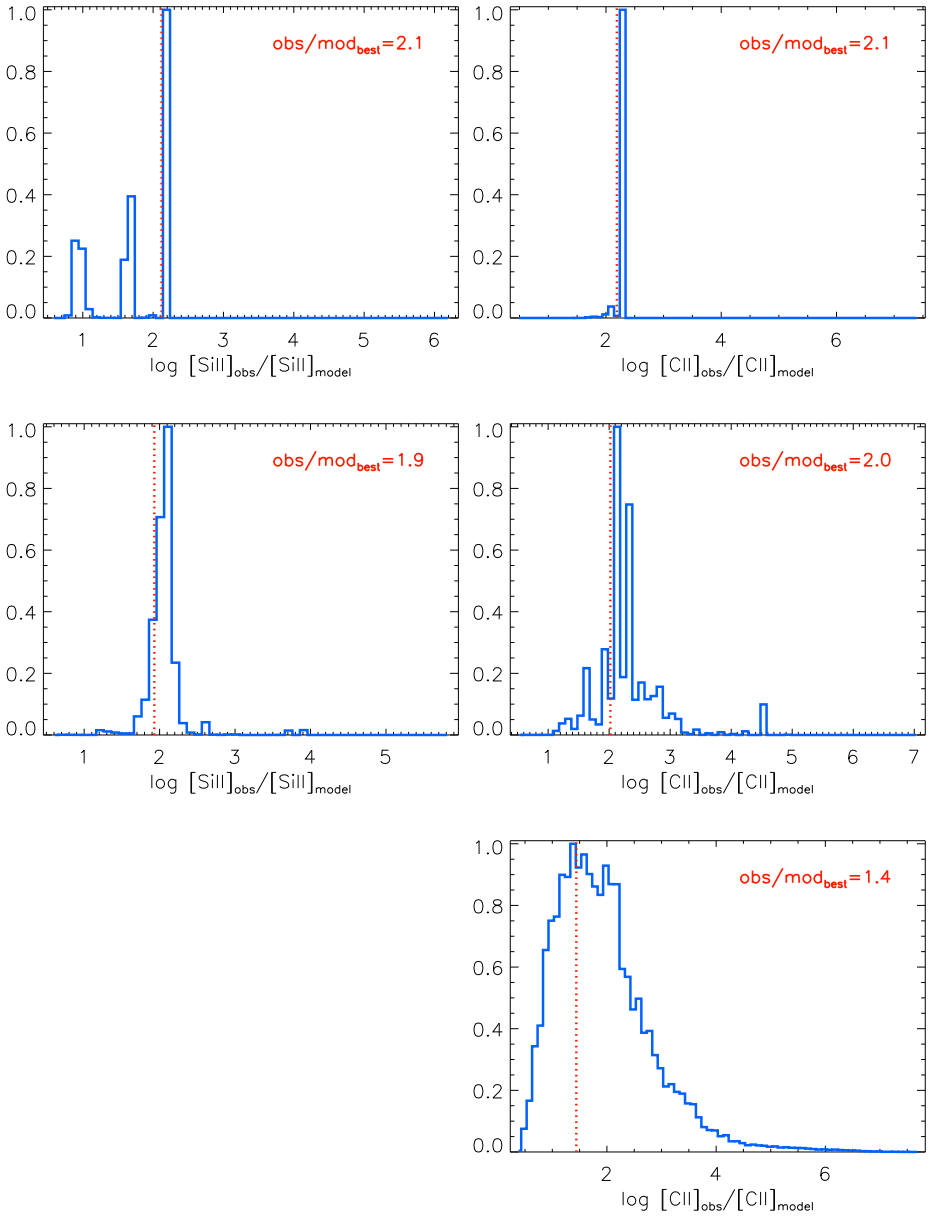

Figure 6.2: PDFs of the observed over predicted emission [SiII] 34.8 μm (left) and [CII] 157.7 μm (right) for the zones *Central main zone* (top), *ArcA* (middle) and *ArcB* (bottom). The vertical lines indicate the observed vs. predicted values for the best model (lowest χ^2), with the corresponding value shown in the corner.

The ratios of the observed [CII] 157.7 μm over the best model [CII] 157.7 μm for each region are quite large: they range from about 30 to 150. From this we can conclude that observed [CII] 157.7 μm in the *Central main zone* and both arc zones does not arise from the ionized gas in the HII regions. The same conclusion can be reached for [SiII] 34.8 μm. The fraction of [CII] and [SiII] arising in the ionized gas of the HII regions is a few percent at most.

Figure 6.3 shows the PDFs of the observed over predicted line intensity ratio for [SiII] 34.8 μm ($[SiII]_{obs}/[SiII]_{mod}$) and [FeII]25$\mu$m ($[FeII]_{obs}/[FeII]_{mod}$) for the *North* zone, which is the only zone with a clear detection in [FeII]25μm. Both PDFs (for [SiII] and [FeII]) show distributions with two peaks, with the lower probability peak corresponding to the model solution (which, as a reminder, is found by using ionized gas emission-lines). Again, the result shows that the fraction of [SiII] and [FeII] arising in the ionized gas of the HII regions is quite low.

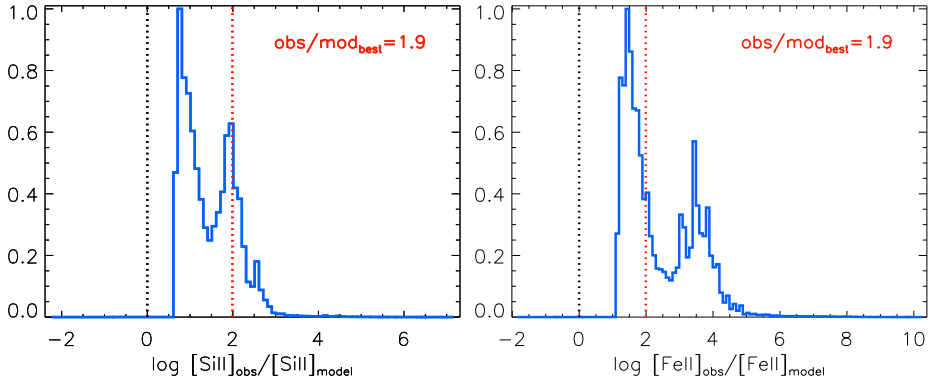

Figure 6.3: PDFs of the observed over predicted [SiII] 34.8 μm (left) and [FeII]25 μm (right), for the *North* zone. See Figure 6.2 for the plot description.

Finally, Figure 6.4 shows the PDFs of $[SiII]_{obs}/[SiII]_{mod}$ for the remaining zones: *Intermediate*, *Diffuse* and *Body*. The distributions for the *Intermediate* and *Body* zones display well-defined peaks that coincide with the best-fit solutions. The corresponding fraction of [SiII] emission in the ionized gas of the HII regions is also quite low, as for the other regions. However, the PDF of the *Diffuse* zone, has a much broader distribution and the value of the observed [SiII] 34.8 μm emission over the best model solution is at the low end cutoff of the PDF, preventing a definite conclusion on the origin of the observed [SiII] for this zone. As discussed in Chapter 5, there is no satisfactory solution for the *Diffuse* zone so the "best" solution considered should be regarded with caution.

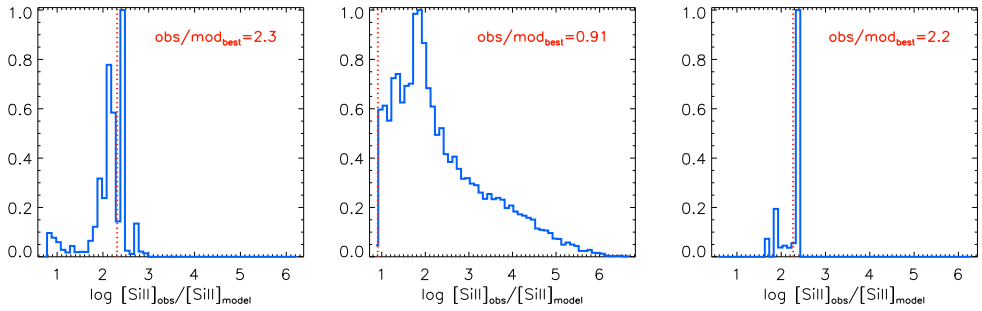

Figure 6.4: PDFs of the observed over predicted [SiII] 34.8 μm for the zones *Intermediate* (left), *Diffuse* (middle) and *Body* (right). See Figure 6.2 for the plot description. Note that for the *Diffuse* zone, the value of the observed [SiII] 34.8 μm emission over the best model solution is only an upper limit.

Hence, using the model solutions to compare to the observed [CII], [SiII], and [FeII], I find that these lines seem to originate either in the PDR or in a potential diffuse ionized gas component (which is not accounted for in the models). This result holds for the integrated zones, as the calculation for the clumps was not possible.

Another method to estimate the fraction of [CII] in the ionized gas is to use N^+ as a tracer of C^+ in the ionized gas (Section 1.2.4 and Section 3.2.2). Knowing the elemental abundance and knowing the ionization fractions C^+/C and N^+/N, the theoretical ratio [CII]/[NII] 122μm is then a function of gas density and temperature. The temperature plays a minor role and the ratio mostly depends on density. In Figure 3.10, one can see that the observed [CII]/[NII] calculated pixel-by-pixel is much larger than the theoretical ratio, for any density. The difference is due to the presence of [CII] in the neutral gas. Hence, this result confirms our previous findings using the model predictions that [CII] does not arise significantly from the ionized gas in the HII region. It also suggests that [CII] does not arise from a potential diffuse ionized gas component either. We have to conclude, therefore, that [CII] emission is, in fact, dominated by PDRs.

Apart from [CII]/[NII], other ratios can be used to estimate the fraction of [CII] in the ionized gas, such as [CII]/[ArII] or [CII]/[NeII]. The latter ratios, however, are much more sensitive to density as compared to [CII]/[NII], because of the larger critical density for [ArII] and [NeII] (Figure 1.5). Nevertheless, I find that both methods, using [CII]/[ArII] or [CII]/[NeII] result in a negligible fraction of [CII] arising from the ionized gas for the zones in Table 6.3 with [CII] detections (plots not shown). Results for [SiII], using [SiII]/[ArII] and [SiII]/[NeII] to estimate the fraction of [SiII] in the ionized

gas, show that [SiII] emits predominantly in the neutral gas. The fraction arising in the neutral gas is much less, however, than for [CII]. We note that this result bears significant uncertainties because the silicon abundance is not well measured.

In summary, [CII] emission arises mostly in the neutral gas, and [CII] can therefore be used without any correction for the future PDR modeling effort. For [SiII], our results are less clear, in particular because the silicon abundance is not well known, but it seems [SiII] also emits mostly in the neutral gas. For [FeII], we were not able to differentiate possible emission from the neutral gas or from a diffuse ionized gas component not accounted for in the models.

6.1.5 Physical conditions inferred at different spatial scales

The analysis of the physical properties at different spatial scales allows me to investigate how the integrated emission lines can be used to infer the physical conditions in *unresolved* objects. In other words, I wish to examine how the physical conditions derived with integrated measurements relate to the measurements at smaller scales (typically the size of star-forming regions/clumps such as those I examined in IC 10).

While the physical depth parameter and the density change depending on the spatial scale examined (Section 6.1.3), similar stellar cluster age and ionization parameter are found for the integrated *Central main zone* as compared to the star-forming clumps *Center c1*, *Center c2* and *Center c3* which are the brightest components in *Central main zone* (Table 5.5 and Table 5.6). The same conclusion is reached for the *ArcA* zone and the *ArcA c1* and *ArcA c2* clumps. This suggests that the properties estimated at the $\sim$ 300 pc scale (zones) are dominated by the brightest compact clumps ($\sim$ 25 pc scales). The largest scale accessible corresponds to most of the optical body (608 pc $\times$ 855 pc). For this zone, the physical properties obtained are compatible with the bright regions associated with star formation. Thus, once again, the model solution corresponding to the large scale reflects the properties of the brightest clumps, which are the ones associated with star formation.

A caveat should be added about the presence of diffuse ionized gas. While I find similar physical conditions are obtained for various spatial scales as long as bright components dominate the emission in the integrated zone, this is assuming a *single* component in the models. The results concerning the largest scales show, however, that another ionized gas component, more

diffuse, may be required. Therefore, while the denser component related to the young clusters seems to be well constrained by a model with a single component at any spatial scale, such a model misses and ignores other phases that may be important, depending on the scientific objective.

6.2 Conclusion

In this chapter I have analyzed the nature of ionizing sources as well as the physical properties of the ionized gas at different spatial scales of IC10, based on the observational constraints (Chapter 3) and the modeling solutions obtained in the previous Chapter 5. The main results are the following:

- The physical properties of the clumps are quite uniform, suggesting a common origin for their star formation activity. The origin of the ionizing sources in the HII regions analyzed in this study, could be related to the feedback from stellar winds or supernovae of a previous generation of stars.

- For each clump, I have estimated the total extinction with two different methods: 1) based on the model solution, I compared the observed Hα with that predicted by the model, and 2) using Huα(7-6), I used the the theoretical ratio of Huα(7-6)/Hα(3-2) to calculate the expected Hα. The values obtained with the two methods are similar. The discrepancy between the extinction values estimated with this work and those in the literature can be explained by the fact that I used infrared tracers, which can probe the extinction over deeper regions within the clouds, as compared to UV and optical tracers. I have also estimated that the extinction due to the silicate absorption features is not significant.

- Using [ArII] 6.9 μm and [NII] 121.9 μm I determined that the clumps are matter-bounded clouds, i.e., with a significant fraction of ionizing photons escaping the nebula. Solutions for larger spatial scales suggest that the clouds are almost radiation-bounded. The matter-bounded nature at almost any spatial scale indicates that the ISM is quite porous, which is possibly due to the low metallicity of the environment.

- I have investigated the origin of the [CII] 157.7 μm, [FeII] 25.9 μm and [SiII] 34.8 μm emission to determine the fraction of the emission arising from the ionized gas phase. Comparing the predicted line emission of the best-fit model with that observed, I found that most of the emission of the [CII], [FeII], and [SiII] arises in the PDR component.

- The physical properties derived when using integrated measurements are very similar to those of the star-forming clumps. However, a diffuse component was already suggested in the previous Chapter for the largest scale, and a multi-component model would be useful to determine the properties of this diffuse phase.

This investigation of the physical properties of IC 10 confirms the importance of the ionized gas in a porous ISM which seems to characterize low-metallicity environments (Cormier et al. 2012; Cormier et al. 2015; Chevance et al. 2016). As a consequence of the low dust abundance, the hard photons from the star-forming sites leak from the HII regions (Hidalgo-Gámez 2005) and traverse the larger scales. This picture is consistent with the fact that we find in this study that photon leakage seems to decrease with the increasing size of the region considered, suggesting that on the global scale, the galaxy appears to behave more like a radiation-bounded object.

However, in order to verify this hypothesis of local to global scales, a thorough modeling at full global scales is required. Moreover, this work suggests that a large scale simple single-component model cannot reproduce well all of the observed line emission, in particular the [NeII] and [OIII]. Cormier et al. (2012) have also demonstrated that for the case of the more distant, unresolved, starburst galaxy Haro 11, an additional low-ionization component reproduces better the [NeII] 12μm emission without affecting the other ionic tracers.

Chapter 7

Conclusion

Contents

The main purpose of my PhD project is to infer the physical conditions of the ionized phase in a nearby low-metallicity environment, with special emphasis on the consequence of which observational constraints are used and on the spatial scales examined, to go one step forward in the understanding the ISM properties. The nearby star-forming dwarf galaxy IC 10 has been chosen for this work because its proximity (700 kpc) enables access to various spatial scales, from bright compact clumps ($\sim$ 25 pc) to the whole star-forming body of the galaxy ($\sim$ 650 pc). IC 10 is one of the very few galaxies close enough to disentangle individual HII regions and, at the same time, far enough to be fully mapped in spectroscopy with infrared observatories such as *Spitzer* and *Herschel*. Hence, IC 10 provides a template for the analysis of ionized gas through various scales accessible in a single object, whereas other studies either rely on global integrated scales (e.g., Cormier et al. 2012 for DGS galaxies) or on specific star-forming regions, for instance in the Magellanic Clouds (e.g., Lebouteiller et al. 2012; Chevance et al. 2016).

IC 10 is also used as a template for a moderately metal-poor dwarf galaxy, with a metallicity ($1/3\,Z_{\odot}$) halfway between the LMC and SMC. IC 10 is the closest example of a low-metallicity starbursting dwarf galaxy with numerous giant molecular clouds. Hence, another objective is to understand whether the low-metallicity, combined with young massive stars, has an impact on the ISM properties through the structure and conditions in the ionized phase (HII regions and diffuse ionized gas) and in photodissociation regions.

MIR and FIR spectroscopic and photometric maps of the main star-forming body of the galaxy have been obtained with the *Spitzer* and *Herschel* telescopes (Chapter 2). Infrared fine-structure cooling lines are used in this study to infer the physical conditions in the ionized gas, by providing access to various species in different ionization stages, and through transitions with different excitation temperatures and critical densities. These observations give us access to almost every phase of the ISM (dust, ionized gas, neutral atomic gas, neutral molecular gas), making a unique and powerful dataset on its own. Such a dataset provides an interesting alternative or complement to the recent progress made with optical integral field units/spectrographs. Furthermore, MIR and FIR gas tracers are much less affected by dust extinction compared to optical lines (Section 1.2.5), which is especially important in the case of IC 10, which lies at low Galactic latitude (3°).

In this concluding chapter, I provide a summary of the IC 10 study, highlighting the main scientific results, and also identifying the main caveats. Finally, I present new/complementary approaches to the investigation of the ISM characteristics and future projects.

7.1 Summary of the main findings

7.1.1 Preliminary analysis

The preliminary spatial analysis of the infrared cooling lines (linear resolution $\sim$ 40 pc; Chapter 3) shows that [OIII] 88.4 μm is the brightest infrared cooling line throughout the body of the galaxy. This is remarkably different from that observed in more metal-rich sources, where [CII] 157.7 μm (arising in PDRs) is usually the brightest infrared line. I argue that this is not due to a lower heating efficiency in PDRs (which would result in a weaker [CII] 157.7 μm) but rather to a relatively large filling factor of ionized gas in the galaxy. It is likely that the ISM becomes more porous as metallicity decreases, because of the lower dust abundance and also possibly because of the different structure of dense clouds, allowing hard photons (such as those creating the O^{2+} ion) to leak from the HII regions and penetrate over large distances across the body of the galaxy. This result confirms that suggested by Cormier et al. (2015) for global galaxy scales in the DGS sample.

The second brightest infrared line in IC 10 is [CII] 157.7 μm. Due to the low ionization potential of C^+ (11.3 eV; Section 1.2.4), the [CII] 157.7 μm line can arise from the ionized gas (with electrons as collision partners) and from the neutral gas (with H^0 and H_2 as collision partners). Following the method used in several other studies (e.g., Oberst et al. 2006), I used [NII] as a tracer of [CII] in the ionized gas, and I estimated the fraction of [CII] 157.7 μm arising in both phases by comparing the observed [CII]/[NII] ratio to the theoretical value expected in the ionized gas. The result shows that most of the [CII] emission arises in PDRs and not from the ionized gas.

7.1.2 Various scales

One of the objectives of this study is to understand how the spatial scales over which the models are performed drive the derived physical properties. Thus, I chose three spatial scales to be examined: "clumps" (size few tens of pc), "zones" (integrated over $\sim$kpc) and the "body" (i.e., most of the star-forming body of the galaxy, corresponding to 608 pc$\times$855 pc). The "clumps" represent the smallest scale accessible thanks to the resolution of the *Spitzer*/IRS SL observations (4″), corresponding to $\sim$ 14 pc at the distance of IC 10. The clumps have been disentangled from each other and from the diffuse extended component by using a simultaneous fit.

7.1.3 Models

For the modeling, I used the spectral synthesis code Starburst99 (Leitherer et al. 2010) and the photoionization and photodissociation code Cloudy (Ferland et al. 2013) to infer the physical conditions (e.g., density, radiation field) of the regions. All the available MIR and FIR gas tracers were used as constraints. Cloudy , allows a self-consistent computation of the thermal and chemical structure of the gas, throughout the HII region and the PDR (Section 1.2), and is thus an ideal tool to extract the physical information out of the numerous infrared tracers, originating in different ISM phases.

I built grids of models adapted to the specific case of IC 10 (Section 4.3). Observed elemental abundances were used when possible. For some elements, no constraints on the abundances were available, and in general, abundances bear some uncertainties due to systematic errors related to the abundance determination method, ionization correction factors, or extinction of tracers by dust. Rather than building an unnecessary immense grid of models with varying abundances, we have simply propagated the abundance uncertainties on the predicted line fluxes (assuming, and verifying, that they scale linearly with the abundance).

The star formation history of the clusters responsible for the gas ionization was assumed to be represented by a single burst. While this hypothesis likely holds for an individual HII region, the gas distributed over larger scales may be ionized and heated by stellar populations of various ages. A continuous star formation rate may be envisaged, but the shape of the UV spectrum below 10^3 Å (i.e., for energies above 13.6 eV) is almost age-independent in this case, making this scenario difficult to test based on ionized gas tracers alone. Follow-up studies, involving the modeling of ionized and neutral gas tracers, may be able to analyze the hypothesis of continuous star formation, thanks to the relatively wider energy range probed.

The modeling strategy for IC 10 is adapted to the available tracers and the map coverages. There is almost no line combination in the infrared tracing unambiguously any given physical parameter (apart from the [SIII] line ratio which traces the gas density). Furthermore, I implemented a strategy with a parameter describing whether the gas is matter-bounded or radiation-bounded, in addition to usual physical parameters such as the gas density, the ionization parameter, and the age of the stellar population.

Because of the relatively small number of constraints, especially for the *clump* analysis, and the limited spatial resolution, a rather simple model geometry is assumed, which consists of a single central source surrounded by a single cloud (matter- or radiation-bounded) with uniform physical conditions. As explained in Chapter 5, the use of such a simple model becomes more and

more problematic as the spatial scales examined become larger, since larger scales are more likely to include either other ISM phases and/or a different ionizing stellar population.

7.1.4 Results concerning the use of available constraints to infer the physical parameters at various spatial scales

I considered two methods in order to use the observed line fluxes as constraints to the model: **line ratios** and **absolute fluxes**. The main differences between the two is the way the parameter space in the models is probed. The **line ratio** method presents several advantages, such as choosing lines arising in the same instrument (thereby minimizing instrumental uncertainties) or lines from the same element (cancelling the abundance uncertainties), but also several unforeseen consequences. Hence the choice of how lines are combined as ratios has an impact on the process of finding the best models. On the other hand, the **absolute flux** method simply considers all lines available without combining them in anyway.

The **line ratio** method was not deemed satisfactory because of the high χ^2 values obtained and the impossibility to reproduced all of the line ratios selected, at any spatial scale. This could be due to the fact that the model is incomplete (e.g., need of a multi-component model; Section 7.2.2), or assumes simple hypotheses (uniform physical conditions, central ionizing source...), or that the uncertainties have been underestimated. One possible improvement concerning this method could be apply the covariance matrix to calculate the χ^2, such as in the case of the **absolute flux** method.

On the other hand, the **absolute flux** method overall provides better results in terms of χ^2 (reduced χ^2 between 1 and 3). However, at the *clump* scale the density was not well determined unless we use the [SIII] line *ratio* as a constraint. Nevertheless, comparing the observed line emission with the models, this method suggests the need for an additional, more diffuse, ionized gas component, in order to better reproduce some of the lines such as [OIII] 88.4 μm.

7.1.5 Results concerning the interpretation of the inferred physical conditions

The physical properties of the ionized gas in IC 10 are discussed in Chapter 6. First, I derived the extinction seen by the gas, by comparing the observed Hα with the model prediction. I find significantly larger values than those

derived using optical or near-infrared lines. This suggests that most of the ionized gas in IC 10 lies in regions that are not accessible through optical observations, likely corresponding to regions that are more embedded in star-forming clouds. Optical spectroscopy is thus complementary to the infrared dataset used here.

By comparing the observed [CII] and [SiII] emission with the model predictions, I showed that most of the [CII] and [SiII] arises in the neutral gas, and can therefore be used as constraints to a future PDR modeling effort (Section 7.2.3).

An important result for the *clumps* is that they appear to be matter-bounded, i.e., a significant fraction of the ionizing photons is able to escape the HII regions. As we move to larger spatial scales, the gas becomes almost radiation-bounded, which is expected since ionizing photons leaking from HII regions are more likely to be absorbed as the volume of gas increases. The scenario of leaking ionizing photons, and the typical spatial scales over which they can travel before they get absorbed is interesting to put in perspective with the proposition that the ISM at low metallicity is very porous (Cormier et al. 2012, 2015; Chevance et al. 2016).

I also demonstrated that the physical conditions inferred from the largest spatial scale (i.e., the main body of the galaxy) are similar to those inferred from the bright HII regions. This suggests that, in a starburst galaxy, the integrated properties are dominated by the HII regions.

7.2 Perspectives

7.2.1 SOFIA observations

One of the main limitations in this study is the assumption of uniform physical conditions. Ideally, one would like to use a model with, for instance, a non-uniform density. However, I was able to use only one unambiguous density tracer ([SIII] line ratio). The density determined this way effectively corresponds to the gas where S^{2+} exists. Another density may have been found if I had used the [SII] lines in the optical, since they trace the denser shells, where the gas is radiation-bounded. Similarly, another density may be found when using the [OIII] lines in the optical (with a bias toward denser regions because of the larger critical densities as compared to the infrared [OIII] lines). For future work, a combination of several density tracers will be very useful to extract the density structure of the ionized gas (e.g., Spinoglio et al. 2015).

The combination of the [OIII] 51.8 μm and [OIII] 88.4 μm lines is poten-

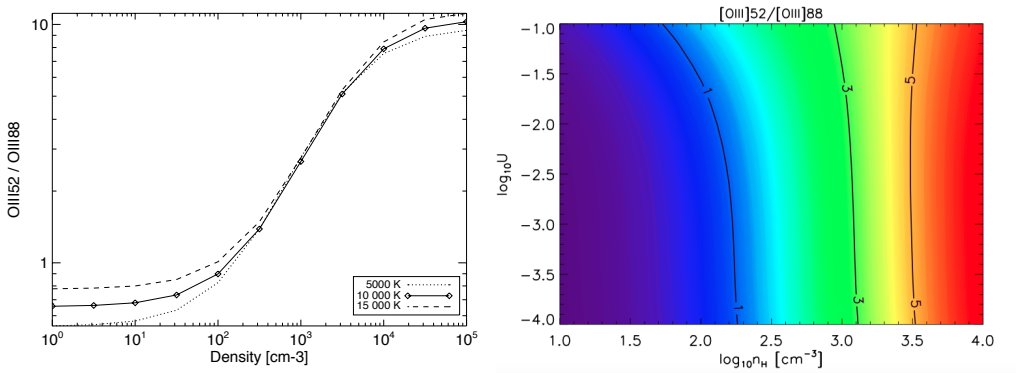

Figure 7.1: Density diagnostic plot using the [OIII] 51.8 μm/[OIII] 88.4 μm ratio. *Left*: Theoretical ratio [OIII] 51.8 μm/[OIII] 88.4 μm as a function of the density in the ionized gas. The different lines represent the line ratio for different temperatures. *Right*: [OIII] 51.8 μm/[OIII] 88.4 μm ratio (colors and contours) calculated from our Cloudy models of the central region of IC 10 for different values of the ionization parameter (U in the y-axis) and density (n_H in the x-axis).

tially a powerful density diagnostic, with critical density of 4.38×10^3 cm^{-3} and 500 cm^{-3} respectively, making the ratio of these two lines sensitive to an ionized phase of lower density than that traced by [SIII] or the optical lines (Chapter 1). Figure 7.1 shows that the [OIII] line ratio is sensitive to densities in the range $10^2 - 10^4$ cm^{-3}, with little temperature dependence. This temperature dependence implies some dependence on the ionization parameter (Figure 7.1 right panel).

[OIII] 51.8 μm was not accessible with *Herschel*, but it is with the FIFI-LS instrument on the airborne observatory SOFIA (Section 2.4.3). I am leading an observing program that targeted the *Central main zone* and *ArcA* zone during Cycle 5. Figure 7.2 shows the preliminary maps I obtained during the flights carried out in February 2017[1]. These new observations will allow me to obtain an additional constraint on the gas density, sensitive to lower density compare to [SIII] ratio, for the zones and for the clumps as well. A follow-up study with the upGREAT instrument on SOFIA would spectrally resolve the [OIII] lines, thereby identifying several ionized gas components along the line of sight (Section 7.2.2).

[1]The fully reduced cubes have just been delivered by the instrument team and have not yet been analyzed at the time of this manuscript writing.

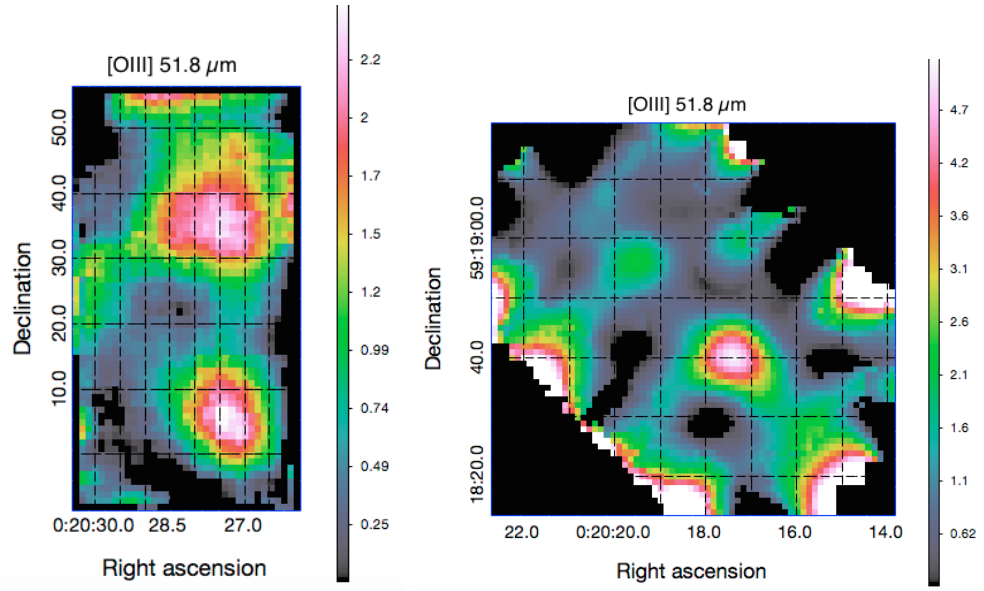

Figure 7.2: SOFIA/FIFI-LS Cycle 5 preliminary maps of the FIR fine structure line [OIII] 51.8μm in *Central main zone* (*left*) and *ArcA* zone (right) in units of [Jy].

7.2.2 Multi-component model

The current model solutions indirectly suggest that for all of the spatial scales examined, the ionized gas may include several components with different characteristics (e.g., density). For instance, the observed vs. predicted [OIII] 88.4 μm intensities suggest the existence of an extended diffuse component ionized by young stellar clusters over distances much larger than the scale of an HII region. A similar conclusion is reached for [NeII] 12.8 μm, although in this case, the gas may be ionized by older stellar populations. The model is therefore likely incomplete.

Adding another component in the models is possible and provides satisfactory results (i.e., the observed line fluxes are all well reproduced by the model), but this is mostly due to the fact that more degrees of freedom are considered, with the same number of constraints. Figure 7.3 shows a preliminary multi-component analysis performed for the *Central main zone*. Using the line ratio method, I model the region combining a dense HII phase with a diffuse ionized gas. However, I currently do not have enough constraints to build a reliable multi-component model. A possibility could be to include optical lines as additional constraints. For instance, the ratio of the two optical lines [SII] 6716 Å and 6731 Å is a good tracer of the density in HII region shells. Optical spectra have already been obtained

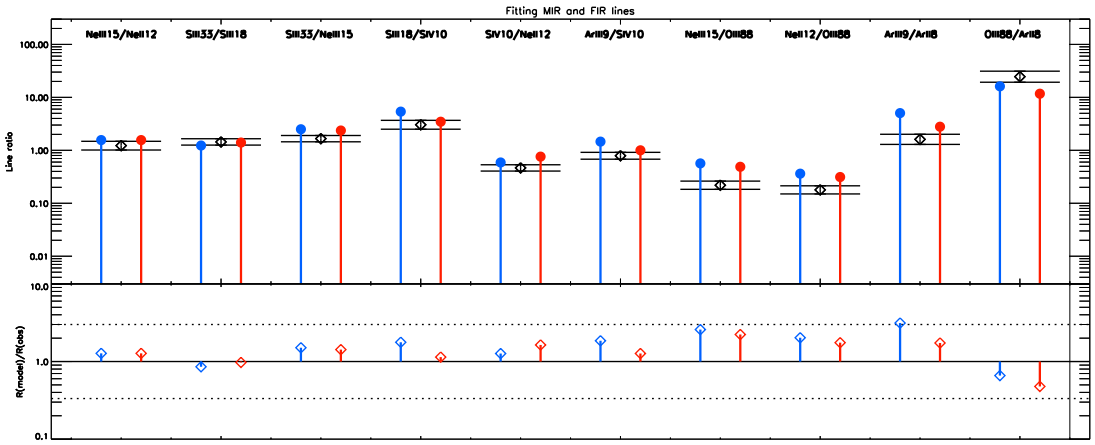

Figure 7.3: Multi-component modeling of the *Central main zone*. The black points are the observed line ratio values with the relative uncertainties. The red lines represent the predicted ratios of best fit solution for a single component model, while the blue lines represent the predicted ratios of the best solution for the two-component model: dense HII region and diffuse ionized gas.

for the *Center c*1 clump, using integral field spectroscopy with the Potsdam Multi-Aperture Spectrograph available at the 3.5m telescope at Calar Alto Observatory, with a spatial resolution of 3.9×3.9 pc (López-Sánchez et al. 2011). Optical spectroscopy, despite being plagued with extinction effects, provides greater spatial resolution compared to infrared lines (Section 7.1), and possibly allows more detailed modeling of the ISM structure.

Another interesting prospect is the *James Webb* Space Telescope, a NASA mission with a launch scheduled at the end of 2018. In particular, the Mid-Infrared Instrument (MIRI) instrument covers the wavelength range $4.9 - 28.8\,\mu$m. It will allow the observation of the same suite of spectral lines as the IRS, in addition to fainter lines thanks to its improved sensitivity, at higher spectral ($\lambda/\Delta\lambda \sim 1550 - 3250$) and spatial (sub-arcsecond) resolution, which will be sufficient to disentangle various ionized gas components. However, the relatively small field-of-view of MIRI ($3.9'' - 7.7''$) prevents us from obtaining a full map of IC 10, and only small, targeted HII regions will be accessible in IC 10 and other nearby galaxies.

7.2.3 PDR models

The final objective, using the rich dataset available for IC 10, is to understand how metallicity impacts the structure and properties of the ISM. For this, one needs to examine both the ionized gas and the neutral gas (PDRs and

molecular clouds). The analysis of the ionized gas is a first step towards a model that combines all phases. From the present study, I was able to obtain results that provide the necessary and crucial information for input to constrain the PDR models. I showed, for instance, that [CII] and [SiII] originate mostly in PDRs. Furthermore, I calculated the physical parameters (density, ionization parameter, starburst age) that will be used as input/edge conditions for PDR models. Such constraints are useful because only few observational constraints are available for the neutral gas alone (mostly [CII], [OI], [SiII]). Finally, I showed that the ionized gas clouds are matter-bounded, which implies that only a fraction of the clouds (at any given spatial scale examined) include a neutral gas component.

To model the transition between the ionized phase and the neutral phase, and across the neutral phase, I will assume a constant pressure, following, e.g., Cormier et al. (2012). Figure 7.4 shows the temperature and cooling contributions across a typical cloud, from the illuminated phase of the cloud to the molecular layer, calculated by CLOUDY. The temperature is constant, $\sim 10^4$K in the HII region. At the ionizing front, where the phase transition occurs, the temperature falls to a few hundred K, and continues to drops inside the PDR phase.

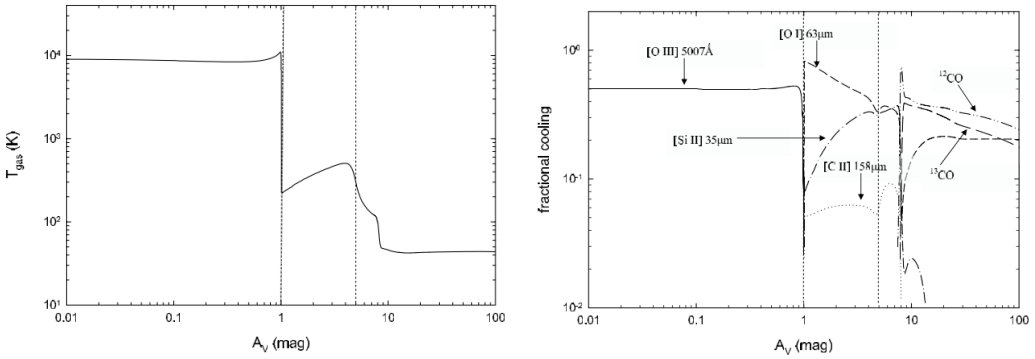

Figure 7.4: *Left*: Gas temperature calculated by CLOUDY from the illuminated phase of the cloud to the molecular layer. *Right*: Main lines responsible for the cooling in the different phases of the cloud. Figures from Abel et al. (2005).

The main constraints for the PDR component are [OI] 63.2 μm, [OI] 145.5 μm , [CII] 157.7 μm, [SiII] 34.8 μm and the L_{TIR} (Chapter 3), in addition to CO ($J = 1 - 0$) emission. One of the objectives is to use the PDR model to infer the mass of CO-dark molecular gas *spatially* in a low-metallicity environment. The CO-dark gas corresponds to regions where CO is photodissociated but H_2 is self-shielded. Some of the most important parameters to account for are the dust-to-gas mass ratio, the cloud extinction,

and the input stellar radiation field.

7.2.4 Application of the method to other galaxies

In the era of ALMA, NOEMA and JWST, ground-breaking high spatial-resolution observations will be available for high-z galaxies. It is therefore important to use the nearby galaxies as templates (i.e. building a method) and complementary samples (e.g., in terms of mass, metallicity, SFR, and morphology).

During my PhD, I have analyzed a variety of fine-structure line observations along with state-of-the-art theoretical models on different size scales within the dwarf irregular galaxy IC 10. This galaxy is an ideal template to investigate the effect of low-metallicity on the properties of the ISM. The method I developed is potentially applicable to other nearby galaxies with different properties, such as M51 and M33.

The spiral galaxy M 51 M 51 is a metal-rich (distance = 8.4 Mpc; Z = $Z_{\odot}$) massive spiral galaxy whose dynamical properties, as well as molecular cloud population and star formation, have been well studied (e.g., Chandar et al. 2016; Meidt et al. 2013). The modeling of this galaxy would allow a better understanding of the interplay between the ISM, star formation, and galaxy-wide conditions for an environment that is drastically different from IC 10. M 51 has been observed at multiple wavelengths. For example, [CII] 157.7 μm, [NII] 121.9 μm, [OIII] 88.4 μm, [OI] 63.2 μm and [OI] 145.5 μm and ^{12}CO lines, as well as dust continuum data, are available from the *Herschel* VNGS and Plateau de Bure Interferometry (PdBI) PAWS surveys (Parkin et al. 2013; Schinnerer et al. 2013). In addition, a radial strip across M 51 has been observed with MIR gas tracers from *Spitzer* as part of the SINGS survey.

The spiral galaxy, M 33 M 33 is a low-mass, relatively metal-poor galaxy (distance = 840 kpc; Z = $1/2_{\odot}$) without a bulge or a ring. It has been observed at optical and UV wavelengths with HST. *Herschel* (HERM33ES program) observed all of the important fine-structure cooling lines, such as [CII] 157.7 μm, [NII] 121.9 μm, [NII] 205.2 μm, [NIII] 57.3 μm, [OIII] 88.4 μm, [OI] 63.2 μm and [OI] 145.5 μm along the major axis (e.g., Mookerjea et al. 2011). Additionally, the dust emission has been completely mapped by *Herschel* at 160, 250, 350 and 500 μm.

One of the main and most exciting prospect for galaxy evolution, is to better understand how processes acting on local scales, such as star formation, depend on processes acting on larger or galaxy-wide scales, such as the ISM or the global dynamics of a galaxy. With this aim, characterizing the ISM properties (densities, radiation fields, masses, filling factors, etc.) in galaxies probing a wide range of conditions, will provide better connection between the small and large scales and direct diagnostics on the galaxy properties as a function of the environment. Some of my results, such as matter- or radiation-bounded regions or the importance of the ionized gas phase, reflect changes in the phase balance and transport of radiation in low-metallicity galaxies, and this may have strong implications for the cooling and evolution of galaxies in the early universe.

Acknowledgements

I did my thesis at CEA Saclay in the laboratory of AIM (Service d'Astrophysique), thanks to a ministry grant. Thus, I'm very grateful to the Ecole Doctorale 127 and to the DAp's chef, Annie Decourchelle, for giving me the instruments and funding to carry out this project. In this regard, I would like to thank Suzanne Madden for these three years, for what I learnt, for the people I met during my PhD and for the amazing experience of the SOFIA observations; I will never forget them. Thank you also for the great team you have built, in which all the members, present or previous, are always available to help and contribute. Yes, thanks to all of the *NUAGES* team: Vianney, Fred, Pierre, Diane, Maud, Min, Mélanie, Sofia, Oskar, ... Sacha and Ronin; all of you made me feel part of the team. Thank you for all the science I learnt from you as well as for the funny lunches, tea breaks, picnics and dinners at Suzanne's place. I will miss you and our group meetings (with a lot of sugar). In particular, thanks Vianney for everything you have taught me, for your patience and availability, as well I thank my officemates: Mélanie, Min and Diane. It has been a pleasure to share the office with you, many thanks for the science discussions and for all the good times. Thanks Diane, Min and Maud, for being more than colleges, for yours suggestions, support and all the fun!

However, *NUAGES* team are not the only people that made me feel at home at CEA, thus thanks to all the other CEA students, post-docs and friends I shared these years with: Mathilde, Jeremy, Yueh-Ning, Bilal, Rose, Paula, Andrea, Valeska, Vera, Arabindo and Giulia; and thanks to you, Anaëlle, for really taking care of the students and help us as much as possible!

Moving outside CEA ... How could I forget my crazy friends in Paris??? This PhD experience couldn't be so unforgettable without you: Fernando, Gaël, William, Anelise, Isadora, Caterina, Carolina ... and, of course, Paola. Thanks Paola for being a very good friend, I am glad to have shared with you so many memories, good times, as well as very hard working moments,

and thanks for opening your house to me every time that I need it!

So far, I thanked the people that I met during my PhD, but I cannot forget to thank the people that encouraged me to follow my dream, without which I would never had started this adventure in Paris: thanks Ande, Tias, mum and dad. Thanks family for supporting me in my aims and teach me to never give up and to all my 'old' friends, Ste, Any, Ely, Patty, Marty, Gio and Eli, that even from the distance and despite the few occasions that we can meet, you are still very important in my life, always supporting me and being available for my craziness.

Thanks to all of you!

Acronyms

AGN	Active galactic nucleus
CA	Cryogenic Assembly (*Spitzer*)
CNM	Cold Neutral Medium
EXES	Echelon-Cross-Enchelle Spectrograph (*Spitzer*)
FIFI-LS	Field Imaging Far-Infrared Line Spectrometer (*Spitzer*)
FIR	Far Infrared
FLITECAM	First Light Infrared Test Experiment CAMera (*Spitzer*)
FOV	Field of view
FORCAST	Faint Object Infrared CAmera for the SOFIA Telescope (*Spitzer*)
FPI+	Focal Plane Imager Plus (*Spitzer*)
FTS	Fourier Transform Spectrometer
FWHM	Full Width at Half Maximum
GMC	Giant Molecular Cloud
GREAT	German REceiver for Astronomy at Terahertz frequencies (*Spitzer*)
HAWC+	High-resolution Airborne Wideband Camera-Plus (*Spitzer*)
HIPO	High-speed Imaging Photometer for Occultations (*Spitzer*)
HIM	Hot Ionized Medium
IFU	Integral field unit
IMF	Initial Mass Function
IR	Infrared
IRS	Infrared Spectrograph (*Spitzer*)
IRAC	Infrared Array Camera (*Spitzer*)
ISM	Interstellar Medium
KAO	Kuiper Airborne Observatory
LH	Long-High (*Spitzer*)
LL	Long-Low (*Spitzer*)
LMC	Large Magellanic Cloud
LTE	Local Thermal Equilibrium
MIPS	Multiband Infrared Photometer (*Spitzer*)
MIR	Mid Infrared

MIRI	Mid-Infrared Instrument
OPD	Optical Path Difference
PDF	Probability Distribution Function
PAHs	Polycyclic Aromatic Hydrocarbons
PDR	PhotoDissociation Region
PSF	Point Spread Function
RMS	root mean square
SED	Spectral energy distribution
SF	Star formation
SH	Short-High (*Spitzer*)
SMC	Small Magellanic Cloud
SSP	simple stellar population
SL	Short-Low (*Spitzer*)
SOFIA	Stratospheric Observatory for Infrared Astronomy
SPIRE	Spectral and Photometric Imaging Receiver
UV	Ultra Vaiolet
WEA	Warm Electronics Assembly (*Spitzer*)
WIM	Warm Ionized Medium
WNM	Warm Neutral Medium
WC	Wolf-Rayet star which spectrum is dominated by lines of carbon
WN	Wolf-Rayet star which spectrum is dominated by lines of nitrogen
WR	Wolf-Rayet star

Bibliography

Abel, N. P., Ferland, G. J., Shaw, G., & van Hoof, P. A. M. 2005, ApJS, 161, 65

Abel, N. P., Sarma, A. P., Troland, T. H., & Ferland, G. J. 2007, ApJ, 662, 1024

Accurso, G., Saintonge, A., Catinella, B., et al. 2017, Deriving a multivariate CO-to-H_2 conversion function using the [CII]/CO(1-0) ratio and its application to molecular gas scaling relations, Tech. rep.

Allen, M. G., Groves, B. A., Dopita, M. A., Sutherland, R. S., & Kewley, L. J. 2008, ApJS, 178, 20

Aller, L. H. & Czyzak, S. J. 1983, ApJS, 51, 211

Aniano, G., Draine, B. T., Gordon, K. D., & Sandstrom, K. 2011, PASP, 123, 1218

Ashley, T., Elmegreen, B. G., Johnson, M., et al. 2014, The Astronomical Journal, 148, 130

Asplund, M., Grevesse, N., Sauval, A. J., & Scott, P. 2009, ARA&A, 47, 481

Baldwin, J. A., Ferland, G. J., Martin, P. G., et al. 1991, ApJ, 374, 580

Baldwin, J. A., Phillips, M. M., & Terlevich, R. 1981, PASP, 93, 5

Bennett, C. L., Fixsen, D. J., Hinshaw, G., et al. 1994, ApJ, 434, 587

Bernard-Salas, J., Habart, E., Arab, H., et al. 2012, A&A, 538, A37

Bertelli, G., Bressan, A., Chiosi, C., Fagotto, F., & Nasi, E. 1994, A&AS, 106

Bigiel, F., Leroy, A., Walter, F., et al. 2008, AJ, 136, 2846

Boissier, S., Prantzos, N., Boselli, A., & Gavazzi, G. 2003, MNRAS, 346, 1215

Bolatto, A. D., Leroy, A. K., Jameson, K., et al. 2011, ApJ, 741, 12

Borissova, J., Georgiev, L., Rosado, M., et al. 2000, A&A, 363, 130

Boselli, A., Eales, S., Cortese, L., et al. 2010, PASP, 122, 261

Bradač, M., Garcia-Appadoo, D., Huang, K.-H., et al. 2017, ApJLett, 836, L2

Braine, J., Gratier, P., Kramer, C., et al. 2012, A&A, 544, A55

Brauher, J. R., Dale, D. A., & Helou, G. 2008, ApJS, 178, 280

Bridge, C. R., Teplitz, H. I., Siana, B., et al. 2010, ApJ, 720, 465

Cannon, J. M., Walter, F., Armus, L., et al. 2006, ApJ, 652, 1170

Cardelli, J. A., Clayton, G. C., & Mathis, J. S. 1989, ApJ, 345, 245

Chabrier, G. 2001, ApJ, 554, 1274

Chandar, R., Whitmore, B. C., Dinino, D., et al. 2016, ApJ, 824, 71

Charlot, S. & Bruzual, A. G. 1991, ApJ, 367, 126

Chevance, M., Madden, S. C., Lebouteiller, V., et al. 2016, A&A, 590, A36

Ciardullo, R., Jacoby, G. H., Ford, H. C., & Neill, J. D. 1989, ApJ, 339, 53

Cormier, D. 2012, PhD thesis

Cormier, D., Lebouteiller, V., Madden, S. C., et al. 2012, A&A, 548, A20

Cormier, D., Madden, S. C., Lebouteiller, V., et al. 2015, A&A, 578, A53

Cormier, D., Madden, S. C., Lebouteiller, V., et al. 2014, A&A, 564, A121

Cowie, L. L., Barger, A. J., & Trouille, L. 2009, ApJ, 692, 1476

Cowie, L. L. & Songaila, A. 1986, ARA&A, 24, 499

Cowie, L. L., Songaila, A., Hu, E. M., & Cohen, J. G. 1996, AJ, 112, 839

Crowther, P. A., Drissen, L., Abbott, J. B., Royer, P., & Smartt, S. J. 2003, A&A, 404, 483

Dale, D. A., Aniano, G., Engelbracht, C. W., et al. 2012, ApJ, 745, 95

Dale, D. A., Cook, D. O., Roussel, H., et al. 2017, ApJ, 837, 90

Dawson, J. R., Ntormousi, E., Fukui, Y., Hayakawa, T., & Fierlinger, K. 2015, The Astrophysical Journal, 799, 64

de Graauw, T., Helmich, F. P., Phillips, T. G., et al. 2010, A&A, 518, L6

De Looze, I., Baes, M., Bendo, G. J., Cortese, L., & Fritz, J. 2011, MNRAS, 416, 2712

Dekel, A. & Silk, J. 1986, ApJ, 303, 39

Demers, S., Battinelli, P., & Letarte, B. 2003, A&A, 410, 795

Demers, S., Battinelli, P., & Letarte, B. 2004, A&A, 424, 125

Dimaratos, A., Cormier, D., Bigiel, F., & Madden, S. C. 2015, A&A, 580, A135

Draine, B. T. & Hensley, B. 2012, ApJ, 757, 103

Dudik, R. P., Weingartner, J. C., Satyapal, S., et al. 2007, ApJ, 664, 71

Fahrion, K., Cormier, D., Bigiel, F., et al. 2016

Fazio, G. G., Hora, J. L., Allen, L. E., et al. 2004, ApJS, 154, 10

Ferland, G. J., Korista, K. T., Verner, D. A., et al. 1998, PASP, 110, 761

Ferland, G. J., Porter, R. L., van Hoof, P. A. M., et al. 2013, Revista Mexicana de Astronomia y Asrtrofisica, 49, 137

Ferland, G. J. & Shields, G. A. 1978, ApJ, 226, 172

Ferland, G. J. & Truran, J. W. 1981, ApJ, 244, 1022

Galametz, M., Kennicutt, R. C., Calzetti, D., et al. 2013, MNRAS, 431, 1956

Galametz, M., Madden, S. C., Galliano, F., et al. 2011, A&A, 532, A56

Galliano, F., Hony, S., Bernard, J.-P., et al. 2011, A&A, 536, A88

Galliano, F., Madden, S. C., Jones, A. P., et al. 2003, A&A, 407, 159

García-Benito, R., Pérez, E., Díaz, Á. I., Maíz Apellániz, J., & Cerviño, M. 2011, AJ, 141, 126

Garnett, D. R. 1990, ApJ, 363, 142

Gil de Paz, A., Madore, B. F., & Pevunova, O. 2003, ApJS, 147, 29

Girardi, L., Bressan, A., Bertelli, G., & Chiosi, C. 2000, A&AS, 141, 371

Goldsmith, P. F., Langer, W. D., Pineda, J. L., & Velusamy, T. 2012, ApJS, 203, 13

Gordon, K. D., Clayton, G. C., Misselt, K. A., Landolt, A. U., & Wolff, M. J. 2003, ApJ, 594, 279

Grebel, E. K., Gallagher, III, J. S., & Harbeck, D. 2003, AJ, 125, 1926

Grenier, I. A., Casandjian, J.-M., & Terrier, R. 2005, Science, 307, 1292

Grevesse, N. & Anders, E. 1989, in American Institute of Physics Conference Series, Vol. 183, Cosmic Abundances of Matter, ed. C. J. Waddington, 1–8

Grevesse, N., Asplund, M., Sauval, A. J., & Scott, P. 2010, Ap&SS, 328, 179

Grevesse, N., Noels, A., & Sauval, A. J. 1993, A&A, 271, 587

Griffin, M. J., Abergel, A., Abreu, A., et al. 2010, A&A, 518, L3

Guillard, P., Boulanger, F., Cluver, M. E., et al. 2010, A&A, 518, A59

Guillard, P., Boulanger, F., Pineau Des Forêts, G., & Appleton, P. N. 2009, A&A, 502, 515

Helou, G. 1986, ApJLett, 311, L33

Henney, W. J., Arthur, S. J., Williams, R. J. R., & Ferland, G. J. 2005, ApJ, 621, 328

Hidalgo-Gámez, A. M. 2005, A&A, 442, 443

Higdon, S. J. U., Devost, D., Higdon, J. L., et al. 2004, PASP, 116, 975

Hjellming, R. M. 1966, ApJ, 143, 420

Hodge, P. & Lee, M. G. 1990, PASP, 102, 26

Hodge, P., Smith, T., Eskridge, P., MacGillivray, H., & Beard, S. 1991, ApJ, 379, 621

Houck, J. R., Roellig, T. L., van Cleve, J., et al. 2004, ApJS, 154, 18

Hubble, E. P. 1936, Realm of the Nebulae

Huchtmeier, W. K. 1979, A&A, 75, 170

Hummer, D. G. & Storey, P. J. 1987, MNRAS, 224, 801

Hunter, D. A. 2001, ApJ, 559, 225

Hunter, D. a. & Elmegreen, B. G. 2004, The Astronomical Journal, 128, 2170

Indebetouw, R. 2015, IAU General Assembly, 22, 2257849

Inutsuka, S.-i., Inoue, T., Iwasaki, K., & Hosokawa, T. 2015, A&A, 580, A49

Izotov, Y. I., Stasińska, G., Meynet, G., Guseva, N. G., & Thuan, T. X. 2006, A&A, 448, 955

Kapala, M. J., Groves, B., Sandstrom, K., et al. 2017, The Survey of Lines in M31 (SLIM): The Drivers of the [CII]/TIR Variation, Tech. rep.

Kaufman, M. J., Wolfire, M. G., & Hollenbach, D. J. 2006, ApJ, 644, 283

Kaufman, M. J., Wolfire, M. G., Hollenbach, D. J., & Luhman, M. L. 1999, ApJ, 527, 795

Kawada, M., Takahashi, A., Yasuda, A., et al. 2011, PASJ, 63, 903

Kennicutt, R. C., Calzetti, D., Aniano, G., et al. 2011, Pasp, 123, 1347

Kennicutt, R. C. & Evans, N. J. 2012, ARA&A, 50, 531

Kennicutt, Jr., R. C. 1989, ApJ, 344, 685

Khromov, G. S. 1989, Space Sci. Rev., 51, 339

Kim, M., Kim, E., Hwang, N., et al. 2009, ApJ, 703, 816

Kroupa, P. 2001, in Astronomical Society of the Pacific Conference Series, Vol. 228, Dynamics of Star Clusters and the Milky Way, ed. S. Deiters, B. Fuchs, A. Just, R. Spurzem, & R. Wielen, 187

Krumholz, M. R. & McKee, C. F. 2005, ApJ, 630, 250

Kunth, D. & Östlin, G. 2000, A&A Rev., 10, 1

Lebouteiller, V., Barry, D. J., Spoon, H. W. W., et al. 2011, ApJS, 196, 8

Lebouteiller, V., Bernard-Salas, J., Sloan, G. C., & Barry, D. J. 2010, PASP, 122, 231

Lebouteiller, V., Cormier, D., Madden, S. C., et al. 2012, A&A, 548, A91

Lebouteiller, V., Kunth, D., Lequeux, J., et al. 2006, A&A, 459, 161

Lebouteiller, V., Péquignot, D., Cormier, D., et al. 2017, A&A, 602, A45

Lee, M.-Y., Madden, S. C., Lebouteiller, V., et al. 2016, A&A, 596, A85

Leitet, E., Bergvall, N., Hayes, M., Linné, S., & Zackrisson, E. 2013, A&A, 553, A106

Leitherer, C., Ortiz Otálvaro, P. A., Bresolin, F., et al. 2010, ApJS, 189, 309

Lequeux. 2005, The Interstellar Medium

Lequeux, J., Peimbert, M., Rayo, J. F., Serrano, A., & Torres-Peimbert, S. 1979, A&A, 80, 155

Leroy, a., Bolatto, a., Walter, F., & Blitz, L. 2006, The Astrophysical Journal, 643, 825

Leroy, A., Bolatto, A. D., Simon, J. D., & Blitz, L. 2005, ApJ, 625, 763

Leroy, A. K., Walter, F., Bigiel, F., et al. 2009, AJ, 137, 4670

Lim, S. & Lee, M. G. 2015

López-Sánchez, Á. R., Mesa-Delgado, A., López-Martín, L., & Esteban, C. 2011, MNRAS, 411, 2076

Madden, S. C., Galliano, F., Jones, A. P., & Sauvage, M. 2006, A&A, 446, 877

Madden, S. C., Geis, N., Genzel, R., et al. 1993, ApJ, 407, 579

Madden, S. C., Poglitsch, A., Geis, N., Stacey, G. J., & Townes, C. H. 1997, Astrophy, 483, 200

Madden, S. C., Rémy-Ruyer, A., Galametz, M., et al. 2013, PASP, 125, 600

Magrini, L. & Gonçalves, D. R. 2009, MNRAS, 398, 280

Marigo, P., Girardi, L., Bressan, A., et al. 2008, A&A, 482, 883

Markwardt, C. B. 2009, in Astronomical Society of the Pacific Conference Series, Vol. 411, Astronomical Data Analysis Software and Systems XVIII, ed. D. A. Bohlender, D. Durand, & P. Dowler, 251

Massey, P. 2003, in IAU Symposium, Vol. 212, A Massive Star Odyssey: From Main Sequence to Supernova, ed. K. van der Hucht, A. Herrero, & C. Esteban, 316

Massey, P. & Armandroff, T. E. 1995, AJ, 109, 2470

Massey, P. & Holmes, S. 2002, ApJLett, 580, L35

Mathis, J. S. 1972, ApJ, 176, 651

Mathis, J. S., Rumpl, W., & Nordsieck, K. H. 1977, ApJ, 217, 425

Mayall, N. U. 1935, PASP, 47, 317

Meidt, S. E., Schinnerer, E., García-Burillo, S., et al. 2013, ApJ, 779, 45

Meynet, G., Maeder, A., Schaller, G., Schaerer, D., & Charbonnel, C. 1994, A&AS, 103

Mookerjea, B., Kramer, C., Buchbender, C., et al. 2011, A&A, 532, A152

Morisset, C. 2006, in IAU Symposium, Vol. 234, Planetary Nebulae in our Galaxy and Beyond, ed. M. J. Barlow & R. H. Méndez, 467–468

Morisset, C., Delgado-Inglada, G., Sánchez, S. F., et al. 2016, A&A, 594, A37

Naslim, N., Kemper, F., Madden, S. C., et al. 2015, MNRAS, 446, 2490

Neeleman, M., Kanekar, N., Prochaska, J. X., et al. 2017, Science, 355, 1285

Negishi, T., Onaka, T., Chan, K.-W., & Roellig, T. L. 2001, A&A, 375, 566

Nidever, D. L., Ashley, T., Slater, C. T., et al. 2013, ApJLett, 779, L15

Oberst, T. E., Parshley, S. C., Nikola, T., et al. 2011, ApJ, 739, 100

Oberst, T. E., Parshley, S. C., Stacey, G. J., et al. 2006, ApJLett, 652, L125

Osterbrock, D. & Ferland, G. 2005, Astrophysics of Gaseous Nebulae and Active Galactic Nuclei

Osterbrock, D. E., Tran, H. D., & Veilleux, S. 1992, ApJ, 389, 305

Ostriker, E. C., McKee, C. F., & Leroy, A. K. 2010, ApJ, 721, 975

Pagel, B. E. J. 1997, Nucleosynthesis and Chemical Evolution of Galaxies, 392

Parkin, T. J., Wilson, C. D., Schirm, M. R. P., et al. 2013, ApJ, 776, 65

Peeters, E., Allamandola, L. J., Hudgins, D. M., Hony, S., & Tielens, A. G. G. M. 2004, in Astronomical Society of the Pacific Conference Series, Vol. 309, Astrophysics of Dust, ed. A. N. Witt, G. C. Clayton, & B. T. Draine, 141

Peimbert, M., Peimbert, A., & Delgado-Inglada, G. 2017, PASP, 129, 082001

Pequignot, D. & Dennefeld, M. 1983, A&A, 120, 249

Planck Collaboration, Ade, P. A. R., Aghanim, N., et al. 2011, A&A, 536, A19

Poglitsch, A., Krabbe, A., Madden, S. C., et al. 1995, ApJ, 454, 293

Poglitsch, A., Waelkens, C., Geis, N., et al. 2010, A&A, 518, L2

Press, W. H., Teukolsky, S. A., Vetterling, W. T., & Flannery, B. P. 1992, Numerical recipes in FORTRAN. The art of scientific computing (Cambridge University Press)

Rémy-Ruyer, A., Madden, S. C., Galliano, F., et al. 2014, A&A, 563, A31

Rémy-Ruyer, A., Madden, S. C., Galliano, F., et al. 2013, A&A, 557, A95

Rémy-Ruyer, A., Madden, S. C., Galliano, F., et al. 2015, A&A, 582, A121

Richer, M. G., Bullejos, A., Borissova, J., et al. 2001, A&A, 370, 34

Rieke, G. H., Young, E. T., Engelbracht, C. W., et al. 2004, ApJS, 154, 25

Roussel, H., Helou, G., Hollenbach, D. J., et al. 2007, ApJ, 669, 959

Rubin, R. H. 1968, ApJ, 153, 761

Rubin, R. H., Dufour, R. J., & Walter, D. K. 1993, ApJ, 413, 242

Rubin, R. H., Simpson, J. P., Haas, M. R., & Erickson, E. F. 1991, ApJ, 374, 564

Sakai, S., Madore, B. F., & Freedman, W. L. 1999, ApJ, 511, 671

Salpeter, E. E. 1955, ApJ, 121, 161

Sandage, A. & Tammann, G. A. 1974, ApJ, 194, 559

Sanna, N., Bono, G., Stetson, P. B., et al. 2009, ApJLett, 699, L84

Sauvage, M., Vigroux, L., & Thuan, T. X. 1990, A&A, 237, 296

Savage, B. D. & Mathis, J. S. 1979, ARA&A, 17, 73

Savage, B. D. & Sembach, K. R. 1996, ApJ, 470, 893

Schaller, G., Schaerer, D., Meynet, G., & Maeder, A. 1992, A&AS, 96, 269

Schinnerer, E., Meidt, S. E., Pety, J., et al. 2013, ApJ, 779, 42

Schruba, A., Leroy, A. K., Walter, F., et al. 2012, AJ, 143, 138

Shaw, G., Ferland, G. J., Abel, N. P., Stancil, P. C., & van Hoof, P. A. M. 2005, ApJ, 624, 794

Shetty, R., Glover, S. C., Dullemond, C. P., & Klessen, R. S. 2011, MNRAS, 412, 1686

Shostak, G. S. & Skillman, E. D. 1989, A&A, 214, 33

Smith, J. D. T., Armus, L., Dale, D. A., et al. 2007, PASP, 119, 1133

Smith, J. D. T., Croxall, K., Draine, B., et al. 2017, ApJ, 834, 5

Spinoglio, L., Pereira-Santaella, M., Dasyra, K. M., et al. 2015, ApJ, 799, 21

Thuan, T. X. & Martin, G. E. 1981, ApJ, 247, 823

Thurow, J. C. & Wilcots, E. M. 2005, AJ, 129, 745

Tielens, A. G. G. M. 2005, The Physics and Chemistry of the Interstellar Medium

Tielens, A. G. G. M. & Hollenbach, D. 1985, ApJ, 291, 722

Tielens, A. G. G. M. & Hollenbach, D. J. 1993, in IAU Symposium, Vol. 155, Planetary Nebulae, ed. R. Weinberger & A. Acker, 155

Tosi, M., Aloisi, A., Mack, J., & Maio, M. 2007, in IAU Symposium, Vol. 235, Galaxy Evolution across the Hubble Time, ed. F. Combes & J. Palouš, 65–66

Vacca, W. D., Sheehy, C. D., & Graham, J. R. 2007, ApJ, 662, 272

van Hoof, P. A. M., Weingartner, J. C., Martin, P. G., Volk, K., & Ferland, G. J. 2004, in Astronomical Society of the Pacific Conference Series, Vol. 313, Asymmetrical Planetary Nebulae III: Winds, Structure and the Thunderbird, ed. M. Meixner, J. H. Kastner, B. Balick, & N. Soker, 380

Wang, Q. D., Whitaker, K. E., & Williams, R. 2005, MNRAS, 362, 1065

Weingartner, J. C. & Draine, B. T. 2001, ApJ, 548, 296

Werner, M. W., Roellig, T. L., Low, F. J., et al. 2004, ApJS, 154, 1

Wilcots, E. M. & Miller, B. W. 1998, AJ, 116, 2363

Wilson, C. D., Warren, B. E., Israel, F. P., et al. 2009, ApJ, 693, 1736

Wolfire, M. G., Hollenbach, D., & McKee, C. F. 2010, ApJ, 716, 1191

Wolfire, M. G., Tielens, A. G. G. M., & Hollenbach, D. 1990, ApJ, 358, 116

Yin, J., Magrini, L., Matteucci, F., et al. 2010, A&A, 520, A55

Ysard, N., Juvela, M., & Verstraete, L. 2011, A&A, 535, A89

Zubko, V., Dwek, E., & Arendt, R. G. 2004, ApJS, 152, 211

université PARIS-SACLAY

ÉCOLE DOCTORALE
Astronomie et Astrophysique d'île-de-France

Titre : Propriétés du milieu interstellaire dans la galaxie à formation d'étoiles IC 10 à diverses échelles spatiales

Mots clefs : milieu interstellaire, faible métallicité, régions HII, raie de refroidissement de structure fine

Résumé : Les propriétés du milieu interstellaire (MIS) influencent fortement l'environnement et les processus menant à la formation d'étoiles qui, à son tour, dicte l'évolution d'une galaxie. Les galaxies naines du Groupe Local sont de parfaits laboratoires pour comprendre comment le contenu en métaux (ou métallicité) du MIS affecte l'interaction entre le gaz, la poussiére et les étoiles. Mon travail de thése porte sur les propriétés physiques des régions HII et du gaz diffus ionisé de la galaxie naine IC 10, de métallicité 1/3 solaire. La proximité de cette galaxie (d=700kpc) permet l'analyse du MIS à différentes échelles spatiales: des nuages brillants compacts (∼25pc) au corps entier de la galaxie formant des étoiles (∼650pc). Afin de mesurer les propriétés physiques du MIS, j'ai modélisé les raies d'émission en infrarouge observées avec *Spitzer* et *Herschel* grâce é des modéles de photoionisation et de photodissociation. Je présente une exploration compléte de plusieurs méthodes pour déterminer, de maniére la plus fiable et selon les contraintes disponibles, les propriétés du MIS à diverses échelles. J'ai contraint les propriétés des nuages compacts les plus brillants dans IC 10 et montré que l'émission à plus grande échelle (∼300pc) est dominée par celle de ces nuages. Enfin, je démontre le besoin d'un modéle à plusieurs composantes pour reproduire les observations dans leur ensemble.

Title : Properties of the interstellar medium of the star-forming galaxy, IC 10, at various spatial scales

Keywords : interstellar medium, low-metallicity, HII regions, fine-structure cooling lines

Abstract : The properties of the Inter Stellar Medium (ISM) strongly influence the environment and processes that lead to star-formation, which in turn, drives the evolution of a galaxy. Dwarf galaxies in the Local Group are perfect laboratories to investigate how the metal-poor ISM affects the interplay between gas, dust and stars. In this thesis I investigates the properties of the HII regions and the diffuse ionized gas of the nearby dwarf galaxy IC 10, which has a metallicity of 1/3 solar. Its proximity (d=700 kpc) enables the analysis on different spatial scales: from the compact clumps (∼25 pc) to the whole star-forming body of the galaxy (∼650pc). In order to measure the physical properties of the ISM, I model the infrared emission lines observed with Spitzer and Herschel, with photoionization and photodissociation models. I present an extensive exploration of different methods to determine the most reliable ISM properties, based on the available constraints. I determined the properties of the brightest star-forming clumps within the galaxy and show that the emission at large scales (∼300 pc) is dominated by that of the compact, bright clumps that lie within the region. I further demonstrate the need for a multi-component model to fully reproduce the observations.

Université Paris-Saclay
Espace Technologique / Immeuble Discovery
Route de l'Orme aux Merisiers RD 128 / 91190 Saint-Aubin, France